



**University of
Nottingham**

UK | CHINA | MALAYSIA

THE UNIVERSITY OF NOTTINGHAM

Department of Mechanical, Materials and Manufacturing Engineering,

Faculty of Science and Engineering

**Vibration Transmission and Power Flow in Nonlinear
Smooth and Non-smooth Dynamical Systems**

by

Wei Dai

Submitted to the University of Nottingham for the degree of Doctor of Philosophy

January 2021

Vibration power flow analysis (PFA) approach has been widely used as a tool for investigating the dynamic behaviour of coupled structures and complex systems. There have been numerous PFA studies on linear systems; however, limited research has been reported on the power flow behaviour of nonlinear systems, especially on the nonlinear non-smooth systems. This research attempts to address the issue by seeking a deeper understanding of the effects of smooth and non-smooth nonlinearities on vibration transmission and power flow in nonlinear dynamical systems, and for an improved design of nonlinear isolation structures to obtain better vibration mitigation performance based on the findings from PFA.

The vibration transmission characteristics of non-smooth impact oscillators with linear constraint and different types of geometrically nonlinear motion constraints are firstly investigated. It is shown that the inclusion of nonlinear motion constraint can lead to a higher proportion of the input power dissipated at the interface compared to that of the linear constraint. The nonlinear constraints can be designed to tailor the level of force transmission and vibration power flow near the peak frequencies. The use of force transmissibility and time-averaged power flow as measures of the vibration transmission level may result in different evaluation outcomes. Nonlinear constraint can lead to bifurcations as well as super-harmonic and sub-harmonic response components. Secondly, the vibration mitigation performance of a nonlinear isolation system with a geometrically nonlinear element based on linkage mechanism is studied. It is found that the addition of the nonlinear element to a linear isolator can enlarge the effective isolation frequency range and bring about softening effect on the system. The curves of frequency response, force transmissibility and power transmission are shifted to the low-frequency range and the peaks of the curves can bend to the low frequencies with possibly reduced peak values. Thirdly, the dynamic behaviour of the non-smooth friction oscillators is explored from the vibration energy perspective. It is shown that the discontinuous dry friction nonlinearity can lead to a significant increase in the force transmissibility, energy transfer and energy dissipation at high frequencies, while there are slight reductions in the peak values of these indices. The findings from this study contribute to an enhanced understanding of vibration transmission and power flow characteristics within both smooth and non-smooth nonlinear dynamical systems and assist dynamic design of engineering systems for better performance.

Keywords: non-smooth systems; vibration transmission; nonlinear vibration isolation; force transmissibility; vibration power flow; geometric nonlinearity

Contents

Abstract.....	ii
Contents	iii
List of Figures.....	vi
Acknowledgements.....	xiii
Acronyms.....	xiv
Nomenclature.....	xv
Chapter 1 Introduction.....	1
1.1. Engineering background	1
1.2. Current state of research.....	4
1.3. Motivations of the research	6
1.4. Aims and objectives	8
1.5. Thesis outline	8
Chapter 2 Literature review.....	11
2.1. Overview of the evaluation methods on vibration transmission	11
2.2. Review of energy transmission analysis	15
2.2.1. Statistical energy analysis approach	15
2.2.2. Analytical PFA approaches	16
2.2.3. FEA and Substructure approach	19
2.2.4. PFA in nonlinear systems	21
Chapter 3 Methodologies	23
3.1. General vibration transmission formulations	23
3.1.1. Force transmissibility formulations	23
3.1.2. Power flow formulations	24
3.2. Numerical integration methods	25
3.2.1. Fourth-order Runge-Kutta method	25
3.2.2. Adaptive Runge-Kutta method	26
3.3. Harmonic balance approximations.....	27
3.3.1. Harmonic balance method	27
3.3.2. Alternating frequency/time domain technique.....	30
3.4. Numerical continuation method.....	31
3.5. Exemplary application to a 2DOF coupled Duffing oscillator system.....	35
3.5.1. Mathematical model and frequency response.....	35
3.5.2. Force transmissibility and PFA analysis.....	38

3.6. Summary	35
Chapter 4 Vibration transmission analysis of impact oscillators with linear and nonlinear QZS constraints	41
4.1. SDOF impact oscillator with a linear constraint	42
4.1.1. Mathematical modelling	42
4.1.2. Vibration transmission analysis	46
4.1.3. Effects of linear constraint.....	47
4.2. SDOF impact oscillator with a nonlinear QZS constraint.....	50
4.2.1. Mathematical modelling	50
4.2.2. Vibration transmission analysis	52
4.2.3. Effects of nonlinear QZS constraint	52
4.3. A 2DOF impact oscillator with a linear or nonlinear constraint	55
4.3.1. Mathematical modelling	55
4.3.2. Vibration transmission analysis	58
4.3.3. A 2DOF impact oscillator with a linear constraint	59
4.3.4. A 2DOF impact oscillator with a QZS nonlinear constraint.....	65
4.4. Summary	69
Chapter 5 Vibration transmission analysis of impact oscillators with nonlinear motion constraints created by DSLM	70
5.1. Mathematical model.....	71
5.1.1. Nonlinear constraint based on DSLM	71
5.1.2. Impact oscillators with the nonlinear constraint	73
5.2. SDOF impact oscillator with the nonlinear constraint	75
5.2.1. Dynamic response.....	75
5.2.2. Force transmissibility and vibration power flow	78
5.3. 2DOF impact oscillators with multiple nonlinear constraints.....	80
5.3.1. The model and power flow formulations.....	80
5.3.2. Use of constraint C1 only	83
5.3.3. Two constraints case with C1 and C2.....	90
5.3.4. Two-sided constraints case with C1 and C3	95
5.4. Summary	102
Chapter 6 Vibration energy flow and force transmissibility of nonlinear isolators with nonlinear spring based on DSLM.....	103
6.1. Nonlinear stiffness mechanism	104
6.2. SDOF nonlinear isolator for force excitations	106
6.2.1. Mathematical model	106
6.2.2. Nonlinear analysis	110

6.2.3.	Performance indices.....	110
6.2.4.	Performance evaluations.....	111
6.3.	SDOF nonlinear isolator for base excitations.....	118
6.3.1.	Mathematical model	118
6.3.2.	Performance indices.....	119
6.3.3.	Performance evaluations.....	119
6.4.	2DOF nonlinear isolation system for force excitation	124
6.4.1.	Mathematical model	124
6.4.2.	Performance indices.....	126
6.4.3.	Performance evaluations.....	127
6.5.	Summary	134
Chapter 7	Vibration transmission and energy flow analysis of oscillators with Coulomb friction element.....	135
7.1.	Mathematical modelling.....	136
7.1.1.	Dry friction force models.....	136
7.1.2.	Dynamic analysis of systems with dry friction.....	138
7.2.	SDOF system with friction.....	141
7.2.1.	Dynamic response.....	141
7.2.2.	Force transmission and power flow	145
7.3.	2DOF system with friction at the interface	151
7.3.1.	Mathematical modelling	151
7.3.2.	Force transmission and power flow formulations.....	153
7.3.3.	Dynamics and power flow results.....	154
7.4.	Summary	164
Chapter 8	Conclusions and future work	166
8.1.	Conclusions	166
8.2.	Future work	170
Appendix	List of publications	171
Bibliography	172

List of Figures

Figure 2.1. Schematic of the 2DOF linear isolation system.....	12
Figure 2.2. The force transmissibility TR_B to the base structure.	13
Figure 2.3. A SDOF force-excited oscillator on a flexible foundation (Goyder and White, 1980c).	14
Figure 3.1. Algorithm of alternating frequency/time domain scheme for the treatment of nonlinear force.	31
Figure 3.2. Algorithm of pseudo-arclength continuation method.	32
Figure 3.3. Schematic of procedures of harmonic balance approximation in conjunction with the numerical continuations.....	34
Figure 3.4. Schematic of a 2DOF coupled Duffing oscillator system (Shi and Yang, 2019) ...	35
Figure 3.5. The steady-state response amplitude results of (a) X_{1_amp} for the primary mass and (b) X_{2_amp} for the secondary mass. The solid line is HB-AFT result and symbols are the RK results.	37
Figure 3.6. Comparison between HB-AFT method and RK method on the result of (a) the force transmissibility TR_S , (b) the time-averaged input power \bar{P}_{in} , (c) the time-averaged transmitted power \bar{P}_{ts} and (d) the time-averaged dissipated power \bar{P}_{d3} . The solid line is HB-AFT result and symbols are the RK results.	39
Figure 4.1. A schematic representation of an SDOF impact oscillator with a linear constraint.	42
Figure 4.2. Approximation of the Heaviside function using Fourier expansion ($\delta = 0.4 + 0.8\cos\theta$). Solid line: exact value of $U(\delta)$; dotted line: first order expansion; dashed line: 2nd order expansion.....	44
Figure 4.3. Effects of (a) stiffness and (b) damping properties of the linear constraint on the maximum displacement X_{1_max} . The solid line and circles, dashed line and triangles, dotted line and squares, dash-dot lines and rhombuses are for $\lambda = 0, 0.5, 1$ and 2 , respectively in (a), and for $\rho = 0, 1, 2$ and 5 , respectively in (b).	47
Figure 4.4. Effects of stiffness and damping properties of the linear constraint on force transmissibility TR_L and TR_R . The solid line and circles, dashed line and triangles, dotted line and squares, dash-dot lines and rhombuses are for $\lambda = 0, 0.5, 1$ and 2 , respectively, in (a) and (b), and for $\rho = 0, 1, 2$ and 5 , respectively, in (c) and (d). 48	
Figure 4.5. Effects of linear constraint on the power flow behaviour. Influence of (a) constraint stiffness on \bar{P}_{in} , and constraint damping on (b) \bar{P}_{in} , (c) \bar{P}_{dc} and (d) R_{ac} . In (a), solid line and circles, dashed line and triangles, dotted line and squares, and dash-dot line and rhombuses for $\lambda = 0, 0.5, 1$ and 2 , respectively; In (b), (c) and (d), dashed line and triangles, dotted line and squares, and dash-dot line and rhombuses are for $\rho =$ $1, 2$ and 5 , respectively.	49
Figure 4.6. A schematic representation of an SDOF impact oscillator with a nonlinear constraint.	50
Figure 4.7. Effects of (a) spring length ratio α and (b) spring stiffness ratio β of the nonlinear constraint on the maximum displacement X_{1_max} . In (a), the solid, dashed and dotted lines for $\alpha = 1.0, 1.5$ and 2 , respectively; In (b), the solid, dashed and dotted lines are for $\beta = 0, 0.5$ and 1 , respectively.	53
Figure 4.8. Effects of spring length ratio α and spring stiffness ratio β of the nonlinear constraint on TR_L and TR_R , respectively. In (a) and (c), the solid, dashed and dotted lines for $\alpha = 1.0, 1.5$ and 2 , respectively; In (b) and (d), the solid, dashed and dotted lines are for $\beta = 0, 0.5$ and 1 , respectively. Symbols: RK results.....	54

Figure 4.9. Effects of spring length ratio α and spring stiffness ratio β of the nonlinear constraint on \bar{P}_{in} and R_{ac} . In (a) and (c), the solid, dashed and dotted lines for $\alpha = 1.0, 1.5$ and 2 , respectively; In (b) and (d), the solid, dashed and dotted lines are for $\beta = 0, 0.5$ and 1 , respectively. Symbols: RK results.	55
Figure 4.10. A 2DOF impact oscillator with a linear or nonlinear constraint. (a) A schematic representation, (b) a linear constraint and (c) a nonlinear constraint.	56
Figure 4.11. Effects of the linear constraint on X_{1_max} and $ X_1 - X_2 _{max}$. In (a) and (b), the solid, dashed, dotted and dash-dot lines for $\lambda = 0, 0.5, 1$ and 2 , respectively; In (c) and (d), the solid, dashed, dotted and dash-dot lines are for $\rho = 0, 1, 2$ and 5 , respectively. Symbols: RK results.	60
Figure 4.12. Effects of the linear constraint on force transmissibility TR_L and TR_S . In (a) and (b), the solid, dashed, dotted and dash-dot lines for $\lambda = 0, 0.5, 1$ and 2 , respectively; In (c) and (d), the solid, dashed, dotted and dash-dot lines are for $\rho = 0, 1, 2$ and 5 , respectively. Symbols: RK results.	62
Figure 4.13. Effects of the linear constraint on \bar{P}_t and \bar{P}_{d3} . In (a) and (b), the solid, dashed, dotted and dash-dot lines for $\lambda = 0, 0.5, 1$ and 2 , respectively; In (c) and (d), the solid, dashed, dotted and dash-dot lines are for $\rho = 0, 1, 2$ and 5 , respectively. Symbols: RK results.	63
Figure 4.14. Effects of the linear constraint on displacement response, F_{ts} and P_{d3} at $\Omega = 1.0$ for $\lambda = 0$ in (a)-(c) and for $\lambda = 1$ in (d)-(f). (a) and (d): displacement response; (b) and (e): transmitted force F_{ts} ; (c) and (f): P_{d3} . For (a) and (d), the solid, dashed and dotted lines for X_1, X_2 , and $X_1 - X_2$ respectively.....	64
Figure 4.15. Effects of the nonlinear constraint on the maximum displacement X_{1_max} and $ X_1 - X_2 _{max}$. the solid, dashed and dotted lines for $K_2 = 0, 0.2$ and 1 with $K_1 = 0$, respectively. The dash-dot line is for $K_1 = 1$ and $K_2 = 0$. Symbols: RK results..	65
Figure 4.16. Effects of the nonlinear constraint on the force transmissibilities T_{RL} and T_{RS} . the solid, dashed and dotted lines for $K_2 = 0, 0.2$ and 1 with $K_1 = 0$, respectively. The dash-dot line is for $K_1 = 1$ and $K_2 = 0$. Symbols: RK results.....	67
Figure 4.17. Effects of the nonlinear constraint on the (a) power transmission \bar{P}_t , (b) power dissipation ratio of R_{d2} , (c) power dissipation \bar{P}_{d3} at the interface and (d) power dissipation ratio of R_{d3} . The solid, dashed and dotted lines for $K_2 = 0, 0.2$ and 1 while $K_1 = 0$, respectively. The dash-dot line is for the case with $K_1 = 1$ and $K_2 = 0$. Symbols: RK results.	68
Figure 5.1. Schematics of the nonlinear constraint (a) with the spring un-stretched and (b) subjected to a force.	71
Figure 5.2. Variations of the dimensionless (a) restoring force F_r and (b) stiffness K_r with respect to the distance Y between the two ends of the nonlinear constraint. The solid, dashed, dotted and dash-dotted lines are for cases with $Y_0 = 0.3, 0.5, 0.7$ and 0.8 , respectively.	73
Figure 5.3. (a) A SDOF impact oscillator with a nonlinear constraint, and (b) a linear spring constraint.....	75
Figure 5.4. Effects of the spring stiffness ratio λ and the initial angle θ_0 of the nonlinear constraint on (a) and (c): the steady-state oscillating position of the mass R_0 , and on (b) and (d): the response amplitude X_{1_amp} . In (a) and (b), the solid, dashed and dotted lines are for nonlinear constraint with $\lambda = 0, 1$ and 2 , respectively. The dash-dot line is for linear constraint with $\lambda = 1$; in (c) and (d), the solid, dashed, dotted and dash-dot lines are for $\theta_0 = 20, 30, 45$ and 60 degrees, respectively. Symbols: RK results.	77
Figure 5.5. Effects of (a) the spring stiffness ratio λ and (b) the initial angle θ_0 of the nonlinear constraint on the force transmissibility TR_R . In (a), the solid, dashed and dotted lines	

are for nonlinear constraint with $\lambda = 0, 1$ and 2 , respectively. The dash-dot line is for linear constraint with $\lambda = 1$; in (b), the solid, dashed, dotted and dash-dot lines are for $\theta_0 = 20, 30, 45$ and 60 degrees, respectively. Symbols: RK results. 79

Figure 5.6. Effects of the spring stiffness λ and the initial angle θ_0 of the nonlinear constraint on (a) and (c): the time-averaged input power \bar{P}_{in} , and on (b) and (d): the maximum kinetic energy K_1 . In (a) and (b), the solid, dashed and dotted lines are for nonlinear constraint with $\lambda = 0, 1$ and 2 , respectively. The dash-dot line is for linear constraint with $\lambda = 1$; in (c) and (d), the solid, dashed, dotted and dash-dotted lines are for $\theta_0 = 20, 30, 45$ and 60 degrees, respectively. Symbols: RK results. 80

Figure 5.7. (a) A 2DOF impact oscillator with linear or nonlinear constraints, (b) nonlinear constraint and (c) linear spring constraint. 81

Figure 5.8. Effects of the nonlinear constraint on (a) and (c): $X_{1,max}$, and on (b) and (d): $|X_1 - X_2|_{max}$. In (a) and (b), the solid, dashed and dotted lines are for the nonlinear constraint with $\lambda = 0, 1$ and 2 , respectively. The dash-dot line is for linear constraint with $\lambda = 1$; in (c) and (d), the solid, dashed, dotted and dash-dotted lines are for $\theta_0 = 20, 30, 45$ and 60 degrees, respectively. Symbols: RK results. 85

Figure 5.9. Effects of (a) the spring stiffness ratio λ and (b) the initial angle θ_0 of the nonlinear constraint on the force transmissibility TR_S . In (a), the solid, dashed and dotted lines are for nonlinear constraint with $\lambda = 0, 1$ and 2 , respectively. The dash-dot line is for linear constraint with $\lambda = 1$; in (b), the solid, dashed, dotted and dash-dotted lines are for $\theta_0 = 20, 30, 45$ and 60 degrees, respectively. Symbols: RK results. . 86

Figure 5.10. Effects of nonlinear constraint on (a) and (c): \bar{P}_{ts} , and on (b) and (d): \bar{P}_{di} . In (a) and (b), the solid, dashed and dotted lines are for nonlinear constraint with $\lambda = 0, 1$ and 2 , respectively. The dash-dot line is for linear constraint with $\lambda = 1$; in (c) and (d), the solid, dashed, dotted and dash-dotted lines are for $\theta_0 = 20, 30, 45$ and 60 degrees, respectively. Symbols: RK results. 87

Figure 5.11. Effects of (a) the spring stiffness ratio λ and (b) the initial angle θ_0 of the nonlinear constraint on the power dissipation ratio R_{di} . In (a), the solid, dashed and dotted lines are for nonlinear constraint with $\lambda = 0, 1$ and 2 , respectively. The dash-dot line is for linear constraint with $\lambda = 1$; in (b), the solid, dashed, dotted and dash-dotted lines are for $\theta_0 = 20, 30, 45$ and 60 degrees, respectively. Symbols: RK results. . 88

Figure 5.12. Steady-state response of the mass m_1 in the 2DOF impact oscillator with nonlinear constraint C1, excited at $\Omega = 0.94$ for (b)-(c), and at $\Omega = 0.96$ for (d)-(f). (a): bifurcation diagram; (b) and (e): Poincare sections; (c) and (f): frequency spectra of response displacement X_1 ; (d): phase diagram. 89

Figure 5.13. Effects of nonlinear constraints C1 and C2 on (a) and (c): $X_{1,max}$, and on (b) and (d): $|X_1 - X_2|_{max}$. In (a) and (b), the solid, dashed and dotted lines are for nonlinear constraints with $\lambda = 0, 1$ and 2 , respectively. The dash-dot line is for linear constraints with $\lambda = 1$; in (c) and (d), the solid, dashed, dotted and dash-dotted lines are for $\theta_0 = 20, 30, 45$ and 60 degrees, respectively. Symbols: RK results. 91

Figure 5.14. Effects of (a) the spring stiffness ratio λ and (b) the initial angle θ_0 of the nonlinear constraints C1 and C2 on the force transmissibility TR_S . In (a), the solid, dashed and dotted lines are for nonlinear constraints with $\lambda = 0, 1$ and 2 , respectively. The dash-dot line is for linear constraints with $\lambda = 1$; in (b), the solid, dashed, dotted and dash-dotted lines are for $\theta_0 = 20, 30, 45$ and 60 degrees, respectively. Symbols: RK results. 92

Figure 5.15. Effects of nonlinear constraints C1 and C2 on (a) and (c): \bar{P}_{ts} , and on (b) and (d): \bar{P}_{di} . In (a) and (b), the solid, dashed and dotted lines are for nonlinear constraints with $\lambda = 0, 1$ and 2 , respectively. The dash-dot line is for linear constraints with $\lambda = 1$; in (c) and (d), the solid, dashed, dotted and dash-dotted lines are for $\theta_0 = 20, 30, 45$ and 60 degrees, respectively. Symbols: RK results. 94

Figure 5.16. Effects of (a) the spring stiffness ratio λ and (b) the initial angle θ_0 of the nonlinear constraints C1 and C2 on the power dissipation ratio R_{di} . In (a), the solid, dashed, and dotted lines are for nonlinear constraints with $\lambda = 0, 1$ and 2 , respectively. The dash-dot line is for linear constraints with $\lambda = 1$; in (b), the solid, dashed, dotted and dash-dotted lines are for $\theta_0 = 20, 30, 45$ and 60 degrees, respectively. Symbols: RK results. 94

Figure 5.17. Effects of nonlinear constraints C1 and C3 on (a) and (c): $X_{1,max}$, and on (b) and (d): $|X_1 - X_2|_{max}$. In (a) and (b), the solid, dashed, and dotted lines are for nonlinear constraints with $\lambda = 0, 1$ and 2 , respectively. The dash-dot line is for linear constraints with $\lambda = 1$; in (c) and (d), the solid, dashed, dotted and dash-dotted lines are for $\theta_0 = 20, 30, 45$ and 60 degrees, respectively. Symbols: RK results. 96

Figure 5.18. Effects of (a) the spring stiffness ratio λ and (b) the initial angle θ_0 of the nonlinear constraints C1 and C3 on the force transmissibility TR_S . In (a), the solid, dashed, and dotted lines are for nonlinear constraints with $\lambda = 0, 1$ and 2 , respectively. The dash-dot line is for linear constraints with $\lambda = 1$; in (b), the solid, dashed, dotted and dash-dotted lines are for $\theta_0 = 20, 30, 45$ and 60 degrees, respectively. Symbols: RK results. 97

Figure 5.19. Effects of nonlinear constraints C1 and C3 on (a) and (c): \bar{P}_{ts} , and on (b) and (d): \bar{P}_{di} . In (a) and (b), the solid, dashed and dotted lines are for nonlinear constraints with $\lambda = 0, 1$ and 2 , respectively. The dash-dot line is for linear constraints with $\lambda = 1$; in (c) and (d), the solid, dashed, dotted and dash-dotted lines are for $\theta_0 = 20, 30, 45$ and 60 degrees, respectively. Symbols: RK results. 99

Figure 5.20. Effects of (a) the spring stiffness ratio λ and (b) the initial angle θ_0 of the nonlinear constraints C1 and C3 on the power dissipation ratio R_{di} . In (a), the solid, dashed and dotted lines are for nonlinear constraints with $\lambda = 0, 1$ and 2 , respectively. The dash-dot line is for linear constraints with $\lambda = 1$; in (b), the solid, dashed, dotted and dash-dotted lines are for $\theta_0 = 20, 30, 45$ and 60 degrees, respectively. Symbols: RK results. 99

Figure 5.21. Effects of the damping ratio ζ_1 of the primary system on (a): $X_{1,max}$ and on (b): $|X_1 - X_2|_{max}$. The solid, dashed, dotted and dash-dot lines are for $\zeta_1 = 0.02$ and $\epsilon = 1.0$, $\zeta_1 = 0.04$ and $\epsilon = 0.5$, $\zeta_1 = 0.10$ and $\epsilon = 0.2$, and $\zeta_1 = 0.20$ and $\epsilon = 0.1$, respectively. Symbols: RK results.. 100

Figure 5.22. Effects of the damping ratio ζ_1 of the primary system on (a): the force transmissibility TR_S , (b): the power transmission \bar{P}_{ts} , (c): the power dissipation \bar{P}_{di} and (d): the power dissipation ratio R_{di} . The solid, dashed, dotted and dash-dot lines are for $\zeta_1 = 0.02$ and $\epsilon = 1.0$, $\zeta_1 = 0.04$ and $\epsilon = 0.5$, $\zeta_1 = 0.10$ and $\epsilon = 0.2$, and $\zeta_1 = 0.20$ and $\epsilon = 0.1$, respectively. Symbols: RK results... 101

Figure 6.1. Schematic of the nonlinear D-spring (a) with the horizontal spring un-stretched, and (b) subjected to a force..... 104

Figure 6.2. Variations of the dimensionless (a) restoring force F_r and (b) stiffness K_r of the nonlinear D-spring against the dimensionless terminals distance Y . The solid, dashed, dotted and dash-dotted lines are for $Y_0 = 0.3, 0.5, 0.7$ and 0.8 , respectively. 106

Figure 6.3. Schematic of a nonlinear isolator with the D-spring for isolation of force excitation. 107

Figure 6.4. Effects of the nonlinear D-spring on (a) and (c): the dimensionless linearized dynamic stiffness K_L , and on (b) and (d): dimensionless linearized natural frequency Ω_L . In (a) and (b), The solid line, dashed line, dotted line and dash-dotted line are for $\lambda = 0, 1, 2$ and 3 , respectively; in (c) and (d), The solid line, dashed line, dotted line and dash-dotted line are for $Y_0 = 0.3, 0.5, 0.7$ and 0.8 , respectively. 109

Figure 6.5. Effects of (a) the spring stiffness ratio λ and (b) the initial angle θ_0 of the nonlinear D-spring on the steady-state response amplitude of the mass $X_{1,amp}$. In (a), the solid,

	dashed, dotted and dash-dotted lines are for $\lambda = 0, 3, 4$ and 5 , respectively; in (b), The solid, dashed, dotted and dash-dotted lines are for $\theta_0 = 30, 45, 55$ and 60 degrees, respectively. Symbols: RK results.	113
Figure 6.6.	Effects of (a) the spring stiffness ratio λ and (b) the initial angle θ_0 of the nonlinear D-spring on the force transmissibility TR_G . In (a), The solid, dashed, dotted and dash-dotted lines are for $\lambda = 0, 3, 4$ and 5 , respectively; in (b), The solid, dashed, dotted and dash-dotted lines are for $\theta_0 = 30, 45, 55$ and 60 degrees, respectively. Symbols: RK results.	114
Figure 6.7.	Time history of the dimensionless total transmitted force F_{tG} and the dimensionless displacement response of the mass X_1 with the system parameters set as (a) $\lambda = 5, \theta_0 = 45^\circ, F_0=0.002, \Omega = 0.75$, and (b) $\lambda = 2$ and $\theta_0 = 60^\circ, F_0=0.0025, \Omega = 0.5$, respectively; The solid line and the dashed line are the dimensionless response X_1 and the dimensionless total transmitted force F_{tG} , respectively.....	115
Figure 6.8.	Effects of (a) the spring stiffness ratio λ and (b) the initial angle θ_0 of the nonlinear D-spring on the maximum kinetic energy K_1 . In (a), The solid, dashed, dotted and dash-dotted lines are for $\lambda = 0, 3, 4$ and 5 , respectively; in (b), The solid, dashed, dotted and dash-dotted lines are for $\theta_0 = 30, 45, 55$ and 60 degrees, respectively. Symbols: RK results.	116
Figure 6.9.	Effects of (a) the spring stiffness ratio λ on \bar{P}_{in} , and the distance Y_1 on (b) the steady-state response amplitude X_{1_amp} , (c) the force transmissibility TRG and (d) the maximum kinetic energy K_1 . In (a), the solid, dashed, dotted and dash-dotted lines are for $\lambda = 0, 3, 4$ and 5 , respectively; in (b-d), the solid, dashed, dotted and dash-dotted lines are for $Y_1 = 0.3, 0.4, 0.5$ and 0.6 , respectively. Symbols: RK results.	117
Figure 6.10.	Schematic of a nonlinear isolator with the D-spring for isolation of base excitation.	118
Figure 6.11.	Effects of (a) the spring stiffness ratio λ and (b) the initial angle θ_0 of the nonlinear D-spring on the steady-state response amplitude of the mass X_{1_amp} . In (a), The solid, dashed, dotted and dash-dotted lines are for $\lambda = 0, 3, 4$ and 5 , respectively; in (b), The solid, dashed, dotted and dash-dotted lines are for $\theta_0 = 30, 45, 55$ and 60 degrees, respectively. Symbols: RK results.	120
Figure 6.12.	Effects of (a) the spring stiffness ratio λ and (b) the initial angle θ_0 of the nonlinear D-spring on the force transmissibility TR_B . In (a), The solid, dashed, dotted and dash-dotted lines are for $\lambda = 0, 3, 4$ and 5 , respectively; in (b), The solid, dashed, dotted and dash-dotted lines are for $\theta_0 = 30, 45, 55$ and 60 degrees, respectively. Symbols: RK results.	121
Figure 6.13.	Effects of (a) the spring stiffness ratio λ and (b) the initial angle θ_0 of the nonlinear D-spring on the maximum kinetic energy K_1 . In (a), The solid, dashed, dotted and dash-dotted lines are for $\lambda = 0, 3, 4$ and 5 , respectively; in (b), The solid, dashed, dotted and dash-dotted lines are for $\theta_0 = 30, 45, 55$ and 60 degrees, respectively. Symbols: RK results.	122
Figure 6.14.	Effects of spring stiffness ratio λ (a) on \bar{P}_{in} , and distance Y_1 on (b) X_{1_amp} , (c) TR_B and (d) K_1 . In (a), the solid, dashed, dotted and dash-dotted lines are for $\lambda = 0, 3, 4$ and 5 , respectively; in (c-d), the solid, dashed, dotted and dash-dotted lines are for $Y_1 = 0.3, 0.4, 0.5$ and 0.6 , respectively. Symbols: RK results.	123
Figure 6.15.	Schematic of a 2DOF nonlinear isolation system with the D-spring for isolation of force excitation.	124
Figure 6.16.	Effects of (a) the spring stiffness ratio λ and (b) the initial angle θ_0 of the nonlinear D-spring on the steady-state response amplitude X_{1_amp} of the machine mass. In (a), The solid, dashed, dotted and dash-dotted lines are for $\lambda = 0, 3, 4$ and 5 , respectively;	

	in (b), The solid, dashed, dotted and dash-dotted lines are for $\theta_0 = 30, 45, 55$ and 60 degrees, respectively. Symbols: RK results.	128
Figure 6.17.	Effects of nonlinear D-spring on (a) and (c): TR_B , and on (b) and (d): TR_G . In (a) and (b), The solid, dashed, dotted and dash-dotted lines are for $\lambda = 0, 3, 4$ and 5 , respectively; in (c) and (d), The solid line, dashed line, dotted line and dash-dotted line are for $\theta_0 = 30, 45, 55$ and 60 degrees, respectively. Symbols: RK results.	130
Figure 6.18.	Effects of (a) the spring stiffness ratio λ and (b) the initial angle θ_0 of the nonlinear D-spring on the time-averaged transmitted power to the base structure \bar{P}_{tB} . In (a), The solid, dashed, dotted and dash-dotted lines are for $\lambda = 0, 3, 4$ and 5 , respectively; in (b), The solid, dashed, dotted and dash-dotted lines are for $\theta_0 = 30, 45, 55$ and 60 degrees, respectively. Symbols: RK results.	130
Figure 6.19.	Effects of the terminals distance Y_1 of the D-spring on (a) the response amplitude X_{1_amp} , (b) the force transmissibility to the base structure TR_B , (c) the force transmissibility to the ground TR_G and (d) the time-averaged transmitted power to the base structure \bar{P}_{tB} . The solid, dashed, dotted and dash-dotted lines are for $Y_1 = 0.3, 0.4, 0.5$ and 0.6 , respectively. Symbols: RK results.	132
Figure 6.20.	Effects of (a) the spring stiffness ratio λ and (b) the initial angle θ_0 and (c) the terminals distance Y_1 of the nonlinear D-spring on the power dissipation ratio R_{tB} . In (a), The solid, dashed, dotted and dash-dotted lines are for $\lambda = 0, 3, 4$ and 5 , respectively; in (b), The solid, dashed, dotted and dash-dotted lines are for $\theta_0 = 30, 45, 55$ and 60 degrees, respectively; in (c), The solid, dashed, dotted and dash-dotted lines are for $Y_1 = 0.3, 0.4, 0.5$ and 0.6 , respectively. Symbols: RK results.	133
Figure 7.1.	Schematic of (a) dry friction between two solid contacting bodies, (b) dry friction element, (c) the classical Coulomb model and (d) the Karnopp model.	137
Figure 7.2.	Dry friction force f_c by the classical Coulomb friction model and by the smooth Coulomb friction model. The solid line is for the classical Coulomb friction model. The dashed, dotted and dash-dotted lines are for the smooth Coulomb friction model with $\epsilon = 0.1, 0.2$ and 0.3 , respectively.	138
Figure 7.3.	(a) A SDOF oscillator with (a) a dry friction element and (b) a viscous damper element.	141
Figure 7.4.	Effects of the dynamic friction force F_d on the steady-state response amplitude X_{1_amp} . The solid and dashed lines are for the linear system with $\rho = 0$ and 2 , respectively. The dotted and dash-dotted lines are for the nonlinear system having dry friction element with $F_d = 0.02$ and 0.04 , respectively.	143
Figure 7.5.	Time history of element force and response for friction element case in (a) and (b) with $F_d = 0.04$ and $\rho = 0$, and for viscous damper case in (c) and (d) with $F_d = 0$ and $\rho = 2$. The excitation frequency in (a) and (c) is $\Omega = 0.3$, while in (b) and (d) is $\Omega = 1$	144
Figure 7.6.	Effects of the dynamic friction force F_d on the force transmissibility TR_L . The solid and dashed lines are for the linear system with $\rho = 0$ and 2 , respectively. The dotted and dash-dotted lines are for the nonlinear system having dry friction element with $F_d = 0.02$ and 0.04 , respectively.	147
Figure 7.7.	Effects of the dynamic friction force F_d on (a) the time-averaged input power \bar{P}_{in} and (b) the maximum kinetic energy K_1 . The solid and dashed lines are for the linear system with $\rho = 0$ and 2 , respectively. The dotted and dash-dotted lines are for the nonlinear system having dry friction element with $F_d = 0.02$ and 0.04 , respectively.	148
Figure 7.8.	Effects of the dynamic friction force F_d on (a) the time-averaged dissipated power by the element \bar{P}_{de} and (b) the power dissipation ratio R_{de} . The solid and dashed lines are for the linear system with $\rho = 0$ and 2 , respectively. The dotted and dash-	

dotted lines are for the nonlinear system having dry friction element with $F_d = 0.02$ and 0.04 , respectively.	149
Figure 7.9. Instantaneous power flow indices against time for friction element case with $F_d = 0.04$ and $\rho = 0$ in (a) and (b) while for viscous damper case with $F_d = 0$ and $\rho = 2$ in (c) and (d) at $\Omega = 0.3$. In (a) and (c): the instantaneous input power P_{in} ; in (b) and (d): the instantaneous power dissipation by element P_{de} and by the system damper P_{d1}	150
Figure 7.10. (a) A 2DOF oscillator with (b) a dry friction element and (c) a viscous damper at coupling interface.	151
Figure 7.11. Effects of dynamic friction force F_d on the steady-state maximum response displacement (a) X_{1_max} for the primary mass and (b) X_{2_max} for the secondary mass, respectively. The solid and dashed lines are for the linear system with $\rho = 0$ and 4 , respectively. The dotted and dash-dotted lines are for the nonlinear system having dry friction element with $F_d = 0.10$ and 0.15 , respectively.	156
Figure 7.12. Time history of element force and the velocity responses in steady-state for the dry friction element case with $F_d = 0.15$, $\rho = 0$ at (a) $\Omega = 0.4$, (b) $\Omega = 1.41$, (d) $\Omega = 1.74$ and (e) $\Omega = 3$, respectively; For the viscous damper element case with $F_d = 0$, $\rho = 4$ at (c) $\Omega = 1.41$ and (f) $\Omega = 3$, respectively. The solid line is the dry friction force F_c by the friction element at the interface in (a), (b), (d) and (e), while in (c) and (f) is the damping force F_{cd} by the viscous damper element at the interface. The dashed line and dotted lines are the response velocity of the primary mass X'_1 and the secondary mass X'_2 , respectively.....	157
Figure 7.13. Effects of dynamic friction force F_d on the steady-state maximum relative response displacement $ X_1 - X_2 _{max}$ between two masses. The solid and dashed lines are for the linear system with $\rho = 0$ and 4 , respectively. The dotted and dash-dotted lines are for the nonlinear system having dry friction element with $F_d = 0.10$ and 0.15 , respectively.....	158
Figure 7.14. Effects of dynamic friction force F_d on (a) the force transmissibility to the secondary system TR_s and (b) the time-averaged input power \bar{P}_{in} into the system, respectively. The solid and dashed lines are for the linear system with $\rho = 0$ and 4 , respectively. The dotted and dash-dotted lines are for the nonlinear system having dry friction element with $F_d = 0.05$ and 0.15 , respectively.	160
Figure 7.15. Effects of dynamic friction force F_d on (a) the time-averaged transmitted power \bar{P}_{ts} to the secondary system and (b) the power transmission ratio R_{ts} , respectively. The solid and dashed lines are for the linear system with $\rho = 0$ and 4 , respectively. The dotted and dash-dotted lines are for the nonlinear system having dry friction element with $F_d = 0.05$ and 0.15 , respectively.....	161
Figure 7.16. Time history of the instantaneous transmitted power P_{ts} to the secondary system when the excited at $\Omega = 5$ for (a) the friction element case with $F_d = 0.15$ and $\rho = 0$ and for (b) the linear damper case with $F_d = 0$ and $\rho = 4$	162
Figure 7.17. Effects of dynamic friction force F_d on (a) the time-averaged dissipated power P_{di} at the interface and (b) the power transmission ratio R_{di} , respectively. The solid and dashed lines are for the linear system with $\rho = 0$ and 4 , respectively. The dotted and dash-dotted lines are for the nonlinear system having dry friction element with $F_d = 0.05$ and 0.15 , respectively.	163
Figure 7.18. Instantaneous dissipated power P_{di} for the dry friction element case with $F_d = 0.15$ and $\rho = 0$ in (a-c) and for the viscous damper element case with $F_d = 0$ and $\rho = 4$ in (d-f). The system is excited at $\Omega = 0.4$ in (a) and (c), at $\Omega = 1.74$ in (b) and (e), and at $\Omega = 5$ in (c) and (f).	164

Acknowledgements

I would like to express my sincere gratitude to my supervisor Dr. Jian Yang for his continuous guidance throughout my PhD study. His expertise, patience and encouragement have walked me through the tough times till this day of thesis completion. I would like to thank the rest of my supervision team, too, Dr. He Zhang, Dr. Dunant Halim and Dr. Zeyuan Xu for sharing their insightful suggestions and rendering me support whenever it is needed.

My sincere thanks also go to Prof. Chris Gerada, who provided me an opportunity to become a part of the Power Electronics, Machines and Control (PEMC) research group where I could widen my research from the perspective of multi-physics.

My thankfulness is extended to the colleagues and friends in the University of Nottingham, and I am particularly grateful for the assistance from Dr. Baiyang Shi, Dr. Weiduo Zhao, Mr. Yinli Wang and Mr. Chendi Zhu.

Last but not least, I would like to thank my parents and my girlfriend for their emotional support and enduring love in the pursuit of my goals. None of my personal achievements would have been possible without their care and encouragement.

Acronyms

AFT	alternating frequency/time domain
DOF	degree-of-freedom
DSLMM	diamond-shaped linkage mechanism
DFT	discrete Fourier transform
FE	finite element
FEA	finite element analysis
HB	harmonic balance
IDFT	inverse discrete Fourier transform
NSM	negative stiffness mechanism
MDOF	multiple degree-of-freedom
PFA	power flow analysis
QZS	quasi-zero-stiffness
RK	Runge-Kutta
RKDP	Runge-Kutta-Dormand-Prince
SEA	statistical energy analysis
SDOF	single-degree-of-freedom
SLS	scissor-like structure
LHS	left hand side
RHS	right hand side
2DOF	2 degree-of-freedom

Nomenclature

a	displacement response amplitude
c	damping coefficient
c_h	damping coefficient of the constraint
$[C]$	damping matrix;
$[\tilde{D}_n]$	dynamic stiffness matrix;
f_0	excitation force amplitude
f_d	nonlinear restoring force of the Duffing-type spring in Chapter 3; amplitude of the dynamic dry friction force in Chapter 7
f_D	nonlinear force of the D-spring
f_t	instantaneous transmitted force to the foundation
f_T	transmitted force from j -th DOF to $(j + 1)$ -th DOF
f_{dn}	dissipative force generated by the nonlinear element
F_{NC}	the nonlinear constraint force
$\{f_n\}$	nonlinear force vector
$\{f_{ex}\}$	external excitation force vector in Chapters 3, 4 and 5; external resultant force in Chapter 7;
$\{F_c\}$	nonlinear restoring force of the constraint in Chapters 4 and 5; dimensionless friction force in Chapter 7
F_{ex}	dimensionless external excitation force
F_r	dimensionless restoring force of the nonlinear constraint in Chapter 5; dimensionless restoring force of the D-spring in Chapter 6
h	step size for the RK method
j	j -th element in N -DOF system;
k	stiffness coefficient
k_{d1}	linear stiffness coefficient
k_{d2}	nonlinear stiffness coefficient
k_h	linear spring stiffness of the constraint

\dot{K}	rate of change of the kinetic energy
K_r	dimensionless stiffness of the constraint in Chapter 5; dimensionless stiffness of the D-spring in Chapter 6
K_L	linearized stiffness of the system
$[K]$	stiffness matrix;
K_1	maximum kinetic energy of the mass
l_b	length of each rod for the DSLM
l_s	original length of the linear spring in the DSLM
L_r	effective length of the rotor
m_1	mass of the base structure in Chapter 2; mass of the primary oscillator in Chapters 4, 5, 6 and 7
m_2	mass of the machine in Chapters 2; mass of the secondary oscillator in Chapters 4, 5 and 7; mass of the base structure in Chapter 6
$[M]$	mass matrix;
n	n -th order harmonic approximation
p_t	instantaneous power flow to the foundation
p_d	instantaneous power dissipation by the system damping
p_n	total rate of work by all nonlinear forces in the system
p_{in}	instantaneous input power by the external excitation forces
\bar{P}_{in}	time-averaged input power by the external excitation forces
P_t	instantaneous transmitted power
\bar{P}_t	time-averaged transmitted power to the foundation
\bar{P}_{ts}	time-averaged transmitted power
\bar{P}_d	time-averaged dissipated power by the system damping
\bar{P}_{di}	time-averaged dissipated power at the interface
\bar{P}_{dn}	time-averaged dissipated power by the dissipative nonlinear element
\bar{P}_{dc}	time-averaged dissipated power by the constraint

\bar{P}_{de}	time-averaged dissipated power by the element
Q	Q -DOF system;
R	Fourier coefficient of the response
R_{di}	power dissipation ratio at the interface
R_{de}	power dissipation ratio by the element
R_{tB}	power transmission ratio to the base structure
s	arclength in continuation method
t	physical time
TR	force transmissibility
\dot{U}	change rate of the potential energy stored in the system
\tilde{v}_t	instantaneous velocity of the foundation
v_r	relative sliding velocity of the contacting surfaces
V_d	dimensionless boundary velocity of the dead zone
x	displacement of subsystem
x_c	the initial gap between the mass and the constraint
X_{1_max}	maximum displacement response X_{1_max} of the primary mass
y	displacement response solution in Chapter 3; terminal distance of the DSLM in Chapters 5 and 6
Y	dimensionless terminal distance of the DSLM
Z	dimensionless displacement excitation to the base
α	coefficients of the linearized stiffness of the D-spring
β	point mobility of the foundation
γ	undamped natural frequency ratio
Δ	dimensionless distance between the oscillator and the constraint
Δs	step length for the continuation method
ϵ	dimensionless damping ratio for the interfacial damper in Chapter 4; tolerance parameter of the tanh-regularization in Chapter 7
ζ	damping ratio of the linear damper

η	gap width ratio in equilibrium in Chapters 4 and 5; ratio of tolerance parameter of tanh-regularization in Chapter 7
θ_0	initial angle of the DSLM
θ	angle of the DSLM under deformation
κ	dimensionless stiffness for the interfacial spring
λ	spring stiffness ratio of the constraint in Chapters 4 and 5; spring stiffness ratio of the D-spring in Chapter 6
μ	mass ratio
ρ	damping ratio of the constraint in Chapter 4; damping ratio of the viscous damper element in Chapter 7
τ_p	averaging time span
τ_0	starting time for averaging;
τ	dimensionless time
ω	excitation frequency
Ω	dimensionless excitation frequency
Ω_L	linearized natural frequency of the system

Chapter 1

Introduction

1.1. Engineering background

Nonlinearity is an inherent property of dynamical systems which can originate from structural design, material properties, manufacturing tolerance, external disturbance, etc. It might be valid to make linear approximations for some simple and uniform structures, such as rods, beams and plates, under the assumption of ideal boundary conditions, small strains, small displacement, small rotations, etc. The linear analytical solutions for the system response can then be easily computed at low cost by classical mechanics. However, in the practical design of high-performance dynamical systems with a more complexed structure, nonlinearities should not be neglected. Nonlinear analysis is of importance to understand the dynamic behaviour of the system and provide a more accurate estimation on system operation than the linear approach.

There are three major types of nonlinearity: geometric nonlinearity, material nonlinearity and contact nonlinearity (Peksen, 2018). Geometric nonlinearity usually refers to the nonlinearity in kinematic quantities such as nonlinear force-displacement relation. It arises when the system geometry undergoes considerable changes including large deformation, deflection or rotation. This kind of nonlinearity can be also obtained by mechanisms, such as linkages and cam-follower mechanisms. Although the strain-displacement or force-displacement relation may be linear for the unassembled moving component of the mechanism, the integrated structure can exhibit a nonlinear relationship between the restoring / damping force and the response. Material nonlinearity exists when there is a nonlinear constitutive relation of a component, i.e. a nonlinear stress-strain relationship for the material. A typical example is the metal material which exhibits material nonlinearity at high strains. Contact nonlinearity (namely boundary nonlinearity) refers to the nonlinear effect of contact interaction between two or multiple components, which introduces abrupt changes to the stiffness of the sub-structure or the assembly. The friction effect from the rough contact surface is also taken as contact nonlinearity. Those systems with discontinuous or non-differentiable force, or displacement characteristics can be classified as nonlinear non-smooth systems (Popp, 2000).

The non-smoothness in the dynamical systems can be generated by physical effects such as impacts, intermittent contact, backlash, friction or combinations of these effects

(Popp, 1998). Nonlinear phenomena widely exist in many mechanical engineering applications, such as the percussion of the drilling rigs, the intermittent contact between the roller and race in the roller bearings, frictional chatter in the tooling machinery and meshing gears. The nonlinear effects caused by the non-smoothness can have a strong influence on the system performance and should not be neglected in the dynamic design. Non-smooth dynamical systems have received great attention in the past decades. The impact oscillator and Coulomb friction oscillator have been widely accepted as representative models of the non-smooth dynamical systems with intermittent contact or friction, respectively (Ing et al., 2010; Popp, 1998). Those refined models can precisely reflect the non-smooth force and motion characteristics, which helps gain insights of complexities of the nonlinear dynamic behaviour in the non-smooth systems. Therefore, to achieve a better design of non-smooth engineering systems, it is of importance to have an in-depth understanding of the nonlinear dynamic behaviour of the impact oscillators and friction oscillators.

Vibration transmission is one of the key factors bearing upon the dynamic performance of engineering systems. Excessive vibration transmission in engineering structures can be harmful to human health and comfort (Lee et al., 2007; Le and Ahn, 2013), precision of sensitive instruments (Palomares et al., 2018), reliability and lifetime of the powertrain (Rao, 2011) and safety of structural constructions (Ibrahim, 2008). To control the undesired vibration transmitted from the vibrating source to the receiving structure, active or passive vibration isolators are commonly inserted onto the vibration transmission path (Rivin, 2004). Compared with active isolators, passive isolators do not need power supply or controller, and have simpler structure (Carrella et al., 2007). For the improvement of the isolation performance under low-frequency excitations, appropriate nonlinear element can be introduced into the passive isolation system (Palomares et al., 2018). The linearized natural frequency of a nonlinear isolator can be substantially reduced to an ultra-low value or even zero, and the effective vibration isolation frequency band is widened (Liu and Yu, 2018; Yang et al., 2013). One kind of such elements is characterized by a negative stiffness mechanism (NSM). Nonlinear elements created by linkage mechanisms can also be employed in vibration isolators to create geometry nonlinearities (Carrella et al., 2009; Sun et al., 2014).

For some engineering applications such as tooling machinery and drilling systems, a moderate level of vibration transmission to the workpiece is desirable for higher efficiency of operations (Wiercigroch and Krivtsov, 2001; Liao et al., 2018). However, these engineering systems belong to the nonlinear non-smooth dynamical systems and may even comprise different types of nonlinearities mentioned before. Therefore, a

straightforward analysis approach should be developed and employed to understand the vibration transmission mechanism for the typical nonlinear non-smooth dynamical systems, such as impact oscillators and Coulomb friction oscillators. The findings will benefit the dynamic design of the system for required performance.

The quantification of vibration transmission between two sub-structures can provide essential information to reveal the mechanism of vibration transmission. Traditional assessment of vibration transmission within engineering systems usually uses individual measures of displacement, velocity and force, which are not sufficient for determining the pathway of vibration transmission (Zheng et al., 2016; Sun et al., 2020). Power flow analysis (PFA) solves this problem by evaluating energy transmission and distribution in the vibration system. The PFA indices consider the combined effects of force and velocity amplitudes as well as their relative phase angle in a single concept, providing an insight of vibration energy transmission between sub-systems and energy dissipation by sub-structures within an integrated dynamic system (Goyder and White, 1980a, 1980b, 1980c).

The first ideas related to PFA were proposed by Lyon and Maidanik (1962). Goyder and White (1980a, 1980b, 1980c) first introduced the fundamental expressions of PFA and used power flow to quantify vibration transmission in mono- or bi-dimensional structures. In the past decades, PFA has been widely adopted and developed for investigating energy flow characteristics within different coupled structures and complex engineering systems. Findings by the PFA approach were used to improve the dynamic performance of linear systems by tailoring power transmission on the vibration transmission path. Many applications of PFA in vibration control were reported, by minimizing the vibrational power transmission from the vibration source to the receiving structure. Some examples can be found in the research of vibration isolators (Wei et al., 2016; Sun et al., 2015; Alberdi-Muniain et al., 2012; Liu et al., 2010; Collette and Preumont, 2010; Choi et al., 2009) and vibration absorbers (Chen and Wang, 2014; Vakakis et al., 2008). Moreover, since the change in structure properties can affect vibration transmission and lead to differences in power flow behaviour, PFA can also be used for non-destructive detection of defects (Zhu et al., 2006; Guyomar et al., 2011; Wong et al., 2009) by comparing the data of power flow between the referenced healthy structure and the defective structure. In addition, PFA has been developed for noise reduction in the transportation system (Wang et al., 2020, Acri et al., 2019; Liu and Yuan et al., 2017; Liu and Leng et al., 2018), such as vehicles. As the vibrational energy from the powertrain and bumpy road transmits to the cabin and radiate in the form of structure-borne sound (Lee, 2000), PFA can be used to

identify the power transmission path and assist vibration suppression or mitigation design of the structure to improve passenger ride quality.

1.2. Current state of research

There have been many works reported on the dynamic analysis of non-smooth impact oscillators with a single linear or rigid constraint. Such systems have been shown to exhibit distinct nonlinear dynamic phenomena. Nordmark (1991) considered a periodically forced SDOF impact oscillator with a rigid constraint on the one side and found a special type of bifurcation when a stable periodic orbit comes to grazing impact. Luo et al. (2018) analytically studied the dynamics of a forced two-degree-of-freedom (2DOF) impact oscillator with an end-stop and found the occurrence of sticking and non-sticking phases due to the plastic impact. Wiercigroch et al. (2020) designed an impact oscillator rig with an electromagnetic exciter. Various periodic orbits, co-existence of attractors, multi-stability and chaotic behaviour observed in engineering systems were validated. Some research has focused on the study of impact oscillators with multiple linear constraints which have many practical applications, such as energy harvesters (Lai et al., 2018), and showed new dynamic behaviour compared to that of the impact oscillators with a single constraint. Ing et al. (2006) experimentally and mathematically examined the near-grazing bifurcation scenarios of a SDOF impact oscillator with two-sided linear-spring constraints. It was found that the presence of two linear-spring constraints may stabilise the additional periodic orbits. However, limited studies have been carried out on the dynamics of impact oscillators with a nonlinear main system or a nonlinear constraint, or multiple nonlinear constraints. Even fewer works have been reported on the vibration transmission, especially on the quantification of vibration energy transfer and dissipation within such systems.

The past research on the non-smooth Coulomb friction oscillators was mainly focusing on dynamic behaviour. Feeny (1992) applied a qualitative technique to describe the dynamics of a forced multi-valued Coulomb friction oscillator. van de Vrande et al. (1999) investigated the dynamic motion of both SDOF and 2DOF friction oscillator models by using smooth functions of friction force and found the unstable solutions branches and an extra stable solution branch. Luo and Gegg (2006) developed the force criteria for stick and non-stick motions in forced friction oscillators based on local theory of non-smooth dynamical systems. Pascal (2014) examined a 2DOF linearly coupled oscillator with one of the masses sliding on a rough surface and the friction force is characterized by Coulomb friction law. Several kinds of periodic orbits including one or more stops per cycles were observed. Few previous studies have

considered the force transmission and energy dissipation in SDOF friction oscillator systems. Marino et al. (2019) examined displacement transmissibility of a SDOF Coulomb friction oscillator under joined base-wall excitation. Lopez et al. (2004, 2009) experimentally validated the accuracy of using the Coulomb friction model to predict the energy dissipation in the SDOF friction oscillator. However, the investigations on energy transmission and dissipation in the coupled 2DOF friction oscillators are still rare.

Since the earliest discussions of its fundamental concepts discussed by Goyder and White (1980a, 1980b, 1980c), PFA has been developed in the past decades to embody different approaches, the dynamic stiffness method (Langley, 1989), the receptance method (Clarkson, 1991), the mobility method (Cusshieri, 1990), the travelling wave method (Langley, 1992), the power flow based finite-element approach (Nefske and Sung, 2000), the PFA approach based on continuum dynamics (Xing and Price, 1999), the energy flow progressive approach (Xiong et al., 2001) and the power flow mode theory (Xiong et al., 2005a), to study energy transmission in various linear dynamic structures and vibration control systems. In recent research, advances were made in the PFA theory to deal with linear systems having complex structures or boundary conditions. Xiong et al. (2003) proposed generalized mathematical formulations of PFA for a multiple channel structure-control system. The theoretical model was capable of assessing the dynamic behaviour and effectiveness of vibration control of a complex integrated system comprising a number of substructures and work well with different dynamic systems. Later, Kwon et al. (2011) presented a power flow boundary element method to solve the multi-domain problem. Besides, Park and Hong (2007a, 2007b) provided a hybrid analytical method which combined PFA and statistical energy analysis (SEA) to estimate the vibrational and acoustic responses of systems with low system damping.

The PFA method has been applied to investigate various linear systems, including coupled structures (Seo et al., 2003; Wang et al., 2002a; Wang et al., 2004; Chen and Liu, 2019), phononic structures (Al ba'ba'a and Nouh, 2017), acoustic black hole beams (Wang et al., 2019a), cracked functionally graded beams (Zhu and Ke et al., 2020) and laminated composite plates with different inerter-based suppression configurations (Zhu and Yang et al., 2020). Power flow indices were also used as a performance indicator of active vibration control system (Howard et al., 2000; Liu et al., 2010), hybrid vibration control system (Xiong et al., 2003; Kandasamy et al., 2016), semi-active isolation system (Sun et al., 2015; Collette and Preumont, 2010) and passive linear vibration control system (Choi et al., 2009; Dong et al., 2008).

There has been an increasing shift in focus to PFA of nonlinear dynamical systems. Royston and Singh (1996, 1997) applied power flow scheme to assess and enhance the performance of the nonlinear mounting system. Xiong et al. (2005b) studied the dynamic characteristics and power flow behaviour of a nonlinear interactive system under wave excitation. It was observed that there exist non-uniqueness and instability on the power transmission path at critical frequencies. Vakakis et al. (2008) studied the targeted energy transfer phenomena in dynamical systems from the primary vibrating structure to the attached passive nonlinear energy sink. Alberdi-Munian et al. (2012) evaluated the vibration mitigation performance of a nonlinear magneto-sensitive vibration isolation system by experimentally quantifying the energy flow. Yang and Xiong et al. (2014, 2015) investigated the power flow behaviour of a Duffing oscillator and the performance of nonlinear vibration absorbers. The PFA approach was also implemented to evaluate the vibration mitigation performance of nonlinear isolators (Yang et al., 2013, 2016, 2019). Moreover, the power flow between the interactive oscillators with a nonlinear coupling interface (Yang et al., 2018, Shi et al., 2019a), with a bilinear coupling interface (Shi et al., 2019b) or with a linear constraint or a nonlinear motion constraint (Dai et al., 2020, 2021) were explored for the evaluation of vibration transmission. While much PFA research has been conducted on the nonlinear dynamical systems, there is still lack of knowledge on the power flow behaviour in the typical nonlinear non-smooth dynamical systems, i.e. impact oscillator and Coulomb friction oscillator.

1.3. Motivations of the research

In the past research of non-smooth impact oscillators, the motion constraint was usually assumed to be rigid or linear. However, based on the classical contact mechanics, the compliant contact dynamics models may involve nonlinear contact force model when considering elastic deformation of the interface material (Gilardi and Sharf, 2002). Ajibose et al. (2010) compared numerically the influence of different nonlinear contact force models on the global and local dynamics of the drifting impact oscillators and found that the global dynamics may depend on the contact force model applied. Hence the dynamics and vibration transmission behaviour of impact oscillators with nonlinear constraints remains to be investigated so as to predict the dynamic performance of non-smooth engineering systems more accurately.

In the previous research, substantial progress has been made in the power flow behaviour of linear and nonlinear vibrating systems. However, research on the power flow characteristics in different representative nonlinear non-smooth dynamical systems,

such as impact oscillators and friction oscillators, is limited and waits to be promoted. For typical dynamical systems with non-smoothness, a strong nonlinear influence may be confronted during the operation, leading to complicated nonlinear phenomena. For example, in the dynamic modelling of the drilling system or metal cutting lathes, the intermittent collision between the rig and workpiece causes discontinuous stiffness, damping nonlinearities and friction nonlinearities (Dou et al., 2020). A non-smooth relationship between stiffness / damping and displacement as well as a non-smooth relationship between friction force and velocity are needed for accurate estimation of vibration response. For these nonlinear dynamical systems, the existent linear models fail to provide a precise prediction on the dynamic behaviour. The traditional approaches and the PFA methods need to be combined to investigate the vibration transmission mechanism in these nonlinear dynamical systems.

On the other hand, the integration of a nonlinear element created by linkage mechanisms into the vibration control system can lead to enhanced vibration mitigation performance. Different types of linkage mechanisms, such as Watt's linkage (Ibrahim, 2008), Scott-Russel linkage (Winterflood et al., 1996, 1999), torsion crank linkage (Winterflood et al., 1998) and Roberts linkage (Garoi et al., 2003, Bosseti et al., 2014) have been used to create geometric nonlinearities so as to enhance vibration isolation performance for ultra-low-frequency vibrations. Recently, an isolation platform with a Scissor-Like Structure (SLS) created by geometrically nonlinear linkage mechanism and a linear spring was proposed by Sun et al. (2014, 2016). It was demonstrated that the SLS isolation system can have a good isolation performance. However, many previous investigations on the performance of nonlinear vibration isolators with NSMs or linkage mechanisms have been based on SDOF models, in which the isolators are installed on a rigid and massless foundation (Yang and Xiong et al., 2014; Yang and Harne et al., 2014). In engineering structures such as ships, buildings and aircrafts, the foundation structures on which machineries are mounted via vibration isolators are flexible and the flexibility can have large effects on the level of vibration transmission and the performance of vibration isolators (Sciulli and Inman, 2018; Xiong et al., 2005b). The use of a rigid base assumption to measure the effectiveness of vibration isolators can yield inaccurate predictions. Hence it is necessary to examine the effects of the flexibility of the base structure on the performance of nonlinear isolators.

Furthermore, for performance evaluation of vibration attenuation systems, the force/displacement transmissibility was usually used as the performance index (Wang and Jing et al., 2019, Jing et al., 2019a). There is very limited research investigating the energy flow characteristics of systems with nonlinear vibration isolators created by

linkage mechanisms. It is of interest to develop PFA to quantify vibration transmission of nonlinear isolation systems for a deeper understanding of the vibration transmission mechanism of such systems from the energy perspective. More importantly, the findings of PFA will benefit the dynamic design of the isolation system and guarantee better vibration mitigation.

1.4. Aims and objectives

The main aim of this research is to develop and employ the PFA method to investigate the dynamic behaviour of nonlinear smooth and non-smooth dynamical systems, covering vibration power transmission and energy dissipation. The effects of different types of non-smooth nonlinearities on the vibration transmission and power flow of the systems are investigated. Moreover, the research also intends to develop a novel passive nonlinear vibration isolation system based on the developed PFA method.

In order to realize these goals, the research objectives are set as follows

- To develop and apply vibration transmission analysis and the PFA method for nonlinear smooth and non-smooth dynamical systems;
- To study typical nonlinear dynamical systems, such as the impact oscillator with a single constraint or multiple nonlinear motion constraints and Coulomb friction oscillator, from the perspective of energy transfer;
- To examine effects of different contact nonlinearities on vibration transmission and power flow behaviour in a single-degree-of-freedom (SDOF) and a two-degree-of-freedom (2DOF) coupled dynamical systems;
- To investigate the performance of a nonlinear isolation system with a tuneable geometrical nonlinear stiffness mechanism based on power flow variables for improving the effectiveness of vibration mitigation;
- To explore complex nonlinear phenomena such as super-harmonic response components, bifurcations and quasi-periodic responses associated with the steady-state response of nonlinear systems;

1.5. Thesis outline

This thesis falls into 8 chapters, with Chapter 1 serving as an introduction.

In Chapter 2, an overview of the vibration transmission analysis approaches is presented. Also presented is a demonstration of the traditional vibration transmission evaluation approach as well as the PFA approach by using linear models. The energy transmission analysis methods for linear systems and nonlinear systems are classified,

and a brief review of the PFA methods in different dynamical systems is made. The research gap in the PFA of nonlinear dynamical systems is identified.

Chapter 3 gives the fundamental concepts, general definitions and expressions of vibration transmission including power flow formulations. The time-domain numerical integration method, the frequency-domain harmonic balance (HB) approximation approach along with the alternating frequency/time domain (AFT) scheme and numerical continuations used for determination of the steady-state response and vibration transmission quantities of nonlinear dynamical systems in this thesis are provided. An example of the vibration transmission study for a coupled Duffing oscillator system by using the approaches discussed in Chapter 3 is given for demonstration.

Chapter 4 discusses the vibration transmission and power flow behaviour of SDOF or 2DOF impact oscillators comprising linear or quasi-zero-stiffness (QZS) nonlinear constraints. It investigates and compares the effects of stiffness and damping properties of the constraints on the dynamic response and vibration transmission of the nonlinear systems. The force transmissibility and time-averaged power flow variables are obtained by analytical and semi-analytical HB approximations and numerical integrations to quantify vibration transmission in the systems.

Chapter 5 studies the dynamic behaviour and vibration transmission of impact oscillators with geometrical nonlinear constraints. A nonlinear motion constraint with geometric stiffness nonlinearity is proposed, which is created by a linear spring embedded in a diamond-shaped linkage mechanism (DSLML). The harmonic balance method with alternating frequency/time domain scheme (HB-AFT) and numerical integrations are both employed to determine the steady-state response of the systems. The force transmissibility and time-averaged power flows are used as indices to quantify and evaluate vibration transmission and dissipation in the impact oscillator systems with multiple setups of the proposed constraints.

Chapter 6 explores the vibration power flow and force / displacement transmissibility characteristics of the proposed nonlinear isolation system with a geometrically nonlinear element created by DSLML. The steady-state response of the system subjected to force or motion excitations is obtained by HB-AFT with numerical continuations and compared with the results by using numerical integrations. The force / displacement transmissibility and power flow indices are employed to assess the vibration isolation performance of the nonlinear isolator.

In Chapter 7, the dynamic behaviour, vibration transmission and energy flow characteristics of a SDOF friction oscillator and a 2DOF coupled friction oscillator with a nonlinear dry-friction element at the interface are examined. The Karnopp friction model and a smooth Coulomb friction model are used to estimate the dry-friction force. The steady-state response of the system is determined by HB-AFT approach with numerical continuations and time-marching method. The level of vibration transmission and energy dissipation within the systems are evaluated by force transmissibility and power flow variables.

The last Chapter 8 presents conclusions including principal contributions and main findings. Design guidance on the engineering systems is provided based on the findings of this research and some interesting research areas are suggested for future investigation.

Chapter 2

Literature review

To reveal the vibration transmission mechanism in the dynamical system, it is of importance to develop methods for quantifying vibration transmission. In this chapter, the established evaluation methods for the vibration transmission are briefly reviewed, and different approaches developed for the energy transmission in the linear or nonlinear dynamical systems are classified and reviewed. The research gap in typical nonlinear dynamical systems in terms of vibration transmission and energy flow are discussed.

2.1. Overview of the evaluation methods on vibration transmission

The concept of transmissibility has been widely employed in the past research for quantifying vibration transmission from the vibration source to the receiving structure and used as an indicator of the isolation performance for the vibration isolation systems (Fahy and Gardonio, 2007). The transmissibility is defined as the dimensionless ratio of the steady-state response amplitude of the system to the input excitation amplitude (Weaver et al., 1990; Morse et al., 1948). It describes the ability of a system to either enhance or attenuate the input vibration. The transmissibility ratio can be in displacement, velocity, acceleration and force. Some researchers also used receptance magnitude defined as the displacement per unit harmonic excitation force to assess the level of vibration transmission (Ghandchi Tehrani et al., 2013).

There have been many works on vibration transmission analysis using vibration transmissibility. Yan et al. (2010) considered a base-excited active vibration isolation system consisting of a distributed parameter isolator. The velocity transmissibility, i.e., the velocity ratio between the receiving mass and the exciting base, was used for evaluation of the isolator. Elliott et al. (2004) also used velocity transmissibility from the base to the main system mass to assess the performance of the active isolator. Alujevic´ et al. (2011) investigated an active vibration isolation system using blended velocity feedback. The velocity feedback loop transmissibility function, i.e. the ratio of the output velocity and the input excitation force, was used as the index of isolation performance of the system. For the motion-excited system, displacement transmissibility was usually employed. Wu and Tang (2020) used the displacement transmissibility to examine the effectiveness of vibration isolation for a base-excited

geometrically nonlinear isolation system. Sun et al. (2018) investigated a nonlinear isolation structure under base motion excitation by using displacement transmissibility as a performance indicator. Force transmissibility was also widely employed in the examination of vibration transmission in SDOF and multiple degree-of-freedom (MDOF) systems (Zhang et al., 2020; Huang et al., 2014; Liu and Yu, 2020; Tang and Brennan, 2013). The following case study of a linear 2DOF isolation system is presented for illustrating the basic formulations of the force transmissibility.

Figure 2.1 shows a 2DOF linear vibration isolation system comprising a movable SDOF base of a mass m_1 , a linear spring with stiffness k_1 , a viscous damper with damping c_1 . The machine with mass m_2 is mounted on the SDOF base via a linear spring k_2 and a linear damper c_2 . A harmonic excitation force with amplitude of f_0 and time dependence $e^{i\omega t}$ is applied on the machine mass m_2 . The vibration isolation performance can be assessed by examining the force transmission from the machine to the base. The force transmissibility TR_B to the base structure can be defined as the ratio of the maximum magnitude of the transmitted force via the linear isolator to that of input force amplitude:

$$TR_B = \frac{\max(|f_{tB}|)}{f_0}, \quad (2.1)$$

where f_{tB} is the transmitted force to the base structure with $f_{tB} = k_2(x_2 - x_1) + c_2(\dot{x}_2 - \dot{x}_1)$.

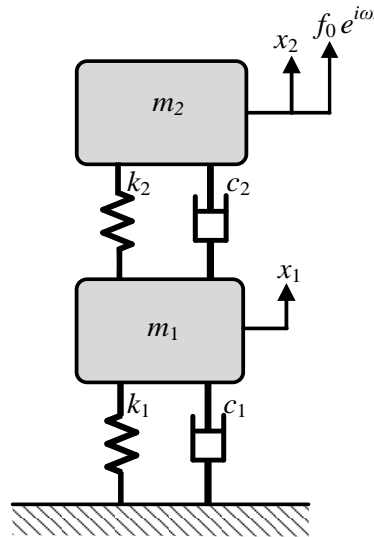


Figure 2.1. Schematic of the 2DOF linear isolation system.

Based on the classical mechanics, the steady-state response of the system can be obtained by solving the equation of motion of the system, which can be substituted into

Eq. (2.1) to determine the force transmissibility. Fig. 2.2 shows the force transmissibility TR_B to the base structure by setting the system parameters as $m_1 = m_2 = 1$, $k_1 = k_2 = 1$, $c_1 = c_2 = 0.02$ and $f_0 = 0.01$. It is shown that the force transmissibility plot can provide the information of unity isolation frequency band, i.e. the force transmissibility value is smaller than unity. The stiffness and damping properties of the system can be adjusted to achieve a broader band of the unity isolation frequency range.

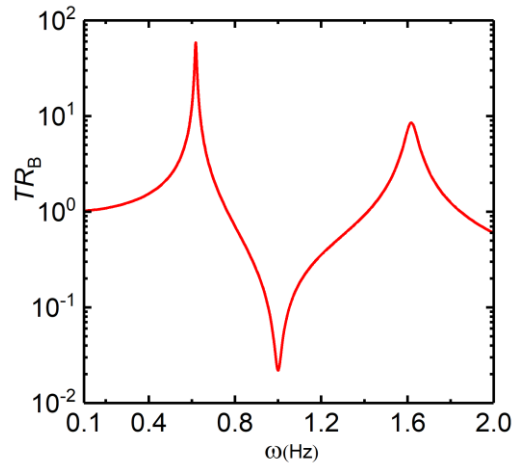


Figure 2.2. The force transmissibility TR_B to the base structure.

It should be pointed out that the transmissibility only takes the amplitude value of the force, velocity or displacement into account. It may be insufficient to quantify the vibration transmission without considering the phase angle of the response. Moreover, the vibration transmission information from the energy perspective is neglected. The vibration power flow considers the combined influence of force and velocity amplitudes as well as their relative phase angle into a single quantity and can be used as a uniform measure for a straightforward evaluation of power transmission between the different components within a structure (Goyder and White, 1980a).

Here a simple case study of a SDOF oscillator mounted on a flexible foundation is used for illustrating the basic concepts and formulations of PFA. Fig. 2.3 shows a single-stage isolation system of a machine m_1 installed on a flexible foundation via a linear spring isolator with stiffness coefficient k_1 . The machine is subjected to a harmonic force with amplitude of f_0 and frequency of ω . The point mobility of the flexible foundation is denoted by β , where the mobility defined as the ratio of complex harmonic velocity to the complex harmonic force.

Based on the theory of PFA (Goyder and White, 1980a), the power flow is the rate of work done, which can be written as the product of force and velocity at a time point

t . For the current system, the instantaneous power flow p_t to the foundation can be expressed as:

$$p_t = \tilde{f}_t \tilde{v}_t, \quad (2.2)$$

where \tilde{f}_t is the instantaneous transmitted force to the foundation and \tilde{v}_t is the instantaneous velocity of the foundation. Here the \tilde{f}_t and \tilde{v}_t are in complex form expressed as $\tilde{f}_t = \tilde{F}e^{i\omega t}$ and $\tilde{v}_t = \tilde{V}e^{i\omega t}$, respectively, in which the \tilde{F} and \tilde{V} are the complex variables.

Since the PFA theory considers the real power as the primary quantity (Xing and Price, 1999). The real instantaneous transmitted power P_t can be obtained as

$$P_t = \Re\{\tilde{f}_t\}\Re\{\tilde{v}_t\}, \quad (2.3)$$

where \Re represents the operation of taking real part.

The time-averaged power flow is of interest in terms of vibration transmission analysis. Here the corresponding power flow averaged over a time span t_p is

$$\bar{P}_t = \frac{1}{t_p} \int_0^{t_p} \Re\{\tilde{f}_t\}\Re\{\tilde{v}_t\} dt. \quad (2.4)$$

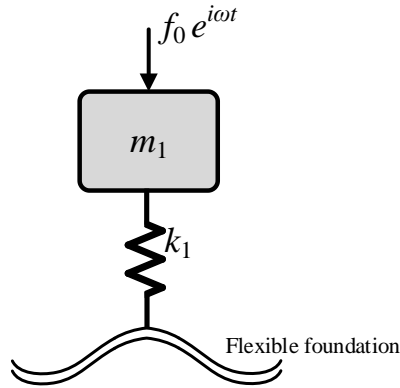


Figure 2.3. A SDOF force-excited oscillator on a flexible foundation (Goyder and White, 1980c).

By a manipulation of Eq. (2.4) according to the established work (Goyder and White, 1980c), we have

$$\bar{P}_t = \Re\{\tilde{F}\tilde{V}^*\}/2 = \Re\{\tilde{F}^*\tilde{V}\}/2 = (\Re\{\tilde{F}\}\Re\{\tilde{V}\} + \text{Im}\{\tilde{F}\}\text{Im}\{\tilde{V}\})/2 = |\tilde{F}|^2 \Re\{\beta\}/2. \quad (2.5)$$

Equation (2.5) shows that the time-averaged power flow combines the velocity, force and their phase angle into a single quantity, which may provide more information of

vibration transmission than the force transmissibility from energy transmission perspective.

2.2. Review of energy transmission analysis

In this subsection, the developed analysis approaches for energy transmission in the dynamical systems are reviewed.

2.2.1. Statistical energy analysis approach

For the systems containing a number of overlapping modes particularly in the high-frequency range, the length scale of vibrations may reach that of structural defects and lead to a divergence of the frequency response for many nominally identical systems (Hawes et al., 2019). The finite element analysis (FEA) may not be able to capture this behaviour at high frequencies, while the statistical methods are more suitable for modelling such systems. The statistical energy analysis (SEA) approach was developed for predicting the statistical behaviour of the dynamical systems with uncertain parameters, where the energy is considered as the primary variable (Antonio, 1984). The SEA splits the integrated system into subsystems with similar properties and each subsystem is excited by random, stationary, distributed forces (Mace, 2005). The vibrational state of the system is described by the total time-averaged vibration energy of each subsystem based on energy conservation (Fahy et al., 1994).

The fundamental study of SEA was firstly presented by Lyon and Maidanik (1962). The power flow between two linearly coupled oscillators under independent and random excitation was investigated. It was found that the power flow is proportional to the difference between the average modal energy between two oscillators. An equivalent power flow circuit between modes was developed and demonstrated the application to two interacting multimodal systems. Later research conducted by Lyon (1975) and Ungar (1967) demonstrated the extensive applications of SEA in dynamical systems with more complicated structures. A wave approach (Langley, 1992) and a mobility approach (Manning, 1994) based on SEA were developed and showed an enhancement compared to the conventional SEA. In recent years, the hybrid finite element-SEA (FE-SEA) modelling method was proposed for structural-acoustic systems and vibration systems in a mid-frequency range (Ma et al., 2016; Yin et al., 2017; Gao et al., 2018; Zheng et al., 2019; Liu and Thompson et al., 2020).

The SEA approach has been accepted to be effective for high-frequency vibration problems. However, the deficiencies of SEA limit its applications (Fahy et al., 1994). The SEA method cannot provide the information of spatial distributions of dynamic

response variables of each subsystem. Moreover, for the narrowband or tonal excitation vibration problems, SEA approach can be employed only if the statistical data for the energy response functions of the subsystems had been obtained (Fahy et al., 1994). In addition, since the SEA approach is inherently probabilistic, the results of parametric sensitivity studies may not be fully trusted. Nevertheless, some assumptions made in SEA, such as low damping and weak coupling, also confine its applications in practice (Hawes et al., 2019). In contrast, there are no such limitations on the excitation frequency range and coupling conditions when using the PFA approach. The power flow indices consider the change of vibration energy. They can describe the power transmission between sub-structures as well as energy dissipation in each component of the system, and hence provide a measure of vibration transmission within an integrated system.

2.2.2. Analytical PFA approaches

In the past decades, there are a number of analytical power flow approaches developed for the vibration investigation of linear dynamical systems. Those methods include a dynamic stiffness method (Langley, 1989), a receptance approach (Clarkson, 1991), a mobility method (Cuschieri, 1990), a travelling wave method (Langley, 1992), a power flow based finite-element approach (Mace and Shorter, 2000), a substructure approach (Wang et al., 2002a, 2002b), a PFA approach based on continuum dynamics (Xing and Price, 1999), an energy flow progressive approach (Xiong et al., 2001) and a power flow mode theory (Xiong et al., 2005a). This subsection presents a brief review of those approaches.

The dynamic stiffness method was firstly proposed by Langley (1989) to examine the vibration behaviour of a row of aircrafts panels under plane acoustic wave excitation or random excitation. The basic idea of the dynamic stiffness method is to derive the relationship between the displacements and forces at the edge of the substructure, the dynamic stiffness matrix for each substructure can be deduced, which can then be assembled to a complete system based on the FEA method. The dynamic behaviour of the system can then be obtained, and the mean stored energy and power flow within the system can be analysed. The same author (Langley, 1990) also applied the same approach to examine the power flow behaviour of the beams and frameworks. Wu et al. (2018) further developed the dynamic stiffness method to investigate the power input and transmission in built-up structures. The in-plane and out-of-plane vibrations of the plates were considered in the dynamic stiffness matrix and their effects on the power flow were examined.

For the receptance approach, the two ends of two structures to be jointed can be described by the end receptance functions which are derived from the normal mode method. The response velocity can then be expressed as the function of end receptance as well as the end moment, such that the expressions of average power flow can be derived (Clarkson, 1991). This approach is suitable for revealing the power flow behaviour across the beam-beam joint or plate-plate junction. Farag and Pan (1996) employed the receptance approach to investigate the power transmission in the joint boundaries of in-plane beams structures. Beshara and Keane (1998) used receptance approach to study the vibrational power flows in a dissipative joint between two rectangular plates. The receptance approach and dynamic stiffness method share some similarities. However, the receptance approach uses coupling forces for the degree of freedom (DOF) at joint, while the displacements are used at joint in the dynamic stiffness method (Beshara and Keane, 1998).

The travelling wave method is based on the wave propagation theory that the global frequency domain model of the dynamics of the system network is assembled from models of local component behaviour, wave propagation along members and scattering behaviour of junctions (Miller and von Flotow, 1989). The wave behaviour of a structure member is determined by the superposition of each travelling wave mode, and the wave set transmission characteristics can be obtained from a transmission matrix. Based on those variables, the power flow through the members and junctions can be extracted. In previous studies, the travelling wave method has been used to examine the power flow transmission behaviour in structural members (Miller and von Flotow, 1989), a plate structure (Langley, 1992), frame structures (Beale and Accorsi, 1995), beam structures (Horner and White, 1991; Walsh and White, 2000), bolted junctions between a plate and a stiffening rib (Bosmans and Nightingale, 2001) and built-up structures involving two- and three-dimensional subsystems (Wester and Mace 2005a, 2005b, 2005c). Tang et al. (2017) employed the travelling wave method to investigate the relationship between power flow behaviour and damage characteristics of a one-dimensional Euler-Bernoulli cracked beam.

Xing and Price (1999) developed a PFA approach based on the governing equations of continuum mechanics. By introducing the concept of an energy-flow density vector as well as defining the energy-flow line, the energy-flow potential and the equipotential surface, the energy flow and energy exchange behaviour within the continuum can be described. The applicability of the approach was validated by investigating two simple oscillators and non-sequential multiple systems. Xiong et al. (2003) established analytical solutions of a generalized structure-control system from the viewpoint of

continuum mechanics. The energy flow density vector was also applied in the modelling of power transmission or exchange within a continuum.

In the mobility approach, the mobility function is used in the power flow method. The basic process of the approach is to model the global system by a group of coupled subsystems where the forces and moments are introduced at the joints. Then the input and transfer structural mobility functions can be used to derive the expressions of power flow input to the subsystems and between subsystems, respectively. The mobility approach has been employed in the investigation of power flow characteristics of different types of structures, such as finite and infinite beam (Pinnington and White, 1981), coupled plate structures (Cuschieri, 1990), coupled cylinder shells (Ming et al., 1999) and a simultaneously excited structure by force and moment (Moohouse, 2002). Li and Wu (2013) employed the power flow based mobility approach to understand the generation mechanism of the dominant frequencies in the vibrations of rail bridges under the excitations of moving trains. To overcome the difficulties of applying conventional mobility method to complex coupled structures, Xiong et al. (2001) further developed the mobility method by proposing generalized mobility/impedance matrices for three-dimensional structures. Moreover, two progressive approaches were presented for the prediction of force, velocity response vector and power flows within the complex coupled systems. This mobility-based power flow progressive approach has been combined with a high-order sandwich theory to examine the power transmission for a sandwich configured flexible raft vibration isolation system (Choi et al. 2009).

In power flow mode theory proposed by Ji et al. (2003), the force sources are transformed to arrays of force distributions, and the eigenvalues, as well as eigenvectors of the real part of the mobility matrix for the receiver are involved in the transformation. Each force in the force arrays has an independent contribution to the vibrational power transmission and also has a corresponding independent power mode. The main advantage of this approach is that the expressions of upper and lower bounds and the mean value of the transmitted power can be obtained straightforwardly. Moreover, both force and moment excitations can be considered in the analysis. However, the information of the system's mobility related to the system's physical properties is needed in the approach to obtain the eigen-properties. In the later studies, Xiong et al. (2005a) developed a damping-based power flow mode theory. The power flow behaviour of the dynamical systems can be determined by the characteristic-damping factor and power flow response vector. The power flow response vector was derived by decomposing the generalized coordinate of the velocity vector in the power flow space. It was demonstrated the power flow control approaches can be obtained based on the

power flow mode theory. The energy flow dissipations levels and patterns can be controlled by adjusting the damping distributions. The power flow mode theory has been applied to investigate the structural vibration transmission between components of assembled structures at low frequencies (Weisser et al. 2015).

2.2.3. FEA and Substructure approach

For complex systems, such as non-uniform structures with special boundary conditions, it may be difficult to obtain the power flow behaviour by the analytical PFA approaches reviewed in the previous content of this subsection. The power flow based finite element (FE) approaches are suitable to deal with those complex systems by solving partial differential equations numerically. In practice, discretization is performed on the targeted complex system in the space dimensions and can obtain an assembly of small parts (i.e., elements) which are connected to one another. The governing equation of each element can then be constructed and assembled to a system equation that describes the global behaviour of the system. Nefske and Sung (1989) showed that the power flow formulations is adaptable into the form of FEA by adjusting the properties of a standard FE model. The power flow based FE model can then be solved by MSC/NASTRAN code. Hambric (1990) developed the power flow formulations and numerical method for NASTRAN program. The contribution by axial and torsional motion to the power flow was considered. The same author (Hambric, 1994) compared the results of structure-borne flexural power in a straight beam predicted by the FEA approach to the experimentally measured results. It was shown a good estimation accuracy of FEA on the direction and spectral trends of beam flexural power. Wohlever and Bernhard (1992) improved power flow based FE approach by proposing a coupling scheme for the connection of rod and beam models. A more realistic built-up structure can be obtained for PFA analysis based on standard FE code. Mace and Shorter (2000) presented computationally efficient methods of FEA for the modelling of the energy flow. A global FEA method and an alternative local FEA method using component-mode synthesis were established. A case study on the energy flow of a system consisting of three, edge-coupled, rectangular plates was conducted with the use of FEA method. McDaniel et al. (2001) put forward a stability analysis approach for brake systems by analysing the power flow behaviour between pad and rotor. It was indicated that the proposed simple model can be extended to the high-fidelity FE models and can provide guidance on the post-processing of the FE models. The FEA approach has been applied in the investigation of power flow behaviour in a T-beam (Szwerc et al., 2000), stiffened plates and shell structures (Xu et al., 2004; Zhu

et al., 2011), a vibrating rectangular plate with a crack (Lee et al., 2006) and the human head (Chang et al., 2018).

While the power flow based FEA approach can be applied for complex systems, the computational cost will increase exponentially when the model size is becoming larger and the frequency is higher. One possible solution to this problem is to use the substructure approach. The fundamental idea of the substructure approach is to divide the whole system into a number of subsystems and perform FEA on each substructure. The approximated solution for the dynamics of the system can be determined by synthesizing the describing data of the dynamic behaviour of each substructure obtained from FEA (Xing et al., 1996). The power flow characteristics through the coupling interface of the substructures can then be calculated based on the response solution and external or internal coupling force. Wang et al. (2002a, 2002b, 2004) used the substructure approach with a free-free interface condition to examine the power flow behaviour in an indeterminate rod system, in L-shaped plates and in a coupled plate-cylindrical shell system. Feng et al. (2009) studied the vibration transmission paths of a coupled beam-cylindrical shell system by quantifying the total injected and transmitted power based on the substructure approach. Zhu and Yang et al. (2020) also used the substructure approach to investigate the vibration transmission and power flow behaviour in the laminated composite plates with inerter-based suppression configurations.

It should be pointed out that the majority of the power flow-based FE models are based on the linear assumption that the global stiffness matrix of the structure is constant. In real engineering problems, the nonlinearities are inherent in the local subsystems and should be considered in the dynamic analysis as discussed in Chapter 1. However, due to the complexity in the modelling of different nonlinearities, nonlinear FE models are more difficult to set up compared to the linear model. Moreover, because of a large number of elements, the calculation efficiency of such method in the analysis of dynamical systems with complex nonlinearity is relatively low due to the sophisticated constitutive laws as well as the incremental-iterative process in the solution procedure. Furthermore, it will generate a larger quantity and wider range of results which may be hard to interpret (Plumbridge et al., 2007). Therefore, to fully understand the energy flow in nonlinear systems, it is sensible to firstly carry out PFA in discretised systems governed by ordinary differential equations. The insights of power flow in the nonlinear subsystems can be obtained in a fast and accurate way. Building on from the current project, continuous systems, which needs FE discretisation, can be further explored in future studies.

2.2.4. PFA in nonlinear systems

In recent years, PFA of the nonlinear dynamical systems has drawn an increasing concern. Royston and Singh (1996, 1997) employed PFA approach to evaluate the effects of the nonlinear interactions in the passive component of the nonlinear mounting system on the vibrational power flow. It was shown that the level of power transmission is highly depending on the nonlinear path. Xiong et al. (2005b) studied the interactive power flow behaviour of a coupled equipment-nonlinear isolator-flexible foundation system under sea wave excitation. The nonlinear isolator was characterized by a general p th power nonlinear damping model and q th power nonlinear stiffness. It was found that the input power spectrum is sensitive to the damping and stiffness nonlinearity near the resonance frequency. Jump-phenomenon and multiple power flow transmission paths were observed in the vicinity of the peak frequencies of the transmitted power. Guidelines for the design of vibration mitigation system in maritime engineering applications were provided based on the findings from PFA. Vakakis et al. (2008) investigated the targeted energy transfer behaviour from the vibrating source to the attached passive nonlinear energy sink in dynamical systems. It was found that the nonlinear energy sink can be designed to effectively modify the dynamics of the main system to which it is attached. Xiong and Cao (2011) investigated the power transmission and energy dissipation characteristics of a nonlinear coupling system with irrational nonlinear stiffness. Yang and Xiong et al. (2014) performed nonlinear PFA on a Duffing oscillator. Compared to the linear systems, significant differences can be found in the power flow behaviour when the nonlinearities are considered. The same authors also employed PFA approach to assess the vibration isolation performance of the nonlinear isolation system with negative stiffness mechanism (Yang et al., 2013), a nonlinear isolator mounted on a nonlinear base (Yang et al., 2016) and nonlinear isolators with nonlinear inertance mechanism (Yang et al., 2019). The effectiveness of nonlinear vibration absorbers (Yang et al. 2015) was also investigated based on PFA.

It is found from those studies that the involvement of the nonlinearities in the vibration control system can help reduce the vibration power transmission and therefore can assist the vibration suppression. In the recent research of vibration control systems, the nonlinear vibration isolators based on geometrically nonlinear linkage mechanisms have aroused extensive attention because of its good performance. Different types of vibration isolators created by linkage mechanisms have been proposed (Bossetti et al., 2014; Sun et al. 2016). Moreover, the potential of integrating such isolators into engineering applications, such as heavy-duty jackhammers (Jing et al., 2019b), has been explored. However, in the evaluation of such linkage-based vibration isolators, the

energy transmission and distribution behaviour have been neglected. For the further development of the linkage-based vibration isolation system, PFA can be employed in the design as a powerful tool.

Although there have been increasing number of studies conducted on the PFA of nonlinear dynamical systems, the main focus of these established PFA research mentioned above is on the nonlinear smooth systems. The PFA research on the non-smooth dynamical systems is very limited. As illustrated in Chapter 1, the nonlinear non-smooth systems are widely existing in mechanical engineering applications. Various types of non-smoothness in the dynamical systems can bring about different nonlinear influence on dynamic behaviour (Gilardi and Sharf, 2002). Shi et al. (2019) investigated energy flow behaviour of a nonlinear coupled oscillating system with a non-smooth bilinear stiffness and damping element. The bilinear stiffness element can be used to model the non-smoothness in the flange-bolts coupling structure having larger compressional stiffness than the tensional stiffness (piecewise linear characteristic). It was shown that the non-smooth bilinear stiffness at the coupling interface has significant effects on the power transmission between coupled systems. Until now, the effects of typical non-smoothness in the engineering systems, such as intermittent elastic contact and dry friction effect, on the vibration transmission and power flow behaviour of the system are still unknown. To understand the vibration transmission mechanism in the nonlinear non-smooth engineering applications. Fundamental vibration transmission analysis and PFA on the representative nonlinear non-smooth dynamical systems, i.e. impact oscillator and Coulomb friction oscillator, are necessary. Guidance for an enhanced dynamic design of engineering systems can be obtained based on findings from PFA.

Chapter 3

Methodologies

In this chapter, the methods for evaluating vibration transmission of the nonlinear dynamical system are illustrated. General formulations for vibration transmission analysis are presented firstly. The numerical integration method and harmonic balance approximations with alternating frequency/time domain (AFT) scheme and numerical continuations are discussed for determining the response and vibration transmission behaviour of the nonlinear dynamical systems investigated in this research. An example of a coupled nonlinear Duffing oscillator system is given for illustrating the use of vibration transmission analysis methods introduced in this chapter.

3.1. General vibration transmission formulations

For a general Q -DOF nonlinear vibration system subjected to a harmonic excitation force, the general equation of motion for the whole system can be written in a matrix form as

$$[\mathbf{M}]\{\ddot{\mathbf{x}}\} + [\mathbf{C}]\{\dot{\mathbf{x}}\} + [\mathbf{K}]\{\mathbf{x}\} + \{\mathbf{f}_n\} = \{\mathbf{f}_{ex}(t)\}, \quad (3.1)$$

where $\{\mathbf{x}\}$, $\{\dot{\mathbf{x}}\}$ and $\{\ddot{\mathbf{x}}\}$ denote the displacement, velocity and acceleration vectors, respectively, and $\{\mathbf{x}\} = \{x_1, x_2, \dots, x_Q\}^T$, $\{\dot{\mathbf{x}}\} = \{\dot{x}_1, \dot{x}_2, \dots, \dot{x}_Q\}^T$ and $\{\ddot{\mathbf{x}}\} = \{\ddot{x}_1, \ddot{x}_2, \dots, \ddot{x}_Q\}^T$, $[\mathbf{M}]$, $[\mathbf{C}]$ and $[\mathbf{K}]$ are the corresponding mass, damping and stiffness matrices, respectively, $\{\mathbf{f}_n\}$ represents the nonlinear force vector arising from the nonlinearities in the system with $\{\mathbf{f}_n\} = \{f_{n1}, f_{n2}, \dots, f_{nQ}\}^T$ while $\{\mathbf{f}_{ex}(t)\} = \{\dots, f_0 e^{i\omega t}, \dots\}^T$ is the external excitation force applied to the j -th DOF ($1 \leq j \leq Q$) of the system, where f_0 and ω are the forcing amplitude and frequency, respectively, and t is the time.

3.1.1. Force transmissibility formulations

The transmitted force f_T from j -th DOF to $(j + 1)$ -th DOF can be obtained by calculating the total interactive force at the interface between j -th DOF to $(j + 1)$ -th DOF. The force transmissibility from the j -th DOF to $(j + 1)$ -th DOF can then be derived as the ratio of the maximum transmitted force at the interface between those two DOFs to the amplitude of the excitation force applied on the j -th DOF:

$$TR = \frac{\max(|f_T|)}{f_0}. \quad (3.2)$$

3.1.2. Power flow formulations

By multiplying Eq. (3.1) by the transpose of velocity vector $\{\dot{\mathbf{x}}\}^T$, the power balance equation can be obtained:

$$\{\dot{\mathbf{x}}\}^T[\mathbf{M}]\{\ddot{\mathbf{x}}\} + \{\dot{\mathbf{x}}\}^T[\mathbf{C}]\{\dot{\mathbf{x}}\} + \{\dot{\mathbf{x}}\}^T[\mathbf{K}]\{\mathbf{x}\} + \{\dot{\mathbf{x}}\}^T\{\mathbf{f}_n(t)\} = \{\dot{\mathbf{x}}\}^T\{\mathbf{f}_{ex}(t)\}, \quad (3.3)$$

and the terms in this equation can be written in the form of energy:

$$\dot{K} + p_d + \dot{U} + p_n = p_{in}, \quad (3.4)$$

where $\dot{K} = \{\dot{\mathbf{x}}\}^T[\mathbf{M}]\{\ddot{\mathbf{x}}\}$ is the change rate of the kinetic energy, $p_d = \{\dot{\mathbf{x}}\}^T[\mathbf{C}]\{\dot{\mathbf{x}}\}$ is the instantaneous power dissipation by the system damping, $\dot{U} = \{\dot{\mathbf{x}}\}^T[\mathbf{K}]\{\mathbf{x}\}$ is the change rate of the potential energy stored in the system, $p_n = \{\dot{\mathbf{x}}\}^T\{\mathbf{f}_n(t)\}$ is the total rate of work done by all nonlinear forces arising from the nonlinearities in the system and $p_{in} = \{\dot{\mathbf{x}}\}^T\{\mathbf{f}_{ex}(t)\}$ is the instantaneous input power by the external excitation forces.

Equation. (3.4) can be integrated and then averaged over a time span τ_p from a starting time τ_0 in the steady-state motion, then we can obtain the time-averaged power flow equation as:

$$\frac{1}{\tau_p} \int_{\tau_0}^{\tau_0+\tau_p} (\dot{K} + p_d + \dot{U} + p_n) dt = \frac{1}{\tau_p} \int_{\tau_0}^{\tau_0+\tau_p} p_{in} dt. \quad (3.5)$$

According to the energy conservation, over one cycle of the periodic oscillation, the time-averaged input power into the system should be fully dissipated by the system damping and the dissipative element of the nonlinearities, such as friction force, therefore we have

$$\bar{P}_d + \bar{P}_{dn} = \bar{P}_{in}, \quad (3.6)$$

where \bar{P}_d and \bar{P}_{dn} are the time-averaged dissipated power by the system damping and the dissipative nonlinear element, respectively, and $\bar{P}_{in} = \frac{1}{\tau_p} \int_{\tau_0}^{\tau_0+\tau_p} p_{in} dt$ is the time-averaged input power by the external forces. The general expressions of \bar{P}_d , \bar{P}_{dn} and \bar{P}_{in} are presented as below:

$$\bar{P}_d = \frac{1}{\tau_p} \int_{\tau_0}^{\tau_0+\tau_p} p_d dt = \frac{1}{\tau_p} \int_{\tau_0}^{\tau_0+\tau_p} \{\dot{\mathbf{x}}\}^T[\mathbf{C}]\{\dot{\mathbf{x}}\} dt, \quad (3.7a)$$

$$\bar{P}_{dn} = \frac{1}{\tau_p} \int_{\tau_0}^{\tau_0+\tau_p} p_{dn} dt = \frac{1}{\tau_p} \int_{\tau_0}^{\tau_0+\tau_p} \{\dot{\mathbf{x}}\}^T\{\mathbf{f}_{dn}(t)\} dt, \quad (3.7b)$$

$$\bar{P}_{\text{in}} = \frac{1}{\tau_p} \int_{\tau_0}^{\tau_0 + \tau_p} p_{\text{in}} dt = \frac{1}{\tau_p} \int_{\tau_0}^{\tau_0 + \tau_p} \{\dot{\mathbf{x}}\}^T \{\mathbf{f}_{\text{ex}}(t)\} dt, \quad (3.7c)$$

where $\{\mathbf{f}_{\text{dn}}(t)\}$ denotes the dissipative force vectors generated by the nonlinear element in the system. Eq. (3.7) shows that the time-averaged power flow characteristics of the system can be obtained after the determination of the steady-state response of the system, i.e. the governing equation Eq. (3.1) of the system should be solved. In this research, the harmonic balance approximation approach and the numerical integration approach are employed to solve the equations of motion of the system model. The numerical integration approach is also applied for the quasi-periodic and chaotic motion analysis. In the following content of this chapter, the basic idea of those two approaches for solving the equations of motion is briefly illustrated.

3.2. Numerical integration methods

Numerical integration methods are the standard time-domain methods for solving the ordinary differential equations. The basic procedure of these methods is the evolution of the dependent variables in discrete time steps starting from pre-defined initial values. The value of the dependent variable at each time step is determined by the one at the last time step. In this research, a widely accepted numerical integration method, the Runge-Kutta (RK) method, is employed for finding the solution of the dynamic response of the nonlinear governing equations.

3.2.1. Fourth-order Runge-Kutta method

The RK methods integrate the ordinary differential equations by taking a trial step at the midpoint of an interval (Lambert, 1991). They are based on more terms of a Taylor expansion than the Euler methods (Gerald and Green, 2003). In the methods of the RK family, the 4th order Runge-Kutta (RK4) is the most commonly used method. For illustration purpose, a differential equation is specified as:

$$\frac{dy}{dt} = f(t, y), \quad (3.8)$$

where the initial value of the equation is set as $y(t_0) = y(0)$.

In the RK4 method, the increment between the current point of (t_a, y_a) to the point of (t_{a+1}, y_{a+1}) in the next time step is determined by the weighted average of four estimated coefficients of K_1, K_2, K_3 and K_4 ,

$$y_{a+1} = y_a + \frac{1}{6}(K_1 + 2(K_2 + K_3) + K_4) + O(h^5), \quad (3.9)$$

where

$$K_1 = hf(t_a, y_a), \quad (3.10a)$$

$$K_2 = hf(t_a + h/2, y_a + K_1/2), \quad (3.10b)$$

$$K_3 = hf(t_a + h/2, y_a + K_2/2), \quad (3.10c)$$

$$K_4 = hf(t_a + h/2, y_a + K_3), \quad (3.10d)$$

h is the step size and $O(h^5)$ is the local error term.

3.2.2. Adaptive Runge-Kutta method

To improve the computational efficiency without losing the accuracy of the result, an optimum step size in the RK method can be considered to reduce the total computing time while ensuring that the estimated error in each step is below the pre-defined value. The adaptive Dormand-Prince (RKDP) method (Dormand and Prince, 1980) has been developed to adjust the step size during the integration.

The RKDP method is based on RK methods. In the procedure of the RKDP method, a fourth-order and a fifth-order approximations (with different orders of errors) from the point of (t_a, y_a) to the next point of (t_{a+1}, y_{a+1}) are calculated. The results of y_{a+1} obtained by those two different estimations are then compared. If there is a good agreement between the two results of y_{a+1} , the approximation result can be accepted. In this case, the step size is increased if the agreement between two results is more than demanded. In contrast, if the agreement did not meet the accuracy requirement, the approximation for this time step should be repeated with a reduced step size. In practice, seven coefficients of $K_1, K_2, K_3, K_4, K_5, K_6$ and K_7 are used in the RKDP method at each time step. The fourth-order and fifth-order of approximations are expressed as

$$y_{a+1} = y_a + \frac{35}{384}K_1 + \frac{500}{1113}K_3 + \frac{125}{192}K_4 - \frac{2187}{6784}K_5 + \frac{11}{84}K_6, \quad (3.11a)$$

$$y_{a+1} = y_a + \frac{5179}{57600}K_1 + \frac{7571}{16695}K_3 + \frac{393}{640}K_4 - \frac{92097}{339200}K_5 + \frac{187}{2100}K_6 + \frac{1}{40}K_7, \quad (3.11b)$$

respectively, where

$$K_1 = hf(t_a, y_a), \quad (3.12a)$$

$$K_2 = hf(t_a + \frac{1}{5}h, y_a + \frac{1}{5}K_1), \quad (3.12b)$$

$$K_3 = hf(t_a + \frac{3}{10}h, y_a + \frac{3}{40}K_1 + \frac{9}{40}K_2), \quad (3.12c)$$

$$K_4 = hf(t_a + \frac{4}{5}h, y_a + \frac{44}{45}K_1 - \frac{56}{15}K_2 + \frac{32}{9}K_3), \quad (3.12d)$$

$$K_5 = hf(t_a + \frac{8}{9}h, y_a + \frac{19372}{6561}K_1 - \frac{25360}{2187}K_2 + \frac{64448}{6561}K_3 - \frac{212}{729}K_4), \quad (3.12e)$$

$$K_6 = hf(t_a + h, y_a + \frac{9017}{3168}K_1 - \frac{355}{33}K_2 - \frac{46732}{5247}K_3 + \frac{49}{176}K_4 - \frac{5103}{18656}K_5), \quad (3.12f)$$

$$K_7 = hf(t_a + h, y_a + \frac{35}{384}K_1 + \frac{500}{1113}K_3 + \frac{125}{192}K_4 - \frac{2187}{6784}K_5 + \frac{11}{84}K_6). \quad (3.12g)$$

There are some other widely used adaptive-step-size methods in the RK family, such as the Runge-Kutta-Fehlberg (RKF45) method. The RKF45 method is similar to the RKDP method. The one of the main differences between RKF45 method and RKDP method is that the RKF45 takes the result of the 4th order approximation to determine to the solution of y_{a+1} , and the 5th order approximation is used for error estimation. While the RKDP method uses the result of the 5th order method for the update of y_{a+1} and uses the 4th order method for comparison. Another main difference is that the RKF45 method is a 6-stage method while the RKDP is a 7-stage method (Gerald, 2004). Compared to the RKF45 method, the RKDP method can provide a better accuracy per unit work. In this research, the nonlinear differential equations are solved by the RKDP method based ODE45 solver in the MATLAB software.

3.3. Harmonic balance approximations

3.3.1. Harmonic balance method

Harmonic balance (HB) method is a widely used frequency-domain method for approximating the response of linear or nonlinear dynamical systems. The idea of this method is assuming that the response and the nonlinear terms of the governing equations can be represented by a Fourier series, i.e. harmonic terms. Those harmonic terms can be substituted into the governing equations, and the corresponding terms with the same order can then be balanced to yield a group of algebraic equations. The solutions to the algebraic equations give a periodic approximation on the steady-state response of the dynamical systems.

For a Q -DOF dynamical system, the general governing equation of the system has been presented as Eq. (3.1), the time history of the steady-state displacement response for the j -th ($j = 1, 2 \dots N$) coordinate can be approximated by a truncated Fourier series with the fundamental frequency the same to the external exciting frequency ω , expressed as

$$x_j(t) = \hat{x}_{(j,0)} + \sum_{n=1}^N (\hat{x}_{(j,2n-1)} \cos n\omega t + \hat{x}_{(j,2n)} \sin n\omega t) = \Re\{\sum_{n=0}^N \tilde{R}_{(j,n)} e^{in\omega t}\}, \quad (3.13)$$

where $\hat{x}_{(j,0)}$ is the steady-state oscillating position of the j -th DOF coordinate, $\hat{x}_{(j,2n-1)}$ and $\hat{x}_{(j,2n)}$ are the coefficients of n -th order harmonic terms for the j -th DOF coordinate, N is the total number of harmonics of the Fourier series, $\tilde{R}_{(j,n)}$ is the corresponding complex coefficient for the n -th order harmonic approximation of the j -th DOF and \Re denotes the operation of taking real part of a complex number.

The corresponding approximation of the velocity and acceleration can be obtained by taking differentiation of $x_j(t)$ expressed in Eq. (3.13), we have

$$\dot{x}_j(t) = -\sum_{n=1}^N n\omega (\hat{x}_{(j,2n-1)} \sin n\omega t - \hat{x}_{(j,2n)} \cos n\omega t) = \Re\{\sum_{n=0}^N in\omega \tilde{R}_{(j,n)} e^{in\omega t}\}, \quad (3.14a)$$

$$\begin{aligned} \ddot{x}_j(t) &= -\sum_{n=1}^N (n\omega)^2 (\hat{x}_{(j,2n-1)} \cos n\omega t + \hat{x}_{(j,2n)} \sin n\omega t) \\ &= -\Re\{\sum_{n=0}^N (n\omega)^2 \tilde{R}_{(j,n)} e^{in\omega t}\}, \end{aligned} \quad (3.14b)$$

respectively.

The nonlinear terms in the governing equation, i.e. the nonlinear force vector $\{f_n\}$, and the external excitation force vector $\{f_{\text{ex}}(t)\}$ can be also approximated by Fourier series with N harmonics terms in a similar way. For the j -th coordinate, the corresponding element of the nonlinear force vector and the external excitation force vector can be expressed as

$$f_n(t) = \hat{h}_{(j,0)} + \sum_{n=1}^N (\hat{h}_{(j,2n-1)} \cos n\omega t + \hat{h}_{(j,2n)} \sin n\omega t) = \Re\{\sum_{n=0}^N \tilde{H}_{(j,n)} e^{in\omega t}\}, \quad (3.15a)$$

$$f_{\text{ex}}(t) = \hat{s}_{(j,0)} + \sum_{n=1}^N (\hat{s}_{(j,2n-1)} \cos n\omega t + \hat{s}_{(j,2n)} \sin n\omega t) = \Re\{\sum_{n=0}^N \tilde{S}_{(j,n)} e^{in\omega t}\}, \quad (3.15b)$$

respectively, where $\tilde{H}_{(j,n)}$ and $\tilde{S}_{(j,n)}$ are the complex coefficient for the nonlinear force and external excitation force, respectively. It is noted that the analytical approximated expression for the simple nonlinear forces (e.g. nonlinearity in a polynomial form) may be possibly obtained when the order of Fourier series is small ($N = 1$ or 2). However, for the nonlinearities with more complicated form, the numerical processes, such as alternating frequency/time domain (AFT) technique, may be needed for the

determination of the coefficients $\tilde{H}_{(j,n)}$ of nonlinear forces in Eq. (3.15a). The AFT technique will be illustrated in following Subsection 3.3.2.

By a substitution of the system responses in Eq. (3.13), (3.14) and forces in Eq. (3.15) to the general governing equations (3.1), and balancing the corresponding the coefficients of the n -th ($0 \leq n \leq N$) harmonic terms, we have

$$(-(n\omega)^2[\mathbf{M}] + i(n\omega)[\mathbf{C}] + [\mathbf{K}])\{\tilde{\mathbf{R}}_n\} = \{\tilde{\mathbf{S}}_n\} - \{\tilde{\mathbf{H}}_n\}, \quad (3.16)$$

where $\{\tilde{\mathbf{R}}_n\} = \{\tilde{R}_{(1,n)}, \dots, \tilde{R}_{(j,n)}, \dots, \tilde{R}_{(Q,n)}\}^T$, $\{\tilde{\mathbf{H}}_n\} = \{\tilde{H}_{(1,n)}, \dots, \tilde{H}_{(j,n)}, \dots, \tilde{H}_{(Q,n)}\}^T$ and $\{\tilde{\mathbf{S}}_n\} = \{\tilde{S}_{(1,n)}, \dots, \tilde{H}_{(j,n)}, \dots, \tilde{H}_{(Q,n)}\}^T$.

By introducing the dynamic stiffness matrix $[\tilde{\mathbf{D}}_n]$ with $[\tilde{\mathbf{D}}_n] = -(n\omega)^2[\mathbf{M}] + i(n\omega)[\mathbf{C}] + [\mathbf{K}]$, Eq. (3.16) can be rewritten as

$$[\tilde{\mathbf{D}}_n]\{\tilde{\mathbf{R}}_n\} = \{\tilde{\mathbf{S}}_n\} - \{\tilde{\mathbf{H}}_n\}. \quad (3.17)$$

Therefore, by combining the balancing conditions for each harmonic from $n = 0$ to $n = N$, we have

$$\begin{bmatrix} \tilde{D}_0 & 0 & \dots & 0 \\ 0 & \tilde{D}_1 & \dots & 0 \\ \vdots & \vdots & \ddots & \vdots \\ 0 & 0 & \dots & \tilde{D}_N \end{bmatrix} \begin{Bmatrix} \tilde{R}_0 \\ \tilde{R}_1 \\ \vdots \\ \tilde{R}_N \end{Bmatrix} = \begin{Bmatrix} \tilde{S}_0 - \tilde{H}_0 \\ \tilde{S}_1 - \tilde{H}_1 \\ \vdots \\ \tilde{S}_N - \tilde{H}_N \end{Bmatrix}. \quad (3.18)$$

For each DOF, by grouping a number of N harmonics equations in Eq. (3.18), we can obtain $(2N + 1)$ real nonlinear algebraic equations. Hence for all DOFs, a total number of $Q(2N + 1)$ real nonlinear algebraic equations can be obtained and solved by the Newton-Raphson technique iteratively. It is noted that to achieve a sufficient approximation accuracy for the response of the system, a higher order of Fourier series approximation may be considered (i.e. the value of N is large). After determining the response of the system, the vibration transmission and power flow can be quantified based on Eqs. (3.2) and (3.7).

Compared to the numerical integration method, the main advantage of the HB method is the efficiency of computation. Since the numerical integration method uses direct time step integration, it usually takes a long time to find the periodic limit state when the transient decays slowly. Moreover, for the stiff ordinary differential equations, such as frictional oscillator system, very small time steps should be controlled considering the accuracy of the solution, which will significantly increase the

computational cost. In contrast, the HB method is based on periodic approximation. The simulation of long transients is not needed in the HB method, which can substantially reduce the computing time. Therefore, the HB method is suitable for studying nonlinear dynamical systems with complex nonlinearities. Apart from the computational efficiency, the HB method is capable of computing both stable and unstable periodic oscillations, which provides more information on dynamics. However, it should be pointed out that the HB method may not be applicable for the transient, random or non-periodic processes (Krack and Gross, 2019).

3.3.2. Alternating frequency/time domain technique

The analytical harmonic balance method illustrated in the previous Subsection 3.3.1 can be employed for the system with simple nonlinearities. For such systems, the coefficients of the harmonic terms of the nonlinear forces can be obtained analytically, and the accuracy of the approximation has reached an acceptable level when the harmonics order N is small. However, when the nonlinearity in the system becomes complex, such as non-smooth contact nonlinearity (e.g. stick-slip, impact contact), or when a high order of Fourier series is needed for a better approximation of the nonlinear force, it may be difficult to determine the Fourier coefficients of the nonlinear force analytically. To overcome this problem, the numerical AFT technique can be employed for resolving the nonlinear force (Von Groll and Ewins, 2002; Cameron and Griffin, 1989; Kim and Noah, 1991).

The basic idea of AFT technique is that the approximation of the response in the frequency domain can be inverse Fourier transformed to the response expression in the time domain. The time history of the nonlinear force can then be obtained, which can be Fourier transformed to find the Fourier coefficients of the nonlinear force. The conversion between the time domain and frequency domain is performed numerically by the discrete Fourier transform (DFT) and its inverse (IDFT). The algorithm of the AFT scheme for the treatment of the nonlinear force term $f_n(t)$ in the governing equation of Eq. (3.1) is illustrated in Fig. 3.1. The approximated coefficient of the Fourier series $\tilde{R}_{(j,n)}$ for the response of the j -th coordinate is shown in Fig. 3.1(a). The time histories of responses $x_j(t)$, $\dot{x}_j(t)$ and $\ddot{x}_j(t)$ for the j -th coordinate are obtained by iDFT shown in Fig. 3.1(b). By a substitution of the time domain responses expressions into the nonlinear force expression $f_n(x_j, \dot{x}_j, \ddot{x}_j)$ for the j -th element, the time history of the nonlinear force $f_n(t)$ can then be obtained and the coefficients of the Fourier series $\tilde{H}_{(j,n)}$ for the j -th element of the nonlinear force vector can be calculated by DFT shown in Fig. 3.1(c) and (d).

The general nonlinear force in the form of Fourier series for the j -th element of the system can be described as

$$f_n = \text{DFT}[\text{IDFT}[\{\tilde{R}_{(j,0)}, \tilde{R}_{(j,1)}, \dots, \tilde{R}_{(j,N)}\}]] \quad (3.19)$$

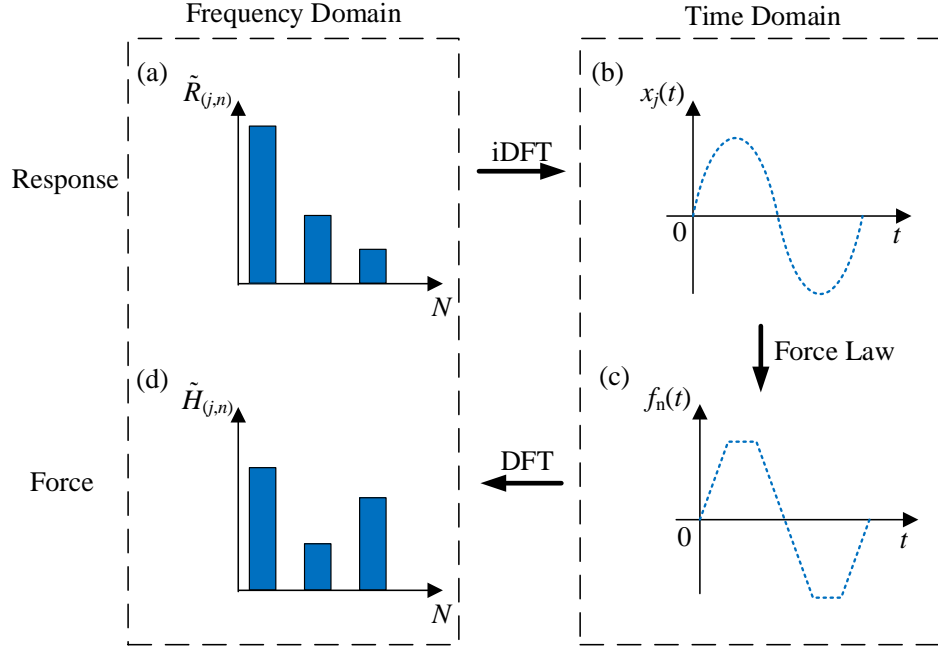


Figure 3.1. Algorithm of alternating frequency/time domain scheme for the treatment of nonlinear force.

3.4. Numerical continuation method

Recalling the use of the harmonic balance method illustrated in Subsection 3.3, a set of real nonlinear algebraic equations is obtained and needed to be solved to determine the dynamic response of the system. The Newton-Raphson iterative method can be used for solving those nonlinear algebraic equations with a good initial guess. In the study of dynamic behaviour of nonlinear vibrating systems, the response solution varying with the excitation frequency, i.e. the frequency response, is usually of interest. A system of nonlinear algebraic equations is written as

$$f(\mathbf{y}, \omega) = 0, \quad (3.20)$$

where \mathbf{y} represents a vector of dimension N and ω is an independent scalar parameter, such as the external excitation frequency. To obtain the frequency response, it is natural to calculate the solution of Eq. (3.20) by Newton-Raphson method for a sequence of frequency points in the range of excitation frequency. However, this procedure will increase the computational burden and reduce computational efficiency. The sequential continuation algorithm can be considered to take the solution at the current frequency

point as the initial guess for determining the next solution point. The next solution point is predicted based on the Newton-Raphson iteration scheme. But this continuation algorithm will encounter the failure of convergence when there are turning and branch points within the solutions due to that the Jacobian matrix is singular at such points. To track the branch or path near the turning point, the predictor-corrector continuation methods can be applied.

In this research, the pseudo-arclength continuation method is employed in conjunction with the harmonic balance method to determine the steady-state response of the dynamical systems. The algorithm of pseudo-arclength continuation method is illustrated in Fig. 3.2 below.

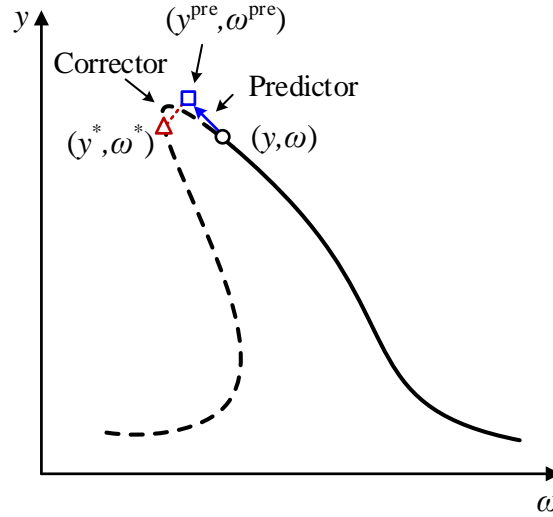


Figure 3.2. Algorithm of pseudo-arclength continuation method.

The continuation step from the solution point of (\mathbf{y}, ω) to the next solution point of (\mathbf{y}^*, ω^*) is divided into two Substeps described as:

$$(\mathbf{y}, \omega) \rightarrow \text{predictor} \rightarrow (\mathbf{y}^{\text{pre}}, \omega^{\text{pre}}) \rightarrow \text{corrector} \rightarrow (\mathbf{y}^*, \omega^*).$$

The predictor Substep from (\mathbf{y}, ω) to $(\mathbf{y}^{\text{pre}}, \omega^{\text{pre}})$ provides an initial guess for the later corrector iterations. The arclength along the solution path is used as the continuation parameter (Von Groll and Ewins, 2001). The direction of the predictor step is along the tangent of the solution branch. Hence the predicted point of $(\mathbf{y}^{\text{pre}}, \omega^{\text{pre}})$ is expressed as

$$\mathbf{y}^{\text{pre}} = \mathbf{y} + \frac{d\mathbf{y}}{ds} \Delta s, \quad (3.21a)$$

$$\omega^{\text{pre}} = \omega + \frac{d\omega}{ds} \Delta s, \quad (3.21b)$$

where Δs is the step length. Here the $\frac{dy}{ds}$ and $\frac{d\omega}{ds}$ remain unknown and can be determined as follows.

By differentiating the Eq. (3.20) respect to the arclength s , we have

$$F_{\mathbf{y}} \frac{d\mathbf{y}}{ds} + F_{\omega} \frac{d\omega}{ds} = [F_{\mathbf{y}}, F_{\omega}] \begin{pmatrix} \mathbf{y}' \\ \omega' \end{pmatrix} = 0, \quad (3.22)$$

where $F_{\mathbf{y}} = \frac{\partial f(\mathbf{y}, \omega)}{\partial \mathbf{y}}$, $F_{\omega} = \frac{\partial f(\mathbf{y}, \omega)}{\partial \omega}$ and $\begin{pmatrix} \mathbf{y}' \\ \omega' \end{pmatrix}$ is the tangent vector having a unit length (Seydel, 2009). Therefore, a relation of the arclength s can be obtained as

$$\left(\frac{dy_1}{ds}\right)^2 + \dots + \left(\frac{dy_N}{ds}\right)^2 + \left(\frac{d\omega}{ds}\right)^2 = 1. \quad (3.23)$$

The predicted point of $(\mathbf{y}^{\text{pre}}, \omega^{\text{pre}})$ can be obtained by solving the Eqs. (3.21-3.23).

For the corrector process, the correction vector in the pseudo-arclength continuation is normal to the tangent vector of $\begin{pmatrix} \mathbf{y}' \\ \omega' \end{pmatrix}$, we have

$$\begin{pmatrix} \mathbf{y}^* - \mathbf{y}^{\text{pre}} \\ \omega^* - \omega^{\text{pre}} \end{pmatrix}^T \begin{pmatrix} \mathbf{y}' \\ \omega' \end{pmatrix} = 0. \quad (3.24)$$

To identify the solution points mathematically, the parameterization on the solution branch is performed by using the parameter of the arclength s . By substitution of Eqs. (3.21) into (3.24), an additional scalar equation is obtained: (Nayfeh and Balachandran, 2008)

$$0 = f_{\text{pa}}(\mathbf{y}, \omega, s) = (y_1^* - y_1) \frac{dy_1}{ds} + \dots + (y_N^* - y_N) \frac{dy_N}{ds} + (\omega^* - \omega) \frac{d\omega}{ds} - \Delta s. \quad (3.25)$$

Then an extended system can be formulated by a combination of Eqs. (3.20) and (3.25),

$$\mathbf{F}(\mathbf{y}, \omega, s) = \begin{pmatrix} f(\mathbf{y}, \omega) \\ f_{\text{pa}}(\mathbf{y}, \omega, s) \end{pmatrix}. \quad (3.26)$$

The correctors can be obtained by solving the Eq. (3.26), where the Newton iteration method is employed. When the next point of (\mathbf{y}^*, ω^*) is reached, the correction iteration process is finished. It is noted that the ending condition for the corrector iteration is controlled by the parameterization equation of $0 = f_{\text{pa}}(\mathbf{y}, \omega, s)$. Moreover, the step-length is adaptively controlled within a range and the control strategy is determined empirically and varied with the solver and tolerances (Krack and Gross, 2019).

Figure. 3.3 shows the summarized procedures of HB approximation method and numerical continuation method in this study for solving the governing equations of the nonlinear dynamical system. The solution for the corresponding linear system is taken as the initial guess of the problem. If the nonlinear force in the dynamical system can be directly expanded to harmonic terms in an analytical way and a sufficient accuracy has been achieved by first-order terms ($N = 1$), those systems can be regarded as simple systems and the analytical 1st order HB method can be applied on those systems. The obtained nonlinear algebraic equations can then be solved by the bisection method (Press et al., 1989) straightforwardly or by the pseudo-arclength numerical continuation method.

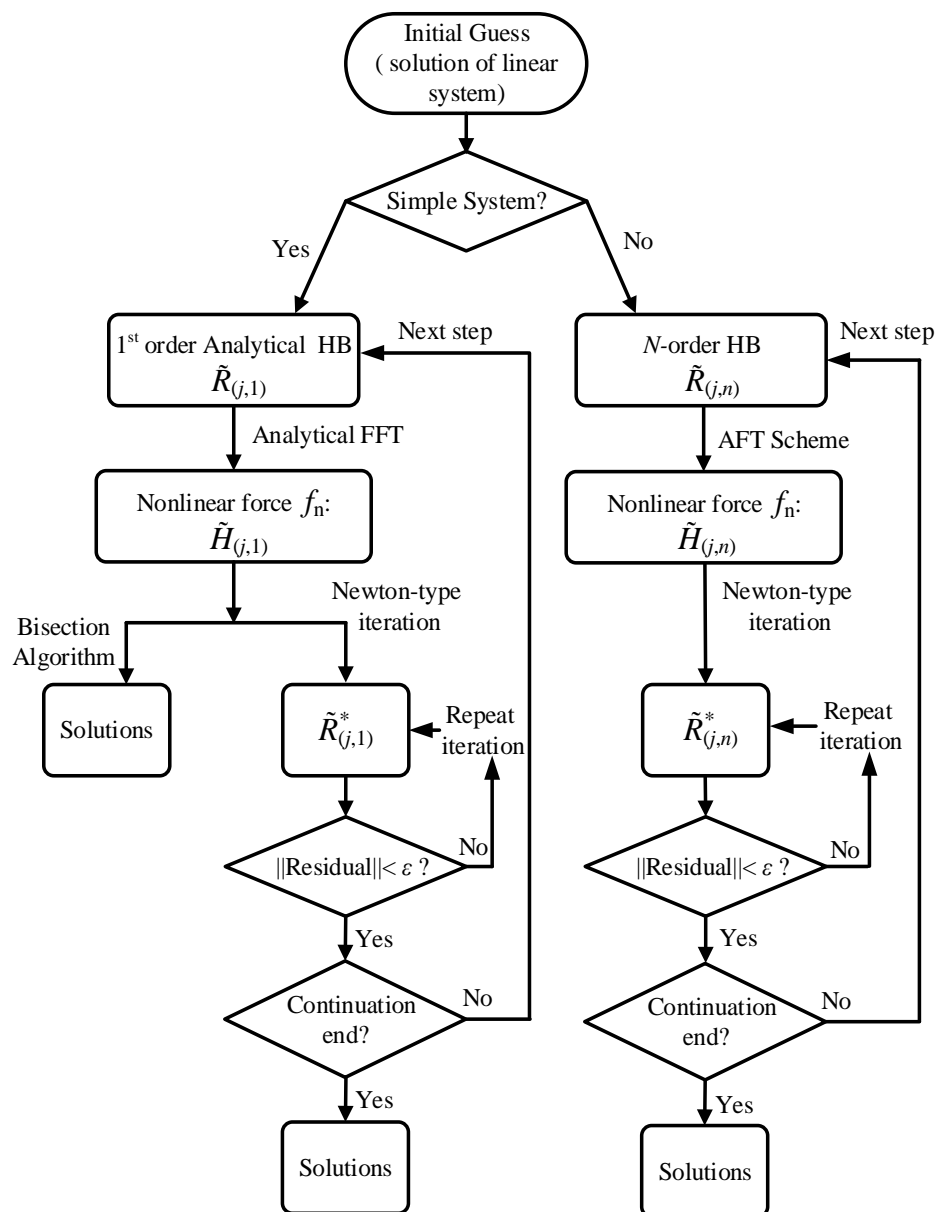


Figure 3.3. Schematic of procedures of harmonic balance approximation in conjunction with the numerical continuations

For the complex systems, the nonlinear force is more generic and the structure of the system is more complicated. The AFT scheme illustrated in Subsection 3.3.2 is needed to resolve the nonlinear force and a higher order of HB method with $N > 1$ should be applied for capturing more dynamic information of the system. The numerical continuation method is combined with HB to trace the solution path of the nonlinear algebraic equations within a range of parameter values. The Newton-Raphson based correction process is repeated until the result is on the solution branch, i.e. the residual of the Eq. (3.26) is small enough ($\|\text{Residual}\| < \varepsilon$, and ε is the user-defined tolerance value). During the continuation process, the current solution point is used as the initial guess for the next solution. When the frequency in the continuation reaches the boundary of the pre-defined frequency range, the numerical continuation is ended.

3.5. Exemplary application to a 2DOF coupled Duffing oscillator system

Duffing oscillator has been widely accepted as a prototype of nonlinear dynamics. It has been used to model different physical processes, such as stiffening springs and beam buckling (Duffing, 1918). In this Subsection, a 2DOF coupled Duffing oscillator system, which has been investigated by Shi and Yang (2019), is used as an example for demonstrating the harmonic balance approximation method and the vibration transmission analysis method presented in this chapter.

3.5.1. Mathematical model and frequency response

As shown in Fig. 3.4, the system consists of two SDOF systems coupled via a linear interface. The linear interface is formed by a linear spring of stiffness k_3 and a linear damper of damping c_3 . The primary system comprises a Duffing-type nonlinear spring, a linear damper of c_1 and a mass of m_1 subjected to a harmonic force excitation with amplitude of f_0 and frequency of ω . The secondary system consists of another identical nonlinear spring, a linear damper of c_2 and a mass of m_2 .

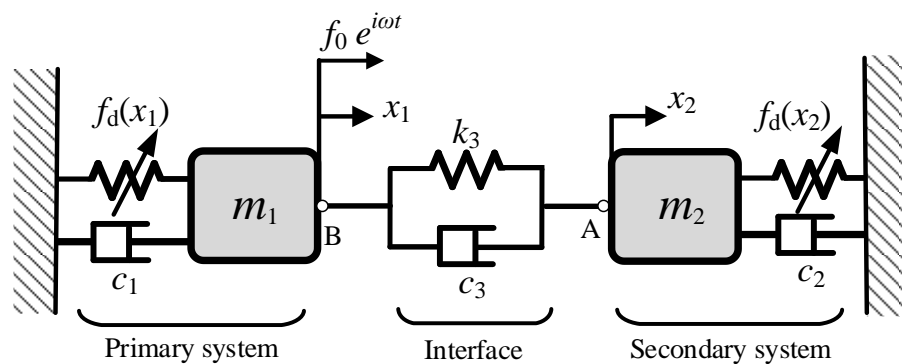


Figure 3.4. Schematic of a 2DOF coupled Duffing oscillator system (Shi and Yang, 2019)

The governing equation of the system can be written in a matrix form as

$$\begin{bmatrix} m_1 & 0 \\ 0 & m_2 \end{bmatrix} \begin{Bmatrix} \ddot{x}_1 \\ \ddot{x}_2 \end{Bmatrix} + \begin{bmatrix} c_1 + c_3 & -c_3 \\ -c_3 & c_2 + c_3 \end{bmatrix} \begin{Bmatrix} \dot{x}_1 \\ \dot{x}_2 \end{Bmatrix} + \begin{bmatrix} k_1 + k_3 & -k_3 \\ -k_3 & k_2 + k_3 \end{bmatrix} \begin{Bmatrix} x_1 \\ x_2 \end{Bmatrix} + \begin{Bmatrix} f_d(x_1) \\ f_d(x_2) \end{Bmatrix} = \begin{Bmatrix} f_0 e^{i\omega t} \\ 0 \end{Bmatrix}. \quad (3.27)$$

where $f_d(x)$ is the function of nonlinear restoring force of the nonlinear spring with $f_d(x) = k_{d1}x + k_{d2}x^3$, k_{d1} and k_{d2} are the stiffness coefficients for the nonlinear springs.

Based on the harmonic balance method illustrated in Subsection 3.3.1, the steady-state response of the system can be approximated as

$$\{x_1, x_2\}^T = \Re\{\sum_{n=0}^N \tilde{R}_{(1,n)} e^{in\omega t}, \sum_{n=0}^N \tilde{R}_{(2,n)} e^{in\omega t}\}^T, \quad (3.28)$$

The corresponding velocity and acceleration are

$$\{\dot{x}_1, \dot{x}_2\}^T = \Re\{\sum_{n=0}^N in\omega \tilde{R}_{(1,n)} e^{in\omega t}, \sum_{n=0}^N in\omega \tilde{R}_{(2,n)} e^{in\omega t}\}^T, \quad (3.29a)$$

$$\{\ddot{x}_1, \ddot{x}_2\}^T = \Re\{-\sum_{n=0}^N (n\omega)^2 \tilde{R}_{(1,n)} e^{in\omega t}, -\sum_{n=0}^N (n\omega)^2 \tilde{R}_{(2,n)} e^{in\omega t}\}^T, \quad (3.29b)$$

respectively.

The nonlinear restoring force $f_d(x)$ of the nonlinear spring can be approximated by a truncated Fourier series as

$$\{f_d(x_1), f_d(x_2)\}^T = \Re\{\sum_{n=0}^N \tilde{H}_{(1,n)} e^{in\omega t}, \sum_{n=0}^N \tilde{H}_{(2,n)} e^{in\omega t}\}^T. \quad (3.30)$$

In accordance of the AFT scheme presented in Subsection 3.3.2, the approximated displacement response in time domain expressed in Eq. (3.28) is firstly substituted into the restoring force function of the nonlinear spring $f_d(x) = k_{d1}x + k_{d2}x^3$. The time history of the nonlinear restoring force acting on the two masses can be obtained as

$$\{f_d(x_1), f_d(x_2)\}^T = \Re\left\{ \begin{array}{l} \sum_{n=0}^N (k_{d1} \tilde{R}_{(1,n)} e^{in\omega t} + k_{d2} \tilde{R}_{(1,n)}^3 e^{i3n\omega t}) \\ \sum_{n=0}^N (k_{d1} \tilde{R}_{(2,n)} e^{in\omega t} + k_{d2} \tilde{R}_{(2,n)}^3 e^{i3n\omega t}) \end{array} \right\}, \quad (3.31)$$

which can then be Fourier transformed to determine the coefficients of $\tilde{H}_{(1,n)}$ and $\tilde{H}_{(2,n)}$ in Eq. (3.30) numerically.

By substituting the Eqs. (3.28-3.30) into Eq. (3.27) and balancing the corresponding coefficients of the corresponding n -th order harmonic terms, the Eq.

(3.27) can be transformed in the form of Eq. (3.17) with $[\tilde{D}_n] = -(n\omega)^2 \begin{bmatrix} m_1 & 0 \\ 0 & m_2 \end{bmatrix} + i(n\omega) \begin{bmatrix} c_1 + c_3 & -c_3 \\ -c_3 & c_2 + c_3 \end{bmatrix} + \begin{bmatrix} k_1 + k_3 & -k_3 \\ -k_3 & k_2 + k_3 \end{bmatrix}$ and $\{\tilde{S}_n\} = \{F_0, 0, \dots, 0\}^T$. A set of $2(2N + 1)$ algebraic equations is obtained by grouping a number of N harmonics equations, which can be solved by Newton-Raphson method. The pseudo-arclength continuation method illustrated in Subsection 3.4 is also used for tracking the solution path. In this example, the harmonic order N in the HB-AFT is set as $N = 2$. When the numerical continuation is used, the initial guess of the system is obtained by solving the corresponding linear governing equation of the system with $k_{d2} = 0$. The default step size is pre-defined as $\Delta s = 0.01$ and the range for adaptive step size control is set as $[\Delta s/5, 2\Delta s]$.

The results of steady-state frequency response amplitudes of the two masses are shown in Fig. 3.5 below. The solid line represents the 2nd order HB-AFT result, the symbols denote the numerical integration results. Here the system parameters are set as $m_1 = m_2 = 1$ kg, $k_{d1} = k_3 = 1$ N/m, $k_{d2} = 0.1$ N/m, $c_1 = c_2 = c_3 = 0.02$ Nm/s and $f_0 = 0.5$ N. It shows that when the value of k_{d2} is positive, the Duffing-type nonlinearity can bend the curves of the response amplitude of the masses to the high frequencies. It can also lead to a jump phenomenon and multiple solutions near the resonant frequencies. Up to five solutions near the second peak of the response curve can be captured by the HB-AFT method with numerical continuations.

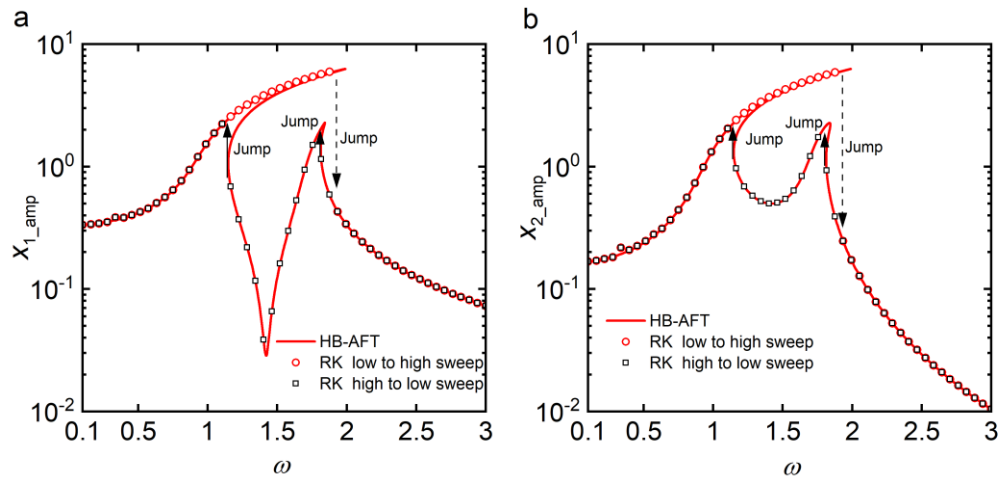


Figure 3.5. The steady-state response amplitude results of (a) X_{1_amp} for the primary mass and (b) X_{2_amp} for the secondary mass. The solid line is HB-AFT result and symbols are the RK results.

3.5.2. Force transmissibility and PFA analysis

For the current system, the transmitted force f_{ts} from the primary system to the secondary system is the total coupling force at the interface, hence we have $f_{ts} = k_3(x_1 - x_2) + c_3(\dot{x}_1 - \dot{x}_2)$. By the definition of force transmissibility in Eq. (3.2), the force transmissibility to the secondary system can be expressed as

$$TR_S = \frac{\max(|f_{ts}|)}{f_0}. \quad (3.32)$$

In accordance of the definitions of power flow variables in Eq. (3.7), the time-averaged input power \bar{P}_{in} , the time-averaged power dissipation by the damper c_2 and c_3 are defined as

$$\bar{P}_{in} = \frac{1}{\tau_p} \int_{\tau_0}^{\tau_0 + \tau_p} \dot{x}_1 f_0 e^{i\omega t} dt, \quad (3.33a)$$

$$\bar{P}_{d2} = \frac{1}{\tau_p} \int_{\tau_0}^{\tau_0 + \tau_p} \dot{x}_2^2 c_2 dt, \quad (3.33b)$$

$$\bar{P}_{d3} = \frac{1}{\tau_p} \int_{\tau_0}^{\tau_0 + \tau_p} (\dot{x}_1 - \dot{x}_2)^2 c_3 dt, \quad (3.33c)$$

respectively, where τ_0 is starting time of averaging, τ_p is the time span for averaging with $\tau_p = 2\pi/\omega$. Based on the energy conservation, over one cycle of oscillation, the total energy transmitted to the secondary system is fully dissipated by the damper c_2 of the secondary system. Therefore, we have the time-averaged power transmission \bar{P}_{ts} to the secondary system equals to \bar{P}_{d2} . By this way, the vibration transmission from the primary system to the secondary system can be evaluated from the energy transmission perspective.

Figure 3.6(a), (b), (c) and (d) shows the force transmission TR_S , the time-averaged input power \bar{P}_{in} , the time-averaged transmitted power \bar{P}_{ts} to the secondary system and the time-averaged dissipated power \bar{P}_{d3} by the interfacial damper, respectively. From Fig. 3.6(a) and (d), an anti-peak is found in the curves of TR_S and \bar{P}_{d3} when the frequency is near the in-phase mode of the corresponding linear system and the anti-peak shows a significant bending to the right. Jump-down and jump-up behaviour as well as multiple solutions can be observed in the force transmissibility curve and the curves of power flow variables. Fig. 3.6(b) and (c) shows that both peaks of \bar{P}_{in} and \bar{P}_{ts} are bending to the high frequencies. Those characteristics are due to the nonlinear effect introduced by the nonlinear spring. Fig. 3.6(b-d) shows that the input energy from the external force excitation, the energy transmission between the sub-systems and the

energy dissipation at the interface can be quantified by the PFA indices, which may provide insight into vibration transmission behaviour and benefit the dynamic design of vibration suppression.

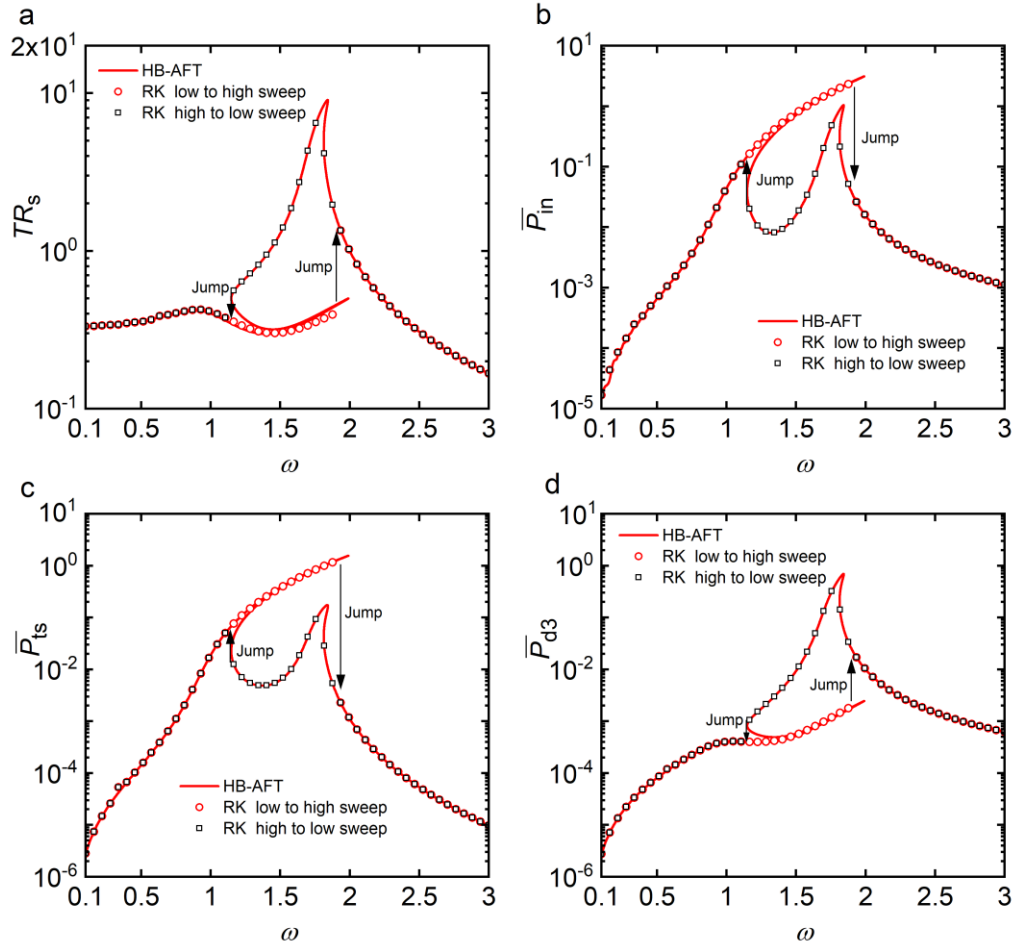


Figure 3.6. Comparison between HB-AFT method and RK method on the result of (a) the force transmissibility TR_s , (b) the time-averaged input power \bar{P}_{in} , (c) the time-averaged transmitted power \bar{P}_{ts} and (d) the time-averaged dissipated power \bar{P}_{d3} . The solid line is HB-AFT result and symbols are the RK results.

3.6. Summary

In this research, analytical, semi-analytical (HB-AFT) and numerical methods discussed in this chapter have been applied in the investigation of dynamics, vibration transmission and PFA of different nonlinear non-smooth dynamical systems, including impact oscillators and Coulomb friction oscillators, and also in the analysis of nonlinear vibration isolators created by a linkage mechanism. For the non-smooth impact oscillator with a linear constraint in Chapter 4, the discontinuity due to the intermittent contact is approximated by Fourier series. The analytical derivation of the steady-state frequency-response relationship, force transmission and power flow indices are

performed by analytical HB method. In the other systems of this research, both semi-analytical HB-AFT with numerical continuations and numerical integrations have been used for comparison and cross verifications of the dynamic behaviour and vibration transmission results. In Chapter 6, the power flow indices obtained from the energy balance equations are used as performance indicators of the proposed nonlinear vibration isolators.

Chapter 4

Vibration transmission analysis of impact oscillators with linear and nonlinear QZS constraints

Impact oscillator models are widely used for dynamic analysis of engineering systems such as rotating machinery with possible rotor and stator contact (Peletan et al., 2014), drilling systems (Chávez et al., 2014), tooling machinery (Theodossiades and Natsiavas, 2000) and bearing systems with clearance (Gupta et al., 2011). Such systems often have the property that a vibrating main substructure may be engaged with another substructure (i.e., a constraint) when its displacement response exceeds a certain clearance. The collision between the substructures leads to abrupt changes in dynamic properties of the integrated system. There may be non-smooth variations in damping or restoring forces and consequently discontinuities in damping or stiffness coefficients. As a result, the integrated system becomes nonlinear and can exhibit complex nonlinear phenomena. Many previous works have been reported on nonlinear dynamic analysis of SDOF, 2DOF or multiple-DOF impact oscillators with a linear elastic or rigid constraint (Shaw and Holmes, 1983; Lau and Zhang, 1992; Ing et al., 2010; Jiang et al., 2017); yet, there are far fewer studies considering impact oscillators comprising a nonlinear main structure or a nonlinear constraint (Chatterjee et al., 1995). Chávez et al. (2017) conducted bifurcation analysis of Duffing oscillators coupled via a soft constraint and showed the destabilization of solutions when decreasing the distance between the oscillating systems and the loss of stability for the solutions due to grazing-induced bifurcations. Gilardi and Sharf (2002) suggested that the continuous contact dynamics models involve nonlinear impact force model i.e. Hertz's model when considering the elastic deformation of the interface material. Therefore there is still a need to examine and reveal the effect of a nonlinear constraint on the dynamics of impact oscillators. Moreover, not much work was reported on the vibration transmission characteristics of impact oscillators. In the dynamic design of such systems, understanding of vibration transmission behaviour is of great importance to ensure both system integrity and also dynamic performance. In particular, the influence of different types of constraint on the level of vibration transmission needs to be explored. In this chapter, the vibration force transmission and power flow characteristics of SDOF and 2DOF impact oscillators with

linear or nonlinear quasi-zero-stiffness (QZS) constraints are investigated. Both HB method and numerical integration method are used to obtain the force transmissibility and time-averaged power flow variables so as to quantify vibration transmission in the systems. The effects of the stiffness and damping levels of the constraint on the dynamic response and vibration transmission are revealed

4.1. SDOF impact oscillator with a linear constraint

4.1.1. Mathematical modelling

Figure 4.1 shows an SDOF oscillator comprising a mass m_1 , a viscous damper with damping coefficient c_1 and a linear spring with stiffness coefficient k_1 . The mass is subjected to a harmonic excitation of amplitude f_0 and frequency ω and moves in horizontal direction. The equilibrium position of the mass, where the spring k_1 is unstretched, is set as a reference with $x_1 = 0$. A linear constraint consisting of a linear spring of stiffness coefficient k_h and a viscous damper of damping coefficient of c_h is placed between the mass and the right-hand wall. The initial gap between the mass and the constraint is denoted by x_c . Throughout this chapter, it is assumed that the constraint has negligible mass and no friction is considered.

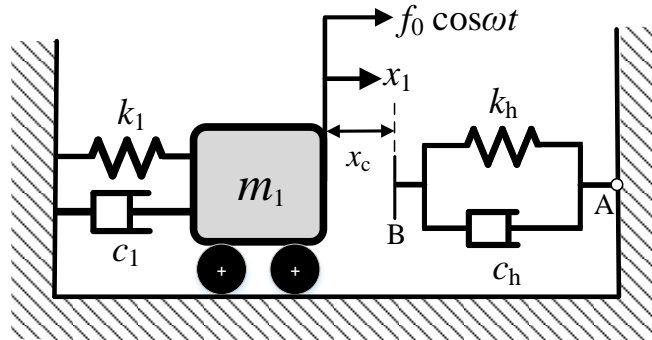


Figure 4.1. A schematic representation of an SDOF impact oscillator with a linear constraint.

When the mass moves to the right, it becomes in contact with the linear constraint when its displacement x_1 increases to x_c . When there is no damping in the constraint, the governing equation of the mass of m_1 is

$$m_1 \ddot{x}_1 + c_1 \dot{x}_1 + k_1 x_1 + U(\delta) k_h \delta = f_0 \cos \omega t, \quad (4.1)$$

where $\delta = x_1 - x_c$ and $U(\delta)$ representing the Heaviside step function expressed by

$$U(\delta) = \begin{cases} 0, & \text{when } \delta \leq 0, \\ 1, & \text{when } \delta > 0. \end{cases} \quad (4.2)$$

Note that if there exists damping in the constraint, physically the contact between the mass and the constraint is lost when the force acted on the mass from the constraint

becomes zero (Chávez et al., 2017). In this chapter, the damping in the constraint is assumed to be weak. When the mass is moving left with the constraint, the restoring force by the constraint spring pushing the mass is generally larger than the damping force by the constraint damper pulling the mass. Therefore, the loss of the contact between the mass and the constraint occurs when the displacement of the mass is only slightly larger than the gap distance such that $x_1 \approx x_c$. This approximation of the loss of contact condition has been made in the modelling of impact oscillators (Narimani et al., 2004; Natsiavas, 1990; Ma et al., 2006), and is also adopted in the current chapter. The equation of motion of the mass with consideration of the constraint damping is

$$m_1 \ddot{x}_1 + c_1 \dot{x}_1 + k_1 x_1 + U(\delta)(k_h \delta + c_h \dot{\delta}) = f_0 \cos \omega t. \quad (4.3)$$

To obtain analytical approximations of frequency-response relationship, the steady-state response of the system is assumed to be

$$\delta = r_0 + r_1 \cos(\omega t + \phi) = r_0 + r_1 \cos \theta = r_1(\cos \theta - \cos \theta_0), \quad (4.4a)$$

$$\dot{\delta} = -\omega r_1 \sin(\omega t + \phi) = -\omega r_1 \sin \theta, \quad (4.4b)$$

where $\theta = \omega t + \phi$, and $\theta_0 = \cos^{-1}(-r_0/r_1)$. Eq. (4.4) implies that the impact of the vibrating mass and the linear constraint occurs in the oscillation cycle so that $r_0 - r_1 < 0 < r_0 + r_1$ and correspondingly we have $|r_0|/r_1 \leq 1$. Over one oscillation cycle with $\theta \in [-\theta_0, 2\pi - \theta_0]$, the linear constraint is engaged with the mass when $\theta \in [-\theta_0, \theta_0]$. The second-order Fourier expansion of the Heaviside step function is

$$U(\delta) \approx B_0 + B_{1c} \cos \omega t + B_{1s} \sin \omega t + B_{2c} \cos 2\omega t + B_{2s} \sin 2\omega t, \quad (4.5)$$

where

$$B_0 = \frac{\omega}{2\pi} \int_0^{2\pi} U(\delta) dt = \frac{\cos^{-1}(-\frac{r_0}{r_1})}{\pi} = \frac{\theta_0}{\pi}, \quad (4.6a)$$

$$B_{1c} = \frac{\omega}{\pi} \int_0^{2\pi} U(\delta) \cos \omega t dt = \frac{2 \cos \phi}{\pi} \sqrt{1 - \left(\frac{r_0}{r_1}\right)^2} = \frac{2 \cos \phi \sin \theta_0}{\pi}, \quad (4.6b)$$

$$B_{1s} = \frac{\omega}{\pi} \int_0^{2\pi} U(\delta) \sin \omega t dt = -\frac{2 \sin \phi}{\pi} \sqrt{1 - \left(\frac{r_0}{r_1}\right)^2} = -\frac{2 \sin \phi \sin \theta_0}{\pi}, \quad (4.6c)$$

$$B_{2c} = \frac{\omega}{\pi} \int_0^{2\pi} U(\delta) \cos 2\omega t dt = \frac{\cos 2\phi \sin 2\theta_0}{\pi}, \quad (4.6d)$$

$$B_{2s} = \frac{\omega}{\pi} \int_0^{2\pi} U(\delta) \sin 2\omega t dt = -\frac{\sin 2\phi \sin 2\theta_0}{\pi}. \quad (4.6e)$$

Thus we have $U(\delta) \approx B_0 + B_1 \cos(\omega t + \phi) + B_2 \cos(2\omega t + 2\phi)$, where $B_1 = \frac{2}{\pi} \sqrt{1 - \left(\frac{r_0}{r_1}\right)^2} = \frac{2}{\pi} \sin \theta_0$, $B_2 = \frac{1}{\pi} \sin 2\theta_0$, so that

$$U(\delta) \approx \frac{1}{\pi} (\theta_0 + 2 \sin \theta_0 \cos \theta + \sin 2\theta_0 \cos 2\theta). \quad (4.7)$$

Figure. 4.2 plots the variations of the exact Heaviside function with respect to δ as well as the approximations based on the first order and the second-order Fourier expansions based on Eq. (4.7). For illustration purpose, variables are set as $r_0 = 0.4$ and $r_1 = 0.8$, and thus $\delta = 0.4 + 0.8 \cos \theta$. Correspondingly, we have $\theta_0 = \cos^{-1}(-r_0/r_1) = 2\pi/3$ and $U(\delta) \approx (4\pi + 6\sqrt{3} \cos \theta + 3\sqrt{3} \cos 2\theta)/(6\pi)$. The figure shows that the use of the 2nd order expansion can generally capture the waveform of the Heaviside function with a degree of accuracy. It enables analytical derivations of the frequency-response relation to gain physical insights into the dynamic behaviour. More accurate approximations of the function may be achievable by higher-order expansions, but at the cost of increasing complexity in the analytical derivation process and higher computational cost.

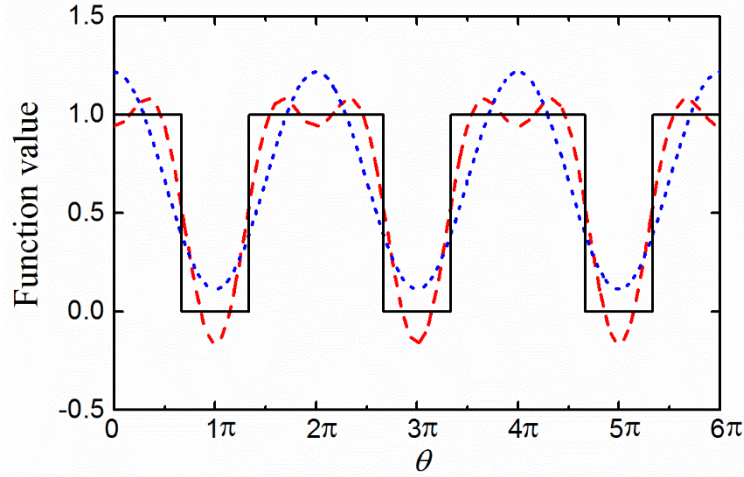


Figure 4.2. Approximation of the Heaviside function using Fourier expansion ($\delta = 0.4 + 0.8 \cos \theta$). Solid line: exact value of $U(\delta)$; dotted line: first order expansion; dashed line: 2nd order expansion.

By inserting Eqs. (4.4) and (4.7) into Eq. (4.3) and balancing the static term and the coefficients of the harmonic terms $\cos \theta$ and $\sin \theta$, we have

$$\frac{k_h}{\pi} (r_0 \theta_0 + r_1 \sin \theta_0) + k_1 (x_c + r_0) = 0, \quad (4.8a)$$

$$(k_1 - m_1 \omega^2) r_1 + k_h r_1 \left(\frac{\theta_0}{\pi} + \frac{\sin 2\theta_0}{2\pi} \right) + k_h r_0 \frac{2 \sin \theta_0}{\pi} = f_0 \cos \phi, \quad (4.8b)$$

$$-c_1 \omega r_1 - c_h \omega r_1 \left(\frac{\theta_0}{\pi} - \frac{\sin 2\theta_0}{2\pi} \right) = f_0 \sin \phi. \quad (4.8c)$$

Recalling that $r_0 = -r_1 \cos \theta_0$, Eq. (4.8a) becomes

$$(k_h \sin \theta_0 - k_h \theta_0 \cos \theta_0 - \pi k_1 \cos \theta_0) r_1 + \pi k_1 x_c = 0. \quad (4.9)$$

By using a manipulation of Eq. (4.8b) and (4.8c) to cancel out the trigonometric terms of ϕ , we have

$$\left[(k_1 - m_1 \omega^2) + \left(\frac{\theta_0}{\pi} - \frac{\sin 2\theta_0}{2\pi} \right) k_h \right]^2 r_1^2 + \left[c_1 + \left(\frac{\theta_0}{\pi} - \frac{\sin 2\theta_0}{2\pi} \right) c_h \right]^2 \omega^2 r_1^2 = f_0^2. \quad (4.10)$$

Therefore, the frequency-response relationship is obtained and expressed by Eqs. (4.9) and (4.10), which are two nonlinear algebraic equations of r_1 and θ_0 . Note that r_1 can be firstly expressed as a function of θ_0 by using Eq. (4.9). By inserting the resultant expression into Eq. (4.10) and employing a standard bisection method, the steady-state dynamic response amplitudes r_1 and θ_0 can be found.

The following parameters are introduced for clarity and later parametric study:

$$\omega_1 = \sqrt{\frac{k_1}{m_1}}, \quad \zeta_1 = \frac{c_1}{2m_1\omega_1}, \quad X_1 = \frac{x_1}{x_c}, \quad \lambda = \frac{k_h}{k_1}, \quad \rho = \frac{c_h}{c_1}, \quad F_0 = \frac{f_0}{k_1 x_c}, \quad \Omega = \frac{\omega}{\omega_1}, \quad \tau = \omega_1 t,$$

where ω_1 and ζ_1 the undamped natural frequency and the damping ratio of the system without the constraint, respectively; X_1 denotes the dimensionless displacement of the mass; λ and ρ are the stiffness ratio and damping ratio of the linear constraint; F_0 and Ω are the dimensionless excitation amplitude and frequency, respectively; and τ is the dimensionless time. Eq. (4.3) can be transformed into

$$X_1'' + 2\zeta_1 X_1' + X_1 + F_{LC} = F_0 \cos \Omega \tau, \quad (4.11)$$

where $F_{LC} = (\lambda \Delta + 2\zeta_1 \rho X_1') U(\Delta)$ is the nonlinear force generated by the linear constraint with $\Delta = X_1 - 1$, and the prime denotes differentiation with respect to τ . Eqs. (4.9) and (4.10) become

$$(\lambda \sin \theta_0 - \lambda \theta_0 \cos \theta_0 - \pi \cos \theta_0) R_1 + \pi = 0, \quad (4.12a)$$

$$\left[(1 - \Omega^2) + \left(\frac{\theta_0}{\pi} - \frac{\sin 2\theta_0}{2\pi} \right) \lambda \right]^2 R_1^2 + 4\zeta_1^2 \left[1 + \left(\frac{\theta_0}{\pi} - \frac{\sin 2\theta_0}{2\pi} \right) \rho \right]^2 \Omega^2 R_1^2 = F_0^2, \quad (4.12b)$$

where $R_0 = r_0/x_c$ and $R_1 = r_1/x_c$ are the dimensionless displacement amplitudes for the static and fundamental frequency components, respectively.

4.1.2. Vibration transmission analysis

For the current system, the dimensionless transmitted force from the mass m_1 to the right-hand-side (RHS) and the left-hand-side (LHS) walls are

$$F_{tR} = F_{LC} = (\lambda\Delta + 2\zeta_1\rho X_1')U(\Delta) \approx (\lambda(R_0 + R_1 \cos \theta) - 2\zeta_1\rho R_1 \sin \theta)U(\Delta), \quad (4.13a)$$

$$F_{tL} = 2\zeta_1 X_1' + X_1 \approx 1 - R_1 \cos \theta_0 + R_1 \cos \theta - 2\zeta_1 \Omega R_1 \sin \theta, \quad (4.13b)$$

respectively, where only components of the static term and the one at the fundamental frequency were considered in the approximations. The force transmissibility can be defined as the maximum magnitude of the transmitted forces to that of the input force:

$$TR_R = \frac{\max(|F_{tR}|)}{F_0}, \quad TR_L = \frac{\max(|F_{tL}|)}{F_0}, \quad (4.14a, 4.14b)$$

where only first-order approximations of the transmitted forces are employed in the HB approximations. To suppress the vibration transmission, a low value of force transmissibility is desirable for the design of the linear constraint.

The steady-state dimensionless time-averaged input power into the system is expressed by

$$\bar{P}_{in} = \frac{1}{\tau_p} \int_{\tau_0}^{\tau_0 + \tau_p} X_1' F_0 \cos \Omega \tau \, d\tau \approx -\frac{F_0 \Omega R_1 \sin \phi}{2} = \zeta_1 \Omega^2 R_1^2 \left[1 + \rho \left(\frac{\theta_0}{\pi} - \frac{\sin 2\theta_0}{2\pi} \right) \right], \quad (4.15)$$

where Eqs. (4.4b) and (4.8c) were used in the approximations of the response, $\tau_p = 2\pi/\Omega$ (e.g., one excitation cycle) is the averaging time and τ_0 is the starting time for averaging. Over one cycle of steady-state periodic response, the dimensionless time-averaged power dissipated by the damper c_h in the constraint and by the damper c_1 is expressed by

$$\bar{P}_{dc} = \frac{1}{\tau_p} \int_{\tau_0}^{\tau_0 + \tau_p} F_{dc} X_1' U(\Delta) \, d\tau \approx \zeta_1 \rho \Omega^2 R_1^2 \left(\frac{\theta_0}{\pi} - \frac{\sin 2\theta_0}{2\pi} \right), \quad (4.16a)$$

$$\bar{P}_{d1} = \frac{1}{\tau_p} \int_{\tau_0}^{\tau_0 + \tau_p} F_{d1} X_1' \, d\tau \approx \zeta_1 \Omega^2 R_1^2, \quad (4.16b)$$

respectively, where $F_{dc} = 2\zeta_1\rho X_1' U(\Delta)$ and $F_{d1} = 2\zeta_1 X_1'$ are the corresponding dimensionless damping forces, and first-order approximations were used. The power dissipation ratios are defined as the ratios between the time-averaged dissipated power and input power \bar{P}_{in} :

$$R_{ac} = \frac{\bar{P}_{dc}}{\bar{P}_{in}} \approx \frac{\rho(2\theta_0 - \sin 2\theta_0)}{2\pi + \rho(2\theta_0 - \sin 2\theta_0)}, \quad R_{a1} = \frac{\bar{P}_{d1}}{\bar{P}_{in}} \approx \frac{2\pi}{2\pi + \rho(2\theta_0 - \sin 2\theta_0)}. \quad (4.17a, 4.17b)$$

Note that based on the conservation of energy, these ratios also provide indications of the relative portion of vibration energy transmitted and dissipated within the oscillator.

4.1.3. Effects of linear constraint

Figure. 4.3(a) and 4.3(b) investigates the effects of the stiffness and damping of the linear constraint on the maximum steady-state displacement response X_{1_max} of the mass, respectively. The first-order HB results are represented by different lines. The numerical integration results based on the fourth-order Runge-Kutta (RK) method are denoted by symbols. The RK method has been widely used to solve smooth differential equations and to study non-smooth systems (Shi et al., 2019). To implement this method, the original governing equation is firstly transformed into a first-order form. By using conditional execution statements in the numerical algorithm to capture to the occurrence of discontinuities in the stiffness and / or damping coefficients, this method can be employed to investigate the dynamics of impact oscillators.

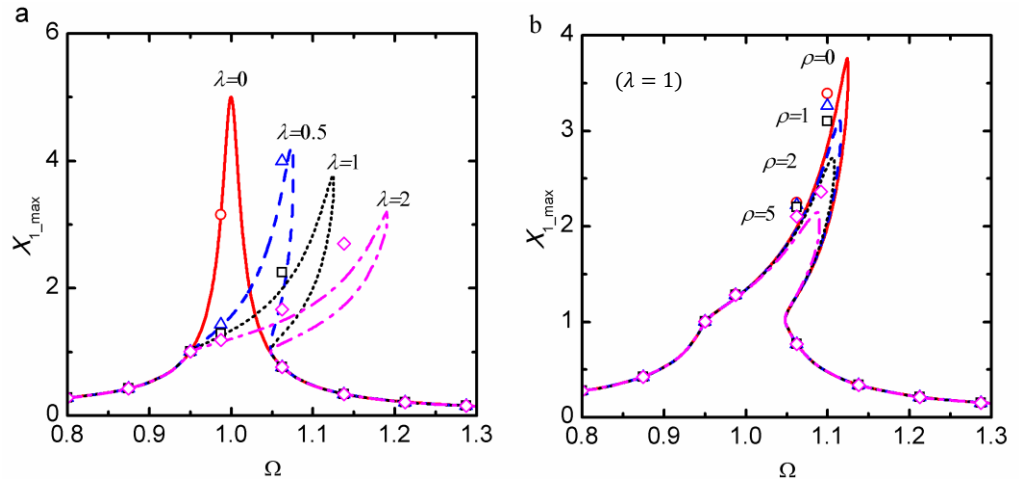


Figure 4.3. Effects of (a) stiffness and (b) damping properties of the linear constraint on the maximum displacement X_{1_max} . The solid line and circles, dashed line and triangles, dotted line and squares, dash-dot lines and rhombuses are for $\lambda = 0, 0.5, 1$ and 2 , respectively in (a), and for $\rho = 0, 1, 2$ and 5 , respectively in (b).

In Figure. 4.3(a), the stiffness ratio λ changes from 0 to 0.5, to 1 and then to 2 while the constraint damping is set as $\rho = 0$. In Fig. 4.3(b), the constraint damping ratio ρ varies from 0, 1, 2 and then to 5 while fixing constraint stiffness as $\lambda = 1$. The other system parameters are set to be $\zeta_1 = 0.01, F_0 = 0.1$. It shows that the HB results agree relatively well with numerical integration results when λ is small. For a larger value of λ , higher order HB may be needed for more accurate approximations. Fig. 4.3(a) shows that the values of X_{1_max} are small than 1 at low and high excitation frequencies,

suggesting that the mass and the constraint are not in contact. When the excitation frequency is approximately between 0.94 and 1.04, the response amplitude of oscillator may exceed the gap width, and the mass is engaged with the linear constraint. As λ increases, the response peak of X_{1_max} curve bends to the high-frequency range with reducing peak value. Fig. 4.3(b) shows that the increase of constraint damping will reduce the peak value of response curves of X_{1_max} .

Figure. 4.4 shows the effects of the linear constraint on the force transmission within the system. Understanding of the property can be useful in the designs of drilling systems or hand tools, in which low or high transmitted force may be desirable. The different lines are for HB approximations and the symbols are for RK results, as used in Fig. 4.3.

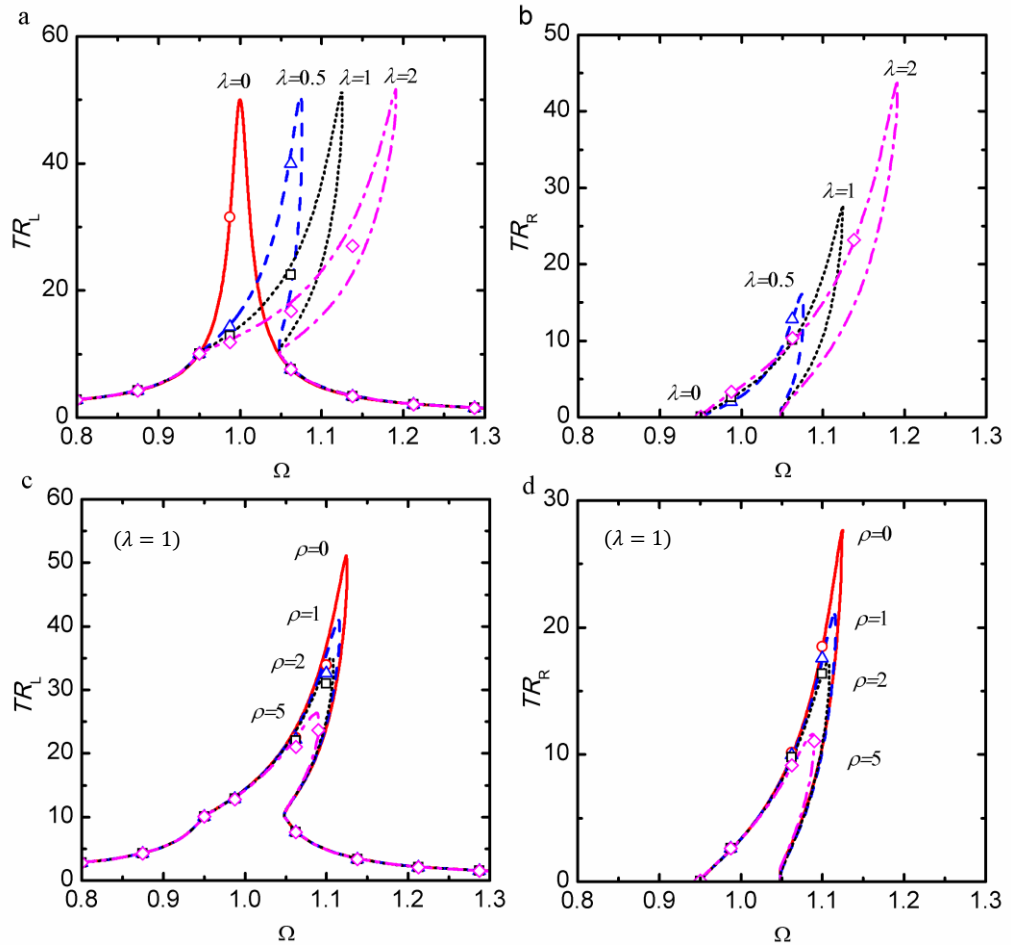


Figure 4.4. Effects of stiffness and damping properties of the linear constraint on force transmissibility TR_L and TR_R . The solid line and circles, dashed line and triangles, dotted line and squares, dash-dot lines and rhombuses are for $\lambda = 0, 0.5, 1$ and 2 , respectively, in (a) and (b), and for $\rho = 0, 1, 2$ and 5 , respectively, in (c) and (d).

Fig. 4.4(a) and (b) examines the influence of the constraint stiffness by setting $\rho = 0, \zeta_1 = 0.01, F_0 = 0.1$. Fig. 4.4(a) and (b) shows that with the increase of linear stiffness coefficient λ , the peaks of force transmissibility curves TR_L and TR_R both bends more

towards higher frequencies. It shows that with λ increasing from 0.5 to 1 and then to 2, there are only slight changes in the peak value of TR_L but significant increases in the peak of TR_R . Fig. 4.4(c) and (d) investigates the effects of constraint damping by setting $\lambda = 1, \zeta_1 = 0.01, F_0 = 0.1$ while changing the damping ratio ρ from 0 to 1, 2 and finally to 5. With the increase of the level of constraint damping, the peak values of force transmissibility TR_L and TR_R reduce. This characteristic demonstrates that larger linear constraint damping ρ is beneficial for the mitigation of vibration force transmission.

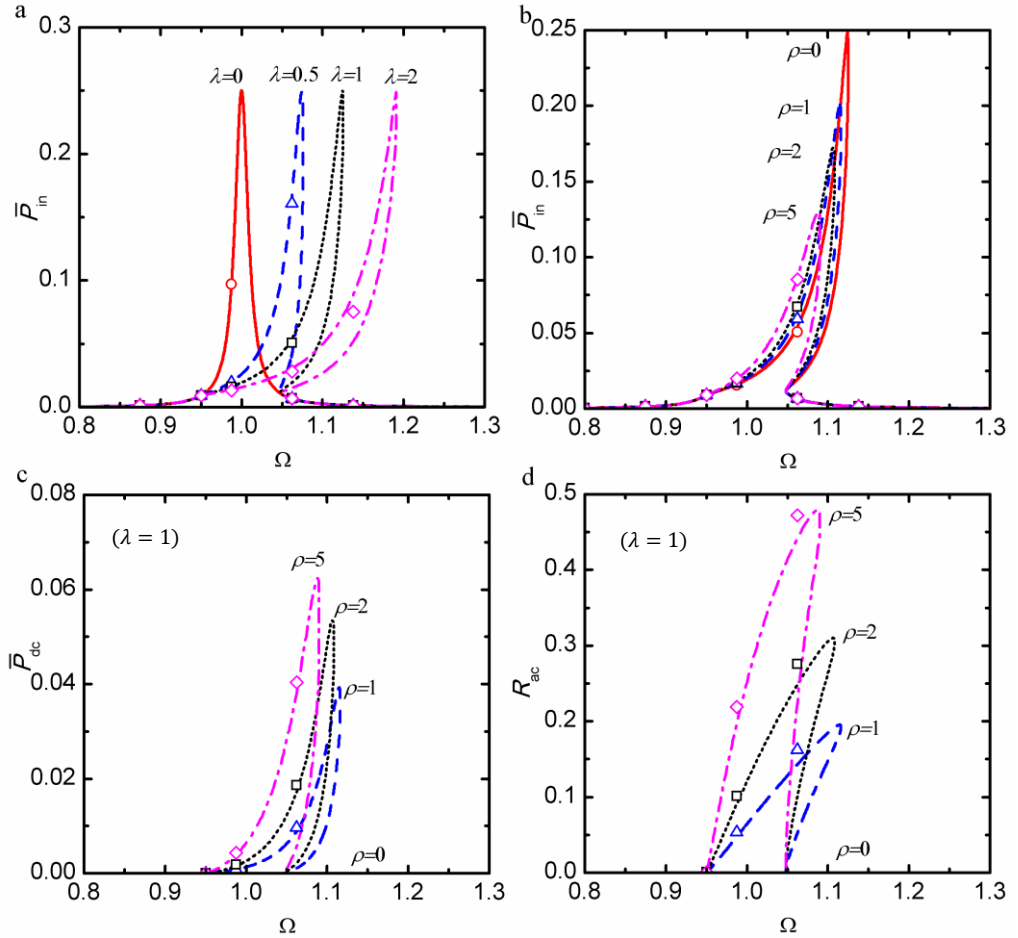


Figure 4.5. Effects of linear constraint on the power flow behaviour. Influence of (a) constraint stiffness on \bar{P}_{in} , and constraint damping on (b) \bar{P}_{in} , (c) \bar{P}_{dc} and (d) R_{ac} . In (a), solid line and circles, dashed line and triangles, dotted line and squares, and dash-dot line and rhombuses for $\lambda = 0, 0.5, 1$ and 2 , respectively; In (b), (c) and (d), dashed line and triangles, dotted line and squares, and dash-dot line and rhombuses are for $\rho = 1, 2$ and 5 , respectively.

Figure. 4.5 investigates the influence of the linear constraint on the vibration power flow behaviour. The lines and symbols represent HB and RK results, respectively. Fig. 4.5(a) examines the effects of constraint stiffness λ on the time-averaged input power \bar{P}_{in} while setting $\rho = 0, \zeta_1 = 0.01, F_0 = 0.1$. It shows that a larger value of λ bends the peak of \bar{P}_{in} more to the high-frequency range. However, the peak value of \bar{P}_{in} remains nearly the same for the different constraint stiffness values. Fig. 4.5(b), (c) and (d)

considers the effects of constraint damping ρ on \bar{P}_{in} , the time-averaged dissipated power by the constraint \bar{P}_{dc} and power dissipation ratio R_{ac} , respectively. The parameters are set as $\lambda = 1, \zeta_1 = 0.01, F_0 = 0.1$ while ρ changes from 0, to 1, to 2 and then to 5. It shows that a higher level of constraint damping ρ leads to a substantial reduction in the peak value of \bar{P}_{in} . Fig. 4.5(c) and (d) shows that a larger value of constraint damping ρ generally results in less bending of the curves of \bar{P}_{dc} and R_{ac} . It also shows that as ρ increases from 1 to 5, there is a larger amount of peak power dissipation as well as the relative proportion of power dissipated in the constraint as compared to the total power input. It shows that a high damping ratio can effectively dissipate vibration power transmitted to the constraint.

4.2. SDOF impact oscillator with a nonlinear QZS constraint

4.2.1. Mathematical modelling

Here the dynamics and vibration transmission within an SDOF impact oscillator with a nonlinear constraint is considered. Fig. 4.6 shows the system placed in the horizontal plane comprising a nonlinear constraint having geometric stiffness nonlinearities. Comparing with the linear constraint case shown in Fig. 4.1, the nonlinear constraint includes an extra pair of lateral springs, joined together at point B with the other ends fixed. These lateral springs are of un-stretched length of l_0 and stiffness coefficient k_v . Their length changes to l when point B is in the equilibrium position, i.e., when the lateral springs are oriented in the same direction and the original spring k_h is un-stretched. It is assumed that the block B is massless.

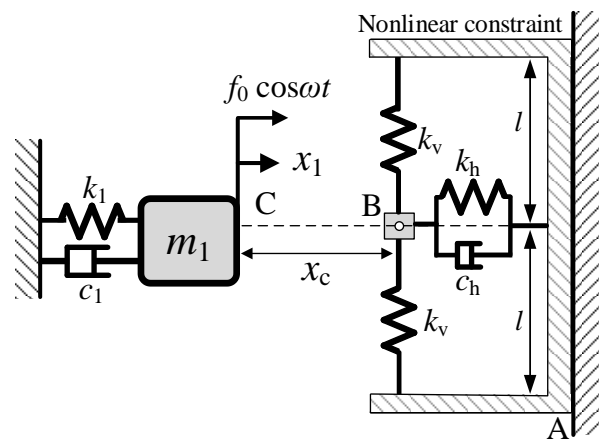


Figure 4.6. A schematic representation of an SDOF impact oscillator with a nonlinear constraint.

The dimensional governing equation of the mass is

$$m_1 \ddot{x}_1 + c_1 \dot{x}_1 + k_1 x_1 + (c_h \dot{\delta} + g(\delta))U(\delta) = f_0 \cos \omega t, \quad (4.18)$$

where $\delta = x_1 - x_c$ as defined previously, $U(\delta)$ was expressed in Eq. (4.2), and $g(\delta)$ represents the nonlinear restoring force generated by the springs in the nonlinear constraint and is expressed by

$$g(\delta) = k_h \delta + 2k_v \delta \left(1 - \frac{l_0}{\sqrt{l^2 + \delta^2}}\right) \approx k_h \delta + 2k_v \left(1 - \frac{l_0}{l}\right) \delta + \frac{k_v l_0}{l^3} \delta^3 = k_{s1} \delta + k_{s2} \delta^3, \quad (4.19)$$

where $k_{s1} = k_h + 2k_v(1 - l_0/l)$, $k_{s2} = k_v l_0/l^3$ and Taylor expansion was employed for the approximation. Eq. (4.19) shows that the use of the pair of lateral springs results in the addition of a linear term and also a nonlinear term of δ in $g(\delta)$. Note that the lateral springs can be tailored in a way such that $k_{s1} = 0$, e.g., the nonlinear constraint has a so-called quasi-zero-stiffness (QZS) characteristic (Cao et al., 2006; Hao and Cao, 2015; Hao et al., 2017). For this purpose, the lateral springs needs to be initially compressed with $l_0/l = 1 + k_h/(2k_v)$. The constraint can be termed a nonlinear QZS constraint.

Non-dimensional parameters are introduced as

$$\alpha = \frac{l_0}{l}, \quad \beta = \frac{2k_v}{k_h}, \quad K_1 = \lambda(1 + \beta(1 - \alpha)), \quad K_2 = \frac{\lambda \alpha \beta}{2\eta^2}, \quad \eta = \frac{l}{x_c},$$

where α is the spring length ratio of un-stretched length l_0 to length l , β is the stiffness ratio of lateral springs in the nonlinear constraint, η is the ratio of stretched length l to the gap width x_c . Using them and $\zeta_1, F_0, \Omega, R_0, R_1, \lambda$ and ρ , that have been defined previously in Section 4.1.1, the approximated dimensionless governing equation is

$$X_1'' + 2\zeta X_1' + X_1 + F_{NC} = F_0 \cos \Omega \tau, \quad (4.20)$$

where $F_{NC} = (2\zeta_1 \rho X_1' + K_1 \Delta + K_2 \Delta^3)U(\Delta)$ represents the nonlinear force arising from the addition of the nonlinear constraint. Eq. (4.20) can be solved using numerical integrations or the HB approximation. For the latter approach, while the analytical derivations of the Fourier coefficients for F_{NC} are possible, as in the previous linear constraint case, the AFT based HB illustrated in Chapter 3 is employed here for numerical determination (Von Groll and Ewins, 2001). Here for the implementation, the steady-state periodic response of the mass X_1, X_1' and X_1'' is firstly expressed by an N -order Fourier series with a fundamental frequency of Ω . The time histories of the nonlinear force F_{NC} can then be obtained by a substitution of X_1, X_1' and X_1'' into its expressions, which are then Fourier transformed to find the Fourier coefficients. By

inserting the expressions of the response and the nonlinear force into Eq. (4.20) and balancing the corresponding coefficients, a total number of $(2N+1)$ nonlinear algebraic equations can be obtained, which can be solved by Newton-Raphson method with a numerical continuation. The steady-state periodic response of the mass can then be determined.

4.2.2. Vibration transmission analysis

The force transmissibility and vibration power transmission characteristics are of interest in this Chapter. For the current system, the dimensionless transmitted force through the nonlinear constraint to the RHS wall changes to $F_{tR} = F_{NC}$. The dimensionless transmitted force to the LHS wall is still expressed by Eq. (4.13b). The force transmissibilities TR_R and TR_L are still defined as shown by Eq. (4.14). The definitions of the dimensionless time-averaged input power \bar{P}_{in} and dissipated powers \bar{P}_{d1} and \bar{P}_{dc} , as well as the power dissipation ratios as in Eq. (4.15)-(4.17) are followed.

4.2.3. Effects of nonlinear QZS constraint

Figures. 4.7, 4.8 and 4.9 investigate the effects of nonlinear parameters of the constraint, i.e., the lateral spring length ratio α and lateral spring stiffness ratio β , on the steady-state response X_{1_max} of the mass as well as the force transmission and power flow behaviour, respectively. With considerations of the accuracy and computational cost, the second-order HB-AFT results are employed and the results are represented by different lines. Numerical integration results based on the fourth-order Runge-Kutta (RK) method are denoted by symbols. The figures show that the HB-AFT results agree relatively well with those obtained from numerical integrations. The system parameters are set as $\lambda = 1, \rho = 1, \zeta_1 = 0.01, \eta = 1, F_0 = 0.1$. In the examination of the parameter α , three possible values are selected with $\alpha = 1, 1.5$ and 2 , while setting $\beta = 1$. Thus we have $K_1 = 1, K_2 = 0.5$ (Case one), $K_1 = 0.5, K_2 = 0.75$ (Case two) and $K_1 = 0, K_2 = 1$ (Case three) and the corresponding results are represented by solid lines and circles, dashed lines and the triangles as well as dotted lines and squares, respectively. When studying the effect of β , three values are used with $\beta = 0, 0.5$ and 1 while setting $\alpha = 2$. Consequently we have $K_1 = 1, K_2 = 0$ (Case four), $K_1 = 0.5, K_2 = 0.5$ (Case five) and $K_1 = 0, K_2 = 1$ (Case six), which are shown by solid lines and circles, dashed lines and the triangles as well as dotted lines and squares, respectively.

Figure. 4.7(a) shows that as the spring length ratio α increases from 1 to 2 , the displacement response curve of X_{1_max} bends less to the high frequencies. It shows that for the three cases considered, the peak values of X_{1_max} are found at a similar exciting

frequency and are almost the same. However, at a prescribed frequency between $\Omega \approx 0.96$ and the peak frequency, a larger α generally leads to a larger maximum displacement X_{1_max} . This is due to the fact that with an increasing α , the linear stiffness K_1 decreases but the nonlinear stiffness K_2 increases so that there is stronger nonlinearity. In Fig. 4.7(b), the spring stiffness ratio β changes from 0 to 0.5 and then to 1, and correspondingly, K_1 decreases but K_2 increases. With an increasing β , there is a slightly lower peak value of X_{1_max} but a higher peak frequency. Also, the response curve bends more to the high-frequency range. The figure shows that comparing with the other two cases, the case with $\beta = 1$ has the largest value of X_{1_max} when the excitation frequency Ω is between approximately 0.96 and 1.07.

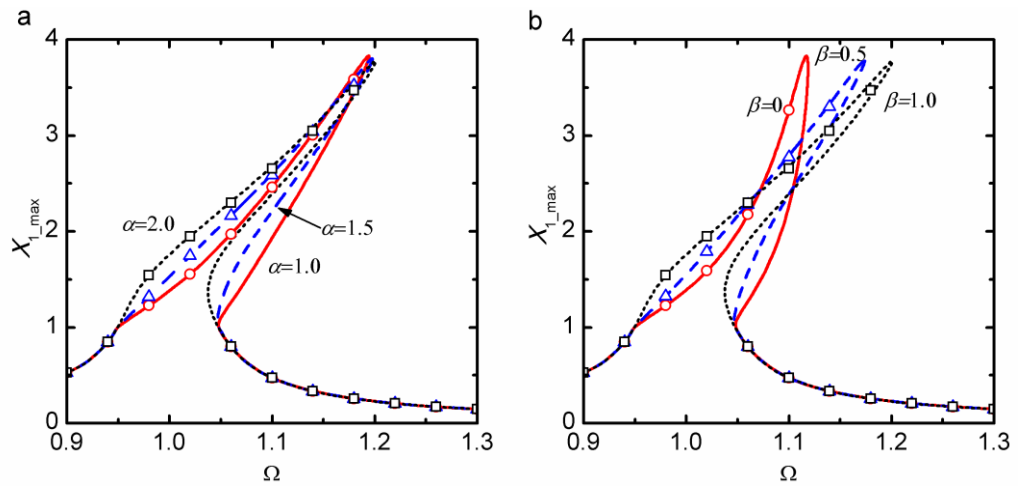


Figure 4.7. Effects of (a) spring length ratio α and (b) spring stiffness ratio β of the nonlinear constraint on the maximum displacement X_{1_max} . In (a), the solid, dashed and dotted lines for $\alpha = 1.0, 1.5$ and 2 , respectively; In (b), the solid, dashed and dotted lines are for $\beta = 0, 0.5$ and 1 , respectively.

Figure. 4.8 investigates the influence of nonlinear constraint on the force transmissibility behaviour of the system. Fig. 4.8(a) and (b) examines the influence of the nonlinear constraint parameters α and β , on the force transmissibility TR_L to the LHS wall, respectively. Comparing with Fig. 4.7, it shows that α and β affect TR_L in a similar way as they affect X_{1_max} . The reason is that the dimensionless transmitted force $F_{tL} = 2\zeta X_1' + X_1$ is directly related to the displacement response of the mass. It shows that the peak value and the associated peak frequency of TR_L change little regardless of the variations in the value of α . In comparison, the changes of stiffness ratio β can lead to substantial differences in the peak frequency of TR_L . Fig. 4.8(c) and (d) examine the influence of parameters α and β of the nonlinear constraint on TR_R , representing the level of force transmission to the RHS wall. It shows that with α increasing from 1 to 1.5 and then to 2, the peak value of TR_R also increases but the corresponding peak frequency is similar for the three cases. Fig. 4.8(d) shows that as the spring stiffness

ratio β changes from 0 to 1, the peak value of TR_R increases significantly. In summary, a lower value of α is beneficial for having a low transmissibility TR_L and TR_R . A small value of stiffness ratio β may assist in reducing the peak value of TR_R , but it can lead to a higher peak value of TR_L .

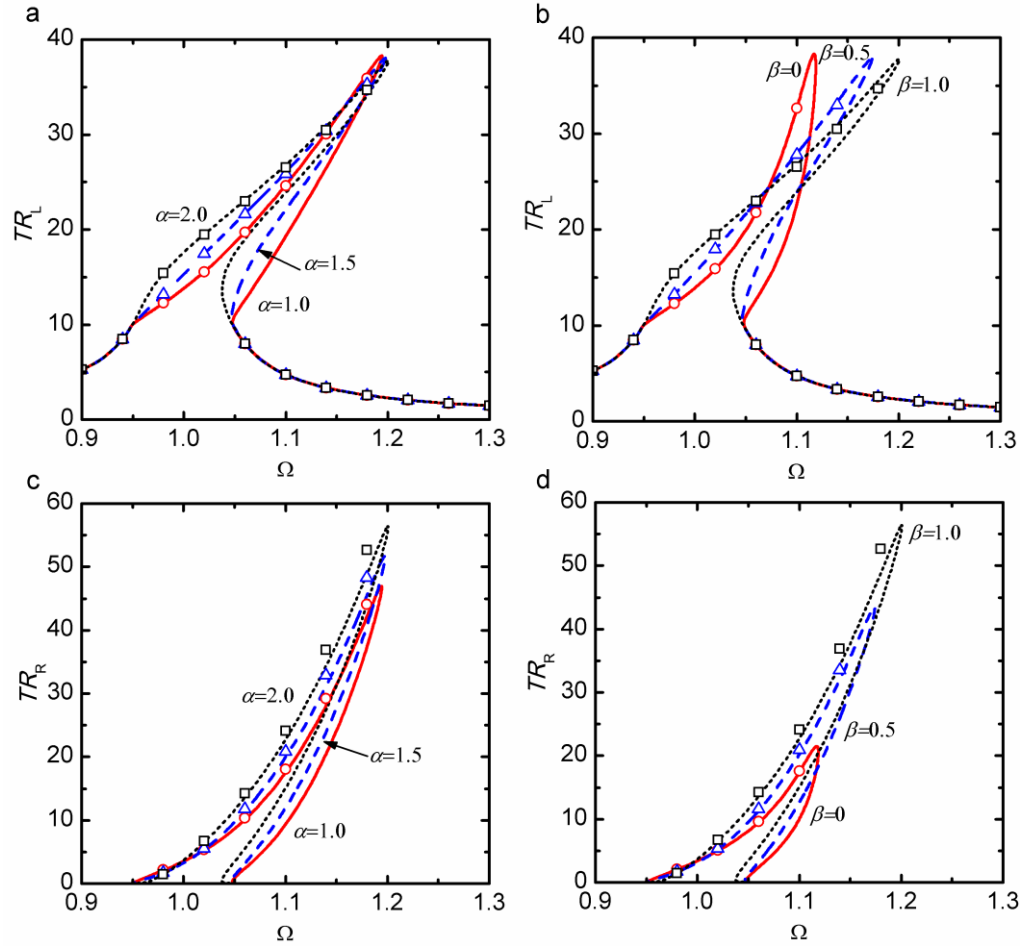


Figure 4.8. Effects of spring length ratio α and spring stiffness ratio β of the nonlinear constraint on TR_L and TR_R , respectively. In (a) and (c), the solid, dashed and dotted lines for $\alpha = 1.0, 1.5$ and 2.0 , respectively; In (b) and (d), the solid, dashed and dotted lines are for $\beta = 0, 0.5$ and 1.0 , respectively. Symbols: RK results.

Figure 4.9 studies the influence of nonlinear constraint parameters α and β on the vibration power flow behaviour. Fig. 4.9(a) and (b) shows that with the variations of the values of α and β for the considered cases, there are very small changes in the peak values of time-averaged input power \bar{P}_{in} . Comparing with Cases one and two, Case three with $\alpha = 2$ can lead to a larger \bar{P}_{in} when the excitation frequency Ω locates between approximately 0.96 and 1.1. Fig. 4.9(b) shows that the addition of the lateral springs with β increases from 0 to 1 can shift the peak frequency to the right. Fig. 4.9(c) and (d) shows the variations of power dissipation ratio R_{ac} by the constraint for the cases considered. It is interesting to note that a larger value of α can usually result in a larger portion of time-averaged input power dissipated by the damper in the constraint.

However, the peak value of R_{ac} for Cases one, two and three cases are similar. Fig. 4.9(d) shows that a stronger lateral spring stiffness with $\beta = 1$ (Case six) can lead to a larger R_{ac} between $\Omega = 0.96$ and $\Omega = 1.07$. However, there is a lower peak value of R_{ac} , comparing with Case four with the absence of the lateral springs and also Case five with $\beta = 0.5$.

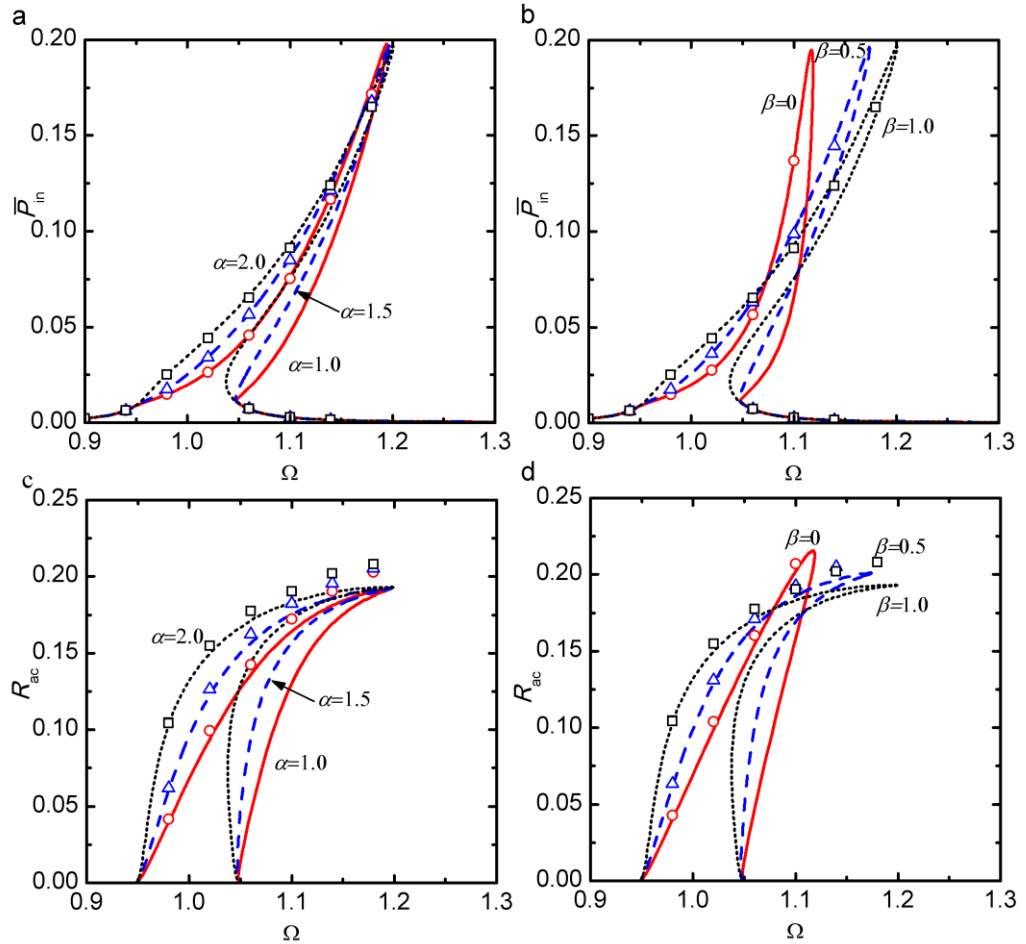


Figure 4.9. Effects of spring length ratio α and spring stiffness ratio β of the nonlinear constraint on \bar{P}_{in} and R_{ac} . In (a) and (c), the solid, dashed and dotted lines for $\alpha = 1.0, 1.5$ and 2 , respectively; In (b) and (d), the solid, dashed and dotted lines are for $\beta = 0, 0.5$ and 1 , respectively. Symbols: RK results.

4.3. A 2DOF impact oscillator with a linear or nonlinear constraint

4.3.1. Mathematical modelling

In this section, the dynamics and vibration transmission characteristics of 2DOF impact oscillators with linear or nonlinear QZS constraints are investigated. Fig. 4.10(a) provides a schematic representation of system comprising two SDOF oscillators coupled via a linear spring with stiffness k_3 and damper with a damping coefficient c_3 . A primary oscillator consists of the primary mass m_1 subject to a harmonic excitation

$f_0 \cos \omega t$, a spring with stiffness coefficient k_1 and a viscous damper c_1 . A secondary oscillator has the secondary mass m_2 , a viscous damper of damping coefficient c_2 , and a linear spring with stiffness coefficient k_2 . The constraint can either be a linear constraint with spring stiffness k_h and damping coefficient c_h or a nonlinear QZS constraint with an additional pair of springs with stiffness coefficient of k_v , as shown in Fig. 4.10(b) and (c), respectively. It is assumed that both two masses can move horizontally without frictions. The equilibrium position of two masses, where the springs k_1 , k_2 and k_3 are un-stretched and $x_1 = x_2 = 0$, is set as reference with the initial gap between m_1 and the constraint being x_c .

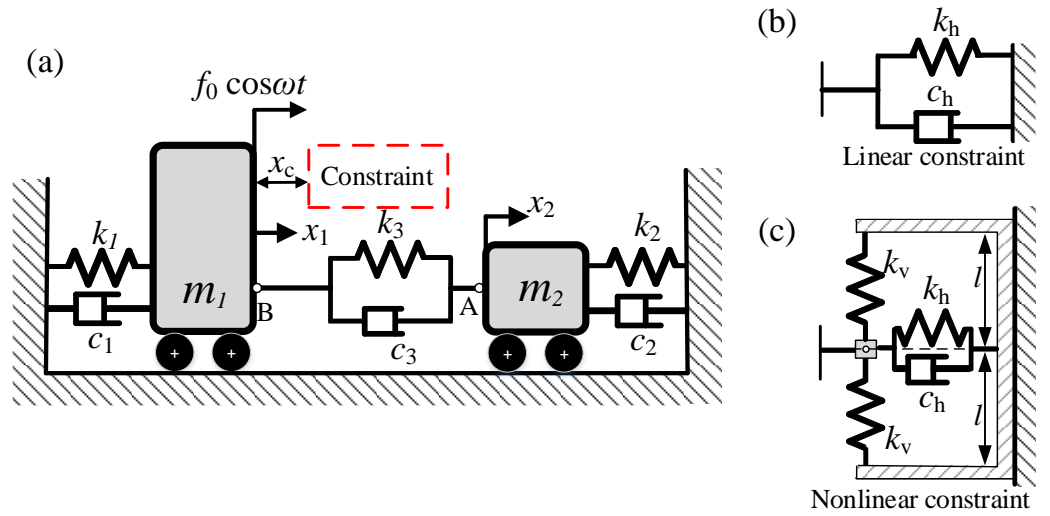


Figure 4.10. A 2DOF impact oscillator with a linear or nonlinear constraint. (a) A schematic representation, (b) a linear constraint and (c) a nonlinear constraint.

For the coupled oscillators with linear or nonlinear constraints, the general dynamic governing equation can be written in a matrix form as

$$\begin{bmatrix} m_1 & 0 \\ 0 & m_2 \end{bmatrix} \begin{Bmatrix} \ddot{x}_1 \\ \ddot{x}_2 \end{Bmatrix} + \begin{bmatrix} c_1 + c_3 & -c_3 \\ -c_3 & c_2 + c_3 \end{bmatrix} \begin{Bmatrix} \dot{x}_1 \\ \dot{x}_2 \end{Bmatrix} + \begin{bmatrix} k_1 + k_3 & -k_3 \\ -k_3 & k_2 + k_3 \end{bmatrix} \begin{Bmatrix} x_1 \\ x_2 \end{Bmatrix} + \begin{Bmatrix} f_c(\delta, \dot{\delta}) \\ 0 \end{Bmatrix} = \begin{Bmatrix} f_0 \cos \omega t \\ 0 \end{Bmatrix}. \quad (4.21)$$

where $\delta = x_1 - x_c$. Here the new non-dimensional parameters are introduced as

$$\omega_2 = \sqrt{\frac{k_2}{m_2}}, \quad \zeta_2 = \frac{c_2}{2m_2\omega_2}, \quad X_2 = \frac{x_2}{x_c}, \quad \gamma = \frac{\omega_2}{\omega_1}, \quad \mu = \frac{m_2}{m_1}, \quad \kappa = \frac{k_3}{k_1}, \quad \epsilon = \frac{c_3}{c_1},$$

where ω_2 and ζ_2 represent the undamped natural frequency and the damping ratio of the secondary oscillator, respectively, X_2 denotes the dimensionless displacement of the secondary mass, γ is the undamped natural frequency ratio between primary and the secondary oscillator, μ is the mass ratio, κ and ϵ are the dimensionless stiffness and

damping ratios for the interfacial spring and damper, respectively. By using them and the previously defined parameters, the dimensionless governing equations are

$$\begin{bmatrix} 1 & 0 \\ 0 & \mu \end{bmatrix} \begin{bmatrix} X_1'' \\ X_2'' \end{bmatrix} + \begin{bmatrix} 2\zeta_1(1+\epsilon) & -2\zeta_1\epsilon \\ -2\zeta_1\epsilon & 2(\mu\zeta_2\gamma + \zeta_1\epsilon) \end{bmatrix} \begin{bmatrix} X_1' \\ X_2' \end{bmatrix} + \begin{bmatrix} 1+\kappa & -\kappa \\ -\kappa & \mu\gamma^2 + \kappa \end{bmatrix} \begin{bmatrix} X_1 \\ X_2 \end{bmatrix} + \begin{Bmatrix} F_c(\Delta, \Delta') \\ 0 \end{Bmatrix} = \begin{Bmatrix} F_{\text{ex}} \\ 0 \end{Bmatrix}, \quad (4.22)$$

where $\Delta = X_1 - 1$ as defined previously, $F_{\text{ex}} = F_0 \cos \Omega\tau$ and $F_c(\Delta, \Delta') = F_{\text{LC}}$ for the nonlinear force from the linear constraint case and $F_c(\Delta, \Delta') = F_{\text{NC}}$ for that generated by the nonlinear constraint, respectively. Considering the steady-state periodic response of the system with oscillation frequency Ω , the displacement and velocity responses corresponding to the j -th ($j = 1$ or 2) coordinate can be approximated by N -harmonics:

$$X_j = \hat{X}_{(j,0)} + \sum_{n=1}^N (\hat{X}_{(j,2n-1)} \cos n\Omega\tau + \hat{X}_{(j,2n)} \sin n\Omega\tau) = \Re\{\sum_{n=0}^N \tilde{R}_{(j,n)} e^{in\Omega\tau}\}, \quad (4.23a)$$

$$X_j' = \sum_{n=1}^N n\Omega(-\hat{X}_{(j,2n-1)} \sin n\Omega\tau + \hat{X}_{(j,2n)} \cos n\Omega\tau) = \Re\{\sum_{n=0}^N in\Omega\tilde{R}_{(j,n)} e^{in\Omega\tau}\}, \quad (4.23b)$$

where $\hat{X}_{(j,2n-1)}$ and $\hat{X}_{(j,2n)}$ provide the coefficients of the n -th harmonic, \tilde{R} is the corresponding complex coefficient, and \Re denotes the operation of taking the real part of a complex number. The nonlinear force generated by the constraint can then be obtained by using Fourier series expansion:

$$F_c(\Delta, \Delta') = \hat{Q}_{(j,0)} + \sum_{n=1}^N (\hat{Q}_{(j,2n-1)} \cos n\Omega\tau + \hat{Q}_{(j,2n)} \sin n\Omega\tau) = \Re\{\sum_{n=0}^N \tilde{Q}_{(j,n)} e^{in\Omega\tau}\}, \quad (4.24a)$$

$$F_{\text{ex}} = \Re\{\sum_{n=0}^N \tilde{S}_{(j,n)} e^{in\Omega\tau}\}. \quad (4.24b)$$

Note that analytical derivation of the Fourier coefficients of the nonlinear constraint force $F_c(\Delta, \Delta')$ is feasible when the number of the order N is small. When a large number of harmonics are considered, the AFT technique can be employed for numerical determinations (Von Groll and Ewins, 2001). By inserting Eqs. (4.23) and (4.24) into Eq. (4.22) and balancing the coefficients of the n -th ($0 \leq n \leq N$) harmonic terms, we have:

$$[\tilde{D}_n]\{\tilde{R}_n\} = \{\tilde{S}_n\} - \{\tilde{Q}_n\}, \quad (4.25)$$

where the dynamic stiffness matrix for the n -th harmonic is

$$[\tilde{\mathbf{D}}_n] = -(n\Omega)^2 \begin{bmatrix} 1 & 0 \\ 0 & \mu \end{bmatrix} + i(n\Omega) \begin{bmatrix} 2\zeta_1(1+\epsilon) & -2\zeta_1\epsilon \\ -2\zeta_1\epsilon & 2(\mu\zeta_2\gamma + \zeta_1\epsilon) \end{bmatrix} + \begin{bmatrix} 1+\kappa & -\kappa \\ -\kappa & \mu\gamma^2 + \kappa \end{bmatrix}, \quad (4.26)$$

$\{\tilde{\mathbf{R}}_n\} = \{\tilde{R}_{(1,n)}, \tilde{R}_{(2,n)}\}^T$, $\{\tilde{\mathbf{S}}_n\} = \{\tilde{S}_{(1,n)}, \tilde{S}_{(2,n)}\}^T$ and $\{\tilde{\mathbf{Q}}_n\} = \{\tilde{Q}_{(1,n)}, \tilde{Q}_{(2,n)}\}^T$. By rewriting the balancing conditions for all the harmonics ($n = 0, 1, \dots, N$), we have

$$\begin{bmatrix} \tilde{D}_0 & 0 & \cdots & 0 \\ 0 & \tilde{D}_1 & \cdots & 0 \\ \vdots & \vdots & \ddots & \vdots \\ 0 & 0 & \cdots & \tilde{D}_N \end{bmatrix} \begin{bmatrix} \tilde{R}_0 \\ \tilde{R}_1 \\ \vdots \\ \tilde{R}_N \end{bmatrix} = \begin{bmatrix} \tilde{S}_0 - \tilde{Q}_0 \\ \tilde{S}_1 - \tilde{Q}_1 \\ \vdots \\ \tilde{S}_N - \tilde{Q}_N \end{bmatrix}. \quad (4.27)$$

This equation can be transformed into a total number of $2(2N + 1)$ real nonlinear algebraic equations, which can then be solved using the Newton-Raphson technique in an iterative way. To track the solution path with variations of parameters, pseudo-arclength continuations are employed, which have been illustrated in chapter 3. Consequently, the system response and vibration transmission within the system can be determined and quantified.

4.3.2. Vibration transmission analysis

The force transmissibility can be defined as the maximum magnitude of the transmitted force at an interested point in the system to that of the input force:

$$TR_S = \frac{\max(|\kappa(X_1 - X_2) + 2\zeta_1\epsilon(X'_1 - X'_2)|)}{F_0}, \quad (4.28a)$$

$$TR_L = \frac{\max(|2\zeta_1 X'_1 + X_1|)}{F_0}, \quad (4.28b)$$

$$TR_C = \frac{\max(|F_c(\Delta, \Delta')|)}{F_0}, \quad (4.28c)$$

for the force transmissibility to mass m_2 , to the LHS wall of the primary oscillator, to the constraint, respectively. The dimensionless transmitted force to mass m_2 is $F_{ts} = \kappa(X_1 - X_2) + 2\zeta_1\epsilon(X'_1 - X'_2)$.

The dimensionless steady-state time-averaged input power into the system is

$$\bar{P}_{in} \approx \frac{1}{\tau_p} \int_{\tau_0}^{\tau_0 + \tau_p} X'_1 F_0 \cos \Omega \tau \, d\tau = \frac{\Omega F_0 \bar{X}_{(1,2)}}{2}, \quad (4.29)$$

where Eq. (4.23b) was used for approximation of velocity X'_1 , the averaging time $\tau_p = 2\pi/\Omega$, i.e., one oscillation cycle, and the orthogonal properties of the trigonometric

functions are used. The steady-state time-averaged dissipated powers by the dampers are

$$\bar{P}_{d1} = \frac{1}{\tau_p} \int_{\tau_0}^{\tau_0+\tau_p} 2\zeta_1 X_1'^2 d\tau, \quad \bar{P}_{d2} = \frac{1}{\tau_p} \int_{\tau_0}^{\tau_0+\tau_p} 2\mu\zeta_2\gamma X_2'^2 d\tau, \quad (4.30a, 4.30b)$$

$$\bar{P}_{d3} = \frac{1}{\tau_p} \int_{\tau_0}^{\tau_0+\tau_p} 2\zeta_1\epsilon(X_2' - X_1')^2 d\tau, \quad (4.30c)$$

$$\bar{P}_{dc} = \frac{1}{\tau_p} \int_{\tau_0}^{\tau_0+\tau_p} 2\zeta_1\rho(\Delta'U(\Delta))^2 d\tau. \quad (4.30d)$$

Note that the corresponding instantaneous dissipated powers are expressed by $P_{d1} = 2\zeta_1 X_1'^2$, $P_{d2} = 2\mu\zeta_2\gamma X_2'^2$, $P_{d3} = 2\zeta_1\epsilon(X_2' - X_1')^2$ and $P_{dc} = 2\zeta_1\rho(\Delta'U(\Delta))^2$. The power dissipation ratios are then defined as

$$R_{d1} = \frac{\bar{P}_{d1}}{\bar{P}_{in}}, \quad R_{d2} = \frac{\bar{P}_{d2}}{\bar{P}_{in}}, \quad R_{d3} = \frac{\bar{P}_{d3}}{\bar{P}_{in}}, \quad R_{dc} = \frac{\bar{P}_{dc}}{\bar{P}_{in}}. \quad (4.31a-4.31d)$$

When the time-averaged power flow is considered over one cycle of a periodic response, it follows that $R_{d1} + R_{d2} + R_{d3} + R_{dc} = 1$, in accordance with the principle of energy balance. It is noted that these variables provide a relative portion of vibration energy transmitted to various subsystems of the 2DOF impact oscillator. Over a cycle of periodic oscillation, the time-averaged transmitted power \bar{P}_t to mass m_2 should be entirely dissipated by the damper c_2 , therefore we have $\bar{P}_t = \bar{P}_{d2}$. Consequently, the level of vibration transmission within the system can be quantified using power flow variables.

4.3.3. A 2DOF impact oscillator with a linear constraint

Figures. 4.11, 4.12 and 4.13 investigate the effects of the linear constraint on the steady-state response, the force transmission and power flow behaviour of the system, respectively. The second-order HB-AFT results with different lines are compared with fourth-order RK method denoted by symbols. The system parameters are set as $\zeta_1 = \zeta_2 = 0.01, \eta = 1, \gamma = 1, \mu = 1, \kappa = 1, \epsilon = 1$, and $F_0 = 0.5$. In the examination of the parameter λ , four possible values are selected with $\lambda = 0, 0.5, 1$ and 2 , while setting $\rho = 0$. The corresponding results are represented by solid lines and circles, dashed lines and the triangles, dotted lines and squares as well as dash-dot lines and rhombuses, respectively. When studying the effect of parameter ρ , four values are used with $\rho = 0, 1, 2$ and 5 while setting $\lambda = 2$, which are shown by solid lines and circles, dashed lines and the triangles, dotted lines and squares as well as dash-dot lines and rhombuses, respectively.

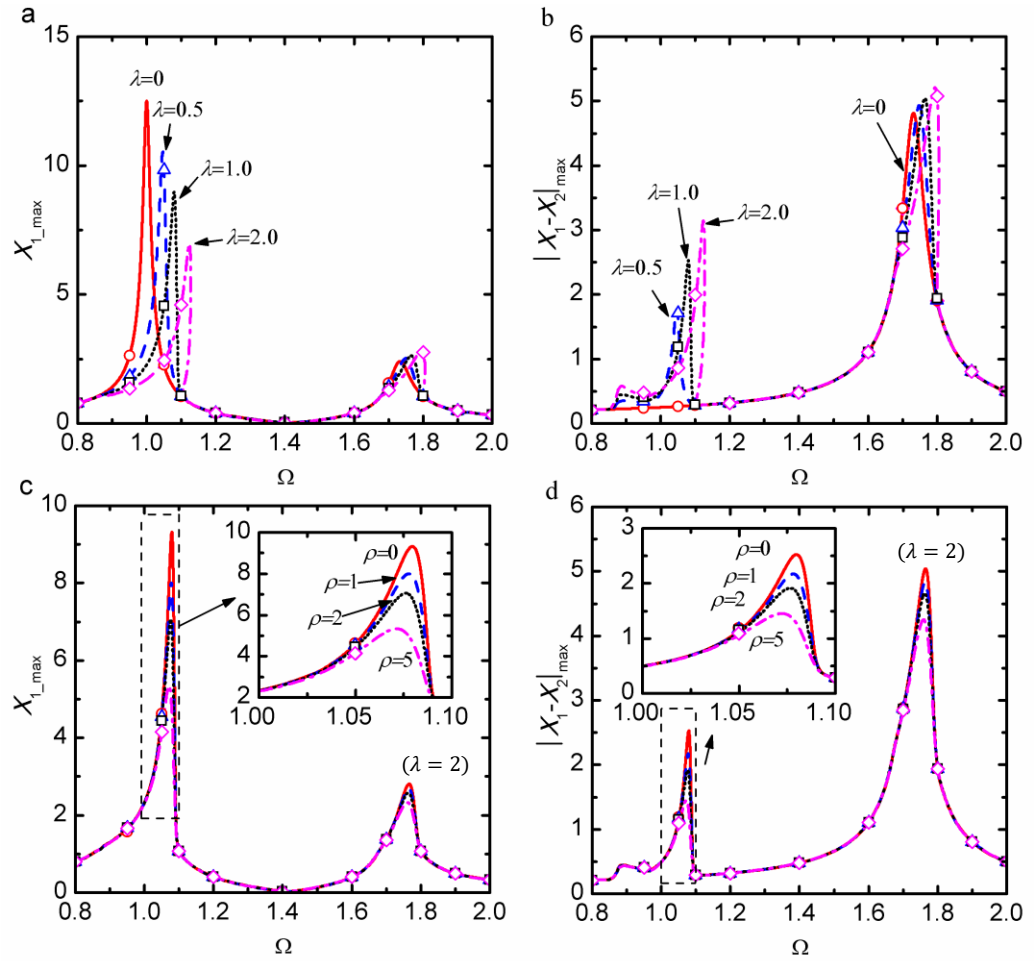


Figure 4.11. Effects of the linear constraint on X_{1_max} and $|X_1 - X_2|_{max}$. In (a) and (b), the solid, dashed, dotted and dash-dot lines for $\lambda = 0, 0.5, 1$ and 2 , respectively; In (c) and (d), the solid, dashed, dotted and dash-dot lines are for $\rho = 0, 1, 2$ and 5 , respectively. Symbols: RK results.

Figure. 4.11 examines the influence of the linear constraint on the maximum steady-state displacement response X_{1_max} of the primary mass m_1 and the amplitude of the relative displacement between the masses $|X_1 - X_2|_{max}$. The effects of the constraint stiffness λ are considered in Fig. 4.11(a) and (b) while those of the constraint damping ρ studied in 4.11(c) and (d). Two resonance peaks can be found in each response curve of X_{1_max} as shown in Fig. 4.11(a) and (c). By carrying out a modal analysis of the un-constrained system with $\rho = 0$, it can be shown that the first peak of X_{1_max} corresponds to the in-phase mode, while the second is associated with the out-of-phase mode. Fig. 4.11(a) shows that as the constraint stiffness ratio λ increases from 0 to 2, both resonance peaks of each response curve X_{1_max} bend towards the high-frequency range. Correspondingly, there is a substantial reduction in the first peak value, but a slight increase in the second peak value. For the relative displacement amplitude, Fig. 4.11(b) shows that there is only one peak in the curve $|X_1 - X_2|_{max}$ when $\lambda = 0$, but when λ changes to 0.5, 1 or 2, two extra peaks are generated in the frequency range

from $\Omega \approx 0.8$ to $\Omega \approx 1.2$. It shows that its first peak near $\Omega = 0.89$ becomes higher as the stiffness ratio λ increases. At the same time, its second and third peaks bend towards high frequencies with larger peak value. Physically, when there is a higher constraint stiffness, the primary mass m_1 is further restrained from moving to the right while at the same time the second mass is not constrained, resulting in a larger relative displacement. Fig. 4.11(c) and (d) studies the effects of damping in the linear constraint. Fig. 4.11(c) shows that with the increase of constraint damping ratio ρ from 0 to 5, there may be a significant reduction in the first peak value of $X_{1,\max}$, and small changes in its second peak. Fig. 4.11(d) shows that the increase in the damping ratio ρ has very small influence on the first peak of $|X_1 - X_2|_{\max}$ near $\Omega \approx 0.89$. In comparison, the second and third peak values of each curve reduce substantially, suggesting the suppression of vibrations near the resonance. It demonstrates that the damping in the linear constraint can effectively reduce the peak displacement responses of the impact oscillator.

Figure. 4.12 investigates the influence of the stiffness ratio λ and the damping ratio ρ of the linear constraint on force transmissibility TR_L and TR_S for the LHS wall and the secondary mass, respectively. Fig. 4.12(a) and (b) shows two peaks in each curve of TR_L , but there may be three peaks in each curve of TR_S when $\lambda \neq 0$. An increase in the linear constraint stiffness ratio λ from 0 to 2 can lead to bending of the peaks in the force transmissibility curves to the high frequencies. The increase in the value of λ can also result in the reduction of the first peak force transmissibility TR_L to the LHS wall, but large increases in the first and second peak values of TR_S to mass m_2 . This characteristic is in correspondence with the variations of displacement responses of $X_{1,\max}$ and $|X_1 - X_2|_{\max}$, as suggested by Eq. (4.28) for the definitions of TR_L and TR_S . The figure also shows that the stiffness ratio has a much smaller influence on the second peak of TR_L and the third peak of TR_S , both associated with the out-of-phase mode of the system. Fig. 4.12(c) and (d) examines the effects of damping ratio ρ of the constraint on TR_L and TR_S . It shows that the increase of ρ from 0 to 5 mainly reduces the first peak value of TR_L and the second peak value of TR_S in the vicinity of $\Omega \approx 1.1$. It shows that a larger linear damping ratio ρ is beneficial for the mitigation of force transmission between the two masses when excited in the neighbourhood of $\Omega \approx 1.1$.

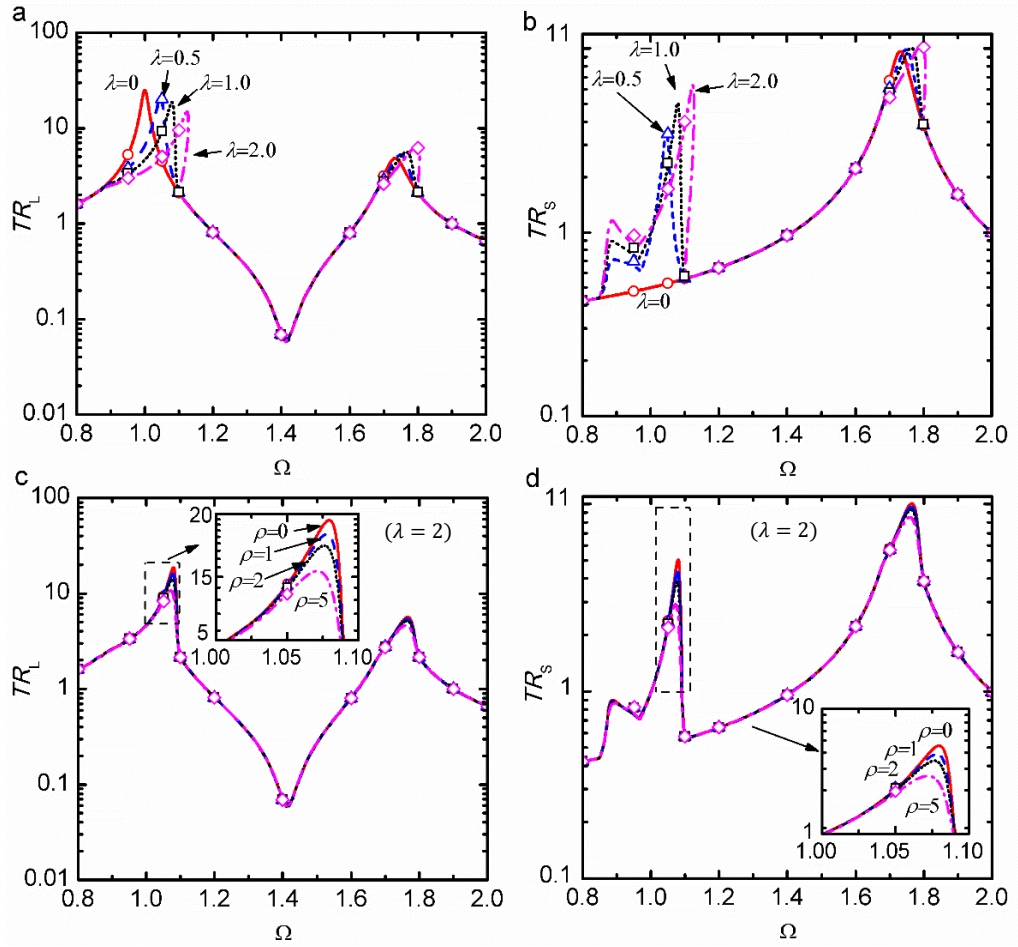


Figure 4.12. Effects of the linear constraint on force transmissibility TR_L and TR_S . In (a) and (b), the solid, dashed, dotted and dash-dot lines for $\lambda = 0, 0.5, 1$ and 2 , respectively; In (c) and (d), the solid, dashed, dotted and dash-dot lines are for $\rho = 0, 1, 2$ and 5 , respectively. Symbols: RK results.

Figure 4.13(a) and (b) examines the effects of stiffness ratio λ of the linear constraint on the time-averaged transmitted power \bar{P}_t to secondary mass m_2 and the time-averaged dissipated power \bar{P}_{d3} at the interface, respectively. Fig. 4.13(a) shows that with the increase of the stiffness ratio λ from 0 to 2, both peaks in each curve of \bar{P}_t bend towards the high-frequency range. As λ increases, the first peak value of \bar{P}_t slightly reduces and its second peak value changes little. Fig. 4.13(b) shows that the addition of the linear constraint stiffness can lead to a much higher level of power dissipation at the interface between $\Omega \approx 0.86$ and $\Omega \approx 1.1$, compared with that of the un-constrained system. The reason is that with the constraint, there is correspondingly a larger amplitude for the relative displacement $|X_1 - X_2|_{max}$. Consequently, there is a larger amount of time-averaged dissipated power \bar{P}_{d3} at the interface. Fig. 4.13(c) and (d) investigates the influence of the damping level in the linear constraint on \bar{P}_t and \bar{P}_{d3} , respectively. It shows that the increase in the damping ratio ρ of the constraint from 0 to 5 can lead to reductions in the two peak values of \bar{P}_t , suggesting lower vibration

energy transmission to mass m_2 . At the same time, there are also a decreasing second and the third peak values of power dissipation \bar{P}_{d3} at the interface. By comparing with Fig. 4.12(b), it is shown that a larger linear stiffness ratio may increase the force transmissibility to the secondary mass, but can reduce the time-averaged power transmission. The characteristic illustrates that the use of force transmissibility and power flow to measure vibration transmission level may lead to different evaluation outcomes.

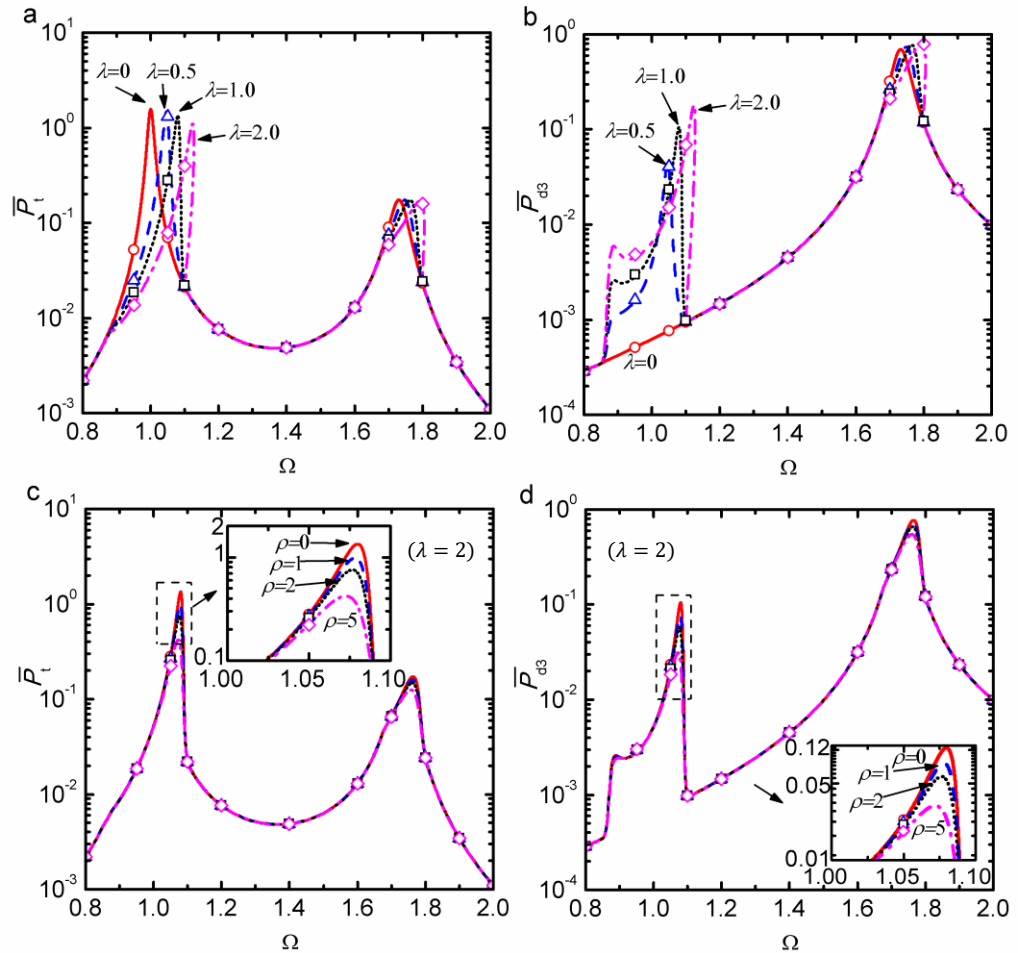


Figure 4.13. Effects of the linear constraint on \bar{P}_t and \bar{P}_{d3} . In (a) and (b), the solid, dashed, dotted and dash-dot lines for $\lambda = 0, 0.5, 1$ and 2 , respectively; In (c) and (d), the solid, dashed, dotted and dash-dot lines are for $\rho = 0, 1, 2$ and 5 , respectively. Symbols: RK results.

Figure. 4.14 further investigates the reasons for the significant change in the force transmissibility TR_S and power flow dissipation \bar{P}_{d3} arising from the addition of the constraint in the frequency range between $\Omega \approx 0.9$ and $\Omega = 1.1$. The system is excited at $\Omega = 1.0$ and the time histories of the steady-state displacement response, dimensionless transmitted force to mass m_2 and the instantaneous dissipated power P_{d3} are obtained. Fig. 4.14(a), (b) and (c) is for the system without the constraint with $\lambda = 0$ while Fig. 4.14(d), (e) and (f) for the coupled system with linear spring constraint with $\lambda = 1$. The other system parameters are set as $\rho = 0, \zeta_1 = \zeta_2 = 0.01, \gamma = 1, \mu = 1, \kappa =$

$1, \epsilon = 1$ and $F_0 = 0.5$. Fig. 4.14(a) shows that the two masses move in an approximately synchronous manner, and their relative displacement $X_1 - X_2$ is of low amplitude. In comparison, Fig. 4.14(d) shows that the addition of the linear constraint changes the phase angle between displacements X_1 and X_2 , and consequently, the relative displacement $X_1 - X_2$ has a much higher amplitude. Fig. 4.14(b) and (e) shows that the amplitude of the transmitted force F_{ts} is increased from approximately 0.24 to 0.5 by the addition of the linear constraint, indicating a larger transmitted force to the secondary system. Fig. 4.14(c) and (f) shows that with the inclusion of the linear constraint, the amplitude of the dissipated power P_{d3} increases. Over an oscillation cycle, there is more energy dissipated at the interface. As a result, there is a much higher amount of the time-averaged dissipated power \bar{P}_{d3} arising from the addition of the linear constraint.

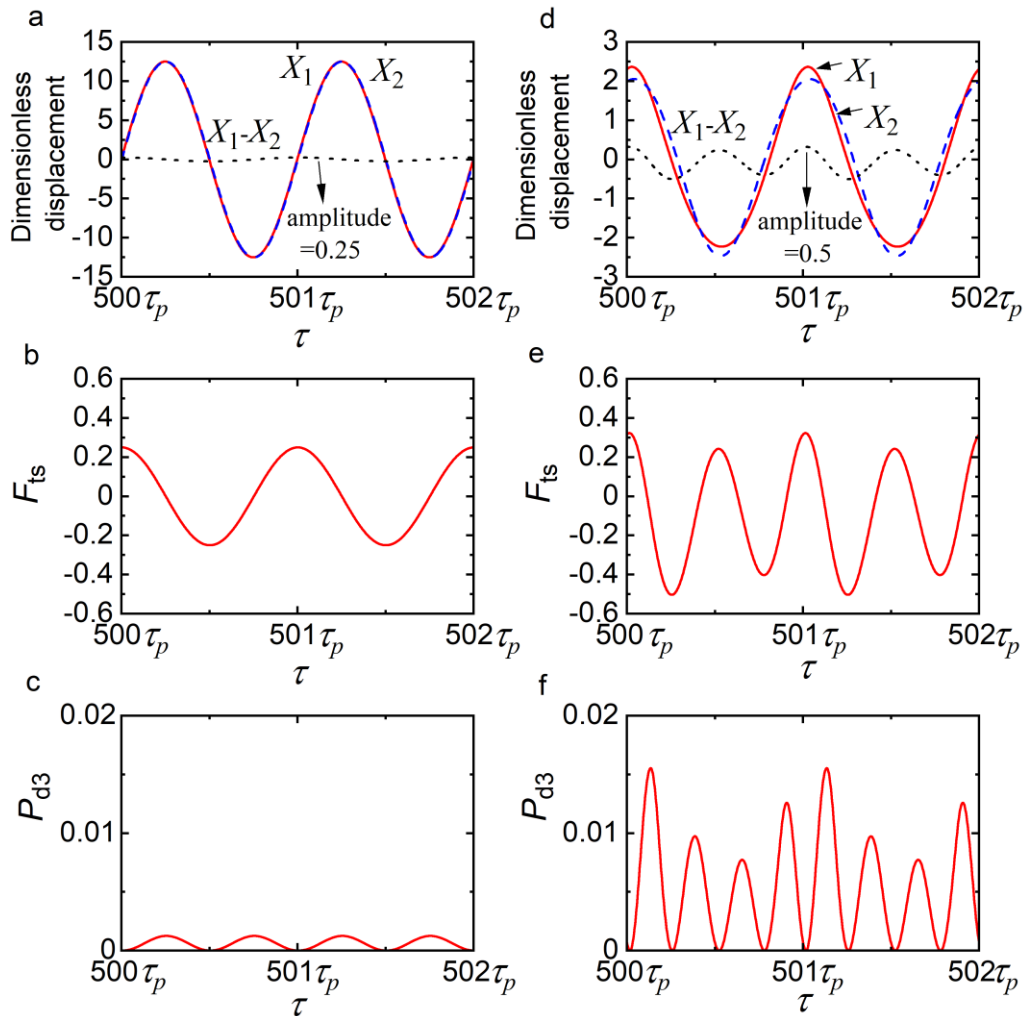


Figure 4.14. Effects of the linear constraint on displacement response, F_{ts} and P_{d3} at $\Omega = 1.0$ for $\lambda = 0$ in (a)-(c) and for $\lambda = 1$ in (d)-(f). (a) and (d): displacement response; (b) and (e): transmitted force F_{ts} ; (c) and (f): P_{d3} . For (a) and (d), the solid, dashed and dotted lines for X_1 , X_2 , and $X_1 - X_2$ respectively.

4.3.4. A 2DOF impact oscillator with a QZS nonlinear constraint

Figures. 4.15, 4.16 and 4.17 examine the influence of the nonlinear constraint on the steady-state response, the force transmission and power flow behaviour of the 2DOF impact oscillator. The system parameters are set as $\rho = 0, \eta = 1, \zeta_1 = 0.01, \zeta_2 = 0.01, \gamma = 1, \mu = 1, \kappa = 1, \epsilon = 1$, and $F_0 = 0.5$. In Case one, the system is not constrained with $K_1 = 0$ and $K_2 = 0$. In Cases two and three, the constraint stiffness ratio λ is set as 0.2 and 1, respectively, while $\alpha = 2$ and $\beta = 1$. The nonlinear QZS constraint is therefore characterised by a purely cubic nonlinear restoring force term so that $K_1 = 0$ with $K_2 = 0.2$ and $K_2 = 1$, respectively. Case four considers a linear constraint with $K_1 = 1, K_2 = 0$ ($\lambda = 1$), used for comparison. The second-order HB-AFT results are represented by different lines and the numerical integration results based on the fourth-order Runge-Kutta (RK) method are denoted by symbols. The results of Cases one to four are represented by solid lines and circles, dashed lines and the triangles, dotted lines and squares as well as dash-dot lines and rhombuses, respectively.

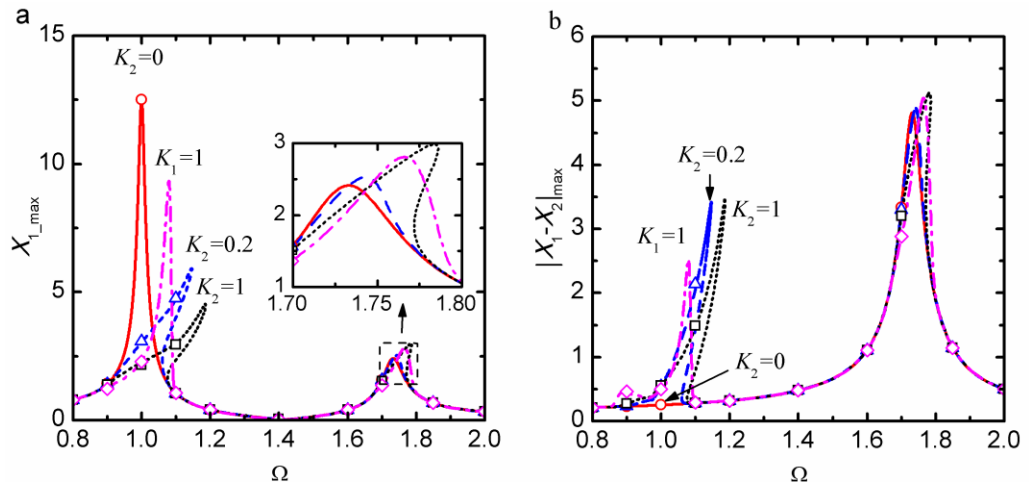


Figure 4.15. Effects of the nonlinear constraint on the maximum displacement X_{1_max} and $|X_1 - X_2|_{max}$, the solid, dashed and dotted lines for $K_2 = 0, 0.2$ and 1 with $K_1 = 0$, respectively. The dash-dot line is for $K_1 = 1$ and $K_2 = 0$. Symbols: RK results.

Figure. 4.15(a) and (b) investigates the effects of the nonlinear constraint on the maximum steady-state displacement response X_{1_max} of the primary mass m_1 and the relative displacement amplitude of the masses $|X_1 - X_2|_{max}$, respectively. Fig. 4.15(a) shows that compared with the un-constrained system (Case one), the addition of the nonlinear constraint in Cases two and three bends the resonance peaks towards the high-frequency range. As K_2 increases from 0, to 0.2 and then to 1, the first peak value of X_{1_max} reduces significantly but the second peak value increases slightly. A comparison of Case three with $K_2 = 1$ and Case four with $K_1 = 1$ shows that the nonlinear

constraint can effectively reduce the first peak value of the X_{1_max} . For relative displacement amplitude $|X_1 - X_2|_{max}$, Fig. 4.15(b) shows only one peak exists in Case one for the un-constrained system, but two peaks in Cases two and three, for the system with the nonlinear constraint. It also shows that the introduction of the nonlinear constraint can lead to a large peak value of $|X_1 - X_2|_{max}$ near $\Omega = 1.1$, the in-phase mode of the un-constrained system. The reason is that with the nonlinear constraint, the primary mass m_1 is further restrained while the second mass is not constrained, leading to a large relative displacement. With the increase of K_2 from 0.2 to 1, there is a small increase in the peak value of the relative displacement $|X_1 - X_2|_{max}$ near the out-of-phase mode of the system without the constraint. By comparing the results associated with the linear constraint case and the nonlinear constraint cases, the figure shows that the inclusion of the nonlinear constraint can provide a stronger restraint to limit the dynamic response of the system. It can lead to further bending of the response peaks to the high-frequency range, as well as the generation of higher peak values of $|X_1 - X_2|_{max}$.

Figure. 4.16(a) and (b) examines the influence of the nonlinear constraint on the force transmissibilities TR_L and TR_S for the LHS wall and the secondary mass m_2 , respectively. In Case one, for the coupled oscillators without any constraint, Fig. 4.16(a) shows two peaks in the curve of TR_L , with the first corresponds to the in-phase mode and the second to the out-of-phase mode, respectively. With the use of the nonlinear constraint in Cases two and three, the first peak of TR_L twists to the higher frequencies and the corresponding peak value reduces as K_2 changes from 0.2 to 1. Its second peak associated with the out-of-phase mode also bends slightly to the right but there is less change in the peak value. When comparing the nonlinear constraint case with $K_2 = 1$ and the linear constraint case with $K_1 = 1$, it is shown that the nonlinear constraint case yields a lower first peak value of TR_L . Fig. 4.16(b) shows only one peak value of TR_S , for the un-constrained system, two peaks of TR_S for each nonlinear constraint case and three peaks for the linear constraint case. An increase in the value of K_2 of the nonlinear constraint can bend the peaks in the curve of TR_S to the high-frequency range. However, the peaks of force transmissibility TR_S to mass m_2 associated with the two considered nonlinear constraint cases are of similar heights. By a comparison between Case three ($K_1 = 0, K_2 = 1$), and Case four ($K_1 = 1, K_2 = 0$), it shows that the introduction of the nonlinear constraint case with cubic restoring force can bring about a more significant hardening effect on the force transmissibility than the linear constraint case. The figure shows that the use of the constraint is able to reduce the peak force transmissibility of TR_L , but can lead to substantial increases in the force transmissibility to the secondary

mass, when the excitation frequency is in the neighbourhood of the in-phase mode of the un-constrained system.

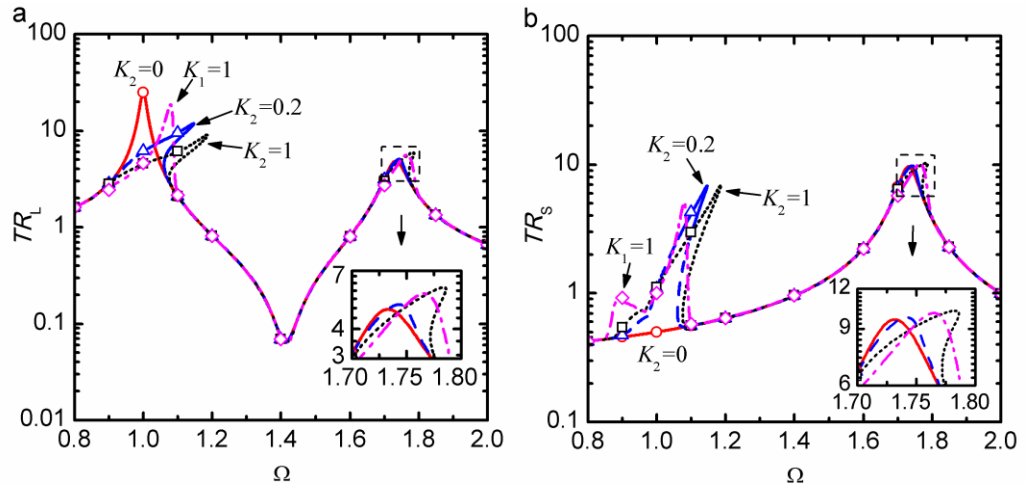


Figure 4.16. Effects of the nonlinear constraint on the force transmissibilities TR_L and TR_S . the solid, dashed and dotted lines for $K_2 = 0, 0.2$ and 1 with $K_1 = 0$, respectively. The dash-dot line is for $K_1 = 1$ and $K_2 = 0$. Symbols: RK results.

Figure. 4.17 investigates the effects of the nonlinear constraint on the power flow behaviour of the system. The characteristics of the time-averaged transmitted power \bar{P}_t to the secondary mass m_2 , power dissipation ratio R_{d2} of the damper c_2 , the time-averaged dissipated power \bar{P}_{d3} at the interface and power dissipation ratio R_{d3} of damper c_3 , are shown in Fig. 4.17(a), (b), (c) and (d), respectively. Fig. 4.17(a) shows that with the introduction of the nonlinear constraint in Cases two and three, both peaks in each curve of \bar{P}_t bend towards the high-frequency range as the nonlinear stiffness K_2 increases from 0.2 to 1. The first peak value of \bar{P}_t reduces substantially but there is much less change in the second peak value. By a comparison of Case three (with $K_2 = 1$) and Case four (with $K_1 = 1$), it shows that the nonlinear QZS constraint characterised by purely cubic restoring force bends the first peak of \bar{P}_t more to the high-frequency range and reduces the peak value of vibration energy transmission to the secondary mass m_2 . Fig. 4.17(b) shows that the nonlinear constraint has a large effect on the power dissipation ratio R_{d2} when the excitation frequency is near the first natural frequency of the un-constrained system (i.e., Case one). The inclusion of the nonlinear constraint in Cases two and three reduces the portion of input power that is dissipated in the secondary system from $\Omega \approx 0.9$ to $\Omega \approx 1.2$. By comparing Case three with Case four, it is shown that the nonlinear constraint provides a lower value of power dissipation ratio R_{d2} from $\Omega \approx 1.0$ to $\Omega \approx 1.2$ while the linear constraint can yield a lower R_{d2} from approximately $\Omega \approx 0.85$ to $\Omega \approx 1.0$.

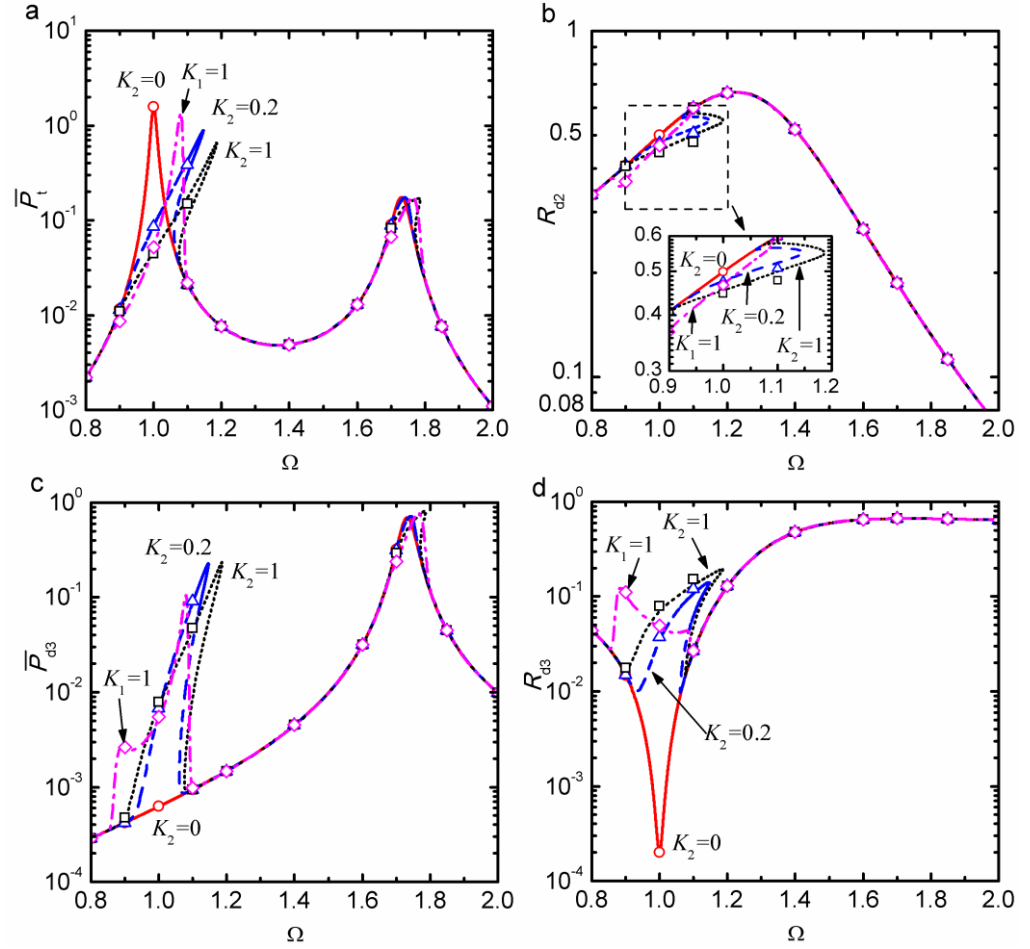


Figure 4.17. Effects of the nonlinear constraint on the (a) power transmission \bar{P}_t , (b) power dissipation ratio of R_{d2} , (c) power dissipation \bar{P}_{d3} at the interface and (d) power dissipation ratio of R_{d3} . The solid, dashed and dotted lines for $K_2 = 0, 0.2$ and 1 while $K_1 = 0$, respectively. The dash-dot line is for the case with $K_1 = 1, K_2 = 0$. Symbols: RK results.

Fig. 4.17(c) shows that only one peak is observed in the curve of \bar{P}_{d3} for the un-constrained system, two peaks for the system with the nonlinear constraint, and three peaks for the system with the linear constraint. It shows that the peaks of \bar{P}_{d3} curves bend to the high-frequency range as the K_2 increases from 0.2 to 1, corresponding to Cases two and three, respectively. However, the peak values of \bar{P}_{d3} remain similar for these two cases. It is shown that the introduction of the linear or the nonlinear QZS constraint can significantly increase the amount of dissipated power at the interface when the excitation frequency is in the vicinity of the first resonance frequency of the un-constrained system. This behaviour is associated with a higher relative displacement between masses, as created by the addition of the constraint. It also shows that the constraint has a much smaller influence on the second peak value \bar{P}_{d3} . Fig. 4.17(d) shows that the nonlinear constraint mainly affects the power dissipation ratio R_{d3} when the excitation frequency Ω is near the first resonance frequency of the un-constrained system. The addition of the nonlinear constraint in Case two and Case three effectively

increases the relative portion of total input power, which is then dissipated at the interface in the frequency range from $\Omega \approx 0.9$ to $\Omega \approx 1.1$. By comparing Case three with Case four, it is shown that the nonlinear constraint can lead to a larger R_{d3} from approximately $\Omega = 0.95$ to $\Omega = 1.2$ while the linear constraint results in a larger value of R_{d3} when the excitation frequency Ω is approximately between 0.85 and 0.95. The results show that the nonlinear constraint can be used to modify the vibration transmission within the impact oscillator when the excitation frequency is in the vicinity of the in-phase mode of the corresponding un-constrained system. It demonstrates that the potential benefits of using nonlinear constraint for vibration suppression purpose.

4.4. Summary

This chapter investigated the dynamic behaviour and the vibration transmission of impact oscillators. The level of vibration transmission in both SDOF and 2DOF impact oscillators incorporating linear or nonlinear QZS constraint was quantified using force transmissibility and time-averaged power flow variables based on the HB approximation and numerical integrations. The effects of stiffness and damping properties of the constraint on the response and vibration transmission were revealed. Main findings based on this investigation are listed as follows:

- (1) The linear constraint in the SDOF system can yield significant changes in the peak values and frequencies of the vibration power input and the distribution of power dissipation within the oscillator.
- (2) A nonlinear constraint can be used in the SDOF impact oscillator such that the level of force transmissibility and vibration power flow can be tailored near the peak frequencies.
- (3) The introduction of a linear constraint at the coupling interface of the 2DOF oscillator system can lead to multiple peaks in the force transmissibility to the secondary mass and the time-averaged dissipated power at the interface.
- (4) The use of a nonlinear QZS constraint for the 2DOF impact oscillator can effectively reduce the peak of time-averaged transmitted power but can increase the force transmissibility to the secondary mass. The use of force transmissibility and time-averaged power flow as measures of the vibration transmission level may lead to different evaluation outcomes.

Chapter 5

Vibration transmission analysis of impact oscillators with nonlinear motion constraints created by DSLM

The impact oscillator with multiple constraints can be used to model the dynamic behaviour of various engineering systems such as meshing gears with gear rattling, passive walking robots, electric impact platforms and energy harvesters. Some researchers have focused on the impact oscillator with multiple linear constraints (Natsiavas, 1990; Li et al., 2019), and described some new dynamic behaviour compared with that of the impact oscillator with a single constraint. Li and Ding (2018) proposed a semi-analytical method to obtain the periodic response of a vibro-impact system with two asymmetric clearances. In the work, the formation mechanism of chatting-impact periodic response with sticking motion influenced by grazing bifurcation was studied. Dou et al. (2020) investigated a friction-influenced Duffing oscillator with two-sided rigid constraints and established analytical conditions of all motions. However, there are very limited studies on the dynamics of impact oscillators with multiple nonlinear constraints. It has been mentioned in previous content that the compliant contact models may contain nonlinear impact force generated by elastic deformation with the contact stiffness varying with the material and geometric properties of the contacting objects (Gilardi and Sharf, 2002). The global dynamics of impact oscillator may depend on contact force models applied (Ajibose et al., 2010). Moreover, previous research on the dynamic characteristics of impact oscillators has been focused on the displacement response (Kundu et al., 2012), with very few studies reported on the vibration transmission, especially on the quantification of vibration energy transfer and dissipation within such systems. In this chapter, a nonlinear motion constraint created by a linear spring embedded in a diamond-shaped linkage mechanism (DSLML) is proposed and used in SDOF and 2DOF impact oscillators. The vibration force transmission and power flow characteristics of such impact oscillators with a single constraint or multiple nonlinear constraints are investigated by using HB-AFT method with numerical continuations and compared with the results obtained by the time-

marching method. The influence of the design parameters of the proposed nonlinear constraints on the dynamic behaviour and vibration transmission is investigated. Moreover, the effects of different locations for adding the nonlinear constraints to 2DOF impact oscillators are studied.

5.1. Mathematical model

5.1.1. Nonlinear constraint based on DSLM

Figure 5.1 shows the schematic diagram of the nonlinear motion constraint based on a geometrically nonlinear diamond-shaped spring (which is named D-spring hereafter) considered in this chapter. Fig. 5.1(a) presents the D-spring comprising a DSLM and a linear vertical spring of stiffness k_s at its original length l_s . The DSLM consists of four identical rigid rods AC, AD, BC, and BD, each with a fixed length of l_b , hinged end to end at points A, B, C and D. When the spring is unstretched, the angle between AC and AB is denoted as θ_0 ($0^\circ \leq \theta_0 < 90^\circ$) and $\sin\theta_0 = l_s/(2l_b)$. Correspondingly, the initial distance y_0 between terminal A and B is $y_0 = 2l_b \cos\theta_0$. The nonlinear D-spring constraint is fixed to the right-hand wall at terminal A. Throughout this chapter, it is assumed that the constraint has negligible mass and damping.

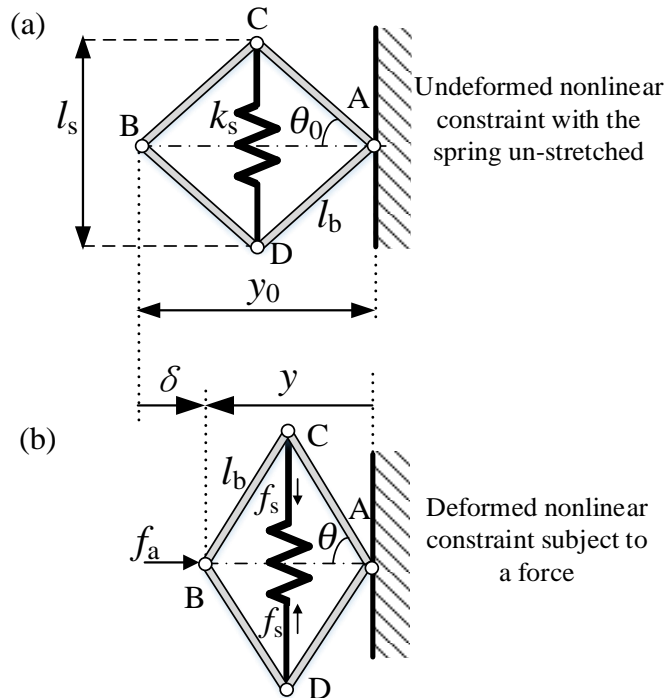


Figure 5.1. Schematics of the nonlinear D-spring constraint (a) with the spring un-stretched and (b) subjected to a force.

Figure 5.1(b) shows the deformed geometry of the nonlinear D-spring constraint with its left terminal B moved by a distance of δ due to a horizontal impact force f_a .

The horizontal distance of point B measured from point A is denoted by $y = y_0 - \delta$. The angle between the AC and AB is represented by θ with $\cos\theta = y/(2l_b)$. For practical applications, we have $\theta_0 < \theta < 90^\circ$. The vertical spring will be extended by $2l_b\sin\theta - l_s$ and therefore its restoring force f_s is expressed by

$$f_s = k_s(2l_b\sin\theta - l_s). \quad (5.1)$$

The restoring force f_r of the nonlinear D-spring is the reaction force corresponding to f_a such that $f_r = f_a$, pointing to the left. From geometric and force equilibrium conditions of the linkage mechanism, we have

$$f_r(y) = f_a = f_s \cdot \frac{\cos\theta}{\sin\theta} = k_s(2l_b\sin\theta - l_s) \frac{\cos\theta}{\sin\theta} = k_s y \left(1 - \frac{l_s}{\sqrt{4l_b^2 - y^2}} \right). \quad (5.2)$$

By introducing $Y_0 = y_0/(2l_b)$, $Y = y/(2l_b)$ and $\Delta = \delta/(2l_b)$, it follows that

$$\cos\theta_0 = Y_0, \quad \sin\theta_0 = l_s/(2l_b) = \sqrt{1 - \cos^2\theta_0} = \sqrt{1 - Y_0^2}, \quad (5.3a, 5.3b)$$

$$\cos\theta = Y, \quad \sin\theta = \sqrt{1 - Y^2}. \quad (5.3c, 5.3d)$$

By using Eq. (5.3) to replace variable θ with Y in Eq. (5.2), we have the non-dimensional restoring force:

$$F_r(Y) = F_a = \frac{f_a}{2l_b k_s} = Y \left(1 - \sqrt{\frac{1 - Y_0^2}{1 - Y^2}} \right), \quad 0 < Y \leq Y_0. \quad (5.4)$$

This equation shows that the restoring force by the nonlinear D-spring depends on the dimensionless initial distance Y_0 and the deformed distance Y between terminals A and B. Therefore, it is straightforward to tailor the characteristics of the constraint to achieve design requirements by adjusting the initial distance Y_0 .

A differentiation of F_r with respect to the non-dimensional deflection Δ of the constraint yields the non-dimensional stiffness:

$$K_r(\Delta) = \frac{dF_r(\Delta)}{d(\Delta)} = -\frac{dF_r(Y)}{d(Y)} = \sqrt{\frac{1 - Y_0^2}{1 - Y^2}} + Y^2 \sqrt{1 - Y_0^2} [1 - Y^2]^{-(3/2)} - 1. \quad (5.5)$$

Figure 5.2(a) and (b) shows the variation of the restoring force F_r and the nonlinear stiffness K_r with respect to the dimensionless distance Y between the two ends of the nonlinear D-spring, respectively. Four different values of the dimensionless initial distance Y_0 are considered with Y_0 increasing from 0.3 to 0.5, to 0.7 and to 0.8. Fig. 5.2(a) shows that for a given value of Y_0 , the restoring force F_r is a nonlinear function

of Y . When the constraint is compressed with the distance Y between its two ends decreasing from Y_0 to 0, the value of the restoring force F_r increases to a maximum point and then decreases to zero. Fig. 5.2(a) also shows that a larger value of Y_0 leads to a higher peak in the curve of F_r . Fig. 5.2(b) shows that for a given value of Y_0 , as the constraint is compressed with the value of Y reducing from Y_0 to 0, the value of the stiffness K_r decreases from positive to zero, and then to negative. Here the positive stiffness refers to the value of constraint stiffness larger than zero while the negative stiffness refers to the value of stiffness smaller than zero. The negative stiffness characteristic is obtained by geometric nonlinearity of the DSLM under large deformation. It is also found that increasing Y_0 from 0.3 to 0.8 can lead to a larger positive static stiffness at $Y = Y_0$, i.e., the un-deformed state. At a pre-determined value of Y close to 0, a larger value of Y_0 can also result in a lower value of the negative stiffness.

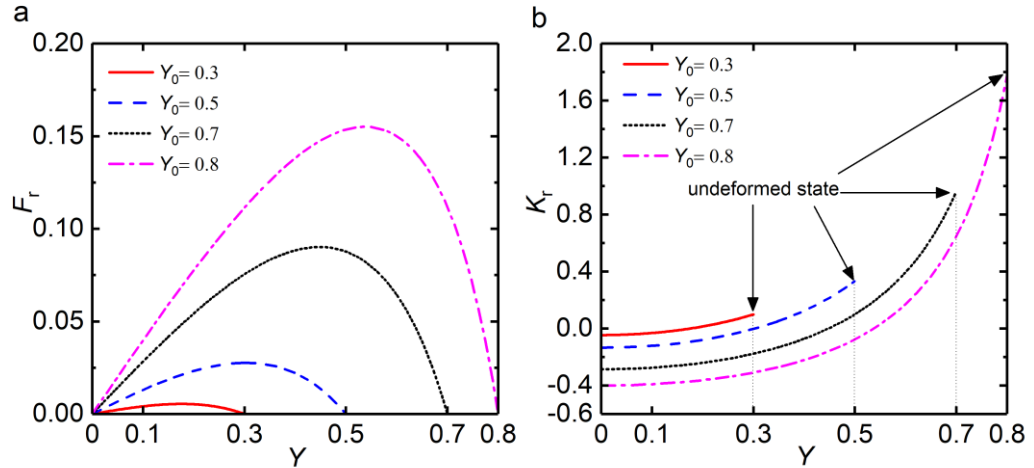


Figure 5.2. Variations of the dimensionless (a) restoring force F_r and (b) stiffness K_r with respect to the distance Y between the two ends of the nonlinear constraint. The solid, dashed, dotted and dash-dotted lines are for cases with $Y_0 = 0.3, 0.5, 0.7$ and 0.8 , respectively.

5.1.2. Impact oscillators with the nonlinear constraint

For a general Q -DOF impact oscillator comprising the proposed nonlinear D-spring constraint, the general non-dimensional dynamic governing equation can be written in a matrix form as

$$[\mathbf{M}]\{\mathbf{X}''\} + [\mathbf{C}]\{\mathbf{X}'\} + [\mathbf{K}]\{\mathbf{X}\} + \{\mathbf{F}_c(X)\} = \{\mathbf{F}_{ex}(\tau)\}, \quad (5.6)$$

where $\{\mathbf{X}\}$, $\{\mathbf{X}'\}$ and $\{\mathbf{X}''\}$ denote the displacement, velocity and acceleration response vectors, respectively, $[\mathbf{M}]$, $[\mathbf{C}]$ and $[\mathbf{K}]$ are the corresponding mass, damping and stiffness matrices of the linear sub-system without considering the constraints, respectively, $\{\mathbf{F}_c(X)\}$ is the nonlinear force arising from the constraints, $\{\mathbf{F}_{ex}(\tau)\} = \{\dots, F_0 e^{i\Omega\tau}, \dots\}^T$ is a harmonic excitation force applied to the j -th DOF ($1 \leq j \leq$

Q) of the system, where F_0 and Ω are the dimensionless excitation amplitude and frequency, respectively, and τ is the non-dimensional time.

The HB-AFT method with numerical continuations is used to obtain the steady-state periodic solution. The steady-state displacement response $\{X\}$ and the nonlinear force $\{F_c(X)\}$ are firstly approximated by a truncated N -order Fourier series with a fundamental frequency of Ω :

$$\{X\} = \left\{ \sum_{n=0}^N \tilde{R}_{(1,n)} e^{in\Omega\tau}, \dots, \sum_{n=0}^N \tilde{R}_{(j,n)} e^{in\Omega\tau}, \dots, \sum_{n=0}^N \tilde{R}_{(Q,n)} e^{in\Omega\tau} \right\}^T, \quad (5.7a)$$

$$\{F_c(X)\} = \left\{ \sum_{n=0}^N \tilde{H}_{(1,n)} e^{in\Omega\tau}, \dots, \sum_{n=0}^N \tilde{H}_{(j,n)} e^{in\Omega\tau}, \dots, \sum_{n=0}^N \tilde{H}_{(Q,n)} e^{in\Omega\tau} \right\}^T, \quad (5.7b)$$

where $\tilde{R}_{(j,n)}$ and $\tilde{H}_{(j,n)}$ are the complex Fourier coefficients of the n -th order Fourier approximations corresponding to the j -th DOF, $\{X'\}$ and $\{X''\}$ can then be obtained by taking differentiation of $\{X\}$ with respect to time τ . The AFT technique discussed in Chapter 3 can be employed to determine the Fourier coefficients \tilde{H} of the nonlinear force $\{F_c(X)\}$. By substituting the expressions of the response and the nonlinear force into Eq. (5.6) and balancing the coefficients of the corresponding harmonic terms, a total number of $Q(2N + 1)$ real nonlinear algebraic equations can then be established. The solution of those equations in the frequency domain can be found by using the Newton-Raphson method with the arc-length continuation illustrated in Chapter 3. Subsequently, the steady-state response of the system and the vibration transmission within impact oscillators can be determined.

For the power flow analysis of the impact oscillator system, the steady-state time-averaged input vibration power into the system is defined as the product of the velocity X'_j of the j -th DOF and the harmonic excitation force $F_0 e^{i\Omega\tau}$ over an averaging time span τ_p . Note that the velocity X'_j can be obtained by the differentiation of X_j as $X'_j = \sum_{n=0}^N in\Omega \tilde{R}_{(j,n)} e^{in\Omega\tau}$, hence we have

$$\bar{P}_{in} = \frac{1}{\tau_p} \int_{\tau_0}^{\tau_0 + \tau_p} \Re\{X'_j\} \Re\{F_0 e^{i\Omega\tau}\} d\tau = \frac{1}{2} F_0 \Re\{(i\Omega \tilde{R}_{(j,1)})^*\}, \quad (5.8)$$

where τ_0 is the starting time for averaging, the averaging time τ_p is set as one cycle of excitation with $\tau_p = 2\pi/\Omega$, and the symbols \Re and $*$ denote the operation of taking the real part and complex conjugate of a complex number, respectively.

The maximum kinetic energy is often used as an index to evaluate the performance of vibration suppression systems (Xiong et al., 2003). For the impact oscillator system, the non-dimensional maximum kinetic energy K_j associated with the j -th mass (i.e., m_j) of the impact oscillator is

$$K_j = \frac{1}{2} (|X_j'|_{\max})^2, \quad (5.9)$$

where $|X_j'|_{\max}$ represents the maximum magnitude of the velocity of the j -th mass in the steady-state motion.

5.2. SDOF impact oscillator with the nonlinear constraint

5.2.1. Dynamic response

In this section, the dynamics and vibration transmission characteristics of an impact oscillator with a SDOF subsystem and the nonlinear D-spring constraint are investigated. Fig. 5.3 shows the SDOF system, comprising a mass m_1 excited by a harmonic force $f_0 e^{i\omega t}$, a viscous damper with damping coefficient c_1 and a linear spring with stiffness coefficient k_1 . The whole system is placed in the horizontal plane. The equilibrium position of the mass, where the spring k_1 is un-stretched, is set as a reference with the displacement $x_1 = 0$. The left-hand terminal of the nonlinear constraint as shown in Fig. 5.1(a) and Fig. 5.3(a), initially with its spring un-stretched, is placed at a distance of d from the mass when $x_1 = 0$. Fig. 5.3(b) shows a corresponding linear constraint with a spring stiffness of k_s , used for comparison.

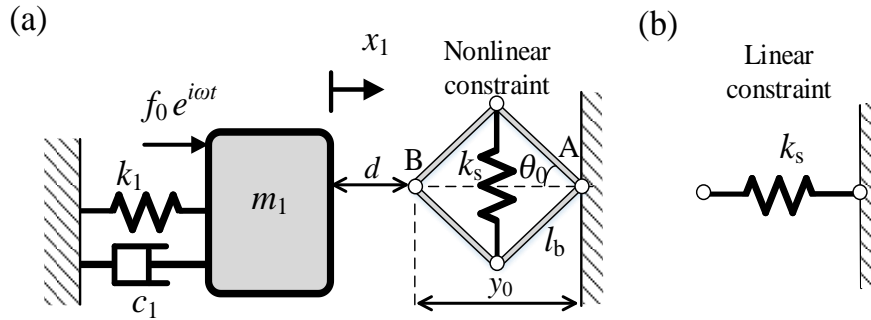


Figure 5.3. (a) A SDOF impact oscillator with a nonlinear constraint, and (b) a linear spring constraint.

The dimensional governing equation of the mass is

$$m_1 \ddot{x}_1 + c_1 \dot{x}_1 + k_1 x_1 + f_c(x_1) = f_0 e^{i\omega t}, \quad (5.10)$$

where $f_c(x_1) = f_r(y)$ is the leftward pointing force applied by the nonlinear D-spring to the mass m_1 , as expressed by Eq. (5.2) with $y = (y_0 + d - x_1)U(\delta)$ and $\delta = x_1 - d$ while $U(\delta)$ representing the Heaviside step function expressed by

$$U(\delta) = \begin{cases} 0, & \text{when } \delta \leq 0, \\ 1, & \text{when } \delta > 0. \end{cases} \quad (5.11)$$

To obtain the non-dimensional governing equation, the following parameters are introduced:

$$\omega_1 = \sqrt{\frac{k_1}{m_1}}, \quad \zeta_1 = \frac{c_1}{2m_1\omega_1}, \quad X_1 = \frac{x_1}{2l_b}, \quad \lambda = \frac{k_s}{k_1}, \quad F_0 = \frac{f_0}{2l_b k_1}, \quad \Omega = \frac{\omega}{\omega_1}, \quad \tau = \omega_1 t, \quad \eta = \frac{d}{2l_b}, \quad (5.12a-5.12h)$$

where ω_1 and ζ_1 are the undamped natural frequency and the damping ratio of the linear subsystem without the constraint, respectively, X_1 denotes the dimensionless displacement of the mass, λ is the spring stiffness ratio of the constraint, F_0 , Ω and τ are the dimensionless excitation amplitude, excitation frequency and the dimensionless time, respectively, and η is the gap width ratio. Eq. (5.10) is transformed into the form of Eq. (5.6), described as

$$X_1'' + 2\zeta_1 X_1' + X_1 + F_c(X_1) = F_0 e^{i\Omega\tau}, \quad (5.13)$$

where $F_c(X_1) = \lambda F_r(Y(X_1))$ represents the non-dimensional force applied by the nonlinear constraint, with $F_r(Y(X_1))$ expressed by Eq. (5.4), and $Y(X_1) = (Y_0 + \eta - X_1)U(X_1 - \eta)$. By using HB-AFT approximations, Eq. (5.13) can be solved and the steady-state dynamic response of the mass m_1 can be determined.

In Fig. 5.4, the influence of the design parameters of the nonlinear D-spring constraint on the steady-state response is examined. The system parameters are fixed as $\zeta_1 = 0.01$, $\eta = 0.1$ and $F_0 = 0.015$. The response curves are obtained based on the second-order HB-AFT. The response amplitude and the steady-state oscillating position of the mass are denoted by X_{1_amp} and R_0 , respectively. Here R_0 is defined by Eq. 5.7(a) with $j = 1$ and $n = 0$. The displacement responses are also obtained by using a time-domain method, i.e., the fourth-order RK method, and are denoted by symbols.

In Fig. 5.4(a) and (b), the effects of the nonlinear constraint stiffness λ are investigated, by changing its value from 0 to 1 and to 2 while setting $\theta_0 = 30^\circ$. The response curves of the linear constraint case with $\lambda = 1$ are also included for comparison. It shows that the HB-AFT results agree relatively well with those obtained from the RK method. Fig. 5.4(a) shows that the value of R_0 keeps negative when the mass is engaged with the constraint. It shows that at a certain excitation frequency, there can be up to five possible solutions. Fig. 5.4(b) shows that there is a frequency interval of $0.92 < \Omega < 1.07$, at the boundary of which the response curves diverge. Fig. 5.4(a) and (b)

shows that the curves of R_0 and X_{1_amp} associated with the nonlinear constraint cases firstly extend to the high-frequency range and then twist back to the low frequencies. This is of contrast to the linear constraint case, for which the curves only extend to the high-frequency range. This phenomenon is due to the fact that when the deformation of the constraint Δ is small, the nonlinear constraint with $\theta_0 = 30^\circ$ has a higher constraint stiffness K_T than the linear constraint, as shown by Eq. (5.5) and Fig. 5.2(b). When the deformation of the constraint is large, the stiffness of the nonlinear constraint can be smaller than that of the corresponding linear constraint. With the increase of λ from 1 to 2 for the nonlinear constraint, the curves of R_0 and X_{1_amp} bend more to the high frequencies due to a larger constraint restoring force but their absolute peak values decrease.

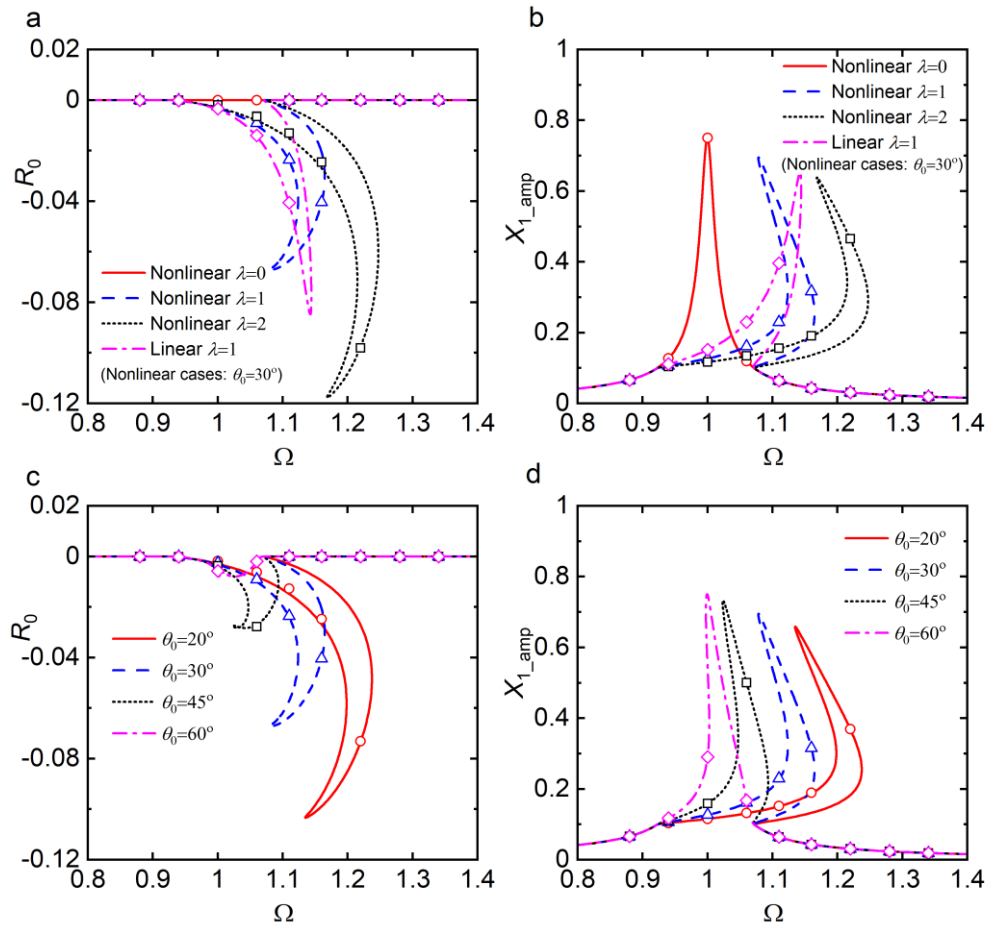


Figure 5.4. Effects of the spring stiffness ratio λ and the initial angle θ_0 of the nonlinear constraint on (a) and (c): the steady-state oscillating position of the mass R_0 , and on (b) and (d): the response amplitude X_{1_amp} . In (a) and (b), the solid, dashed and dotted lines are for nonlinear constraint with $\lambda = 0, 1$ and 2 , respectively. The dash-dot line is for linear constraint with $\lambda = 1$; in (c) and (d), the solid, dashed, dotted and dash-dot lines are for $\theta_0 = 20, 30, 45$ and 60 degrees, respectively. Symbols: RK results.

In Fig. 5.4(c) and (d), the influence of the initial angle θ_0 of the nonlinear constraint is studied while setting $\lambda = 1$. With the θ_0 changing from 60 to 45 , to 30 and to 20

degrees, the response curves of R_0 and X_{1_amp} bend more to the high-frequency range with lower peak values. It can be explained by Eq. (5.5) and Fig. 5.2(b) that a smaller value of θ_0 for the nonlinear constraint can provide a larger constraint stiffness, which leads to a stronger hardening effect on the response curve of the mass. Meanwhile, it is found that the peak of each curve twists back to the low frequencies. This is due to the decreased stiffness of the constraint when the deformation of the constraint Δ is large.

5.2.2. Force transmissibility and vibration power flow

When designing the nonlinear constraint, it is useful to evaluate the level of force transmission and also the amount of vibration power flow into the system. In this chapter, the force transmissibility TR is defined as the maximum magnitude of the transmitted force at an interested point in the system to that of the input force. The force transmissibility from mass m_1 to the RHS wall of the nonlinear constraint is

$$TR_R = \frac{\max(|\Re\{F_{tR}\}|)}{F_0}, \quad (5.14)$$

where $F_{tR} = F_c(X_1)$ represents the non-dimensional transmitted force from mass m_1 to the RHS wall.

For the current system, the time-averaged input power \bar{P}_{in} and the maximum kinetic energy K_1 of the mass m_1 can be obtained from Eq. (5.8) and (5.9) respectively, with $j = 1$. It is noted that according to the conservation of energy, over a cycle of periodic response, the input energy by the external force should be all dissipated by the damper c_1 .

In Figs. 5.5 and 5.6, the effects of the design parameters of the nonlinear constraint on the force transmissibility and the vibration power flow and energy are investigated, respectively. The system parameters are set as $\zeta_1 = 0.01$, $\eta = 0.1$ and $F_0 = 0.015$. The second-order HB-AFT approximations are represented by different lines and the fourth-order RK results are denoted by symbols. In Fig. 5.5(a), 5.6(a) and 5.6(b), the influence of the spring stiffness ratio λ of the nonlinear constraint is examined by changing it from 0 to 1 and to 2, while setting $\theta_0 = 30^\circ$. A linear constraint case with $\lambda = 1$ is also added for comparison. In Fig. 5.5(b), 5.6(c) and 5.6(d), the effects of the initial angle θ_0 of the nonlinear constraint are investigated considering four possible values of 20, 30, 45 and 60 degrees while setting $\lambda = 1$. Fig. 5.5(a) and (b) shows that the TR_R curves for nonlinear constraint cases have flat peaks, of contrast to the shape of the peak for the linear constraint case. The reason is that in the vicinity of the resonance peak, the displacement amplitude of the mass (or the deformation Δ for the nonlinear constraint)

becomes larger than the critical value at which the restoring force $F_c(X_1)$ of the nonlinear constraint reaches its maximum, as shown in Eq. (5.4) and Fig. 5.2(a). As the magnitude of the restoring force is the same as the transmitted force to the RHS wall, the maximum amplitude of the transmitted force remains unchanged in a certain frequency band near the resonance. Consequently, the force transmissibility will have a flat peak. It is noted that in Fig. 5.5(a), in the nonlinear constraint case with $\lambda = 0$, there is no force transmission via the nonlinear constraint to the RHS wall, therefore the corresponding force transmissibility TR_R results are not shown. Fig. 5.5(a) shows that as the spring stiffness ratio λ of the nonlinear constraint increases from 1 to 2, both the peak value and the peak frequency of TR_R increase. By comparing the results of the nonlinear and linear constraint cases both with $\lambda = 1$, it is shown that the peak value of TR_R for the nonlinear constraint case is much smaller than that for the linear constraint case. Fig. 5.5(b) shows that the increase of the initial angle θ_0 from 20 to 30, to 45 and to 60 degrees will result in a substantial reduction in the peak value of TR_R and its corresponding frequency. In summary, a lower value of λ or a higher value of θ_0 maybe beneficial for obtaining lower values of the force transmissibility TR_R .

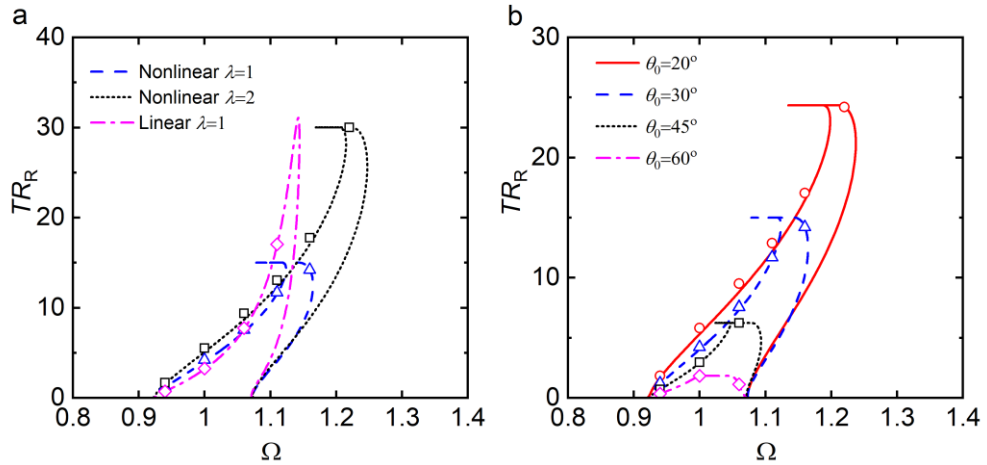


Figure 5.5. Effects of (a) the spring stiffness ratio λ and (b) the initial angle θ_0 of the nonlinear constraint on the force transmissibility TR_R . In (a), the solid, dashed and dotted lines are for nonlinear constraint with $\lambda = 0, 1$ and 2 , respectively. The dash-dot line is for linear constraint with $\lambda = 1$; in (b), the solid, dashed, dotted and dash-dot lines are for $\theta_0 = 20, 30, 45$ and 60 degrees, respectively. Symbols: RK results.

Figure 5.6 shows the effects of the design parameters of the nonlinear constraint on the time-averaged input power \bar{P}_{in} and the maximum kinetic energy K_1 of the mass. The figure shows that the patterns of the curves for \bar{P}_{in} and K_1 are similar. Fig. 5.6(a) and (b) shows that the increase of the spring stiffness ratio λ from 0 to 1 and to 2 for the nonlinear constraint can shift the peaks of \bar{P}_{in} and K_1 to the right, but their peak values change little. By comparing the linear and nonlinear constraint cases both with the same spring stiffness ratio of $\lambda = 1$, it is found that the peak frequency of \bar{P}_{in} for nonlinear

constraint case is lower but the peak values are of similar heights. A similar observation can be made on the peaks of the maximum kinetic energy curves for the linear and nonlinear constraint cases. Fig. 5.6(c) and (d) shows that as the initial angle θ_0 of the constraint reduces from 60 to 20 degrees, there are more extension of the curves of \bar{P}_{in} and K_1 to the high frequencies. As θ_0 decreases, the peak frequencies of \bar{P}_{in} and K_1 curves increase but the peak values change little.

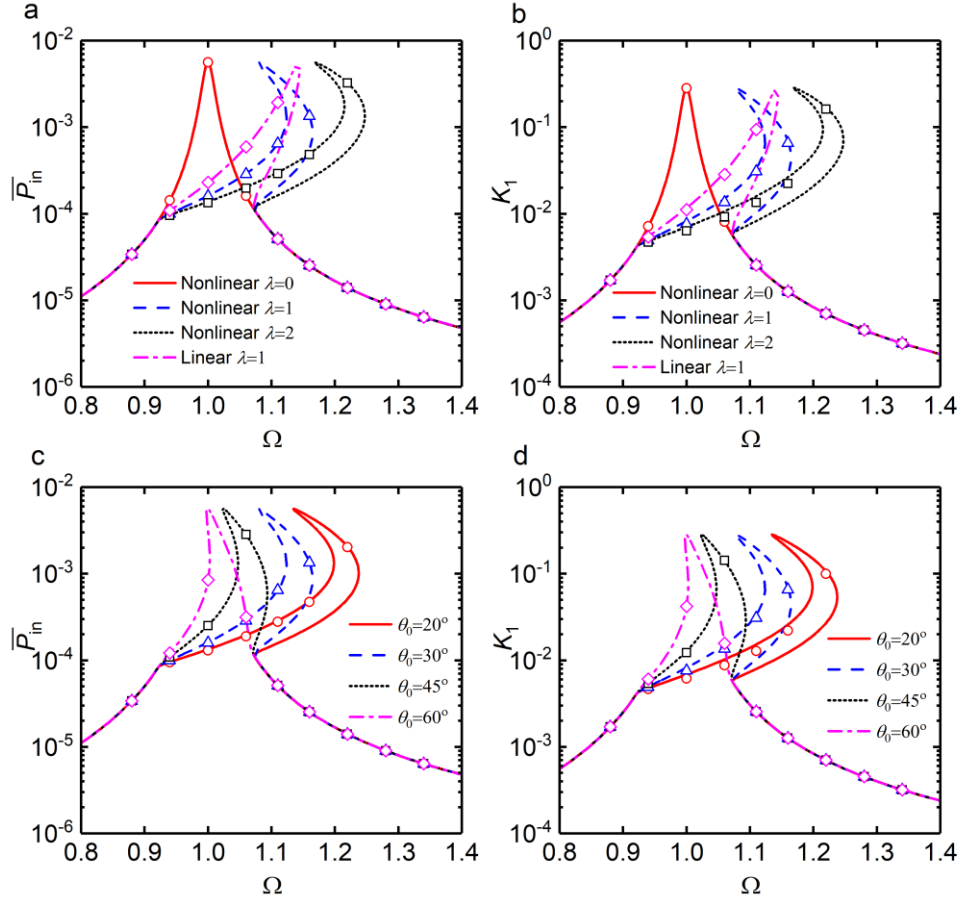


Figure 5.6. Effects of the spring stiffness λ and the initial angle θ_0 of the nonlinear constraint on (a) and (c): the time-averaged input power \bar{P}_{in} , and on (b) and (d): the maximum kinetic energy K_1 . In (a) and (b), the solid, dashed and dotted lines are for nonlinear constraint with $\lambda = 0, 1$ and 2 , respectively. The dash-dot line is for linear constraint with $\lambda = 1$; in (c) and (d), the solid, dashed, dotted and dash-dotted lines are for $\theta_0 = 20, 30, 45$ and 60 degrees, respectively. Symbols: RK results.

5.3. 2DOF impact oscillators with multiple nonlinear constraints

5.3.1. The model and power flow formulations

In this section, the dynamics and vibration transmission characteristics of two-DOF impact oscillators with a single constraint or multiple nonlinear constraints are investigated. The impact oscillator comprises two SDOF systems coupled via a linear interface of a spring with stiffness k_3 and a damper with damping coefficient c_3 . The SDOF primary system on the left consists of the primary mass m_1 subjected to a

harmonic excitation $f_0 e^{i\omega t}$, a spring with stiffness coefficient k_1 and a viscous damper c_1 . The SDOF secondary system on the right has the secondary mass m_2 , a viscous damper of damping coefficient c_2 , and a linear spring with stiffness coefficient k_2 . The static equilibrium positions of the two masses, where $x_1 = x_2 = 0$ and the springs k_1 , k_2 , k_3 are un-stretched, are set as a reference. Constraints C1 and C3 are for the mass m_1 while the constraint C2 is for the mass m_2 . When the springs in the constraints are un-stretched, i.e., $x_1 = x_2 = 0$, the LHS terminals of constraints C1 and C2 are placed at a distance of d to the right of masses m_1 and m_2 , respectively, while the RHS terminal of constraint C3 is located at a distance d from mass m_1 . Note that the constraints C1, C2, C3 can be nonlinear as shown in Fig. 5.7(b) or linear, as shown by Fig. 5.7(c).

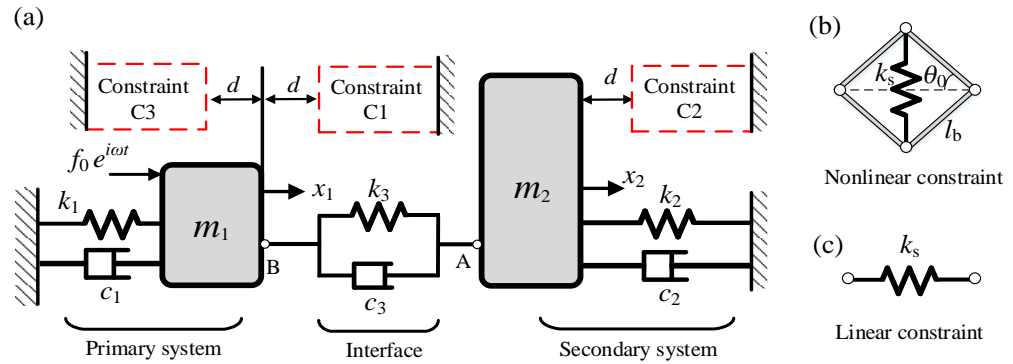


Figure 5.7. (a) A 2DOF impact oscillator with linear or nonlinear constraints, (b) nonlinear constraint and (c) linear spring constraint.

Based on the Newton's 2nd law, the equations of the motion of the system in a matrix form are

$$\begin{bmatrix} m_1 & 0 \\ 0 & m_2 \end{bmatrix} \begin{Bmatrix} \ddot{x}_1 \\ \ddot{x}_2 \end{Bmatrix} + \begin{bmatrix} c_1 + c_3 & -c_3 \\ -c_3 & c_2 + c_3 \end{bmatrix} \begin{Bmatrix} \dot{x}_1 \\ \dot{x}_2 \end{Bmatrix} + \begin{bmatrix} k_1 + k_3 & -k_3 \\ -k_3 & k_2 + k_3 \end{bmatrix} \begin{Bmatrix} x_1 \\ x_2 \end{Bmatrix} + \begin{Bmatrix} f_{c1} - f_{c3} \\ f_{c2} \end{Bmatrix} = \begin{Bmatrix} f_0 e^{i\omega t} \\ 0 \end{Bmatrix}, \quad (5.15)$$

where f_{c1} and f_{c3} represent the forces applied by the nonlinear constraints C1 and C3 to the mass m_1 , respectively, while f_{c2} denotes the force applied by the nonlinear constraint C2 to the mass m_2 . For the convenience of later derivation, new parameters are introduced:

$$\omega_2 = \sqrt{\frac{k_2}{m_2}}, \quad \zeta_2 = \frac{c_2}{2m_2\omega_2}, \quad X_2 = \frac{x_2}{2l_b}, \quad \gamma = \frac{\omega_2}{\omega_1}, \quad \kappa = \frac{k_3}{k_1}, \quad \epsilon = \frac{c_3}{c_1}, \quad \mu = \frac{m_2}{m_1}, \quad (5.16a-5.16g)$$

where ω_2 and ζ_2 denote the undamped natural frequency and the damping ratio of the linear secondary system, respectively, X_2 represents the non-dimensional displacement

of the secondary mass, γ is the undamped natural frequency ratio between primary and the secondary oscillator, κ and ϵ are the dimensionless stiffness and damping ratios for the interfacial spring and damper, respectively, and μ is the mass ratio. By using these parameters and those defined in the previous section, the non-dimensional governing equation of the system is

$$\begin{bmatrix} 1 & 0 \\ 0 & \mu \end{bmatrix} \begin{Bmatrix} X_1'' \\ X_2'' \end{Bmatrix} + \begin{bmatrix} 2\zeta_1(1+\epsilon) & -2\zeta_1\epsilon \\ -2\zeta_1\epsilon & 2(\mu\zeta_2\gamma + \zeta_1\epsilon) \end{bmatrix} \begin{Bmatrix} X_1' \\ X_2' \end{Bmatrix} + \begin{bmatrix} 1+\kappa & -\kappa \\ -\kappa & \mu\gamma^2 + \kappa \end{bmatrix} \begin{Bmatrix} X_1 \\ X_2 \end{Bmatrix} + \begin{Bmatrix} F_{c1} - F_{c3} \\ F_{c2} \end{Bmatrix} = \begin{Bmatrix} F_0 e^{i\Omega\tau} \\ 0 \end{Bmatrix}, \quad (5.17)$$

where F_{c1} , F_{c2} and F_{c3} denote the non-dimensional forces applied by nonlinear constraint C1, C2 and C3, respectively. By the employment of HB-AFT method, the steady-state response of the masses can be determined.

The effects of the constraints on the vibration transmission between the two subsystems and the vibration energy dissipation at the interface are of interest. The force transmissibility from mass m_1 to the mass m_2 is expressed by:

$$TR_S = \frac{\max(|\Re\{F_{ts}\}|)}{F_0}, \quad (5.18)$$

where $F_{ts} = \kappa(X_1 - X_2) + 2\zeta_1\epsilon(X_1' - X_2')$ is the dimensionless transmitted force to mass m_2 .

For the current system in the steady-state motion, the non-dimensional time-averaged input power \bar{P}_{in} over one cycle of the periodic response is obtained by setting $j = 1$ in Eq. (5.8). The time-averaged transmitted power \bar{P}_{ts} to mass m_2 and the time-averaged dissipated power \bar{P}_{di} by the damper c_3 at coupling interface are

$$\bar{P}_{ts} = \frac{1}{\tau_p} \int_{\tau_0}^{\tau_0 + \tau_p} 2\mu\zeta_2\gamma (\Re\{X_2'\})^2 d\tau, \quad \bar{P}_{di} = \frac{1}{\tau_p} \int_{\tau_0}^{\tau_0 + \tau_p} 2\zeta_1\epsilon (\Re\{X_2' - X_1'\})^2 d\tau, \quad (5.19a, 5.19b)$$

respectively. By replacing X_1' and X_2' using a truncated Fourier series shown in Eq. (5.7a), Eq. (5.19) can be transformed into

$$\bar{P}_{ts} = \frac{1}{2} \Re\left\{ \left(\sum_{n=0}^N in\Omega \tilde{R}_{(2,n)} \right)^* \left(2\mu\zeta_2\gamma \sum_{n=0}^N in\Omega \tilde{R}_{(2,n)} \right) \right\} = \mu\zeta_2\gamma \left| \sum_{n=0}^N in\Omega \tilde{R}_{(2,n)} \right|^2, \quad (5.20a)$$

$$\begin{aligned} \bar{P}_{di} &= \frac{1}{2} \Re\left\{ \left[\sum_{n=0}^N in\Omega (\tilde{R}_{(2,n)} - \tilde{R}_{(1,n)}) \right]^* \left[2\zeta_1\epsilon \sum_{n=0}^N in\Omega (\tilde{R}_{(2,n)} - \tilde{R}_{(1,n)}) \right] \right\} = \\ &= \zeta_1\epsilon \left| \sum_{n=0}^N in\Omega (\tilde{R}_{(2,n)} - \tilde{R}_{(1,n)}) \right|^2, \end{aligned} \quad (5.20b)$$

respectively. The power dissipation ratio provides a relative portion of vibration energy that is dissipated within the total input energy into the system by the external force. The power dissipation ratio at the interface is

$$R_{\text{di}} = \frac{\bar{P}_{\text{di}}}{\bar{P}_{\text{in}}}. \quad (5.21)$$

By using power flow variables \bar{P}_{ts} , \bar{P}_{di} and R_{di} , the effects of the nonlinear constraints on the vibration energy transmission within the system and dissipation at the interface can be quantified and evaluated.

In the following Subsections 5.3.2, 5.3.3 and 5.3.4, the influence of three different configurations of the D-spring constraints on the dynamic response and vibration transmission characteristics of the 2DOF impact oscillators are investigated. The effects of having only constraint C1 in the impact oscillators are firstly studied. Then two other cases, with one having two constraints C1 and C2 and the other one having constraints C1 and C3 in impact oscillators are investigated. The HB-AFT method is used to obtain the response and power flow variables. The force transmissibility and power flow variables are defined by Eqs. (5.18)-(5.21). The system parameters are set as $\zeta_1 = \zeta_2 = 0.01$, $\eta = 0.1$, $\gamma = 1$, $\mu = 1$, $\kappa = 1$, $\epsilon = 1$. The HB-AFT results are presented by different types of lines and are compared with those obtained using the fourth-order RK method and denoted by different symbols. When investigating the influence of the spring stiffness ratio λ of the nonlinear constraint, three possible values are chosen with $\lambda = 0, 1$ and 2 while setting the initial angle $\theta_0 = 30^\circ$ and the excitation amplitude $F_0 = 0.035$. A linear constraint case with $\lambda = 1$ and $F_0 = 0.035$ is also added for comparison. When examining the effects of the initial angle θ_0 of the nonlinear constraint, four possible values with $\theta_0 = 20, 30, 45$ and 60 degrees are selected while setting $\lambda = 1$ and $F_0 = 0.02$. When studying the influence of the damping ratio ζ_1 of the primary system, four cases are considered with $\zeta_1 = 0.02, 0.04, 0.10$ and 0.20 while setting $\lambda = 1$, $\theta_0 = 30^\circ$ and $F_0 = 0.02$. In the meantime, to ensure the other system damping coefficients remaining the same value, the ratio of the interfacial damping ϵ is chosen as $\epsilon = 1, 0.5, 0.2$ and 0.1 in four cases, respectively. It is noted that to avoid the self-locking of the nonlinear D-spring constraint when the terminals distance Y is reduced to 0, the amplitude excitation force F_0 should be carefully controlled. For instance, the value of F_0 should be set less than 0.04 when $\lambda = 1$ and $\theta_0 = 30^\circ$.

5.3.2. Use of constraint C1 only

Here the 2DOF impact oscillators with the constraint C1 for mass m_1 is considered. Figs. 5.8, 5.9, 5.10 and 5.11 show the effects of the parameters of the nonlinear

constraint on the steady-state response, the force transmission, the time-averaged power flow and the power dissipation ratio, respectively. The dimensionless governing equation shown by Eq. (5.17) is with $F_{c2} = F_{c3} = 0$, $F_{c1} = F_c(Y(X_1)) = \lambda F_r(Y(X_1))$ where $F_r(Y(X_1))$ has been defined in Eq. (5.4) and $Y(X_1) = (Y_0 + \eta - X_1)U(X_1 - \eta)$.

In Fig. 5.8, the effects of the design parameters of the nonlinear constraint C1 on the steady-state maximum displacement $X_{1,max}$ of the primary mass m_1 and the maximum relative displacement of two masses $|X_1 - X_2|_{max}$ are investigated. In Fig. 5.8(a) and (b), the influence of the spring stiffness ratio λ of the nonlinear constraint is examined while in Fig. 5.8(c) and (d), the effects of the initial angle θ_0 of the nonlinear constraint are studied. Figure 5.8(a) and (c) shows two resonance peaks in each curve of $X_{1,max}$. A modal analysis of the un-constrained system shows that the first peak of $X_{1,max}$ corresponds to the in-phase mode, while the second is associated with the out-of-phase mode. Fig. 5.8(a) shows that the response curves of $X_{1,max}$ diverge from the boundaries of the frequency intervals $0.90 < \Omega < 1.08$ and $1.69 < \Omega < 1.78$. Fig. 5.8(a) also shows that due to the nonlinear constraint, the first peak in each curve of $X_{1,max}$ extends firstly to the right and then twists back to the left. In contrast, for the linear constraint case, the first peak of $X_{1,max}$ curve only extends to the high frequencies. The reason is that, with the increase in $X_{1,max}$ and also the deformation Δ of the nonlinear constraint, the stiffness provided by the constraint reduces from a value larger than the linear constraint stiffness to a value lower than that. As the nonlinear constraint stiffness λ increases from 1 to 2, both peaks of each curve of $X_{1,max}$ bend towards the high frequencies with a slight reduction in the first peak value but a small increase in the second peak value. Fig. 5.8(b) shows that for the case of the corresponding un-constrained system with $\lambda = 0$, there is only one peak in the curve of the relative displacement amplitude $|X_1 - X_2|_{max}$, corresponding to the out-of-phase mode of the associated linear system. However, when the linear or nonlinear constraint C1 is used, one extra peak appears in the frequency range from $\Omega \approx 0.9$ to $\Omega \approx 1.1$. By comparing the nonlinear and linear constraint cases both with $\lambda = 1$, it is found that the nonlinear constraint can lead to a lower first peak value. As λ increases from 1 to 2, both peaks of $|X_1 - X_2|_{max}$ curves become higher. This characteristic is due to the stronger leftward-pointing force applied by the constraint to the primary mass m_1 keeping it from moving more to the right. Consequently, there is a larger relative displacement. Fig. 5.8(c) shows that with the initial angle θ_0 of the nonlinear constraint reducing from 60 to 45, and then 30 and finally to 20 degrees, the first peak in each curve of $X_{1,max}$ curve bends more to the higher frequencies with a lower peak value. This is due to the lower

constraint stiffness when a larger initial angle θ_0 is used. The second peak of X_{1_max} remains nearly unchanged for the four cases considered. Fig. 5.8(d) shows that the increase of the initial angle θ_0 can significantly reduce the first peak of the relative displacement $|X_1 - X_2|_{max}$. This is because that the first peak is induced by the addition of the constraint. As the initial angle θ_0 increases, the stiffness that the constraint provides is lower and consequently there is a lower value of the first peak. In comparison, there is little change in the second peak value regardless of the variations in θ_0 .

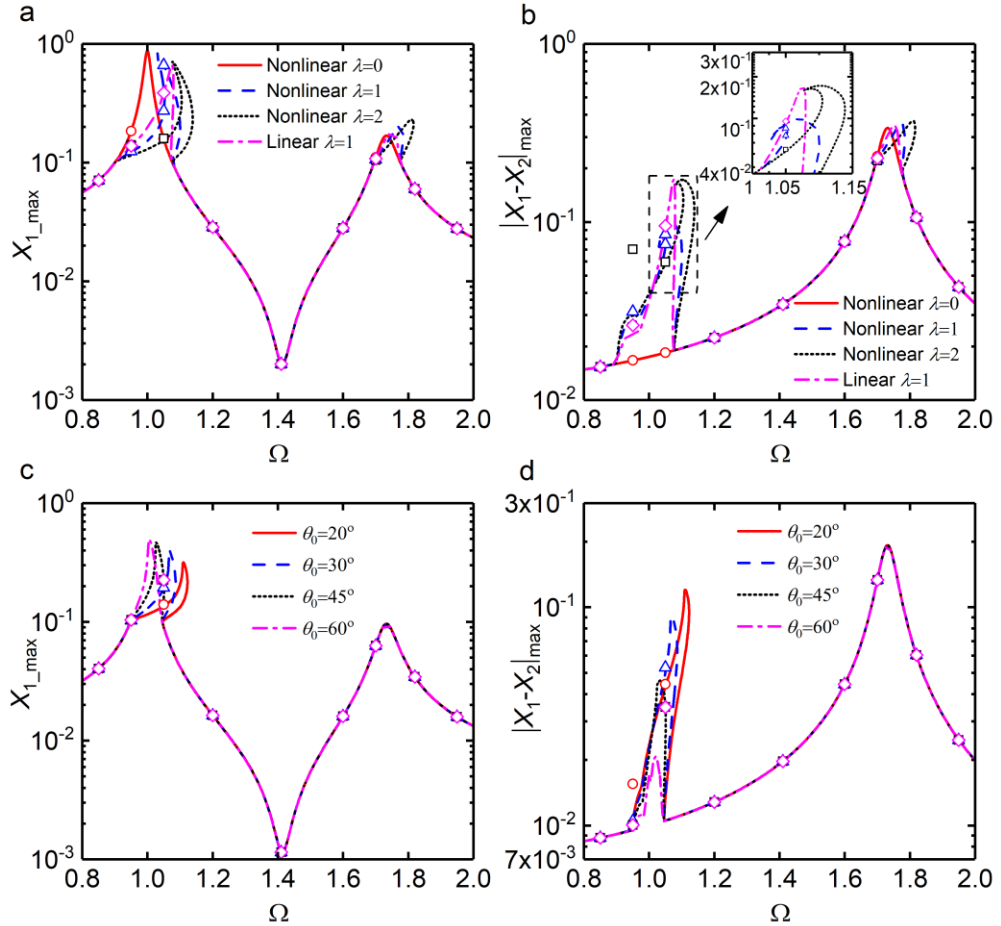


Figure 5.8. Effects of the nonlinear constraint on (a) and (c): X_{1_max} , and on (b) and (d): $|X_1 - X_2|_{max}$. In (a) and (b), the solid, dashed and dotted lines are for the nonlinear constraint with $\lambda = 0, 1$ and 2 , respectively. The dash-dot line is for linear constraint with $\lambda = 1$; in (c) and (d), the solid, dashed, dotted and dash-dotted lines are for $\theta_0 = 20, 30, 45$ and 60 degrees, respectively. Symbols: RK results.

In Fig. 5.9, the influence of the nonlinear constraint on the force transmissibility TR_S to the secondary system is studied. Fig. 5.9(a) shows that for the case of the corresponding un-constrained system with $\lambda = 0$, there exists only one peak in the curve of TR_S . In comparison, for the impact oscillator with constraint C1, two peaks are found in each curve of TR_S , corresponding to the in-phase and out-of-phase modes. In Fig. 5.9(a), by comparing linear and nonlinear constraint cases both with the same spring stiffness ratio $\lambda = 1$, it is found that the nonlinear constraint yields a much lower first

peak near $\Omega = 1.05$, but a relatively higher second peak at $\Omega \approx 1.70$. It also shows that the increase of λ for the nonlinear constraint from 1 to 2 leads to a higher first peak. The increase in the spring stiffness ratio λ also bends the second peak more to the high frequencies with a minor increase in the peak value. Fig. 5.9(b) shows that as the initial angle θ_0 of the nonlinear constraint C1 increases from 20 to 60 degrees, there is less bending of the first peak of TR_S to the right near $\Omega = 1.05$. The increase in the value of θ_0 also leads to substantial reductions in the first peak value, but the second peak remains nearly unchanged. The figure demonstrates that a lower spring stiffness ratio λ or a larger initial angle θ_0 of the nonlinear constraint is beneficial for the suppression of force transmission to mass m_2 when the excitation frequency is in the vicinity of the in-phase mode of the un-constrained system.

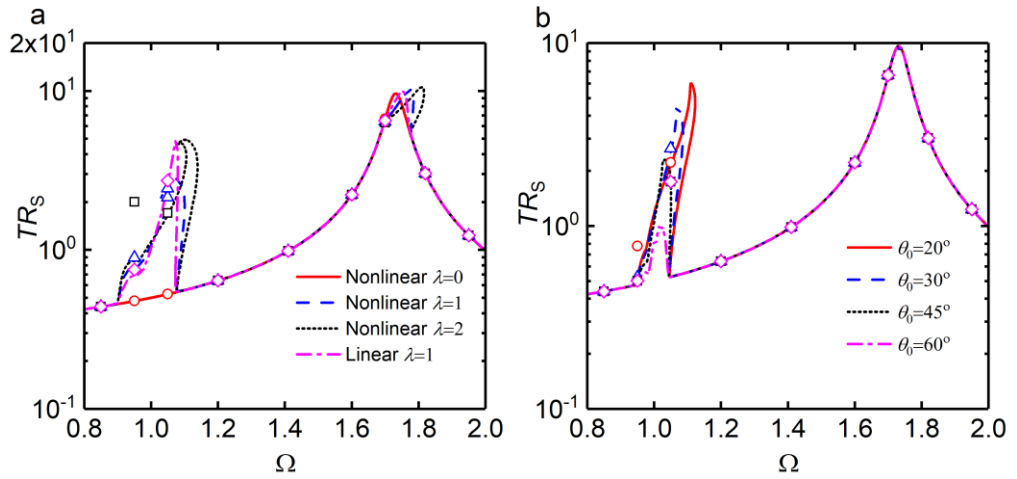


Figure 5.9. Effects of (a) the spring stiffness ratio λ and (b) the initial angle θ_0 of the nonlinear constraint on the force transmissibility TR_S . In (a), the solid, dashed and dotted lines are for nonlinear constraint with $\lambda = 0, 1$ and 2 , respectively. The dash-dot line is for linear constraint with $\lambda = 1$; in (b), the solid, dashed, dotted and dash-dotted lines are for $\theta_0 = 20, 30, 45$ and 60 degrees, respectively. Symbols: RK results.

In Fig. 5.10(a) and (b), the effects of the spring stiffness ratio λ of the nonlinear constraint C1 on the time-averaged transmitted power \bar{P}_{ts} through the interface to the secondary mass m_2 and the time-averaged dissipated power \bar{P}_{di} at the interface are examined, respectively. Fig. 5.10(a) shows that for the impact oscillator with nonlinear constraint C1, both peaks in each curve of \bar{P}_{ts} bend right towards the high frequencies as λ increases from 0 to 1, and to 2. There are slight changes in the two peak values of \bar{P}_{ts} due to the changes in λ . Fig. 5.10(b) shows that for the case of the corresponding un-constrained system with $\lambda = 0$, there is only one peak in \bar{P}_{di} corresponding to the out-of-phase mode. However, for impact oscillators with C1, one extra peak appears when Ω is near the in-phase mode of the un-constrained system. The reason is that the addition of the constraint C1 can lead to a larger amplitude of the relative displacement

$|X_1 - X_2|_{\max}$, and consequently a larger amount of time-averaged dissipated power \bar{P}_{di} at the interface. Fig. 5.10(b) also shows that the increase of the spring stiffness ratio λ of the nonlinear constraint can lead to more power dissipation at the interface from $\Omega \approx 0.86$ to $\Omega \approx 1.1$, as the rightwards motion of the primary mass is more restrained. By the comparison of linear and nonlinear constraint cases both with $\lambda = 1$, Fig. 5.10(a) and (b) shows that the nonlinear constraint can yield a higher peak value of \bar{P}_{ts} and a smaller peak value of \bar{P}_{di} for the power dissipated at the interface.

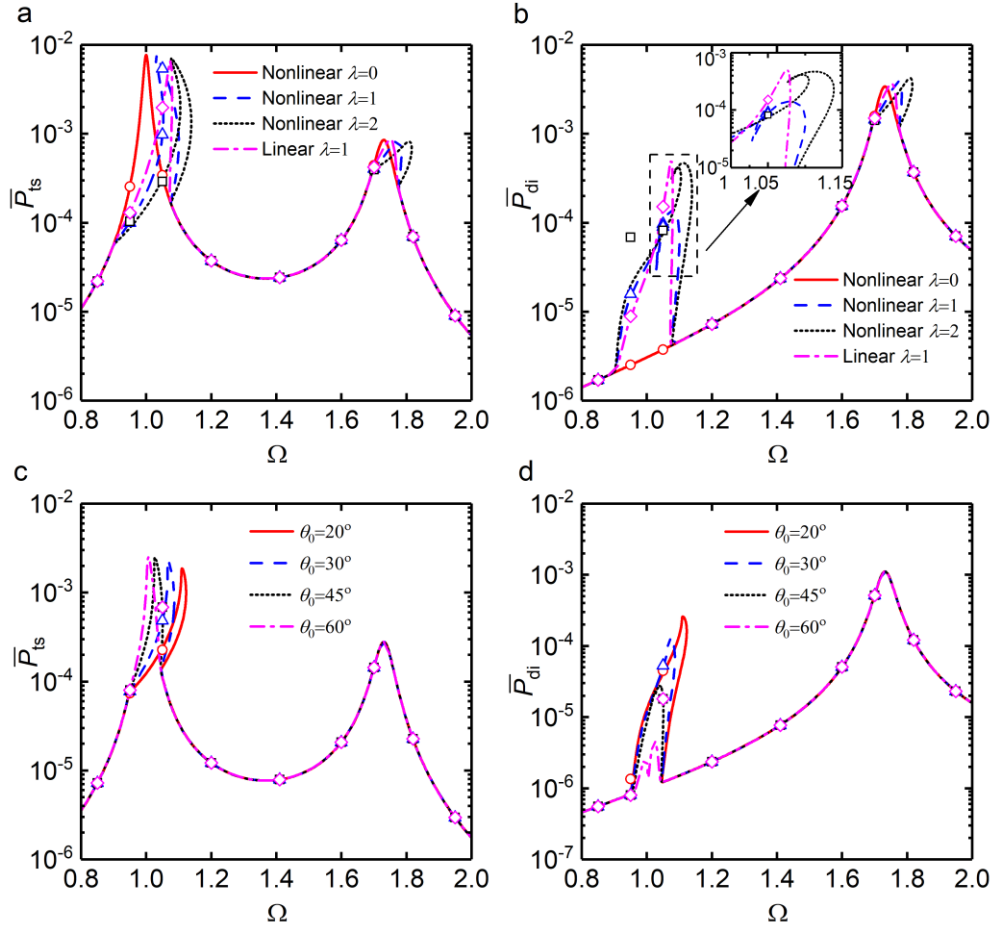


Figure 5.10. Effects of nonlinear constraint on (a) and (c): \bar{P}_{ts} , and on (b) and (d): \bar{P}_{di} . In (a) and (b), the solid, dashed and dotted lines are for nonlinear constraint with $\lambda = 0, 1$ and 2 , respectively. The dash-dot line is for linear constraint with $\lambda = 1$; in (c) and (d), the solid, dashed, dotted and dash-dotted lines are for $\theta_0 = 20, 30, 45$ and 60 degrees, respectively. Symbols: RK results.

Fig. 5.10(c) and (d) shows the influence of the initial angle θ_0 of the nonlinear constraint C1 on \bar{P}_{ts} and \bar{P}_{di} , respectively. Fig. 5.10(c) shows that the reduction of the initial angle θ_0 from 60 to 20 degrees can bend the first peak in each curve of transmitted power \bar{P}_{ts} more to the high frequencies with its first peak value reduced, suggesting lower vibration energy transmission to mass m_2 . Fig. 5.10(d) shows that as the initial angle θ_0 increases, the first peak in each curve of power dissipation \bar{P}_{di} at the interface becomes lower but little difference can be found on the second peak. A

comparison of Fig. 5.10(c) with Fig. 5.9(b) shows that a reduction in the initial angle θ_0 from 60 to 20 degrees can lead to a larger peak value of the force transmissibility TR_S but a lower amount of the peak time-averaged transmitted power to the secondary mass at specific excitation frequencies. This shows the importance of selecting appropriate indices to evaluate the level of vibration transmission in nonlinear systems.

In Fig. 5.11, the effects of the design parameters of the nonlinear constraint on the power dissipation ratio R_{di} at the interface are investigated. Fig. 5.11(a) shows that for the un-constrained case with $\lambda = 0$, there is a local minimum point in the curve of R_{di} near its resonance, i.e., the in-phase mode. This is reasonable as the relative motion between the two masses is small so there is very small power dissipation. Fig. 5.11(a) also shows that the introduction of a linear or nonlinear constraint C1 leads to significant increases in the value of R_{di} near the original local minimum. By comparing the linear constraint case with the corresponding nonlinear constraint case ($\lambda=1$), it is shown that the former yields a higher R_{di} from approximately $\Omega = 1.05$ to $\Omega = 1.07$. However, the latter provides a higher portion of power dissipated at the interface between $\Omega \approx 0.9$ and $\Omega \approx 1.05$. An increase in the spring stiffness ratio λ of the nonlinear constraint from 1 to 2 can lead to a larger value of R_{di} in the frequency band from $\Omega \approx 0.9$ to $\Omega \approx 1.1$. Fig. 5.11(b) shows that as the initial angle θ_0 of the nonlinear constraint increases from 20 to 60 degrees, the value of the power dissipation ratio R_{di} reduces substantially in the frequency range of $\Omega \approx 0.95$ and $\Omega \approx 1.1$. This is due to a smaller constraint stiffness when increasing the initial angle of the nonlinear constraint C1. The primary mass is less constrained, resulting in a lower value of relative displacement $|X_1 - X_2|_{\max}$ and less amount of power dissipated at the interface.

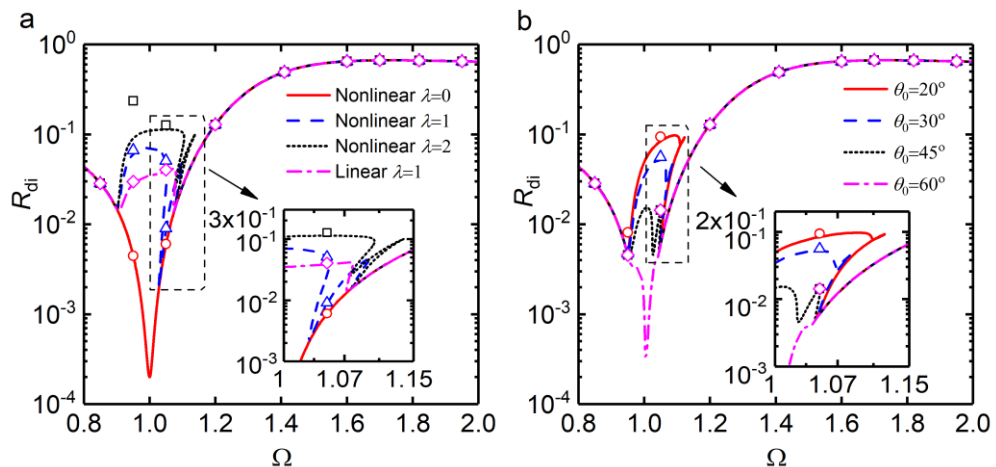


Figure 5.11. Effects of (a) the spring stiffness ratio λ and (b) the initial angle θ_0 of the nonlinear constraint on the power dissipation ratio R_{di} . In (a), the solid, dashed and dotted lines are for nonlinear constraint with $\lambda = 0, 1$ and 2 , respectively. The dash-dot line is for linear constraint with $\lambda = 1$; in (b), the solid, dashed, dotted and dash-dotted lines are for $\theta_0 = 20, 30, 45$ and 60 degrees, respectively. Symbols: RK results.

It should be pointed out that for the nonlinear constraint cases with $\lambda = 2$, $\theta_0 = 30^\circ$, $F_0 = 0.035$ and $\lambda = 1$, $\theta_0 = 20^\circ$, $F_0 = 0.02$ in Subsections 5.3.2, 5.3.3 and 5.3.4, there may be relatively large differences between HB-AFT approximation results and RK results of $|X_1 - X_2|_{\max}$, TR_S , \bar{P}_{di} and R_{di} near $\Omega \approx 0.95$. This phenomenon is further explored considering the system with $\lambda = 2$, $\theta_0 = 30^\circ$, $\zeta_1 = \zeta_2 = 0.01$, $\eta = 0.1$, $\gamma = 1$, $\mu = 1$, $\kappa = 1$, $\epsilon = 1$ and $F_0 = 0.035$. Fig. 5.12(a) shows the bifurcation diagram, 5.12(b) and 5.12(c) is for the system excited at $\Omega = 0.94$ while 5.12(d)-12(f) is for that excited at $\Omega = 0.96$. The responses shown here are all obtained by using the RK method. Fig. 5.12(a) shows the bifurcation diagram by using a low-to-high frequency sweep. The response time histories y_s of the primary mass are sampled using a sampling period of $T = 2\pi/\Omega$ and a starting time of $500T$. Fig. 5.12(b) and (e) shows the Poincare sections while Fig. 5.12(c) and (f) shows the frequency spectra of the steady-state responses at $\Omega = 0.94$ and $\Omega = 0.96$, respectively, obtained based on Fourier transformation of the time histories of the responses. Fig. 5.12(d) shows the phase diagram at $\Omega = 0.96$. Fig. 5.12(a) shows the occurrence of bifurcations. Moreover, non-periodic responses can be found in the frequency range from $\Omega \approx 0.94$ to $\Omega \approx 0.97$. Fig. 5.12(b) and (e) shows that the system excited at $\Omega = 0.94$ and $\Omega = 0.96$ can exhibit quasi-periodic responses. The quasi-periodic response of the system excited at $\Omega = 0.96$ is further confirmed by Fig. 5.12(d) and 5.12(f). Fig. 5.12 also shows that large super-harmonic and noticeable sub-harmonic components appear in the responses.

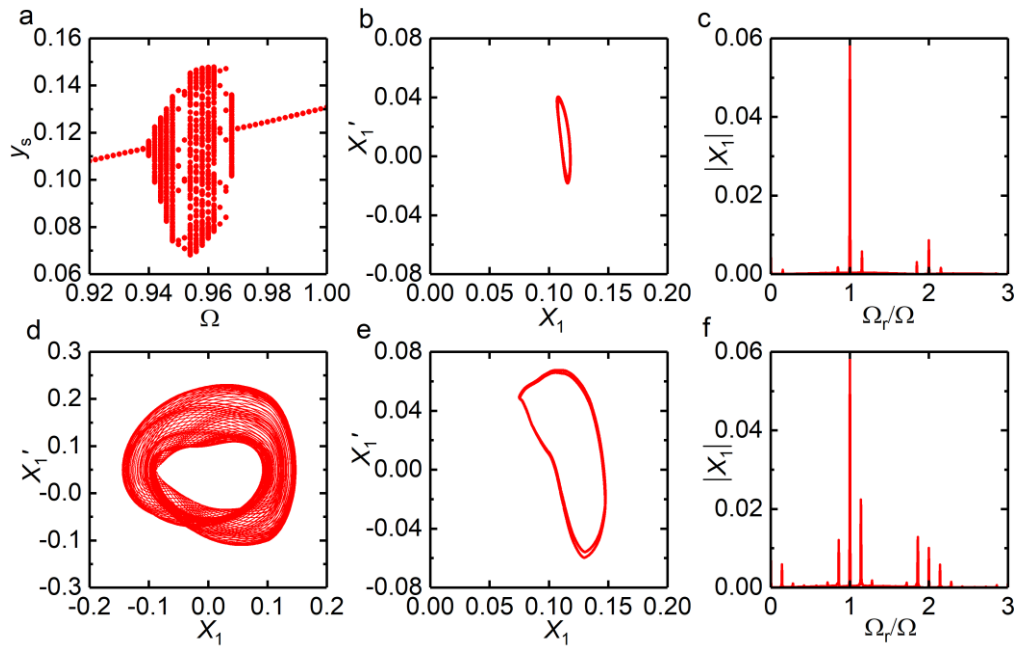


Figure 5.12. Steady-state response of the mass m_1 in the 2DOF impact oscillator with nonlinear constraint C1, excited at $\Omega = 0.94$ for (b)-(c), and at $\Omega = 0.96$ for (d)-(f). (a): bifurcation diagram; (b) and (e): Poincare sections; (c) and (f): frequency spectra of response displacement X_1' ; (d): phase diagram.

5.3.3. Two constraints case with C1 and C2

Here two constraints C1 and C2 are considered to exist in the impact oscillator shown by Fig. 5.7. In Figs. 5.13, 5.14, 5.15 and 5.16, the effects of the design parameters of the nonlinear constraints on the steady-state response, the force transmission, the time-averaged power flow and the power dissipation ratio are examined, respectively. The dimensionless governing equation of the system is obtained by converting Eq. (5.17) with $F_{c3} = 0$, $F_{c1} = F_c(Y(X_1))$ where $F_c(Y(X_1))$ has been defined in Subsection 5.3.2, $F_{c2} = F_c(Y(X_2)) = \lambda F_r(Y(X_2))$ where $F_r(Y(X_2))$ was defined in Eq. (5.4) and $Y(X_2) = (Y_0 + \eta - X_2)U(X_2 - \eta)$.

In Fig. 5.13, the influence of the parameters of the nonlinear constraints C1 and C2 on the maximum steady-state displacement response X_{1_max} of the primary mass m_1 and the amplitude of the relative displacement $|X_1 - X_2|_{max}$ between the masses is investigated. In Fig. 5.13(a) and (b), the effects of the spring stiffness ratio λ of the nonlinear constraints are studied, while in Fig. 5.13(c) and (d), the influence of the initial angle θ_0 of the nonlinear constraints is examined. Fig. 5.13(a) shows that with C1 and C2, both peaks in each curve of X_{1_max} extend firstly to the right and then the first peak twists back to the left near $\Omega = 1.1$. With the increase of the spring stiffness ratio λ of the nonlinear constraints from 1 to 2, there is more bending of both peaks to the right. Fig. 5.13(b) shows that compared with the system without constraints, the use of the nonlinear constraints leads to larger values of $|X_1 - X_2|_{max}$ when $0.9 < \Omega < 1.05$ but lower values when $1.05 < \Omega < 1.25$. Based on the time-domain analysis by RK method, it is found that when the system is excited in the frequency range from $\Omega \approx 0.9$ to $\Omega \approx 1.05$, the rightwards motion of mass m_1 is constrained by C1, while the secondary mass m_2 has not moved beyond the gap width η to engage with the constraint C2. Therefore, there is a large relative displacement between the masses. When $1.05 < \Omega < 1.25$, the mass m_2 becomes in contact with constraint C2 and both masses are constrained from moving to the right, resulting in a small relative displacement. Fig. 5.13(b) also shows that when the spring stiffness ratio λ of the nonlinear constraint increases from 1 to 2, there is a significant increase in the first peak value of $|X_1 - X_2|_{max}$ near $\Omega = 0.95$. In contrast, the value of $|X_1 - X_2|_{max}$ is reduced in the range from $\Omega \approx 1.15$ to $\Omega \approx 1.25$ because the responses of both masses are further restrained by a higher constraint stiffness. Fig. 5.13(c) shows that as the initial angle θ_0 increases from 20 to 30, to 45 and to 60 degrees, the first peak of X_{1_max} bends less to the right but there is no noticeable change in the second peak. With the nonlinear constraints C1 and C2, the variation of θ_0 has little effect on the peak values of X_{1_max} compared to the constraint

C1 only case in Fig. 5.8(c). Fig. 5.13(d) shows that at a given frequency from $\Omega \approx 0.95$ to $\Omega \approx 1.05$, as the initial angle θ_0 increases from 20° to 60° , there are reductions in the values of $|X_1 - X_2|_{\max}$. This is due to the corresponding reduction in the stiffness provided by the nonlinear constraint C1, leading to a smaller limitation effect on the primary mass m_1 from moving to the right. In the meantime, there is no contact between the secondary mass m_2 and the constraint C2. Consequently, it can generate smaller relative displacement in this frequency band. In comparison, the relative displacement $|X_1 - X_2|_{\max}$ may increase with θ_0 when $1.15 < \Omega < 1.25$.

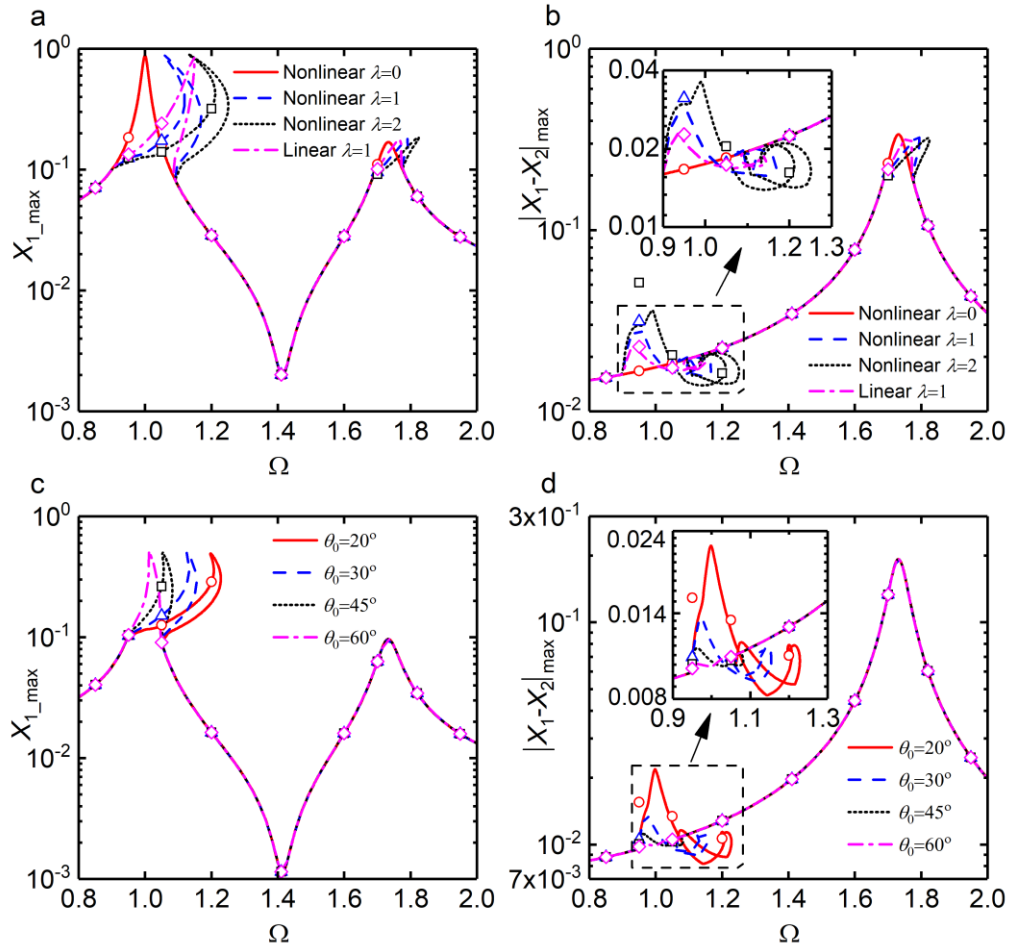


Figure 5.13. Effects of nonlinear constraints C1 and C2 on (a) and (c): $X_{1,\max}$, and on (b) and (d): $|X_1 - X_2|_{\max}$. In (a) and (b), the solid, dashed and dotted lines are for nonlinear constraints with $\lambda = 0, 1$ and 2 , respectively. The dash-dot line is for linear constraints with $\lambda = 1$; in (c) and (d), the solid, dashed, dotted and dash-dotted lines are for $\theta_0 = 20, 30, 45$ and 60 degrees, respectively. Symbols: RK results.

In Fig. 5.14(a) and (b), the influence of the nonlinear constraint on the force transmissibility TR_S to the secondary mass m_2 is examined. Fig. 5.14(a) shows that there are two peaks in each curve of TR_S when the linear or nonlinear constraints C1 and C2 are used. Compared with the results associated with the case of the corresponding un-constrained system, the use of linear or nonlinear constraints leads to larger values of TR_S when $0.9 < \Omega < 1.05$ but lower values when $1.05 < \Omega < 1.25$.

By comparing the linear and the nonlinear constraints cases both with the spring stiffness ratio $\lambda = 1$, it shows that the nonlinear constraint can result in a higher first peak of TR_S near $\Omega = 0.95$ while the second peaks near $\Omega = 1.75$ in two cases are of similar height. An increase in the spring stiffness ratio λ of the nonlinear constraint from 1 to 2 can lead to a higher first peak of TR_S near $\Omega = 0.95$ but a lower value in the frequency range from $\Omega \approx 1.15$ to $\Omega \approx 1.25$. Fig. 5.14(b) shows that as the initial angle θ_0 increases from 20 to 30, then to 45 and finally to 60 degrees, there is a noticeable reduction in the first peak of TR_S . The reason is that when increasing θ_0 , the constraint C1 has a weaker effect on the primary mass m_1 while the secondary mass m_2 has not been in contact with the constraint C2. Consequently, there is a smaller relative displacement between masses and therefore lower force transmissibility. However, in the frequency range between $\Omega \approx 1.15$ and $\Omega \approx 1.25$, the secondary mass m_2 becomes in contact with the constraint C2 and TR_S can increase with θ_0 due to the less motion restraint effect by the constraints on both masses from moving to the right.

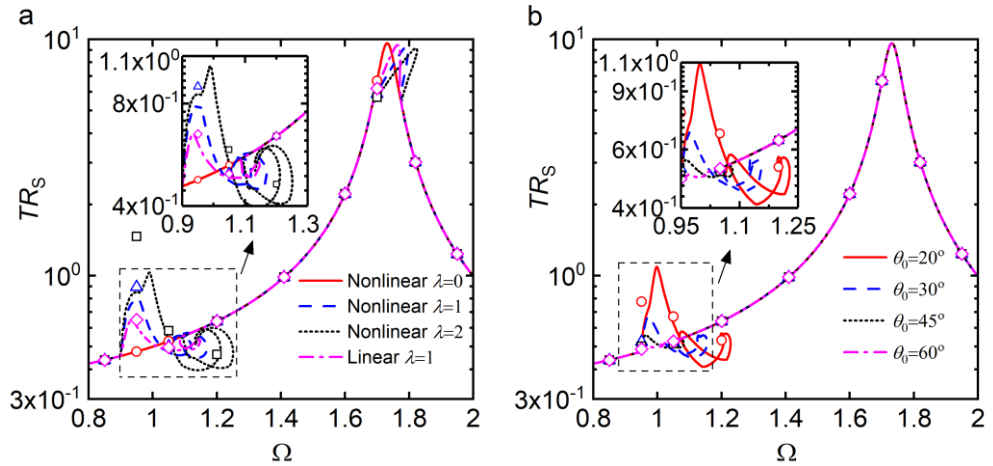


Figure 5.14. Effects of (a) the spring stiffness ratio λ and (b) the initial angle θ_0 of the nonlinear constraints C1 and C2 on the force transmissibility TR_S . In (a), the solid, dashed and dotted lines are for nonlinear constraints with $\lambda = 0, 1$ and 2 , respectively. The dash-dot line is for linear constraints with $\lambda = 1$; in (b), the solid, dashed, dotted and dash-dotted lines are for $\theta_0 = 20, 30, 45$ and 60 degrees, respectively. Symbols: RK results.

In Fig. 5.15(a) and (b), the influence of the spring stiffness ratio λ of the constraints C1 and C2 on the time-averaged transmitted power \bar{P}_{ts} to the secondary mass m_2 via the interface and the time-averaged dissipated power \bar{P}_{di} at the interface is studied, respectively. Fig. 5.15(a) shows that when the linear or nonlinear constraints C1 and C2 are introduced, both peaks of the \bar{P}_{ts} curves extend toward the high frequencies but there are only minor changes on the peak values, compared to those of the corresponding unconstrained system. The first peaks of \bar{P}_{ts} in nonlinear constraints cases twist to the left near $\Omega = 1.1$. As the spring stiffness ratio λ of nonlinear constraints increases from 1 to 2, both peaks of \bar{P}_{ts} curve bend more to the high-frequency range while the peak values

for both peaks change little. Fig. 5.15(b) shows that compared with the un-constrained system, the use of the linear or nonlinear constraints C1 and C2 can lead to a larger power dissipation \bar{P}_{di} at the interface when $0.9 < \Omega < 1.05$. However, there can be a smaller value of \bar{P}_{di} in the frequency range from $\Omega \approx 1.05$ to $\Omega \approx 1.25$. The reason is that the rightwards motion of masses m_1 and m_2 are limited by the constraints when $1.05 < \Omega < 1.25$, leading to a lower relative displacement. Therefore, there is less time-averaged power dissipated at the interface. Moreover, an increase of the spring stiffness ratio λ of the nonlinear constraints from 1 to 2 can result in a higher \bar{P}_{di} when $0.9 < \Omega < 1.05$ while providing a smaller \bar{P}_{di} from $\Omega \approx 1.15$ to $\Omega \approx 1.25$. By the comparison of the linear and the nonlinear constraints cases both with $\lambda = 1$, it shows that the nonlinear constraints can yield a larger first peak of \bar{P}_{di} but there is little difference on the peak values of \bar{P}_{ts} between the linear and the nonlinear constraints cases. In Fig. 5.15(c) and (d), the influence of the initial angle θ_0 of the nonlinear constraints on \bar{P}_{ts} and \bar{P}_{di} is studied. Fig. 5.15(c) shows that as the initial angle θ_0 increases from 20 to 30, to 45 and to 60 degrees, the first peak of \bar{P}_{ts} curve bends less to the right. The variations of the angle θ_0 of the constraints C1 and C2 have very small effects on the first peak value of \bar{P}_{ts} near $\Omega = 1$, compared to the constraint C1 only case shown in Fig. 5.10(c). Fig. 5.15(d) shows that the growth of θ_0 from 20 to 60 degrees can significantly reduce the amount of dissipated power \bar{P}_{di} at the interface when $0.95 < \Omega < 1.05$ due to the reduced relative displacement between masses. In contrast, the increase can result in a higher amount of power dissipation \bar{P}_{di} from $\Omega \approx 1.15$ to $\Omega \approx 1.25$. The figure indicates the possibility of tailoring the energy transmission in the impact oscillator system by the adjustment of nonlinear constraint design parameters, to achieve desired dynamic characteristics.

Figure 5.16 presents the effects of the parameters of the nonlinear constraints C1 and C2 on the power dissipation ratio R_{di} . Fig. 5.16(a) shows that when $0.95 < \Omega < 1.10$, the use of constraints C1 and C2 can lead to a larger dissipation ratio R_{di} compared to the case of the corresponding un-constrained system. In comparison, the addition of C1 and C2 results in a smaller R_{di} compared to un-constrained system from $\Omega \approx 1.1$ to $\Omega \approx 1.2$. When comparing the nonlinear and the linear constraints case both with $\lambda = 1$, it is found that the nonlinear constraint can yield a larger value of R_{di} in the frequency range between $\Omega \approx 0.95$ to $\Omega \approx 1.1$. Moreover, an increase of the spring stiffness ratio λ of the nonlinear constraints from 1 to 2 can lead to a larger value of R_{di} in the range of $0.95 < \Omega < 1.20$. Fig. 5.16(b) shows that as the initial angle θ_0 of the nonlinear constraints increases from 20 to 30, to 45 and finally to 60 degrees, the portion of the time-averaged input power dissipated at the interface is reduced substantially

from $\Omega \approx 0.95$ to $\Omega \approx 1.05$. This is due to the reduced restraint effect on the primary mass m_1 by constraint C1. Meanwhile, with the increase of θ_0 , the frequency of the local minimum point is shifting to the left with a lower local minimum value of R_{di} .

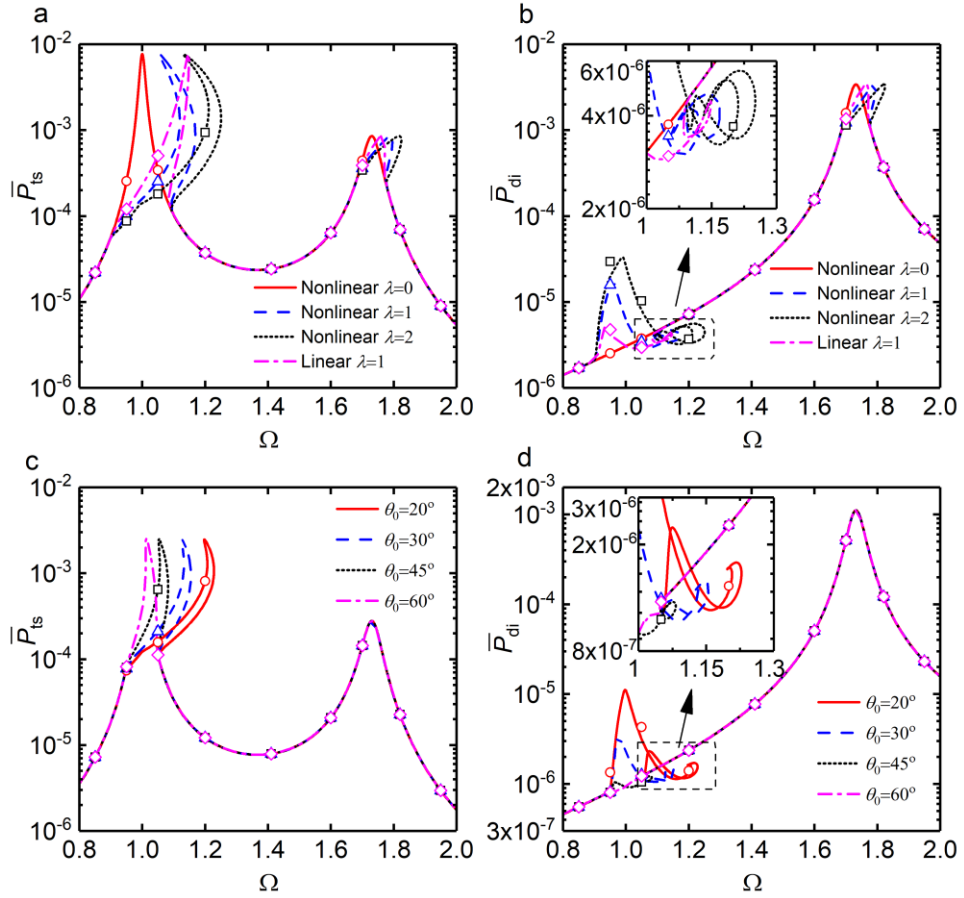


Figure 5.15. Effects of nonlinear constraints C1 and C2 on (a) and (c): \bar{P}_{ts} , and on (b) and (d): \bar{P}_{di} . In (a) and (b), the solid, dashed and dotted lines are for nonlinear constraints with $\lambda = 0, 1$ and 2 , respectively. The dash-dot line is for linear constraints with $\lambda = 1$; in (c) and (d), the solid, dashed, dotted and dash-dotted lines are for $\theta_0 = 20, 30, 45$ and 60 degrees, respectively. Symbols: RK results.

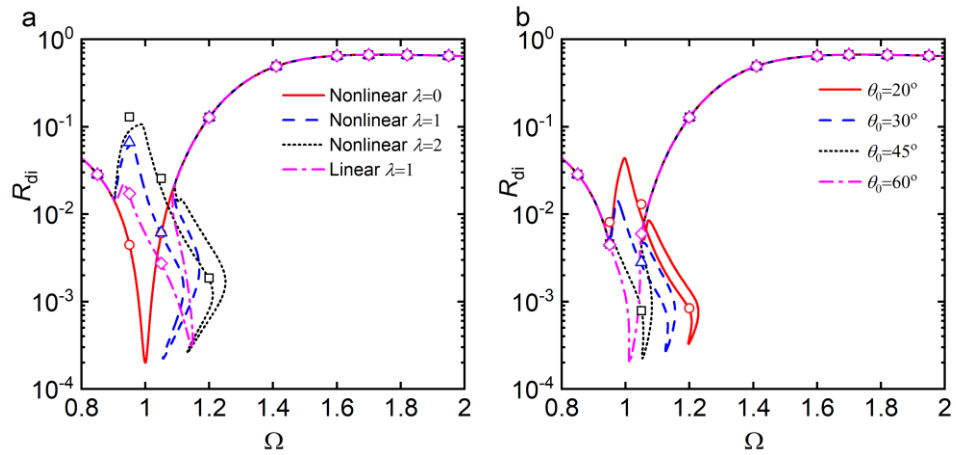


Figure 5.16. Effects of (a) the spring stiffness ratio λ and (b) the initial angle θ_0 of the nonlinear constraints C1 and C2 on the power dissipation ratio R_{di} . In (a), the solid, dashed, and dotted lines are for nonlinear constraints with $\lambda = 0, 1$ and 2 , respectively. The dash-dot line is for linear constraints with $\lambda = 1$; in (b), the solid, dashed, dotted and dash-dotted lines are for $\theta_0 = 20, 30, 45$ and 60 degrees, respectively. Symbols: RK results.

5.3.4. Two-sided constraints case with C1 and C3

Here two constraints C1 and C3 are considered to exist in the impact oscillator system shown by Fig. 5.7. In Figs. 5.17, 5.18, 5.19 and 5.20, the influence of the parameters of the nonlinear constraints on the steady-state response, the force transmission, the time-averaged power flow and the power dissipation ratio is investigated, respectively. In Figs. 5.21 and 5.22, the influence of the damping ratio of the primary system is studied. The dimensionless governing equation of the system is still obtained by converting Eq. (5.17) with $F_{c2} = 0$, $F_{c1} = F_c(Y(X_1))$ where $F_c(Y(X_1))$ has been defined in Subsection 5.3.2, $F_{c3} = F_c(Y(-X_1)) = \lambda F_r(Y(-X_1))$ where $F_r(Y(-X_1))$ was defined in Eq. (5.4) and $Y(-X_1) = (Y_0 + \eta + X_1)U(-X_1 - \eta)$.

In Fig. 5.17, the effects of the design parameters of the nonlinear constraints C1 and C3 on the steady-state maximum displacement X_{1_max} of the primary mass m_1 and the maximum relative displacement of two masses $|X_1 - X_2|_{max}$ are examined. In Fig. 5.17(a) and (b), the influence of the spring stiffness ratio λ of the constraint is studied while in Fig. 5.17(c) and (d), the effects of its initial angle θ_0 are investigated. Fig. 5.17(a) shows that with the use of C1 and C3, both peaks of the X_{1_max} curves extend to the high frequencies. When comparing the linear and the nonlinear constraints case both with $\lambda = 1$, the nonlinear constraints can firstly bend both peaks of X_{1_max} more to the right and then twist the first peak near $\Omega = 1.1$ back to the left. Both peaks of X_{1_max} in the nonlinear constraints case are higher than those in the linear constraints case. As the λ of nonlinear constraints C1 and C3 changing from 1 to 2, both peaks of X_{1_max} bend further to the right with the first peak value substantially reduced but the second peak value increased. By comparing to the constraint C1 only case in Fig. 5.8(a), Fig. 5.17(a) shows that the combined use of C1 and C3 can provide better suppression of the vibration of the primary mass m_1 near the first peak frequency. Fig. 5.17(b) shows that when the constraints C1 and C3 are used, there is a local minimum point in the curve of $|X_1 - X_2|_{max}$ at $\Omega \approx 1.0$ and an extra peak near $\Omega = 1.1$ compared to the case of the corresponding un-constrained system with $\lambda = 0$. The reason is that when the system is excited near $\Omega = 1.0$, the motion of the mass m_1 is largely restrained by C1 and C3. The response amplitudes for both masses become relatively small, leading to a small maximum value of the relative displacement between masses. When the excitation frequency is $\Omega \approx 1.1$, the response amplitude of the mass m_2 becomes larger than that of the mass m_1 and hence results in a peak of $|X_1 - X_2|_{max}$. With the increasing spring stiffness ratio λ of the nonlinear constraints from 1 to 2, both peaks of

$|X_1 - X_2|_{\max}$ show a slight increase with higher peak frequencies. Fig. 5.17(c) shows that as the initial angle θ_0 of the nonlinear constraints increases from 20 to 30, to 45 and to 60 degrees, the first peak of $X_{1_{\max}}$ bends less to the right and the peak value becomes larger. This is due to the reduction of the nonlinear constraints' stiffness with the increasing θ_0 and hence there is less restriction on the leftwards or rightwards motion of the mass m_1 . Fig. 5.17(d) shows that an increase of the angle θ_0 from 20 to 60 degrees can lead to a significant reduction in the first peak of $|X_1 - X_2|_{\max}$ at $\Omega \approx 1.1$ with a slightly lower corresponding frequency. The reason is that with the increasing θ_0 , there is a weaker motion-limitation effect on the mass m_1 , and therefore a smaller relative displacement of masses is obtained.

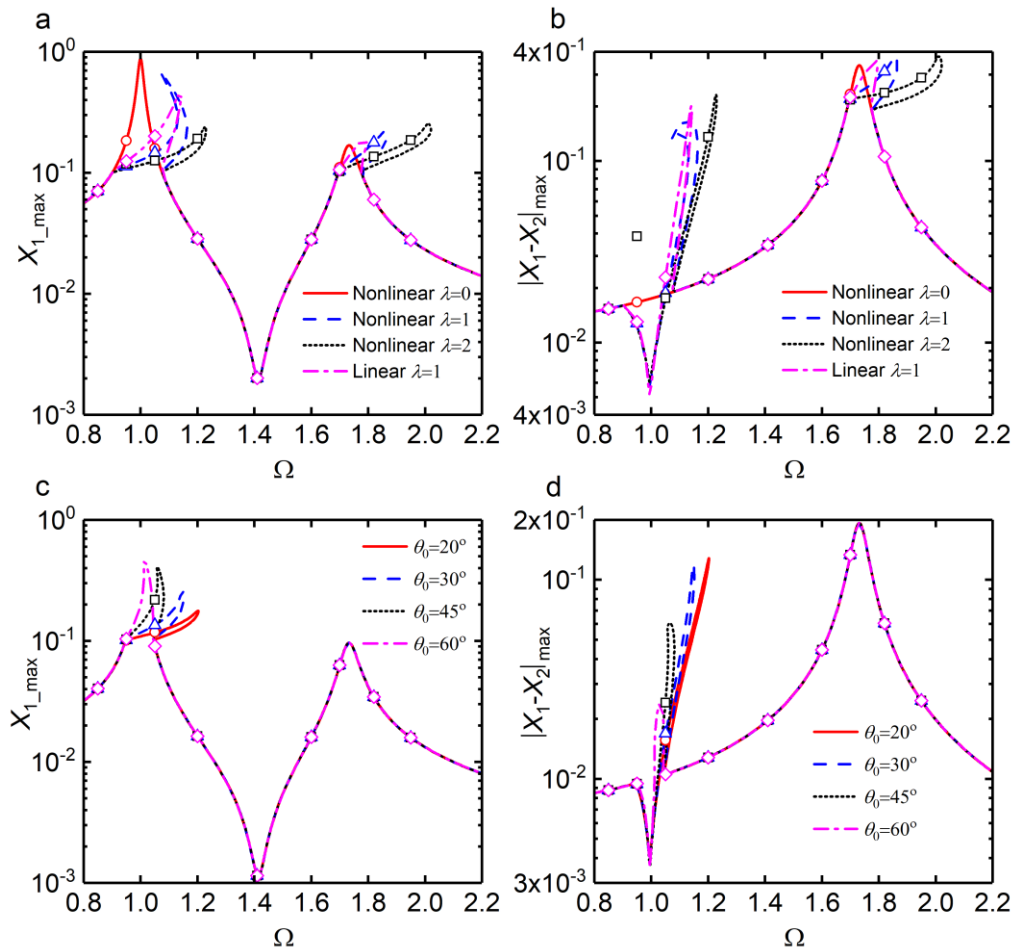


Figure 5.17. Effects of nonlinear constraints C1 and C3 on (a) and (c): $X_{1_{\max}}$, and on (b) and (d): $|X_1 - X_2|_{\max}$. In (a) and (b), the solid, dashed, and dotted lines are for nonlinear constraints with $\lambda = 0, 1$ and 2 , respectively. The dash-dot line is for linear constraints with $\lambda = 1$; in (c) and (d), the solid, dashed, dotted and dash-dotted lines are for $\theta_0 = 20, 30, 45$ and 60 degrees, respectively. Symbols: RK results.

In Fig. 5.18(a) and (b), the influence of the nonlinear constraints C1 and C3 on the force transmissibility TR_S to the secondary mass m_2 is studied. Fig. 5.18(a) shows that with the use of linear or nonlinear constraints C1 and C3, a local minimum point near

$\Omega = 1$ and an extra peak near $\Omega = 1.1$ appear in the curve of TR_S compared to the case of the corresponding un-constrained system. When comparing the linear and the nonlinear constraints case both with $\lambda = 1$, it is found that the nonlinear constraints can lead to a lower first peak of TR_S at $\Omega \approx 1.1$. As the spring stiffness ratio λ of nonlinear constraints C1 and C3 increases from 1 to 2, both peaks bend to the right with slightly larger peak values. Fig. 5.18(b) shows that when the initial angle θ_0 of the nonlinear constraints increases from 20 to 30, to 45 and to 60 degrees, the first peak of TR_S and its corresponding frequency are both reduced. This is due to the reducing stiffness of constraints C1 and C3 when increasing θ_0 , which can lead to a lower relative displacement between masses and hence result in a smaller force transmissibility to the secondary system. In comparison, the second peak in TR_S curve found near $\Omega \approx 1.75$ remains nearly the same regardless of the variations of θ_0 . When comparing to the results of constraint C1 only case in Fig. 5.9, it is found that with the use of constraints C1 and C3, much lower force transmissibility to the secondary system can be achieved near the in-phase mode of the corresponding linear system.

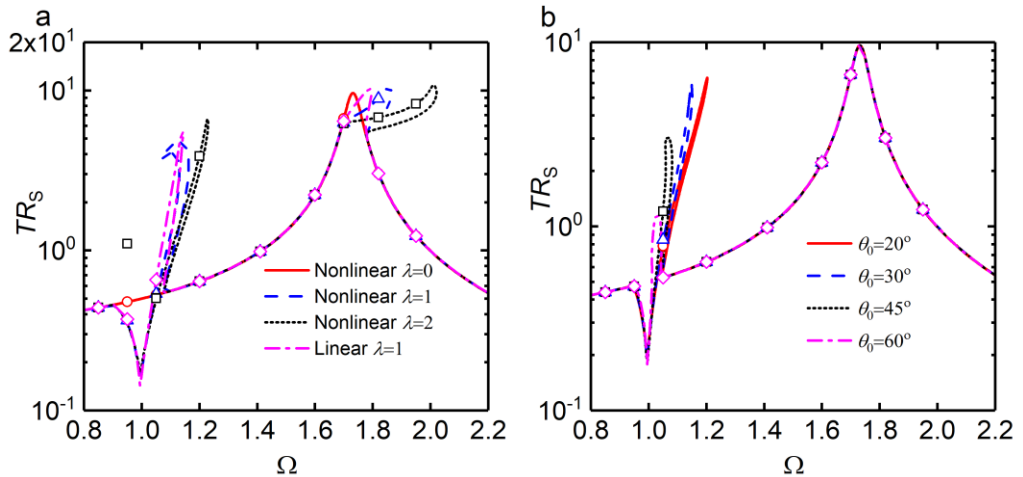


Figure 5.18. Effects of (a) the spring stiffness ratio λ and (b) the initial angle θ_0 of the nonlinear constraints C1 and C3 on the force transmissibility TR_S . In (a), the solid, dashed, and dotted lines are for nonlinear constraints with $\lambda = 0, 1$ and 2 , respectively. The dash-dot line is for linear constraints with $\lambda = 1$; in (b), the solid, dashed, dotted and dash-dotted lines are for $\theta_0 = 20, 30, 45$ and 60 degrees, respectively. Symbols: RK results.

In Fig. 5.19(a) and (b), the effects of the stiffness ratio λ of the constraints C1 and C3 on the time-averaged transmitted power \bar{P}_{ts} and dissipated power \bar{P}_{di} at the interface are investigated, respectively. Fig. 5.19(a) shows that compared to the case of the corresponding un-constrained system, the addition of C1 and C3 can bend both two peaks in the curve of \bar{P}_{ts} to the right with lower peak values. By comparing the linear and the nonlinear constraints cases both with $\lambda = 1$, the latter case can result in a slightly larger amount of power transmission to the secondary mass m_2 near the first peak at $\Omega \approx 1.1$. As the stiffness ratio λ of the nonlinear constraint increases from 1 to 2, there

is more bending of both peaks of \bar{P}_{ts} to the right with reduced peaks values. Fig. 5.19(b) shows that when constraints C1 and C3 are used, there exists one extra peak in the curve of \bar{P}_{di} near $\Omega = 1.1$ and one local minimum point at $\Omega \approx 1.0$, compared to the corresponding case of the un-constrained system. By a comparison of the linear and the nonlinear constraints cases both with $\lambda = 1$, it shows that linear constraints can lead to a smaller local minimum value of \bar{P}_{di} near $\Omega = 1.0$, while the nonlinear constraints result in a slightly lower first peak of \bar{P}_{di} near $\Omega = 1.1$. As the stiffness ratio λ of the nonlinear constraints changes from 1 to 2, both peaks of \bar{P}_{di} increase with higher peak frequencies and the local minimum value of \bar{P}_{di} becomes slightly larger. Fig. 5.19(c) shows that as the initial angle θ_0 of the nonlinear constraints increases from 20 to 30, to 45 and to 60 degrees, there is less rightwards bending of the first peak of the time-averaged transmitted power \bar{P}_{ts} but the peak value becomes larger. Fig. 5.19(d) shows an increase in the initial angle θ_0 from 20° to 60° results in a lower peak of \bar{P}_{di} near $\Omega \approx 1.1$. This is due to the fact that when increasing θ_0 , the nonlinear constraint provides smaller stiffness, leading to a smaller relative displacement between masses and hence less amount of time-averaged power dissipation at the interface. Moreover, as θ_0 increases, there is a smaller value of the local minimum in \bar{P}_{di} found at $\Omega \approx 1.0$.

In Fig. 5.20(a) and (b), the influence of the design parameters of the nonlinear constraints C1 and C3 on the power dissipation ratio R_{di} at the interface is studied. Fig. 5.20(a) and (b) shows that there is a local minimum point in each curve of R_{di} near the in-phase mode of the un-constrained system. Fig. 5.20(a) shows that compared with the corresponding un-constrained system, the use of constraints C1 and C3 can increase the local minimum value of R_{di} near the in-phase mode of the corresponding linear system. When comparing the linear and the nonlinear constraints cases both with $\lambda = 1$, it is found that the nonlinear constraints can lead to a larger R_{di} when $0.95 < \Omega < 1.10$. As the spring stiffness ratio λ of the nonlinear constraints increases from 1 to 2, the value of R_{di} increases slightly in the frequency range between $\Omega \approx 0.95$ and $\Omega \approx 1.20$. Fig. 5.20(b) shows that as the initial angle θ_0 increases from 20 to 30, to 45 and to 60 degrees, the value of the power dissipation ratio R_{di} decreases when the excitation frequency is from $\Omega \approx 0.95$ to $\Omega \approx 1.10$. Comparing the power dissipation ratio results among three configurations of the constraints in Figs. 5.11, 5.16 and 5.20, it shows that the combined use of constraints C1 and C3 is able to yield the lowest portion of input power dissipated at the interface when the excitation frequency is near the in-phase mode of the un-constrained system.

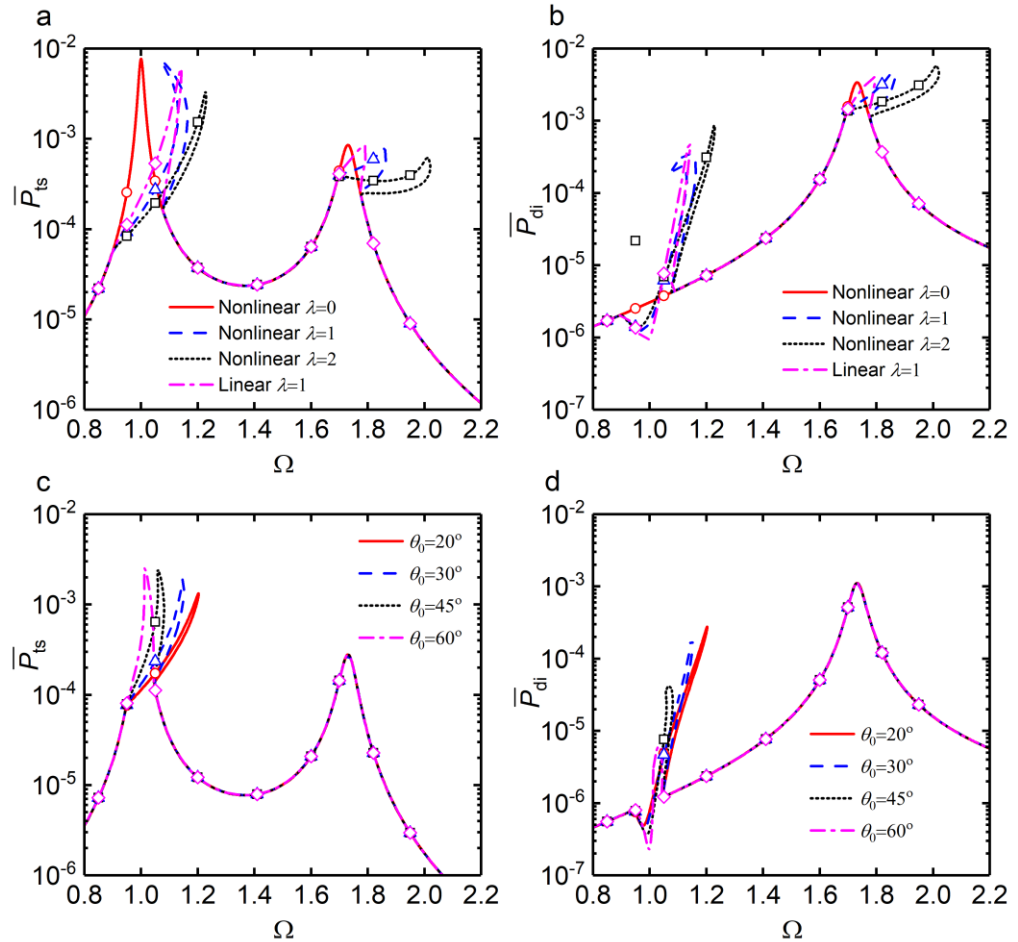


Figure 5.19. Effects of nonlinear constraints C1 and C3 on (a) and (c): \bar{P}_{ts} , and on (b) and (d): \bar{P}_{di} . In (a) and (b), the solid, dashed and dotted lines are for nonlinear constraints with $\lambda = 0, 1$ and 2 , respectively. The dash-dot line is for linear constraints with $\lambda = 1$; in (c) and (d), the solid, dashed, dotted and dash-dotted lines are for $\theta_0 = 20, 30, 45$ and 60 degrees, respectively. Symbols: RK results.

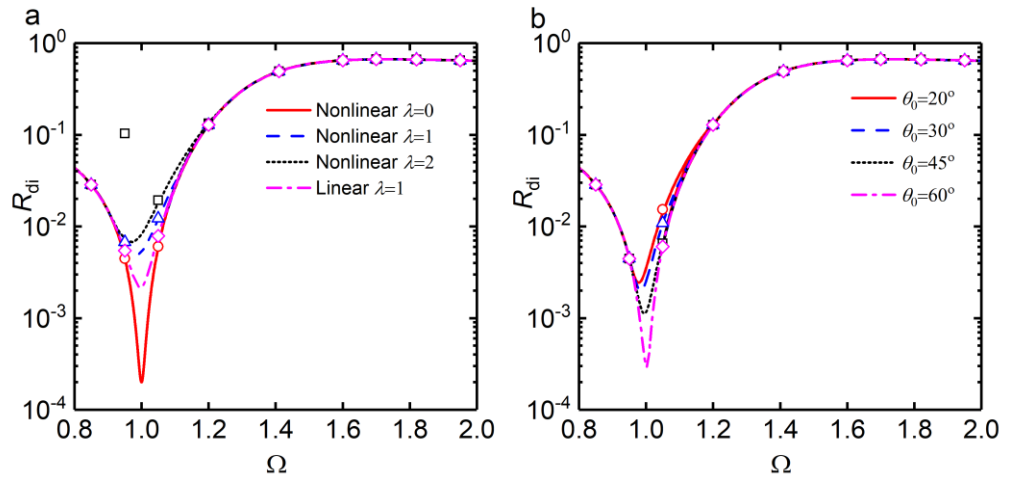


Figure 5.20. Effects of (a) the spring stiffness ratio λ and (b) the initial angle θ_0 of the nonlinear constraints C1 and C3 on the power dissipation ratio R_{di} . In (a), the solid, dashed and dotted lines are for nonlinear constraints with $\lambda = 0, 1$ and 2 , respectively. The dash-dot line is for linear constraints with $\lambda = 1$; in (b), the solid, dashed, dotted and dash-dotted lines are for $\theta_0 = 20, 30, 45$ and 60 degrees, respectively. Symbols: RK results.

In Fig. 5.21, the effects of the damping ratio ζ_1 of the primary system on the steady-state maximum displacement X_{1_max} of the primary mass m_1 and the maximum relative displacement of two masses $|X_1 - X_2|_{max}$ are investigated. Two nonlinear D-spring constraints of C1 and C3 are considered with $\lambda = 1$ and $\theta_0 = 30^\circ$. The damping coefficient at the interface and the secondary system remains unchanged. Fig. 5.21(a) shows that when increasing the damping ratio ζ_1 of the primary system from 0.02 to 0.04, to 0.10 and to 0.20, the heights of both two peaks in the maximum displacement X_{1_max} curve of the primary mass become lower. Both two peaks show less bending to the right and there is also less extension to the low-frequency range in the first peak. The reason is that a larger value of damping ratio ζ_1 can provide a stronger suppression effect on the response amplitude of the mass m_1 and hence result in less deformation of the nonlinear constraints during the contact. Therefore, the nonlinear effects caused by the geometrically nonlinear constraints are weaker at a small deflection, as shown by Fig. 5.2. It is also found that the second peak of X_{1_max} near $\Omega = 1.7$ is no longer bending to the right at a large damping ratio, which is due to that the maximum displacement of the mass has not exceeded the gap width between the mass and the constraints in the out-of-phase mode. Fig. 5.21(b) shows that with the increase of ζ_1 , the absolute value of the anti-peak in the curve of the maximum relative displacement $|X_1 - X_2|_{max}$ is increased while the peaks values at $\Omega \approx 1.1$ and $\Omega \approx 1.7$ are reduced. The reason is that an increase in the damping ratio in the primary system can substantially suppress the motion of the primary system. The deformation of the nonlinear constraint is reduced and there is less influence by the nonlinear D-spring constraints on the relative motion of masses.

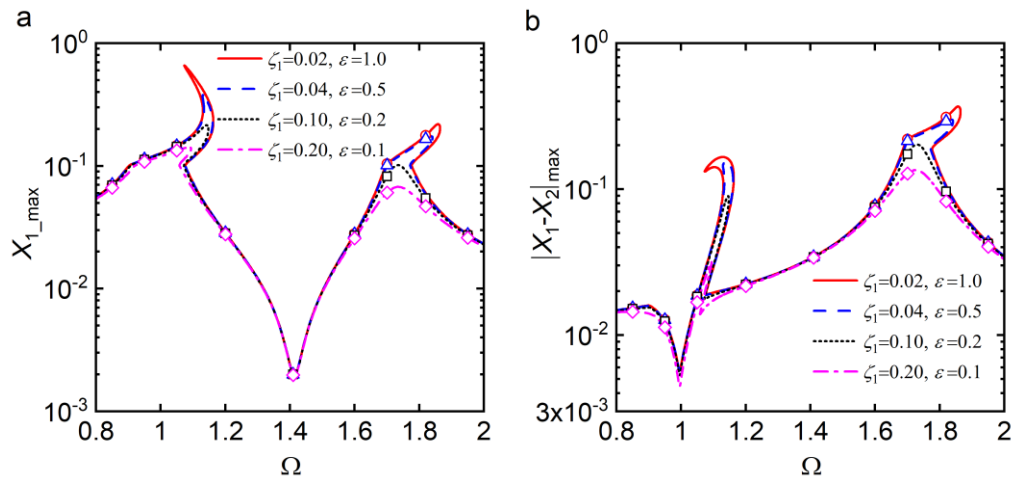


Figure 5.21. Effects of the damping ratio ζ_1 of the primary system on (a): X_{1_max} and on (b): $|X_1 - X_2|_{max}$. The solid, dashed, dotted and dash-dot lines are for $\zeta_1 = 0.02$ and $\epsilon = 1.0$, $\zeta_1 = 0.04$ and $\epsilon = 0.5$, $\zeta_1 = 0.10$ and $\epsilon = 0.2$, and $\zeta_1 = 0.20$ and $\epsilon = 0.1$, respectively. Symbols: RK results.

In Fig. 5.22, the effects of the damping ratio ζ_1 of the primary system on the force transmissibility TR_S to the secondary mass m_2 , the time-averaged transmitted power \bar{P}_{ts} , the time-averaged dissipated power \bar{P}_{di} at the interface and the power dissipation ratio R_{di} at the interface are examined, respectively. Fig. 5.22(a) shows that as the damping ratio ζ_1 increases from 0.02 to 0.04, to 0.10 and to 0.20, the values for both peaks of force transmissibility TR_S are decreased and a lower local minimum of TR_S near the in-phase mode frequency of the corresponding linear system (i.e. $\lambda = 0$) is observed. This phenomenon is corresponding to the relative displacement $|X_1 - X_2|_{\max}$. Fig. 5.22(b) shows that the increase of ζ_1 can substantially reduce the peak time-averaged power transmission \bar{P}_{ts} to the secondary system. From Fig. 5.22(a) and (b), it can be summarized that an increase of the damping in the primary system can further reduce the vibration transmission to the secondary system.

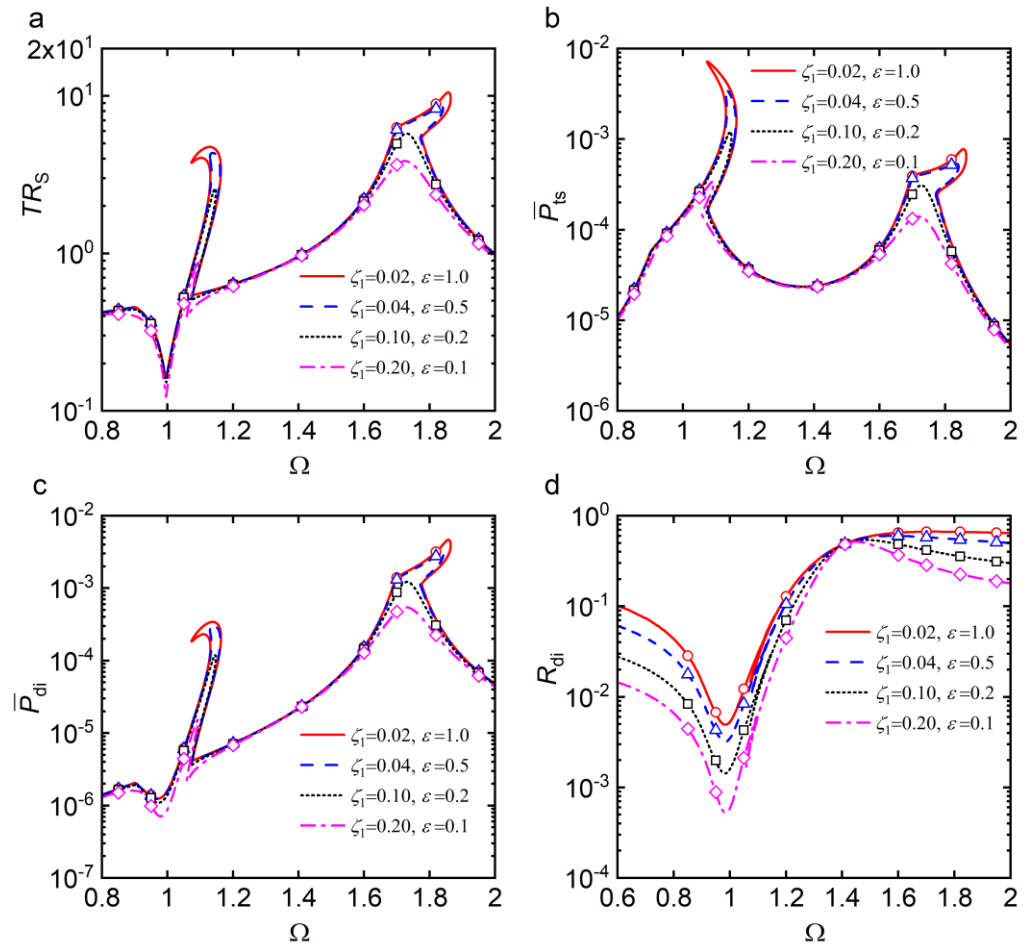


Figure 5.22. Effects of the damping ratio ζ_1 of the primary system on (a): the force transmissibility TR_S , (b): the power transmission \bar{P}_{ts} , (c): the power dissipation \bar{P}_{di} and (d): the power dissipation ratio R_{di} . The solid, dashed, dotted and dash-dot lines are for $\zeta_1 = 0.02$ and $\epsilon = 1.0$, $\zeta_1 = 0.04$ and $\epsilon = 0.5$, $\zeta_1 = 0.10$ and $\epsilon = 0.2$, and $\zeta_1 = 0.20$ and $\epsilon = 0.1$, respectively. Symbols: RK results.

Fig. 5.22(c) shows that when the value of the damping ratio ζ_1 is larger, there is a much smaller amount of power dissipated at the interface when the excitation frequency is near the in-phase mode or the out-of-phase mode of the corresponding linear system. This is due to the less relative motion between the masses. Fig. 5.22(d) shows that with the increasing value of damping ratio ζ_1 , the portion of the input power that is dissipated at the interface becomes lower in a broad frequency range. It is noticed that the power dissipation ratio R_{di} shows a significant decrease at the in-phase mode frequency and low/high frequencies.

5.4. Summary

This chapter investigated the dynamics and vibration transmission behaviour of impact oscillators with a single nonlinear constraint or multiple nonlinear constraints created by DSLM. The force transmissibility and time-averaged power flow were used to quantify the vibration transmission in SDOF and 2DOF impact oscillators with nonlinear constraints. The influence of design parameters and locations of the nonlinear constraints on the response and vibration transmission within the systems were explored. This investigation yields the following main findings:

- (1) For the SDOF impact oscillator with a single constraint, the nonlinear constraint can suppress the response amplitude but increase the force transmission at high frequencies.
- (2) For the 2DOF impact oscillators with a single nonlinear constraint at the interface, the use of the nonlinear constraint can significantly increase the power dissipation at the interface and slightly reduce the peak of the time-averaged transmitted power to the secondary system.
- (3) When the stiffness of the nonlinear constraint is high, 2DOF impact oscillators can exhibit bifurcations and show strong super-harmonic and sub-harmonic response.
- (4) For the 2DOF impact oscillators with two nonlinear constraints, a local minimum point of the force transmissibility can be found. The peak power transmission can be substantially reduced when the two identical nonlinear constraints are set symmetrically on the two sides of the primary DOF.
- (5) The nonlinear D-spring constraint shows the limitation of self-locking under large deformation, which should be considered in the design of such systems.

Chapter 6

Vibration energy flow and force transmissibility of nonlinear isolators with nonlinear spring based on DSLM

To control the undesired vibration transmitted from the vibrating source to the receiving structure, active or passive vibration isolators are commonly inserted into the vibration transmission path (Rivin, 2004). Compared with active isolators, passive isolators usually have simpler structures and also the advantages of not relying on the external power supply (Carrella et al., 2007). For a conventional SDOF linear passive isolator, the frequency range of effective isolation starts from $\sqrt{2}$ times of the natural frequency (Zheng et al., 2018), which limits the applications of such isolator from isolating broadband excitations such as shocks or random ground motion containing ultra-low frequency components (Feng et al., 2019). To improve isolation performance, nonlinear elements can be introduced into the passive isolation system. For instance, the negative stiffness mechanism (NSM) can be connected in parallel with conventional linear springs and damper to widen the effective vibration isolation frequency band (Liu and Yu, 2018). Some researchers also used nonlinear elements created by linkage mechanisms to create geometric nonlinearity in the isolator to enhance vibration isolation performance (Sun et al., 2014; Jing et al., 2019a). However, in the evaluation of the vibration isolation performance of the nonlinear isolators with linkage mechanism, force or displacement transmissibilities were usually used as the performance indices in the past research (Jing et al., 2019a), there is limited research on the vibration power flow behaviour in such nonlinear vibration isolation system. New insights gained by investigating these systems from the perspective of vibration energy input, dissipation, and transmission can assist the better design of the vibration isolator. Moreover, many previous investigations on nonlinear vibration isolation systems are based on the assumption that the isolation system is installed on a rigid and massless foundation (Lu et al., 2013; Yang and Harne et al., 2014). This assumption may not always be valid in some real-life engineering applications, such as aircrafts and ships, where the mounting foundation of the isolator is flexible and can have a large influence on the performance

of the isolator. Only limited research has been reported to consider the situation when the base of the isolated objects is flexible (Xiong et al., 2005b; Yang et al., 2016). In this chapter, a nonlinear vibration isolator with nonlinear elements created by a diamond-shaped linkage mechanism (DSLML) embedded with linear springs is proposed. Both force excitation and base-motion excitation cases are considered. The vibration isolation performance of this nonlinear isolator in SDOF systems and a 2DOF system with a flexible base is assessed by the force / displacement transmissibility and power flow variables. These performance indicators are obtained by using HB-AFT method with numerical continuations and numerical integration. The influence of the design parameters of the proposed nonlinear element on vibration isolation performance is examined systematically.

6.1. Nonlinear stiffness mechanism

Figure 6.1 shows a schematic diagram of a proposed nonlinear spring element based on the geometrical nonlinearity of a linkage mechanism. For clarity, the nonlinear element is named as D-spring hereafter. The D-spring consists a DSLM and an embedded linear spring with un-stretched length of l_s and stiffness coefficient of k_s . The DSLM is formed by four rigid rods AC, AD, BC and BD, which are hinged end to end at points A, B, C and D with a fixed length of l_b for each rod. Terminals C and D are linked by the horizontal linear spring.

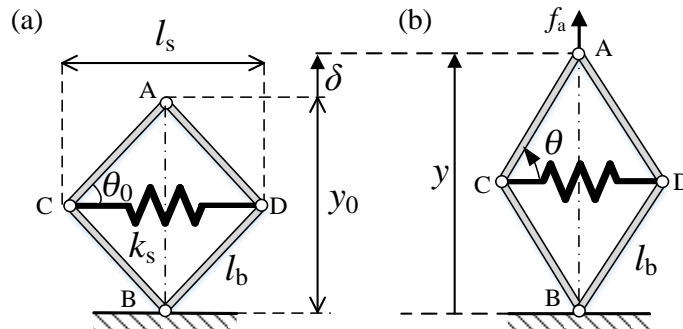


Figure 6.1. Schematic of the nonlinear D-spring (a) with the horizontal spring un-stretched, and (b) subjected to a force.

Fig. 6.1(a) shows that when the horizontal linear spring is at its unstretched length, the angle between AC and CD is represented as θ_0 ($0^\circ \leq \theta_0 < 90^\circ$) such that $\cos \theta_0 = l_s / 2l_b$. The initial distance of terminal A measured from terminal B is denoted by y_0 and correspondingly we have $y_0 = 2l_b \sin \theta_0$. Figure 6.1 shows the situation that terminal A is free to move in the vertical direction while terminal B is fixed on the ground. However, in other application, both terminals A and B of the D-spring can move. The mass and the damping of the D-spring is assumed to be neglected throughout this

chapter. Figure 6.1(b) shows the deformed shape of the D-spring when its terminal A is subjected to a force f_a pointing upwards in the vertical direction. After reaching force equilibrium, the terminal A moves up by a distance of δ and the new vertical distance between terminals A and B becomes $y = y_0 + \delta$. The angle between the rod AC and line CD is denoted by θ , and from Fig. 6.1(b) we have $\sin \theta = y/(2l_b)$. The value of θ is limited to the range of $0 < \theta < 90^\circ$ for practical reasons. From Fig. 6.1(a) to 6.1(b), the horizontal spring will be compressed by $2l_b \cos \theta - l_s$ and its restoring force f_s can be expressed by

$$f_s = k_s(2l_b \cos \theta - l_s). \quad (6.1)$$

The restoring force f_r of the nonlinear D-spring is the counteracting force of f_a such that $f_r = f_a$, pointing to the downwards. From force equilibrium and geometric condition of the DSLM, we have

$$f_r(y) = f_a = -f_s \cdot \frac{\sin \theta}{\cos \theta} = -k_s(2l_b \cos \theta - l_s) \frac{\sin \theta}{\cos \theta} = k_s y \left(\frac{l_s}{\sqrt{4l_b^2 - y^2}} - 1 \right). \quad (6.2)$$

Non-dimensional parameters and variables are introduced as $Y_0 = y_0/(2l_b)$, $Y = y/(2l_b)$ and $\Delta = \delta/(2l_b) = Y - Y_0$, where Y_0 and Y are the non-dimensional initial distance and deformed distance between two ends of the D-spring, respectively, while Δ is the dimensionless deflection of the D-spring. From geometric conditions, we have

$$\sin \theta_0 = Y_0, \quad \cos \theta_0 = l_s/(2l_b) = \sqrt{1 - (\sin \theta_0)^2} = \sqrt{1 - Y_0^2}, \quad (6.3a, 6.3b)$$

$$\sin \theta = Y, \quad \cos \theta = \sqrt{1 - Y^2}, \quad (6.3c, 6.3d)$$

By using Eq. (6.3) to replace the variable θ by Y in Eq. (6.2), the dimensionless restoring force of the D-spring can be obtained as

$$F_r(Y) = F_a = \frac{f_a}{2l_b k_s} = Y \left(\sqrt{\frac{1 - Y_0^2}{1 - Y^2}} - 1 \right), \quad \text{where } 0 < Y < 1. \quad (6.4)$$

The non-dimensional stiffness of the D-spring can be yielded by differentiating F_r with respect to the dimensionless deflection Δ :

$$K_r(\Delta) = \frac{dF_r(\Delta)}{d(\Delta)} = \frac{dF_r(Y)}{d(Y)} = \sqrt{\frac{1 - Y_0^2}{1 - Y^2}} + Y^2 \sqrt{1 - Y_0^2} [1 - Y^2]^{-3/2} - 1. \quad (6.5)$$

Equations (6.4) and (6.5) demonstrate the dependence of the restoring force and stiffness of the D-spring on the initial distance Y_0 and the deformed distance Y between

terminals A and B. It is clear that the dynamic characteristics of the D-spring can be adjusted by changing the initial distance Y_0 .

Figure 6.2(a) and (b) shows the variation of the dimensionless restoring force F_r and the stiffness K_r of the D-spring against the dimensionless terminals distance Y , respectively. Four different values of initial terminals distance Y_0 of the D-spring in the unstretched-state are selected with Y_0 changing from 0.3 to 0.5, to 0.7 and to 0.8. Fig. 6.2(a) shows that for a prescribed value of Y_0 , there exists a non-monotonic relationship between F_r and Y . When the D-spring is compressed with the distance Y decreasing from Y_0 to 0, the value of the restoring force F_r firstly decreases from 0 to a negative peak value and then increases to 0. However, when the D-spring is stretched as the distance Y increases from Y_0 to 1, the value of F_r grows up exponentially from 0 to a positive value. Fig. 6.2(a) also shows that at the same value of Y , a larger value of Y_0 leads to a larger absolute negative peak value of F_r . Fig. 6.2(b) shows that for a given value of Y_0 , with the reduction of distance Y from 1 to 0, K_r decreases from a positive value to zero, and then to be negative. It is found that an increasing value of Y_0 from 0.3 to 0.8 can lead to a stronger negative stiffness effect when Y is close to 0 but a smaller positive stiffness effect when Y is close to 1. Fig. 6.2(b) shows that the nonlinear D-spring can be pre-deformed to a dimensionless distance of $Y = Y_1$ ($0 < Y_1 < Y_0$) to obtain a negative stiffness.

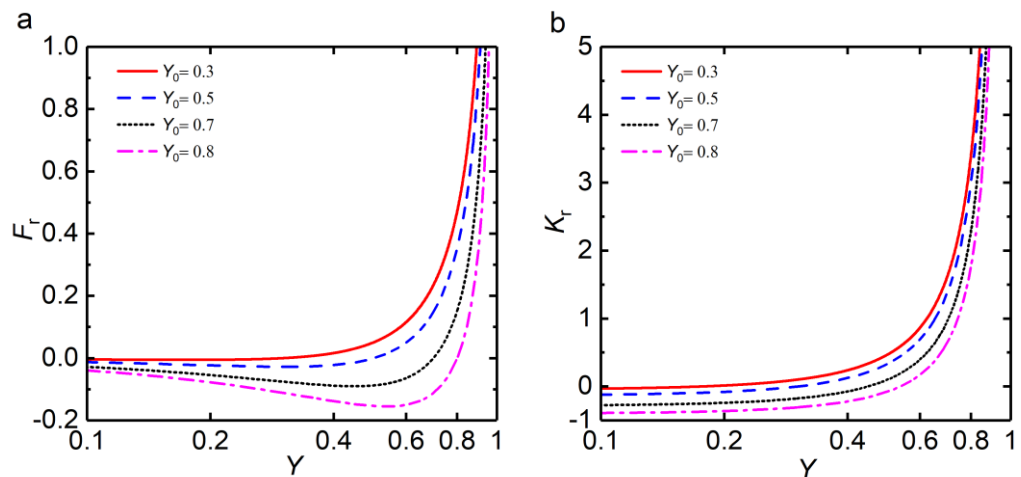


Figure 6.2. Variations of the dimensionless (a) restoring force F_r and (b) stiffness K_r of the nonlinear D-spring against the dimensionless terminals distance Y . The solid, dashed, dotted and dash-dotted lines are for $Y_0 = 0.3, 0.5, 0.7$ and 0.8 , respectively.

6.2. SDOF nonlinear isolator for force excitations

6.2.1. Mathematical model

Figure 6.3 shows the use of the D-spring for vibration isolation of a forced-excited machine. The nonlinear isolator comprises a linear spring with stiffness coefficient k_1 ,

a viscous damper with damping coefficient c_1 , and a nonlinear D-spring as shown in Fig. 6.1(a). The mass m_1 represents a machine subjected to a harmonic force excitation with amplitude of f_0 and frequency of ω . The equilibrium position of the mass, is set as a reference with $x_1 = 0$, at which the distance y between terminals A and B of the D-spring is set as y_1 ($0 < y_1 < y_0$).

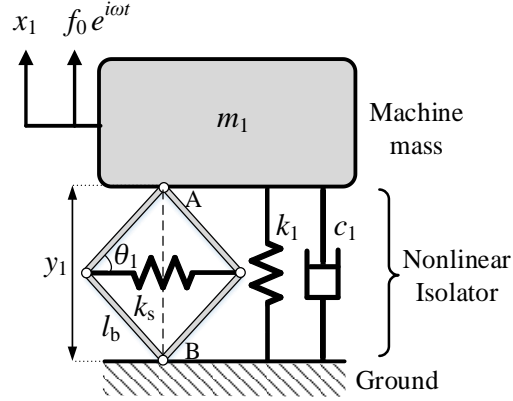


Figure 6.3. Schematic of a nonlinear isolator with the D-spring for isolation of force excitation.

The dimensional equation of motion of the mass is

$$m_1 \ddot{x}_1 + c_1 \dot{x}_1 + k_1 x_1 + f_D(x_1, y_1) = f_0 e^{i\omega t}, \quad (6.6)$$

where $f_D(x_1, y_1) = f_r(y(x_1, y_1)) - f_r(y_1)$ is the dynamic force applied by the nonlinear D-spring to the mass with $y(x_1, y_1) = y_1 + x_1$, and $f_r(y)$ has been expressed by Eq. (6.2). To facilitate later parametric studies, the following parameters are introduced

$$\omega_1 = \sqrt{\frac{k_1}{m_1}}, \quad \zeta_1 = \frac{c_1}{2m_1\omega_1}, \quad X_1 = \frac{x_1}{2l_b}, \quad Y_1 = \frac{y_1}{2l_b}, \quad \lambda = \frac{k_s}{k_1}, \quad F_0 = \frac{f_0}{2l_b k_1}, \quad \Omega = \frac{\omega}{\omega_1}, \quad \tau = \omega_1 t,$$

where ω_1 and ζ_1 are the undamped natural frequency and the damping ratio of the original system without the D-spring, respectively; X_1 represents the non-dimensional displacement of the machine m_1 ; Y_1 denotes the dimensionless distance between terminals A and B of the D-spring when $X_1 = 0$; λ is the stiffness ratio of the nonlinear D-spring; F_0 , Ω and τ are the non-dimensional force excitation amplitude, the excitation frequency and the dimensionless time, respectively. Eq. (6.6) can be transformed into the following non-dimensional form:

$$X_1'' + 2\zeta_1 X_1' + X_1 + F_D(X_1, Y_1) = F_0 e^{i\Omega\tau}, \quad (6.7)$$

where $F_D(X_1, Y_1) = \lambda (F_r(Y(X_1, Y_1)) - F_r(Y_1))$ is the dimensionless dynamic force applied by the nonlinear D-spring to the mass, $Y(X_1, Y_1) = Y_1 + X_1$ and the function of $F_r(Y)$ has been defined by Eq. (6.4).

For small-amplitude vibrations with the distance of two D-spring terminals Y in the vicinity of Y_1 , the restoring force $F_r(Y)$ of the D-spring expressed in Eq. (6.4) can be linearized by a first-order Taylor expansion at $Y = Y_1$:

$$F_r(Y) = Y \left(\sqrt{\frac{1-Y_0^2}{1-Y^2}} - 1 \right) \approx \alpha_0 + \alpha(Y - Y_1), \quad (6.8)$$

where

$$\alpha_0 = Y_1 \left(\sqrt{(1 - Y_0^2)/(1 - Y_1^2)} - 1 \right) = F_r(Y_1), \quad (6.9a)$$

$$\alpha = \left(\sqrt{(1 - Y_0^2)/(1 - Y_1^2)} + Y_1^2 - 1 \right) / (1 - Y_1^2), \quad (6.9b)$$

are the coefficients of the constant and the linear stiffness term, respectively.

By substituting Eq. (6.8) into the expression of $F_D(X_1, Y_1)$, we have $F_D(X_1, Y_1) \approx \lambda \alpha X_1$. Thus Eq. (6.7) can be transformed to a linearized governing equation, expressed by

$$X_1'' + 2\zeta_1 X_1' + (1 + \lambda \alpha) X_1 = F_0 e^{i\Omega \tau}. \quad (6.10)$$

Therefore the linearized stiffness and linearized natural frequency of the system are

$$K_L = (1 + \lambda \alpha), \quad \Omega_L = \sqrt{K_L}, \quad (6.11a, 6.11b)$$

respectively. Eq. (6.11b) shows that the natural frequency of the system can be reduced by adding the D-spring while setting $\alpha < 0$.

Figure 6.4 shows the dimensionless linearized dynamic stiffness K_L and linearized natural frequency Ω_L of the isolation system with respect to the distance Y_1 between two terminals of the D-spring at $X_1 = 0$. Fig. 6.4(a) and 6.4(b) presents the effects of the spring stiffness ratio λ of the nonlinear D-spring. Four different cases with varying values of λ from 0 to 1, to 2 and to 3 are considered. The case with $\lambda = 0$ corresponds to the conventional linear isolator case without using the nonlinear D-spring. The initial distance Y_0 between two ends of D-spring is set as $Y_0 = \sqrt{2}/2$. It shows that for a specific case with a non-zero value of λ , the values of the K_L and Ω_L increase with Y_1 .

At a prescribed value of Y_1 smaller than a critical threshold of approximately 0.45 (obtained by letting $\alpha = 0$ in Eq. (6.8)), the values of K_L and Ω_L reduce as the λ increases from 0 to 3. At a larger value of Y_1 compared to the threshold, both K_L and Ω_L increase with λ . In contrast, the values of K_L and Ω_L will decrease with the increasing λ at a value of Y_1 lower than the threshold. The figure shows that the value of Y_1 of the D-spring can be set smaller than the threshold so as to achieve lower values of K_L and Ω_L compared with the corresponding linear isolator case.

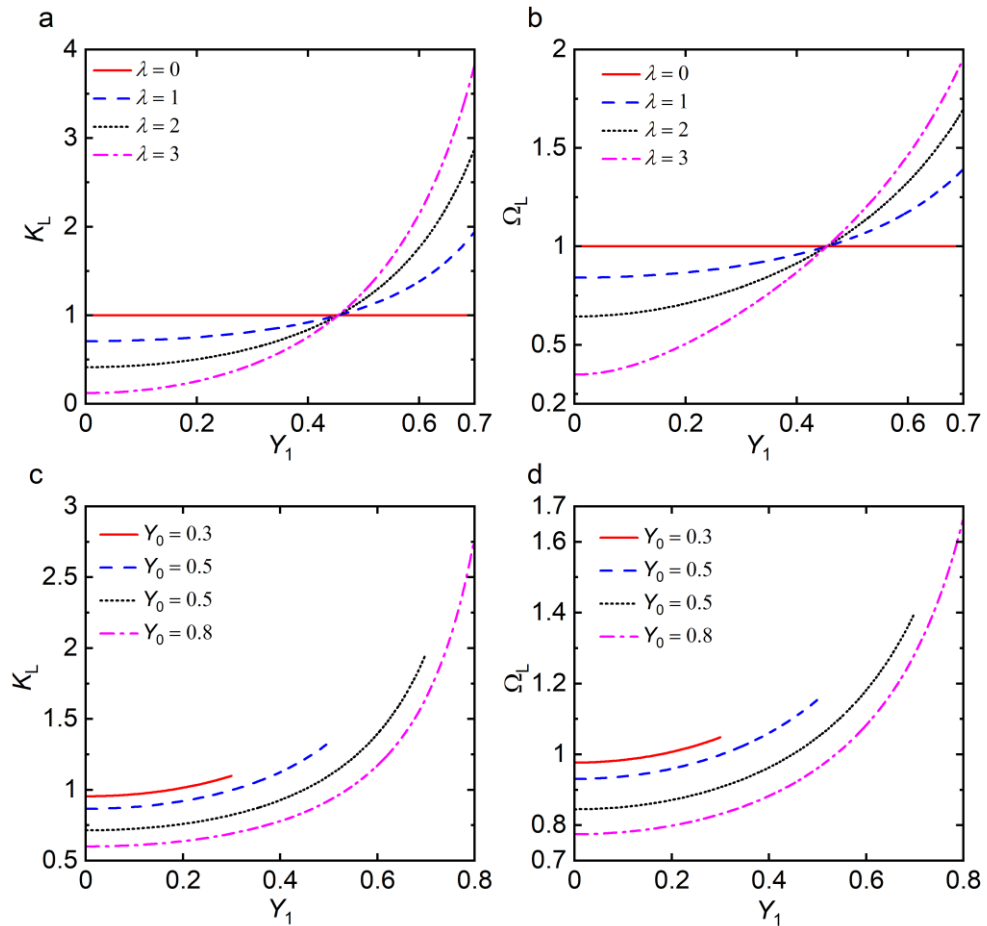


Figure 6.4. Effects of the nonlinear D-spring on (a) and (c): the dimensionless linearized dynamic stiffness K_L , and on (b) and (d): dimensionless linearized natural frequency Ω_L . In (a) and (b), The solid line, dashed line, dotted line and dash-dotted line are for $\lambda = 0, 1, 2$ and 3 , respectively; in (c) and (d), The solid line, dashed line, dotted line and dash-dotted line are for $Y_0 = 0.3, 0.5, 0.7$ and 0.8 , respectively.

In Fig. 6.4(c) and 6.4(d), the influence of the initial distance Y_0 between terminals is examined, by considering four different values of $Y_0 = 0.3, 0.5, 0.7$ and 0.8 . The stiffness ratio of the D-spring is set as $\lambda = 1$. For a pre-described value of Y_0 , as Y_1 decreases from Y_0 to 0, both the linearized system stiffness K_L and the linearized natural frequency Ω_L decreases. At the same Y_1 value, an increase in the value of Y_0 can lead to lower values of K_L and Ω_L .

6.2.2. Nonlinear analysis

To obtain dynamic behaviour and isolation performance, Eq. (6.7) needs to be solved. Here the harmonic-balance method with alternating-frequency-time (HB-AFT) technique is used to determine the steady-state periodic responses of the nonlinear isolation system. The steady-state displacement response X_1 and the nonlinear force F_D are approximated by a truncated N -order Fourier series with a fundamental frequency of Ω :

$$X_1 = \sum_{n=0}^N \tilde{R}_{(1,n)} e^{in\Omega\tau}, \quad F_D = \sum_{n=0}^N \tilde{H}_n e^{in\Omega\tau}, \quad (6.12a, 6.12b)$$

where $F_D \equiv F_D(X_1, Y_1) = \lambda (F_r(Y(X_1, Y_1)) - F_r(Y_1))$ is for the current force-excited system. The symbols $\tilde{R}_{(1,n)}$ and \tilde{H}_n denote the complex Fourier coefficients of the n -th order Fourier approximation. The velocity X_1' and the acceleration X_1'' of the mass can be obtained by taking differentiation of X_1 with respect to time τ . The AFT technique presented in Chapter 3 can be applied to determine the Fourier coefficients \tilde{H} of the nonlinear force F_D . Once the Fourier coefficients are obtained, Eq. (6.12) is substituted into Eq. (6.7). By balancing the corresponding coefficients of the n -th ($0 \leq n \leq N$) order harmonic terms of the resultant equation, we have

$$(-(n\Omega)^2 + i(2n\Omega\zeta_1) + 1)\tilde{R}_{(1,n)} = \tilde{P}_{(1,n)} - \tilde{H}_n, \quad (6.13)$$

where $\tilde{P}_{(1,n)}$ is the n -th order coefficient of the excitation source. For the current SDOF system subjected to the force-excitation we have $\tilde{P}_{(1,1)} = F_0$. Eq. (6.13) provides a total number of N algebraic equations with complex numbers $\tilde{R}_{(1,n)}$ as unknowns. By balancing the real and imaginary parts, a total number of $(2N + 1)$ real nonlinear algebraic equations can be obtained, which are solved by using the Newton-Raphson iterative method. In the meantime, the arc-length continuation method illustrated in Chapter 3 is used to track the solution branch in a range of parameter values. Hence, the steady-state response of the system can be determined and the vibration isolation performance of the isolation system is then evaluated.

6.2.3. Performance indices

To assess the isolation performance of linear or nonlinear isolators, the force and displacement transmissibility, as well as vibration power flow variables have been widely used as performance indicators. Here the following performance indices have been used to evaluate nonlinear vibration isolators (Yang et al., 2019, 2016; Alberdi-Munian et al., 2012; Xiong et al., 2005b) and will also be used in the current study:

- (a) Peak dynamic response displacement amplitude.
- (b) Peak transmissibility.
- (c) Unity isolation frequency range, in which the value of transmissibility is less than unity.
- (d) Time-averaged vibration power flow.

For the current system, the force transmissibility TR_G is defined as the ratio between the maximum magnitude of the dimensionless transmitted force to the ground and the excitation force amplitude:

$$TR_G = \frac{\max(|\Re\{F_{tG}\}|)}{F_0}, \quad (6.14)$$

where F_{tG} is the total non-dimensional transmitted force from mass m_1 to the ground with $F_{tG} = F_D(X_1, Y_1) + 2\zeta_1 X_1' + X_1$, the symbol \Re denotes the operation of taking the real part of a complex number. To isolate the vibration, a low value of force transmissibility is desirable for the design of the isolator.

For the force-excited system, the dimensionless steady-state input power P_{in} by the external excitation is defined as the product of the velocity X_1' of the machine and the harmonic excitation force $F_0 e^{i\Omega\tau}$. The time-averaged input power is

$$\bar{P}_{in} = \frac{1}{\tau_p} \int_{\tau_0}^{\tau_0 + \tau_p} \Re\{X_1'\} \Re\{F_0 e^{i\Omega\tau}\} d\tau = \frac{1}{2} F_0 \Re\{(i\Omega \tilde{R}_{(1,1)})^*\}, \quad (6.15)$$

where $X_1' = \sum_{n=0}^N i n \Omega \tilde{R}_{(1,n)} e^{i n \Omega \tau}$ using Eq. (6.12a), τ_0 is the averaging starting time, τ_p is averaging time span set as one period of the external excitation with $\tau_p = 2\pi/\Omega$, and * represents the operation of taking the complex conjugate of a complex number.

The maximum kinetic energy is often used as an indicator to assess the performance of vibration isolation systems (Xiong et al., 2003). For the current SDOF system, the dimensionless maximum kinetic energy K_1 of the machine mass is given by

$$K_1 = \frac{1}{2} (|X_1'|_{\max})^2. \quad (6.16)$$

where $|X_1'|_{\max}$ is the maximum absolute velocity of the machine mass m_1 in the steady state.

6.2.4. Performance evaluations

In this section, the effects of the design parameters of the D-spring on the steady-state response and the performance of the isolator are investigated. The results are

obtained by both the HB-AFT method and the time-marching method based on the fourth-order Runge-Kutta (RK) method. The HB results are represented by different lines while the RK results are denoted by symbols. The order N of HB-AFT is set as 7 throughout this chapter with a consideration of both the accuracy and the computational cost. When examining the influence of the stiffness ratio λ of the D-spring, four different cases are considered with the value λ changing from 0 to 3, to 4 and to 5 while setting the initial angle θ_0 , the excitation amplitude F_0 and the distance Y_1 between two ends of the D-spring at equilibrium point as $\theta_0 = 45^\circ$, $F_0 = 0.002$ and $Y_1 = 0.4$, respectively. as $\theta_0 = 45^\circ$, $F_0 = 0.002$ and $Y_1 = 0.4$, respectively. The case with $\lambda = 0$ is corresponding to the linear isolator case without the nonlinear D-spring for comparison. When studying the effects of the initial angle θ_0 , four possible values of θ_0 are selected with $\theta_0 = 30, 45, 55$ and 60 degrees while setting $\lambda = 2$, $F_0 = 0.0025$ and $Y_1 = 0.4$. In the investigation of the influence of the distance Y_1 , four different values of Y_1 are chosen with $Y_1 = 0.3, 0.4, 0.5$ and 0.6 while setting $\lambda = 2$, $\theta_0 = 60^\circ$ and $F_0 = 0.002$. In the parameter studies, the damping ratio ζ_1 of the system is fixed as $\zeta_1 = 0.01$.

In Fig. 6.5(a) and (b), the effects of the stiffness ratio λ and initial angle θ_0 of the D-spring on the steady-state response amplitude of the mass X_{1_amp} are studied, respectively. The figure shows that the HB-AFT results agree quite well with those of the RK method. Fig. 6.5(a) shows that compared with linear isolation system with $\lambda = 0$, the addition of nonlinear D-spring can shift the peak in the response curve to the low-frequency range. The reason is that the dynamic stiffness of D-spring is negative near the equilibrium point ($Y = Y_1 = 0.4$) as shown by Eq. (6.5) and Fig. 6.2(b). Therefore the use of the D-spring can reduce the system stiffness and hence reduce the resonant frequency of the isolation system. These characteristics are also indicated by the expressions of the linearized stiffness and the linearized natural frequency in Eq. (6.11). Fig. 6.5(a) also shows that with the D-spring, the peak of the response curve bends to the left, which is due to the nonlinear relationship between the D-spring stiffness and the distance Y between the terminals. Fig. 6.2(b) showed that when the deformation of the D-spring Δ is large, the value of the D-spring stiffness may become larger or smaller than the stiffness value at $\Delta = 0$. It can correspondingly result in a hardening or softening effect on the displacement response curve. As the stiffness ratio λ increasing from 3 to 4 and to 5, the peak in the curve of X_{1_amp} is shifted further to the low frequencies. This is due to the stronger negative stiffness effect provided by the nonlinear D-spring, leading to a smaller system stiffness and therefore a lower

resonance frequency. Moreover, the peak of X_{1_amp} bends more towards left with higher peak value. The reason is the stronger stiffness nonlinearity of the D-spring by a larger λ value. As the response amplitude increases at the resonance frequency with a larger value of λ , the deformation of the D-spring Δ becomes larger and can result in a stronger softening effect on the response. Fig. 6.5(b) shows that when the initial angle θ_0 of the D-spring increases from 30 to 45, to 55 and to 60 degrees, the peak of X_{1_amp} shifts significantly to the left due to the reduction of the D-spring stiffness near the equilibrium point of $Y = Y_1 = 0.4$ as shown by Eq. (6.5). An increasing θ_0 can also bend the peak further to the left with a larger peak value, resulting in multiple solutions at certain excitation frequency near the peak. The reason can be found from Eq. (6.5) and Fig. 6.2(b), i.e., when the response displacement of the mass is large and the position of the mass is away from the equilibrium point, the nonlinear D-spring can provide a lower stiffness with the increasing θ_0 , resulting in a possible softening effect. It is also noticed that when the value of λ or θ_0 becomes larger for the D-spring, the values of X_{1_amp} are increased in the low-frequency range and the super-harmonic responses can be found near $\Omega = 0.3$.

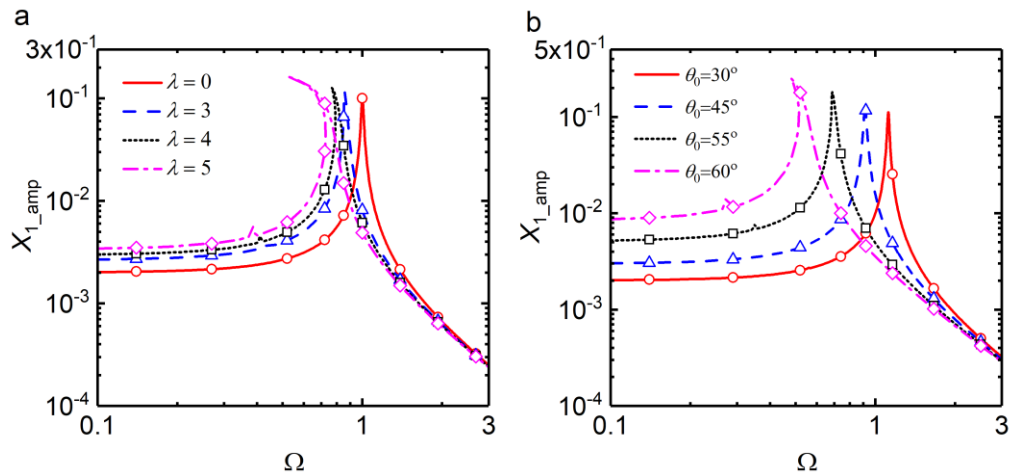


Figure 6.5. Effects of (a) the spring stiffness ratio λ and (b) the initial angle θ_0 of the nonlinear D-spring on the steady-state response amplitude of the mass X_{1_amp} . In (a), the solid, dashed, dotted and dash-dotted lines are for $\lambda = 0, 3, 4$ and 5 , respectively; in (b), The solid, dashed, dotted and dash-dotted lines are for $\theta_0 = 30, 45, 55$ and 60 degrees, respectively. Symbols: RK results.

In Fig. 6.6(a) and (b), the influence of the stiffness ratio λ and initial angle θ_0 of the D-spring on the force transmissibility TR_G is investigated, respectively. Fig. 6.6(a) shows that by adding the D-spring to the linear isolator, the peak in the TR_G curve shifts to the left and a larger effective frequency band is obtained for the attenuation of force transmission. This is due to the negative stiffness provided by the D-spring at the equilibrium point. The peak of the TR_G curve also bends to the low-frequency range

and results in multiple possible levels of TR_G near the resonance frequency. The reason is that there is a nonlinear relationship between the D-spring stiffness and the distance Y between the terminals. When the excitation frequency is in the vicinity of the resonant peak, the stiffness of the D-spring can be reduced with the increase of the response displacement, resulting in the bending behaviour. Fig. 6.6(a) also shows that as the stiffness ratio λ increases from 0 to 3, to 4 and to 5, there is a further shift of the peak in TR_G curve to the low frequencies and its peak shows more bending to the left with higher peak values. Fig. 6.6(b) shows that as the initial angle θ_0 of the D-spring increases from 30 to 45, to 55 and to 60 degrees, the peak of TR_G shifts to the low-frequency range so as to provide a broader frequency band for effective vibration isolation. This is again due to the lower system dynamic stiffness with a larger value of θ_0 , leading to a lower resonant frequency of the system. An increase of the θ_0 value can also introduce stronger nonlinear effect into the system, which can then bend the peak of TR_G curve to the left with a slightly lower peak value of TR_G .

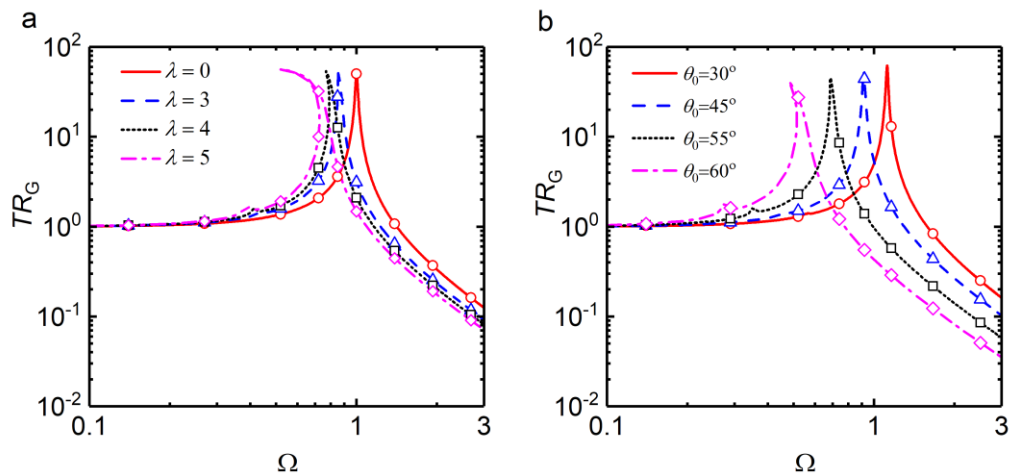


Figure 6.6. Effects of (a) the spring stiffness ratio λ and (b) the initial angle θ_0 of the nonlinear D-spring on the force transmissibility TR_G . In (a), The solid, dashed, dotted and dash-dotted lines are for $\lambda = 0, 3, 4$ and 5 , respectively; in (b), The solid, dashed, dotted and dash-dotted lines are for $\theta_0 = 30, 45, 55$ and 60 degrees, respectively. Symbols: RK results.

In Fig. 6.7, the reasons for the increase of the peak value of force transmissibility TR_G with the increasing stiffness ratio λ in Fig. 6.6(a), and for the decrease of the peak value of TR_G with the increasing initial angle θ_0 in Fig. 6.6(b) are further explored. Fig. 6.7(a) and (b) shows the time histories of the steady-state response X_1 as well as the total transmitted force F_{tG} for the cases of $\lambda = 5$ at $\Omega = 0.75$ and $\theta_0 = 60^\circ$ at $\Omega = 0.5$ shown in Fig. 6.6(a) and (b), respectively. It is found that for both cases, the maximum absolute transmitted force F_{tG} is found when the mass is reaching the highest position ($X_1 \approx 0.06$) and the D-spring is under tension ($Y > Y_0$). From Fig. 6.2(b), it is known that the D-spring stiffness is positive when $Y > Y_0$. Therefore, a larger value of stiffness

ratio λ can increase the D-spring stiffness, leading to a larger maximum absolute value of F_{tG} and hence a higher peak of TR_G . However, as shown in Fig. 6.2(b), an increasing initial angle θ_0 (i.e. an increasing Y_0) will reduce the D-spring stiffness when $Y > Y_0$. Hence it can result in a smaller maximum absolute value of F_{tG} and subsequently a lower peak value of the force transmissibility TR_G .

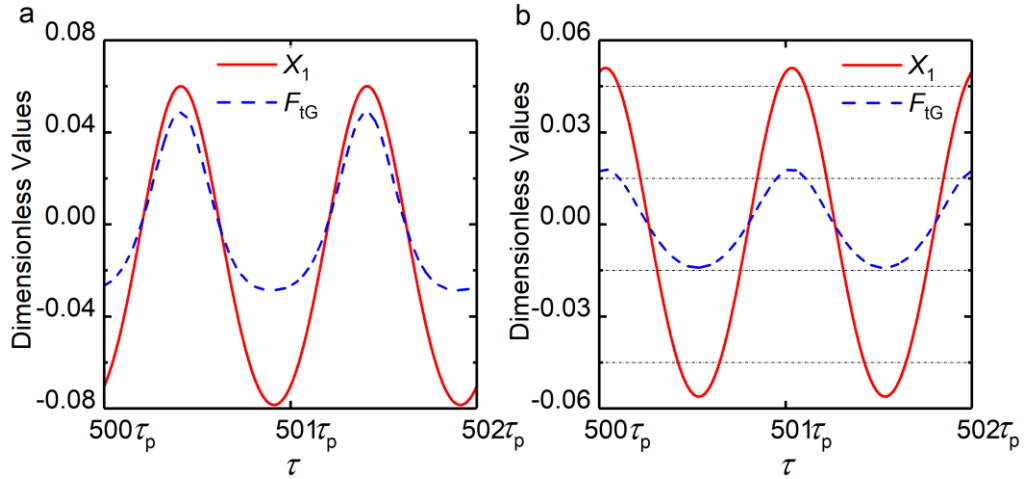


Figure 6.7. Time history of the dimensionless total transmitted force F_{tG} and the dimensionless displacement response of the mass X_1 with the system parameters set as (a) $\lambda = 5$, $\theta_0 = 45^\circ$, $F_0=0.002$, $\Omega = 0.75$, and (b) $\lambda = 2$ and $\theta_0 = 60^\circ$, $F_0=0.0025$, $\Omega = 0.5$, respectively; The solid line and the dashed line are the dimensionless response X_1 and the dimensionless total transmitted force F_{tG} , respectively.

In Fig. 6.8(a) and (b), the effects of D-spring on the maximum kinetic energy K_1 of the machine mass are examined. Fig. 6.8(a) shows that compared with linear isolation system ($\lambda = 0$), the introduction of the D-spring to the isolator can shift the peak in the kinetic energy K_1 curve to the low-frequency range and bend it to the left. The behaviour can bring benefits to the vibration isolation performance. As the stiffness ratio λ of the D-spring increases from 0 to 3, to 4 and to 5, the K_1 curve shifts further to the low frequencies and its peak bends more to the left, but the peak value of K_1 changes little. Fig. 6.8(a) also shows that a larger value of λ can lead to an increase of K_1 at low frequencies when away from the resonant peak. The curves of K_1 for different values of λ tend to merge at high frequencies. Fig. 6.8(b) shows that with the increasing θ_0 from 30 to 45, to 55 and to 60 degrees, the peak frequency of the K_1 curve reduces substantially and the peak bends more to the left. This is due to the reduction of stiffness of the D-spring near the equilibrium point and a stronger stiffness nonlinearity with the increasing θ_0 . However, there is little difference in the peak value of K_1 with the variation of θ_0 . When the frequency is away from the resonant region, a larger initial angle θ_0 can lead to a significantly larger K_1 value in the low-frequency range but the curves for different value of θ_0 are tending to overlap at high frequencies. From Fig.

6.8, an extra peak can be found in each curve of K_1 for nonlinear isolator cases with a non-zero value of λ , which is due to the presence of relatively large super-harmonic components in the response.

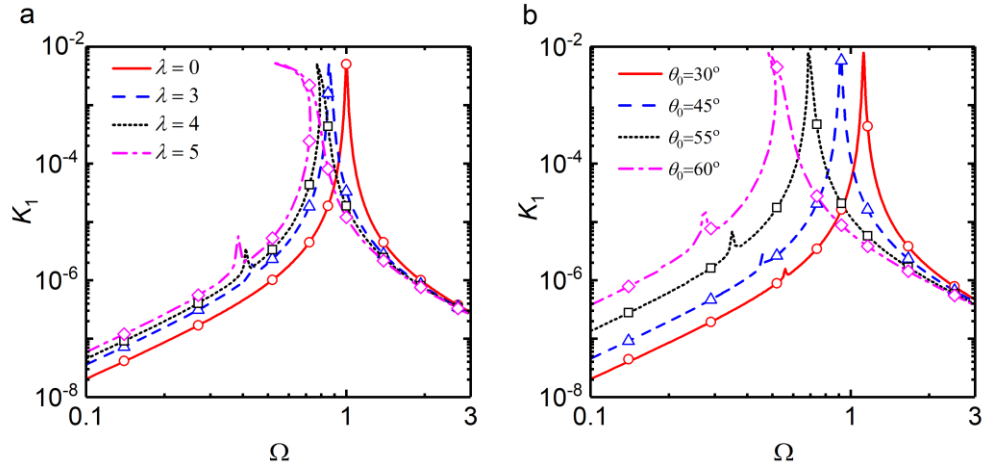


Figure 6.8. Effects of (a) the spring stiffness ratio λ and (b) the initial angle θ_0 of the nonlinear D-spring on the maximum kinetic energy K_1 . In (a), The solid, dashed, dotted and dash-dotted lines are for $\lambda = 0, 3, 4$ and 5 , respectively; in (b), The solid, dashed, dotted and dash-dotted lines are for $\theta_0 = 30, 45, 55$ and 60 degrees, respectively. Symbols: RK results.

In Fig. 6.9(a), the influence of the spring stiffness ratio λ of the D-spring on the time-averaged input power \bar{P}_{in} into the system is studied. By a comparison between the linear isolator case with $\lambda = 0$ and the nonlinear isolator cases using D-spring, it is found that the addition of the D-spring can lower peak frequency of the time-averaged input power but the variations of λ have little effect on the peak value of \bar{P}_{in} . Moreover, with the λ changing from 3 to 4 and to 5, the peak frequency of \bar{P}_{in} further decreases, which benefits the isolation performance of the system. Fig. 6.9(b), (c) and (d) presents the effects of the distance Y_1 between the two ends of the nonlinear D-spring at $X_1 = 0$ on the steady-state response amplitude X_{1_amp} , the force transmissibility TR_G and the maximum kinetic energy K_1 , respectively. Fig. 6.9(b) shows that as the value of Y_1 decreases from 0.6, to 0.5, to 0.4 and to 0.3, the response peak in the curve of X_{1_amp} shifts to the low frequencies due to the reducing stiffness of the D-spring at the equilibrium point, as shown by Eq. (6.5) and Fig. 6.2(b). Moreover, with the decrease of Y_1 , there is more bending of the peak in the X_{1_amp} curve to the left with increasing peak value. This is again due to the non-monotonic relationship between D-spring stiffness and the distance Y between the terminals. When the value of Y_1 is decreased, the stiffness of the D-spring near the equilibrium point of $Y = Y_1$ becomes smaller. The response amplitude of the mass is increased due to the less restraint, which can lead to a larger deformation of the D-spring. Therefore, the stiffness of the D-spring will be further reduced when the position of the mass is lower than the equilibrium point (i.e.

$Y < Y_0$), as shown by Eq. (6.5) and Fig. 6.2(b). Consequently, a softening effect can be observed.

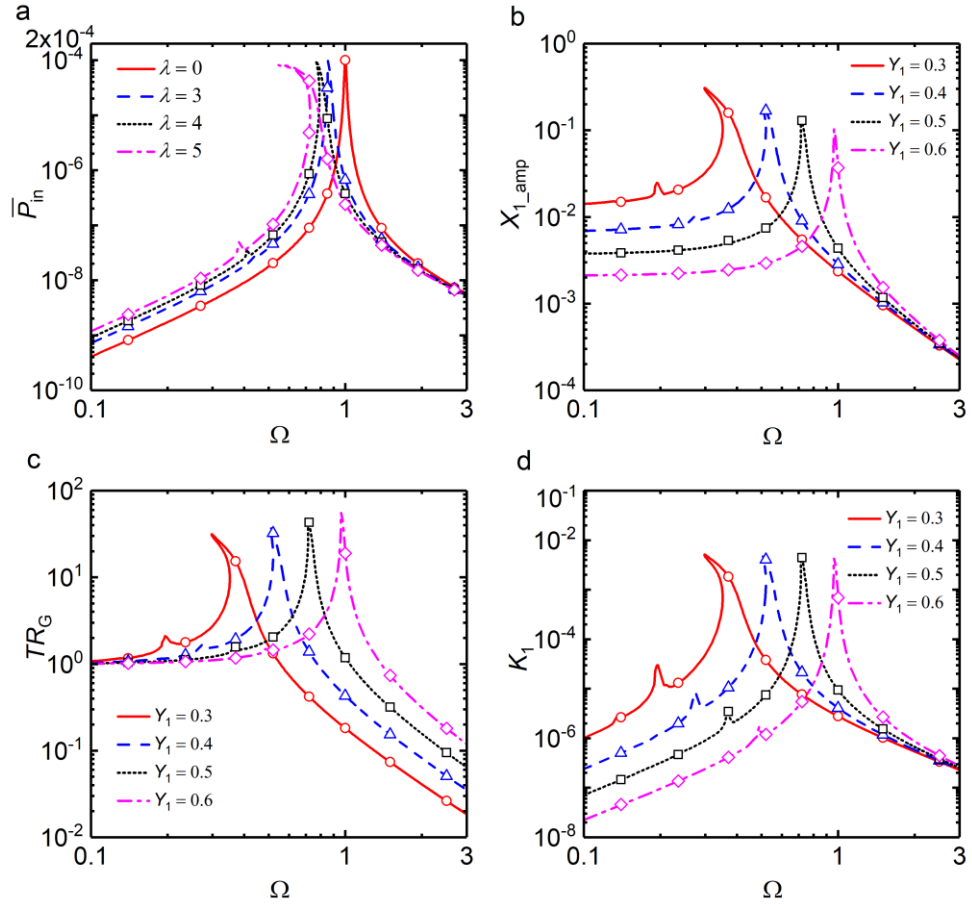


Figure 6.9. Effects of (a) the spring stiffness ratio λ on \bar{P}_{in} , and the distance Y_1 on (b) the steady-state response amplitude X_{1_amp} , (c) the force transmissibility TR_G and (d) the maximum kinetic energy K_1 . In (a), the solid, dashed, dotted and dash-dotted lines are for $\lambda = 0, 3, 4$ and 5 , respectively; in (b-d), the solid, dashed, dotted and dash-dotted lines are for $Y_1 = 0.3, 0.4, 0.5$ and 0.6 , respectively. Symbols: RK results.

Fig. 6.9(c) shows that when the distance Y_1 reduces from 0.6 to 0.3, the peak in the force transmissibility TR_G curve is also shifting to the left while its peak bends more to the left with reducing peak value. This phenomenon demonstrates a possible straightforward way to tailor the isolation characteristic of the D-spring without replacing the embedded spring. Combining the Fig. 6.6(a), 6.6(b) and 6.9(c), it can be found that at high frequencies away from the resonant region, the value of TR_G can be substantially reduced by using a large value of λ or θ_0 , or a small value of Y_1 , by which a wider frequency band of low force transmissibility can be obtained. However, in the low-frequency range close to $\Omega \approx 0.1$, there are little changes in values of TR_G regardless of the variations of design parameters of the D-spring. Fig. 6.9(d) shows that the reduction of the distance Y_1 can significantly shift the curve of the maximum kinetic energy K_1 to the low frequencies and also bend the peak to the left. This behaviour may

assist the vibration isolation. It is found that the change of the Y_1 value has a weak influence on the peak value of K_1 . In contrast, when the excitation frequency is away from resonance, the reduction of Y_1 can result in a much higher K_1 at low frequencies and a higher extra peak near $\Omega = 0.25$ while the curves of K_1 for different values of Y_1 coincide in high frequencies.

6.3. SDOF nonlinear isolator for base excitations

6.3.1. Mathematical model

The nonlinear isolation system may also encounter base-motion excitations in some applications such as vehicle suspension system when travelling down the uneven road. Fig. 6.10 shows the use of the D-spring for suppressing the vibration transmitted from base to the machine. The machine with mass m_1 is mounted on a foundation through a linear spring of stiffness coefficient k_1 , a linear damper with damping coefficient c_1 and the nonlinear D-spring, as shown in Fig. 6.1(a). The foundation base is driven by the harmonic displacement excitation z with $z = z_0 e^{i\omega t}$. The equilibrium position of the mass, is set as a reference with $x_1 = 0$, at which the distance y between terminals A and B of the D-spring is set as y_1 ($0 < y_1 < y_0$).

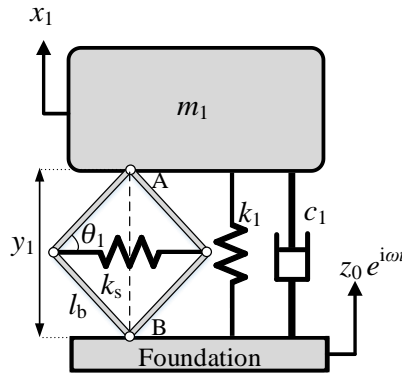


Figure 6.10. Schematic of a nonlinear isolator with the D-spring for isolation of base excitation.

The dynamic governing equation of the mass is

$$m_1 \ddot{x}_1 + c_1 \dot{x}_1 + k_1 x_1 + f_D(x_1, y_1, z) = c_1 \dot{z} + k_1 z, \quad (6.17)$$

where $f_D(x_1, y_1, z) = f_r(y(x_1, y_1, z)) - f_r(y_1)$ is the dynamic force applied by the nonlinear D-spring on the mass with $y(x_1, y_1, z) = y_1 + x_1 - z$, and $f_r(y)$ has been expressed by Eq. (6.2). Here by introducing the dimensionless displacement excitation amplitude Z_0 with $Z_0 = \frac{z_0}{2l_b}$ and reusing the parameters defined previously in the Subsection 6.2.1, the Eq. (6.17) can be transformed to a dimensionless form:

$$X_1'' + 2\zeta_1 X_1' + X_1 + F_D(X_1, Y_1, Z) = 2\zeta_1 Z' + Z, \quad (6.18)$$

where $Z = Z_0 e^{i\Omega\tau}$, $Z' = i\Omega Z_0 e^{i\Omega\tau}$, $F_D(X_1, Y_1, Z) \equiv \lambda(F_r(Y(X_1, Y_1, Z)) - F_r(Y_1))$ is the non-dimensional dynamic force applied by the D-spring on the mass with $Y(X_1, Y_1, Z) = Y_1 + X_1 - Z$ and the function of $F_r(Y)$ has already been defined by Eq. (6.4).

Based on HB-AFT technique and numerical continuation method illustrated in Subsection 6.2.2, by taking the nonlinear force F_D as $F_D = F_D(X_1, Y_1, Z) = \lambda(F_r(Y(X_1, Y_1, Z)) - F_r(Y_1))$ in Eq. (6.12b) and the excitation source $\tilde{P}_{(1,n)}$ as $\tilde{P}_{(1,n)} = 2\zeta_1 Z' + Z = (i2\zeta_1\Omega + 1)Z_0$ in Eq. (6.13), the steady-state response amplitude of the base-excited system can be determined.

6.3.2. Performance indices

For the current base-excited oscillating system, the displacement transmissibility can be used to evaluate the isolation performance. It is defined as the ratio between the amplitude of the response and the input displacement magnitude:

$$TR_D = \frac{|\Re\{X_{1_amp}\}|}{Z_0}, \quad (6.19)$$

The maximum kinetic energy is still defined by Eq. (6.16). In accordance of the energy conservation, the steady-state dimensionless time-averaged input power \bar{P}_{in} into the system is fully dissipated by the damper c_1 , hence we have

$$\bar{P}_{in} = \bar{P}_{d1} = \frac{1}{\tau_p} \int_{\tau_0}^{\tau_0 + \tau_p} 2\zeta_1 (\Re\{Z' - X_1'\})^2 d\tau, \quad (6.20)$$

where \bar{P}_{d1} is the time-averaged power dissipation by the damper c_1 .

6.3.3. Performance evaluations

This section studies the influence of the design parameters of the D-spring on the steady-state response and performance of the nonlinear isolator for base-excitations. The results obtained by the HB-AFT method are represented by different lines while those obtained by the 4th-order RK method are denoted by symbols. In the examination of the effects of the stiffness ratio λ , three cases are considered with the value of λ varying from 3, to 4 and to 5 while setting the initial angle as $\theta_0 = 45^\circ$ and the distance Y_1 between two ends of the D-spring at the equilibrium point as $Y_1 = 0.4$. A reference case with $\lambda = 0$ corresponds to the linear isolator system without the D-spring is also added for comparison. For investigating the influence of θ_0 , four possible values of θ_0

are selected changing from 30 to 45, to 55 and to 60 degrees while setting $\lambda = 2$ and $Y_1 = 0.4$. When studying the effects of Y_1 , four possible values of Y_1 are specified with $Y_1 = 0.3, 0.4, 0.5$ and 0.6 while setting $\lambda = 2$ and $\theta_0 = 60^\circ$. The system parameters are fixed as $\zeta_1=0.01$ and $Z_0 = 0.006$.

In Fig. 6.11(a) and (b), the effects of the stiffness ratio λ and initial angle θ_0 of the D-spring on the steady-state response amplitude of the machine X_{1_amp} are investigated, respectively. Fig. 6.11(a) shows that compared to the linear system with $\lambda = 0$, the peak in the response amplitude curve of the nonlinear isolation system shifts to the left. This characteristic is due to the reduction of the system stiffness by the negative stiffness of the nonlinear D-spring. It is also found that the peak of the nonlinear system bends to the left with lower peak value due to that the stiffness of the D-spring is a nonlinear function of distance Y between the terminals. As the response amplitude of the mass and also the deformation of the D-spring increase near the peak frequency, the stiffness of the D-spring can be decreased as shown by Fig. 6.2(b). When the value of the stiffness ratio λ changes from 3 to 4 and to 5, the X_{1_amp} shifts more to the low frequencies because of the smaller stiffness of the D-spring at the equilibrium point ($X_1 = 0, Y = Y_1$), and the peak bends further to the left due to the stronger nonlinearity of the D-spring stiffness with respect to the distance Y . Moreover, there is a substantial reduction in the peak height of the X_{1_amp} curve.

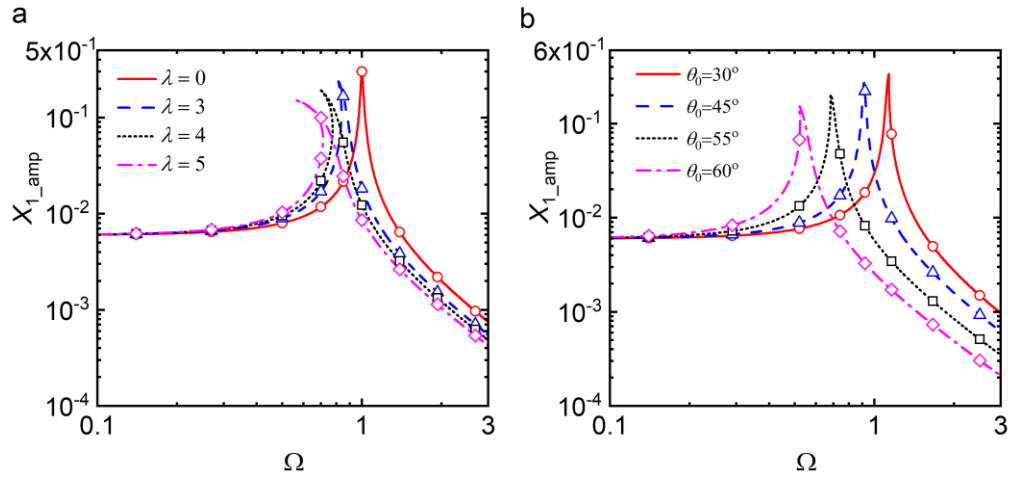


Figure 6.11. Effects of (a) the spring stiffness ratio λ and (b) the initial angle θ_0 of the nonlinear D-spring on the steady-state response amplitude of the mass X_{1_amp} . In (a), The solid, dashed, dotted and dash-dotted lines are for $\lambda = 0, 3, 4$ and 5 , respectively; in (b), The solid, dashed, dotted and dash-dotted lines are for $\theta_0 = 30, 45, 55$ and 60 degrees, respectively. Symbols: RK results.

Fig. 6.11(b) shows that as the initial angle θ_0 increases from 30 to 45, to 55 and to 60 degrees, the X_{1_amp} curve shifts to the left. The peak in the X_{1_amp} curve bends to the high-frequencies with larger peak value when $\theta_0 = 30^\circ$ while it bends to the low-

frequencies with smaller peak value when θ_0 increases from 45 to 55 and to 60 degrees. The reason is due to the nonlinear relationship between the distance Y and stiffness of the D-spring, resulting in a hardening effect when $\theta_0 = 30^\circ$ but a softening effect when $\theta_0 = 55^\circ$ or 60° .

In Fig. 6.12(a) and (b), the influence of the stiffness ratio λ and initial angle θ_0 of the D-spring on the displacement transmissibility TR_D is examined, respectively. Fig. 6.12(a) shows that the addition of the nonlinear D-spring reduces the resonance frequency of TR_D curve compared to the corresponding linear system (i.e. $\lambda = 0$). The peak in the TR_D curve also bends to the left with a smaller value. When the stiffness ratio λ increasing from 3 to 4 and to 5, the peak in the curve of TR_D shifts further to the left due to the reduction of the D-spring stiffness at $X_1 = 0$. Moreover, there is more bending of the TR_D peak to the left with lower peak value. Fig. 6.12(b) shows that with the increase of θ_0 from 30 to 45, to 55 and to 60 degrees, the TR_D curve shifts to the low-frequency range and the effective frequency band for displacement transmission isolation is enlarged. The peak of TR_D curve bends to the right with higher peak value when θ_0 decreases from 45 to 30 degrees while the peak bends to the left when θ_0 increases from 45 to 60 degrees. This is again due to the stiffness nonlinearity of D-spring, leading to different nonlinear effect in the variation of θ_0 .

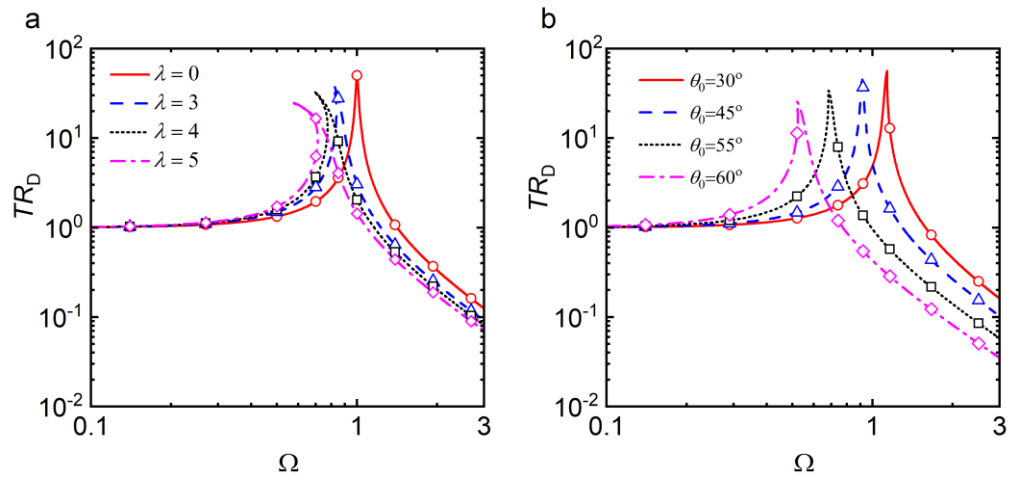


Figure 6.12. Effects of (a) the spring stiffness ratio λ and (b) the initial angle θ_0 of the nonlinear D-spring on the force transmissibility TR_B . In (a), The solid, dashed, dotted and dash-dotted lines are for $\lambda = 0, 3, 4$ and 5 , respectively; in (b), The solid, dashed, dotted and dash-dotted lines are for $\theta_0 = 30, 45, 55$ and 60 degrees, respectively. Symbols: RK results.

In Fig. 6.13(a) and (b), the effects of stiffness ratio λ and initial angle θ_0 of the D-spring on the maximum kinetic energy K_1 of the mass are studied, respectively. Fig. 6.13(a) shows that with the use of the nonlinear D-spring, the peak value of maximum kinetic energy K_1 is reduced and its resonant peak is shifted to the left compared with the linear system ($\lambda = 0$). This behaviour suggests an improvement in the vibration

isolation performance. As the value of stiffness ratio λ increases from 3 to 4 and to 5, the peak value of K_1 and its peak frequency is further reduced. Fig. 6.13(b) shows that when the initial angle θ_0 increases from 30 to 45, to 55 and to 60 degrees, the peak value and the associated frequency of K_1 are both reduced substantially due to the smaller D-spring stiffness at the equilibrium point. When $\theta_0 = 30^\circ$, the peak of the K_1 curve bends to the high frequencies. However, when θ_0 increases from 55 to 60 degrees, the K_1 peak bends to the left. This is again due to the nonlinear effect introduced by the D-spring.

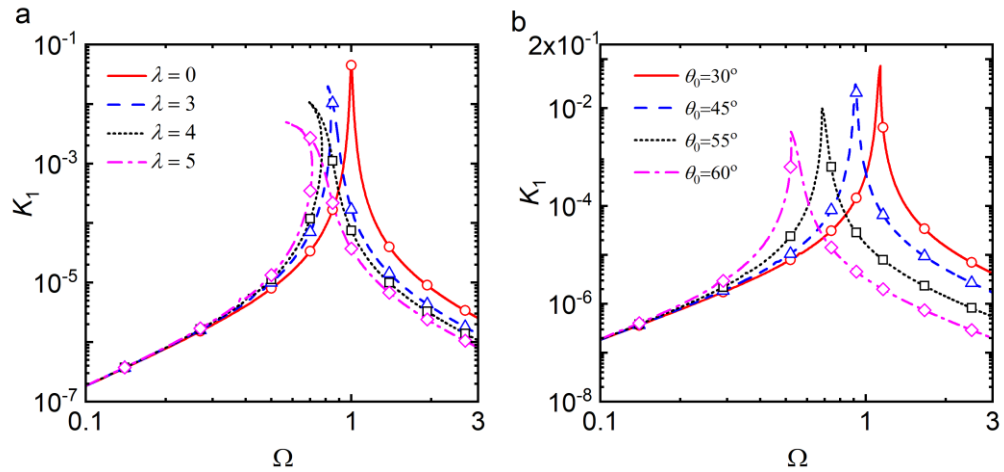


Figure 6.13. Effects of (a) the spring stiffness ratio λ and (b) the initial angle θ_0 of the nonlinear D-spring on the maximum kinetic energy K_1 . In (a), The solid, dashed, dotted and dash-dotted lines are for $\lambda = 0, 3, 4$ and 5 , respectively; in (b), The solid, dashed, dotted and dash-dotted lines are for $\theta_0 = 30, 45, 55$ and 60 degrees, respectively. Symbols: RK results.

In Fig. 6.14(a), the influence of the spring stiffness ratio λ on the time-averaged input power \bar{P}_{in} into the system is investigated. It shows that as the stiffness ratio λ increases from 0 to 3, to 4 and to 5, the curve of \bar{P}_{in} shifts to the low-frequency range and the peak value of \bar{P}_{in} as well as its associated frequency are both reduced. When the excitation frequency is away from the resonance, It can be found that the value of \bar{P}_{in} is increased with λ in the low-frequency range, while the curves of \bar{P}_{in} with different λ values merge in the high-frequency range. Fig. 6.14(b), (c) and (d) presents the effects of the distance Y_1 between the terminals of the nonlinear D-spring at $X_1 = 0$ on the steady-state response amplitude X_{1_amp} of the mass, the displacement transmissibility TR_D to the machine mass m_1 and the maximum kinetic energy K_1 , respectively. Fig. 6.14(b) shows that a decrease of Y_1 from 0.6 to 0.5, to 0.4 and to 0.3 can shift the X_{1_amp} curve to the low-frequency range. In the meantime, the peak shows less bending to the left with a smaller peak value. This is due to that a smaller value of Y_1 can lead to a smaller stiffness of the D-spring at the equilibrium point, which reduces the transmitted force to the mass and results in a lower vibration amplitude X_{1_amp} . Moreover, since the

vibration amplitude is reduced, the deformation of the D-spring is small and therefore the nonlinear effect by the D-spring is minimized, leading to less bending at the peak in the response curve.

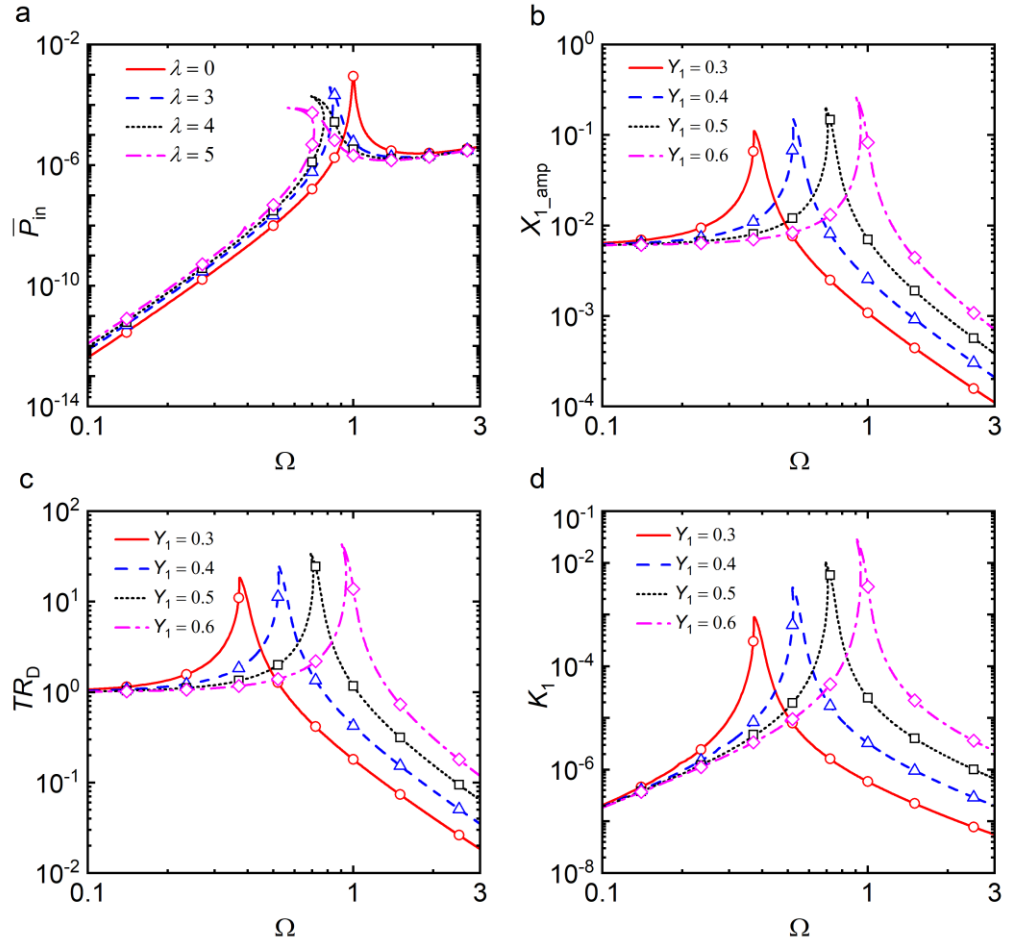


Figure 6.14. Effects of spring stiffness ratio λ (a) on \bar{P}_{in} , and distance Y_1 on (b) X_{1_amp} , (c) TR_D and (d) K_1 . In (a), the solid, dashed, dotted and dash-dotted lines are for $\lambda = 0, 3, 4$ and 5 , respectively; in (c-d), the solid, dashed, dotted and dash-dotted lines are for $Y_1 = 0.3, 0.4, 0.5$ and 0.6 , respectively. Symbols: RK results.

Fig. 6.14(c) shows that by reducing the distance Y_1 from 0.6 to 0.3, the TR_D curve is shifting to the left. In contrast, the peak of TR_D curve bends less to left with lower peak value. From Figs. 6.12(a), (b) and 6.14(c), it is found that a larger λ , a larger θ_0 or a smaller Y_1 can substantially reduce the TR_D at the high frequencies, which shows a good performance for the displacement transmission isolation. Fig. 6.14(d) shows that as the distance Y_1 decreases from 0.6 to 0.3, there is a reduction in the peak value as well as the peak frequency of the maximum kinetic energy curve K_1 . Less bending of the peak is also found in the K_1 curve. From Figs. 6.13(a), (b) and 6.14(d), it is summarized that when the excitation frequency is away from the resonant region, a higher value of λ , θ_0 or a lower value of Y_1 can lead to smaller values maximum kinetic energy at high frequencies, which can assist the vibration isolation of the nonlinear

isolator. At low frequencies away from resonance frequency, the curves of K_1 are tending to coincide, suggesting that the nonlinear isolator may not be effective on the suppression of K_1 in low-frequencies for the isolation from the base-excitation.

6.4. 2DOF nonlinear isolation system for force excitation

6.4.1. Mathematical model

This subsection explores the isolation performance of the nonlinear isolator with D-spring when considering the flexibility of the base structure. Fig. 6.15 provides a schematic representation of a coupled 2DOF system comprises a SDOF base of a mass m_b , a linear spring with stiffness k_b and a linear damper with damping c_b to model a movable base structure. A machine of mass m_1 subjected to a harmonic force-excitation $f_0 e^{i\omega t}$ is mounted on the SDOF base via a linear spring with stiffness k_1 , a linear damper with damping c_1 and the nonlinear D-spring, as shown in Fig. 6.1(a). The equilibrium position of the mass, is set as a reference with $x_1 = x_b = 0$, at which the distance y between terminals A and B of the D-spring is set as y_1 ($0 < y_1 < y_0$).

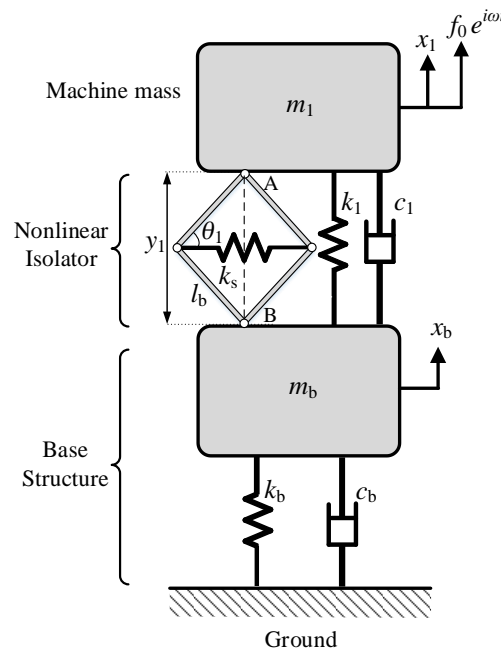


Figure 6.15. Schematic of a 2DOF nonlinear isolation system with the D-spring for isolation of force excitation.

In many applications, it is not possible to add the isolator into the foundation structure. If it is also possible to insert the nonlinear D-spring into the base structure, since the excitation force is applied to the machine mass, the response displacement of the base is naturally smaller than the machine mass and hence there will be less deformation of the D-spring if it was mounted between the base and the ground. Due to

the geometric nonlinearity of the D-spring, the nonlinear effects caused by the D-spring in the base structure will be weaker.

For the current 2DOF nonlinear isolation system, the dimensional equation of motion can be written in a matrix form as

$$\begin{bmatrix} m_1 & 0 \\ 0 & m_b \end{bmatrix} \begin{Bmatrix} \ddot{x}_1 \\ \ddot{x}_b \end{Bmatrix} + \begin{bmatrix} c_1 & -c_1 \\ -c_1 & c_1 + c_b \end{bmatrix} \begin{Bmatrix} \dot{x}_1 \\ \dot{x}_b \end{Bmatrix} + \begin{bmatrix} k_1 & -k_1 \\ -k_1 & k_1 + k_b \end{bmatrix} \begin{Bmatrix} x_1 \\ x_b \end{Bmatrix} + \begin{Bmatrix} f_D(x_1, x_b, y_1) \\ -f_D(x_1, x_b, y_1) \end{Bmatrix} = \begin{Bmatrix} f_0 e^{i\omega t} \\ 0 \end{Bmatrix}. \quad (6.21)$$

where $f_D(x_1, x_b, y_1) = f_r(y(x_1, x_b, y_1)) - f_r(y_1)$ is the dynamic force applied by the nonlinear D-spring with $y(x_1, x_b, y_1) = y_1 + x_1 - x_b$, and $f_r(y)$ has been expressed by Eq. (6.2). Here the new parameters are introduced as

$$\omega_b = \sqrt{\frac{k_b}{m_b}}, \quad \zeta_b = \frac{c_b}{2m_b\omega_b}, \quad X_b = \frac{x_b}{2l_b}, \quad \gamma = \frac{\omega_b}{\omega_1}, \quad \mu = \frac{m_b}{m_1},$$

where ω_b and ζ_b represent the undamped natural frequency of the base structure and the damping ratio of the linear damper in the base structure, respectively, X_b denotes the non-dimensional displacement of the base structure, γ is the undamped natural frequency ratio and μ is the mass ratio. By using them and the previously defined parameters, Eq. (6.21) can be transformed into dimensionless form as

$$\begin{bmatrix} 1 & 0 \\ 0 & \mu \end{bmatrix} \begin{Bmatrix} X_1'' \\ X_b'' \end{Bmatrix} + \begin{bmatrix} 2\zeta_1 & -2\zeta_1 \\ -2\zeta_1 & 2(\zeta_1 + \zeta_b\mu\gamma) \end{bmatrix} \begin{Bmatrix} X_1' \\ X_b' \end{Bmatrix} + \begin{bmatrix} 1 & -1 \\ -1 & 1 + \mu\gamma^2 \end{bmatrix} \begin{Bmatrix} X_1 \\ X_b \end{Bmatrix} + \begin{Bmatrix} F_D(X_1, X_b, Y_1) \\ -F_D(X_1, X_b, Y_1) \end{Bmatrix} = \begin{Bmatrix} F_0 e^{i\Omega\tau} \\ 0 \end{Bmatrix}, \quad (6.22)$$

where $F_D(X_1, X_b, Y_1) = \lambda(F_r(Y(X_1, X_b, Y_1)) - F_r(Y_1))$ is the non-dimensional dynamic force applied by the D-spring with $Y(X_1, X_b, Y_1) = Y_1 + X_1 - X_b$, and the function of $F_r(Y)$ has been defined by Eq. (6.4).

Based on the HB-AFT technique illustrated in Subsection 6.2.2, the steady-state response of the machine mass m_1 is still approximated by Eq. (6.12a). The steady-state response of the base mass m_b can be approximated with $X_b = \sum_{n=0}^N \tilde{R}_{(b,n)} e^{in\Omega\tau}$, and the corresponding velocity and acceleration responses X_b' and X_b'' can then be calculated by taking differentiation of X_b with respect to time τ . The Fourier coefficient \tilde{H}_n of the nonlinear force F_D can be obtained by taking $F_D = F_D(X_1, X_b, Y_1) = \lambda(F_r(Y(X_1, X_b, Y_1)) - F_r(Y_1))$ in Eq. (6.12b). Those expressions can be substituted into

Eq. (6.22) and by balancing the corresponding n -th order harmonic terms of the resultant equations, we have

$$\left(-(n\Omega)^2 \begin{bmatrix} 1 & 0 \\ 0 & \mu \end{bmatrix} + i(n\Omega) \begin{bmatrix} 2\zeta_1 & -2\zeta_1 \\ -2\zeta_1 & 2(\zeta_1 + \zeta_b\mu\gamma) \end{bmatrix} + \begin{bmatrix} 1 & -1 \\ -1 & 1 + \mu\gamma^2 \end{bmatrix} \right) \begin{Bmatrix} \tilde{R}_{(1,n)} \\ \tilde{R}_{(b,n)} \end{Bmatrix} = \begin{Bmatrix} F_0 \\ 0 \end{Bmatrix} + \begin{Bmatrix} -\tilde{H}_n \\ \tilde{H}_n \end{Bmatrix}. \quad (6.23)$$

Recalling that the harmonic order n is within the range of $0 \leq n \leq N$, therefore Eq. (6.23) can be transformed into a total number of $2(2N + 1)$ real nonlinear algebraic equations and solved by using the Newton-Raphson method. The solutions of those algebraic equations in the frequency domain can be obtained by a combined use of HB and arc-length path continuations illustrated in Chapter 3. Subsequently, the steady-state response of the system can be determined and the performance of the nonlinear isolation system can then be evaluated.

6.4.2. Performance indices

The force transmissibility to the base mass m_1 and the force transmissibility to the stationary ground are defined as

$$TR_B = \frac{\max(|F_{tB}|)}{F_0}, \quad TR_G = \frac{\max(|F_{tG}|)}{F_0}, \quad (6.24a, 6.24b)$$

respectively, where $F_{tB} = X_1 - X_b + 2\zeta_1(X_1' - X_b') + F_D(X_1, X_b, Y_1)$ is the dimensionless transmitted force from the machine m_1 to the base structure and $F_{tG} = \mu\gamma^2 X_b + 2\zeta_b\mu\gamma X_b'$ is the dimensionless transmitted force from the base structure to the ground.

Noting that over one cycle of the periodic motion, the power transmitted to the base is fully dissipated by the damper c_1 in the base structure, so the steady-state time-averaged transmitted power \bar{P}_{tB} to the base is

$$\bar{P}_{tB} = \frac{1}{\tau_p} \int_{\tau_0}^{\tau_0 + \tau_p} 2\zeta_b\mu\gamma (\Re\{X_b'\})^2 d\tau. \quad (6.25)$$

By replacing X_b' with a truncated Fourier series $X_b' = \sum_{n=0}^N in\Omega\tilde{R}_{(b,n)} e^{in\Omega\tau}$ obtained from the differentiation of X_b , Eq. (6.25) can be transformed as

$$\bar{P}_{tB} = \frac{1}{2} \Re\left\{ \left(\sum_{n=0}^N in\Omega\tilde{R}_{(b,n)} \right)^* (2\zeta_b\mu\gamma \sum_{n=0}^N in\Omega\tilde{R}_{(b,n)}) \right\} = \zeta_b\mu\gamma \left| \sum_{n=0}^N in\Omega\tilde{R}_{(b,n)} \right|^2. \quad (6.26)$$

To assess the relative portion of power transmitted to the base, the power transmission ratio can then be defined as

$$R_{tB} = \frac{\bar{P}_{tB}}{\bar{P}_{in}}, \quad (6.27)$$

where \bar{P}_{in} is the time-averaged input power into the system, which has been defined by Eq. (6.15).

6.4.3. Performance evaluations

Figures 6.16-6.20 present the effects of the design parameters of the D-spring on the steady-state response and performance of the 2DOF nonlinear isolation system. The results obtained by HB-AFT approximations are represented by different lines and those obtained by RK time-domain method are denoted by different symbols. The system parameters are fixed as $\zeta_1 = \zeta_b = 0.01$, $\gamma = 1$, $\mu = 1$. In the investigation of the spring stiffness ratio λ of the nonlinear D-spring, four cases of λ are investigated with the value of λ changing from 0 to 3, to 4 and to 5 while setting the initial angle $\theta_0 = 45^\circ$, the distance Y_1 between two ends of the D-spring at equilibrium point as $Y_1 = 0.4$ and the excitation force amplitude $F_0 = 0.0025$. The case of $\lambda = 0$ corresponds to the linear isolator without using the D-spring. When examining the effects of the initial angle θ_0 , four values of θ_0 are selected with $\theta_0 = 30, 45, 55$ and 60 degrees while setting $\lambda = 2$, $Y_1 = 0.4$ and $F_0 = 0.002$. For the study of Y_1 , four possible values of Y_1 are chosen with $Y_1 = 0.3, 0.4, 0.5$ and 0.6 while setting $\lambda = 2$, $\theta_0 = 60^\circ$ and $F_0 = 0.0015$.

In Fig. 6.16(a) and (b), the influence of spring stiffness ratio λ and initial angle θ_0 of the nonlinear D-spring on the steady-state response amplitude X_{1_amp} of the machine mass m_1 is examined, respectively. From Fig. 6.16(a) and (b), two resonance peaks are observed in the X_{1_amp} curves. An anti-peak is found near $\Omega = 1.4$ in each of X_{1_amp} curve, where a local minimum point of the response amplitude X_{1_amp} can be obtained. Fig. 6.16(a) shows that with the use of the nonlinear D-spring, both two peaks and the anti-peak shift to the left. The reason is that the use of the D-spring with negative stiffness can lead to a smaller supporting stiffness for the machine mass. It is also observed that the first peak bends to the left due to the nonlinear relationship of the restoring force of the D-spring against its distance Y as shown by Fig. 6.2(a). When the value of X_{1_amp} is large near the first peak, the magnitude of the relative displacement between the base and the machine (and also the terminals displacement of the D-spring) is also increased, the D-spring can exhibit strong nonlinearity and hence largely affect the dynamic behaviour of the machine near the peak. As the increase of stiffness ratio

λ from 3 to 4 and to 5, both peaks and the anti-peak of each X_{1_amp} curve are shifting further to the left with the first peak bending more to the low frequencies, which can be beneficial for the vibration isolation. This behaviour is due to the stronger negative stiffness effect introduced by the D-spring with a higher value of λ . Fig. 6.16(a) also shows that the absolute peak values of the first peak and the anti-peak are both decreased with the increasing λ while minor changes are observed for the second peak value. Fig. 6.16(b) shows that when increasing the initial angle θ_0 from 30 to 45, to 55 and to 60 degrees, both two peaks and the anti-peak shift to the low-frequency range with the first peak bends further to the left. This is again due to a stronger negative stiffness of the D-spring, and an increasing nonlinearity between the restoring force and the distance Y of the D-spring when θ_0 is larger. This characteristic demonstrates the possibility of employing D-spring to improve the isolation performance for such systems. Fig. 6.16(b) also shows that with the growing value of θ_0 , there is a slight increase in the first peak value while reductions can be found in the second peak value and the absolute value of the anti-peak. From Fig. 6.16 it can be summarized that a larger value of λ or θ_0 can suppress the response amplitude of the machine at high frequencies away from the resonant peaks but can increase the response amplitude at low frequencies.

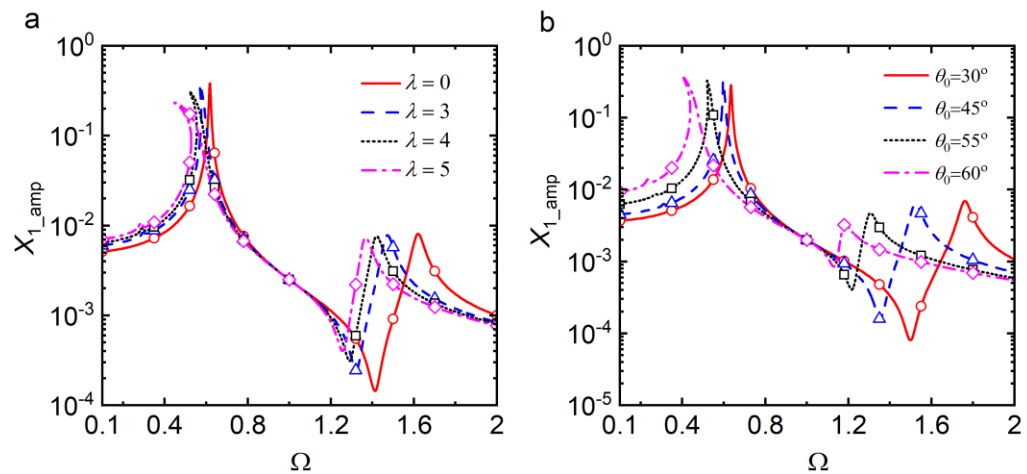


Figure 6.16. Effects of (a) the spring stiffness ratio λ and (b) the initial angle θ_0 of the nonlinear D-spring on the steady-state response amplitude X_{1_amp} of the machine mass. In (a), The solid, dashed, dotted and dash-dotted lines are for $\lambda = 0, 3, 4$ and 5 , respectively; in (b), The solid, dashed, dotted and dash-dotted lines are for $\theta_0 = 30, 45, 55$ and 60 degrees, respectively. Symbols: RK results.

In Fig. 6.17, the effects of D-spring parameters on the force transmissibility TR_B from the machine to the base structure and force transmissibility TR_G from the base to the fixed ground are investigated, respectively. Fig. 6.17(a) and (b) shows the influence of the stiffness ratio λ while Fig. 6.17(c) and (d) presents the effects of the initial angle θ_0 . Two peaks can be found in the TR_B and TR_G curves, and an anti-peak is observed

in each curve of TR_B . Fig. 6.17(a) shows that the use of nonlinear D-spring can bend the first peak of TR_B near $\Omega = 0.6$ to the left and shift the second peak to the low frequencies. This is corresponding to the response amplitude X_{2_amp} curve affected by the D-spring shown in Fig. 6.16(a). It is also found that both peak values of TR_B are reduced. As the stiffness ratio λ changing from 3 to 4 and to 5, the first peak of TR_B bends further to the left and the second TR_B peak shifts more to the low-frequency range. Moreover, with the increasing λ , there are reductions in the values of both TR_B peaks while little changes can be found in the anti-peak near $\Omega = 1$. By conducting modal analysis for the linear system with $\lambda = 0$, it is known that the anti-peak corresponds to the in-phase mode and the relative displacement between the base mass m_1 and the machine m_2 and also the terminals displacement of the D-spring are small. Consequently, the D-spring may have little effect on the TR_B near the frequency of the anti-peak. Fig. 6.17(b) shows that with the addition of the nonlinear D-spring, the first peak of the TR_G bends to the low frequencies and the second peak shift to the low frequencies. When the stiffness ratio λ increases from 3 to 5, there is more bending on the first peak of TR_G with smaller peak value. Moreover, the second peak shifts further to the lower frequencies with the height of the second peak remaining nearly unchanged. Fig. 6.17(c) shows that with the increase of the D-spring initial angle θ_0 from 30 to 45, to 55 and to 60 degrees, both peaks of the TR_B curve shift to the low frequencies with smaller peaks values. The reason is that an increase of the θ_0 value can lead to a smaller negative stiffness of the D-spring, which can alter the resonance frequencies of the isolation system and hence lead to significant changes in the peak frequencies of the TR_B curve. Fig. 6.17(d) shows that by using a larger value of θ_0 , both peaks of TR_G curve shift more to the low frequencies. Moreover, the first peak of TR_G extends further to the left with lower peak value due to a stronger nonlinearity of the restoring force with respect to the distance Y . In comparison, the second TR_G peak shifts to the low frequencies with a minor difference on the peak value. From Fig. 6.17(a-d), it is found that in the high-frequency range away from the resonance peaks, the values of TR_B and TR_G curves become substantially lower by using a larger value of λ and θ_0 . This behaviour may assist the vibration isolation performance.

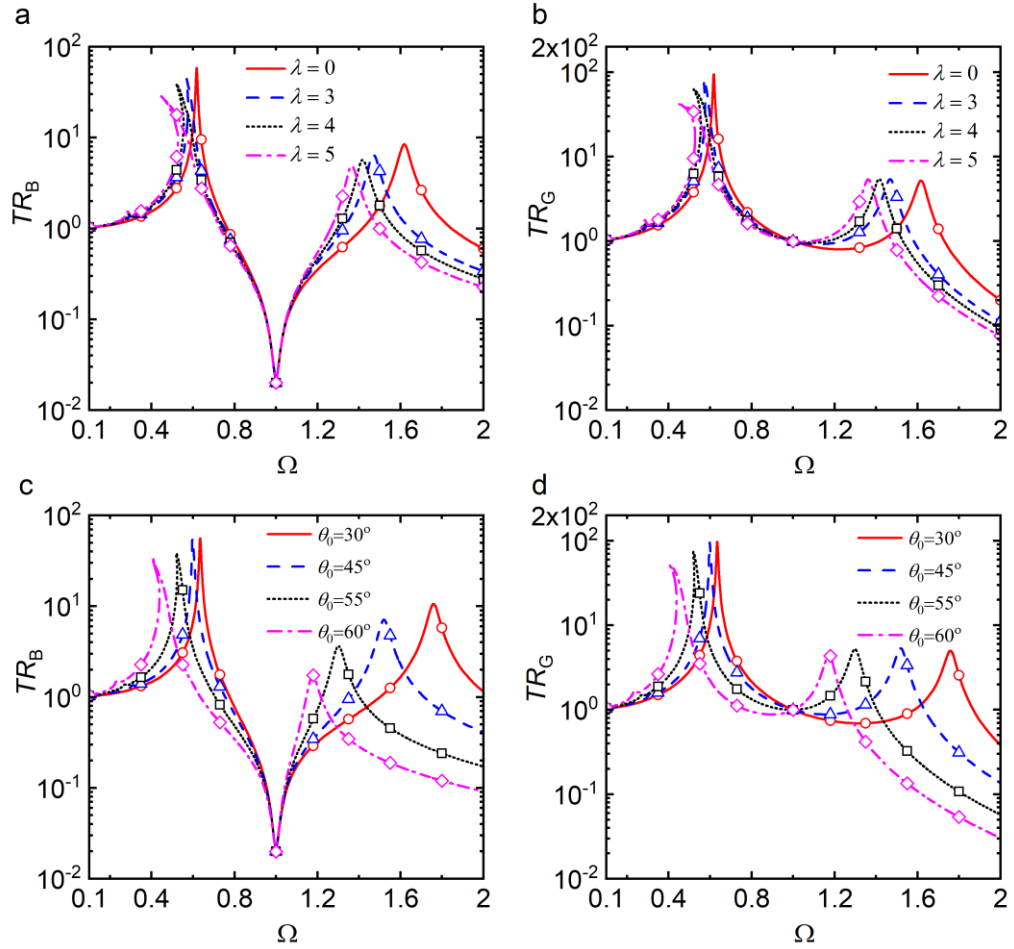


Figure 6.17. Effects of nonlinear D-spring on (a) and (c): TR_B , and on (b) and (d): TR_G . In (a) and (b), The solid, dashed, dotted and dash-dotted lines are for $\lambda = 0, 3, 4$ and 5 , respectively; in (c) and (d), The solid line, dashed line, dotted line and dash-dotted line are for $\theta_0 = 30, 45, 55$ and 60 degrees, respectively. Symbols: RK results.

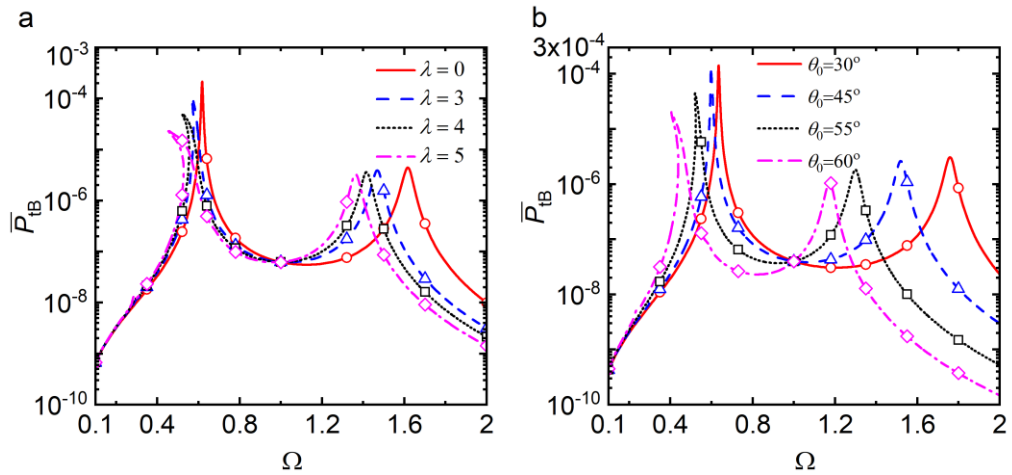


Figure 6.18. Effects of (a) the spring stiffness ratio λ and (b) the initial angle θ_0 of the nonlinear D-spring on the time-averaged transmitted power to the base structure \bar{P}_{TB} . In (a), The solid, dashed, dotted and dash-dotted lines are for $\lambda = 0, 3, 4$ and 5 , respectively; in (b), The solid, dashed, dotted and dash-dotted lines are for $\theta_0 = 30, 45, 55$ and 60 degrees, respectively. Symbols: RK results.

In Fig. 6.18(a) and (b), the influence of the stiffness ratio λ and the initial angle θ_0 on the time-averaged power transmission \bar{P}_{tB} to the base structure is examined, respectively. Two peaks are observed in each curve of \bar{P}_{tB} . Fig. 6.18(a) shows that by using the nonlinear D-spring, both peaks in each curve of the time-averaged transmitted power to the base structure are reduced moderately, indicating a vibration suppression effect by the D-spring. As the value of the stiffness ratio λ increases from 3 to 4 and to 5, the first peak of transmitted power bends to the low-frequency range and the peak value is further reduced. In contrast, the second peak value of \bar{P}_{tB} only shows a slight reduction although the peak frequency is largely decreased. Fig. 6.18(b) shows that by increasing initial angle of the D-spring θ_0 from 30 to 45, to 55 and to 60 degrees, both peaks of the \bar{P}_{tB} curve shift to the low-frequency range with the corresponding peak values reduced. This characteristic shows the possibility of tailoring the vibration power transmission by adjusting the design parameters of the nonlinear D-spring in a direct way. Fig. 6.18 also shows that with the D-spring, there is a substantial reduction in the values of \bar{P}_{tB} when the excitation frequency is high (i.e. $\Omega > 1.7$). Combining the force transmissibility result presented in Fig. 6.17, it can be summarized that a larger value of the λ or θ_0 of the D-spring can enhance the vibration isolation performance of the 2DOF system.

Figure. 6.19(a-d) presents the effects of the distance Y_1 of the D-spring on the steady-state response amplitude of the machine mass X_{1_amp} , the force transmissibility TR_B to the base structure, the force transmissibility TR_G to the fixed ground and time-averaged transmitted power to the base structure \bar{P}_{tB} , respectively. An anti-peak can be found in the each curve of X_{1_amp} and TR_B , which is corresponding to the in-phase mode of the linear system without the D-spring. Fig. 6.19(a) shows that with a decreasing distance Y_1 from 0.6 to 0.5, to 0.4 and to 0.3, both peaks and the anti-resonance peak of X_{1_amp} shift significantly to the low frequencies. This is again due to the stronger negative stiffness effect by the nonlinear D-spring when decreasing the Y_1 . Moreover, the first peak is bending more to the left and the value of the first peak is increased. In contrast, there is a substantial reduction in the second peak value as well as the absolute value of the anti-peak. Fig. 6.19(b) and (c) shows that as the value of distance Y_1 decreases from 0.6 to 0.3, both peaks for each curve of TR_B and TR_G shifts more to the lower frequency range with their corresponding peak values reduced significantly, which can contribute to the suppression of the vibration transmission between the sub-structures. It is also found that the first peaks of the TR_B and TR_G curves near $\Omega = 0.5$ bend more to the low frequencies due to the non-monotonic

relationship between the restoring force and the distance Y of the D-spring. In comparison, it is also noticed from Fig. 6.19(b) that the anti-peak in the curve of TR_B shows little changes at $\Omega \approx 1$ under the variations of Y_1 . Fig. 6.19(d) shows that a decrease of Y_1 can lead to a smaller peak time-averaged power transmission \bar{P}_{tB} to the base structure. The peak values and peak frequencies of both peaks in the curve of \bar{P}_{tB} are reduced with the decreasing Y_1 , showing an improvement to the effectiveness of the vibration isolation. From Fig. 6.19(b-d), it is summarized that a smaller value of Y_1 can reduce the vibration transmission from the machine to the base and from the base to the ground when the excitation frequency is high.

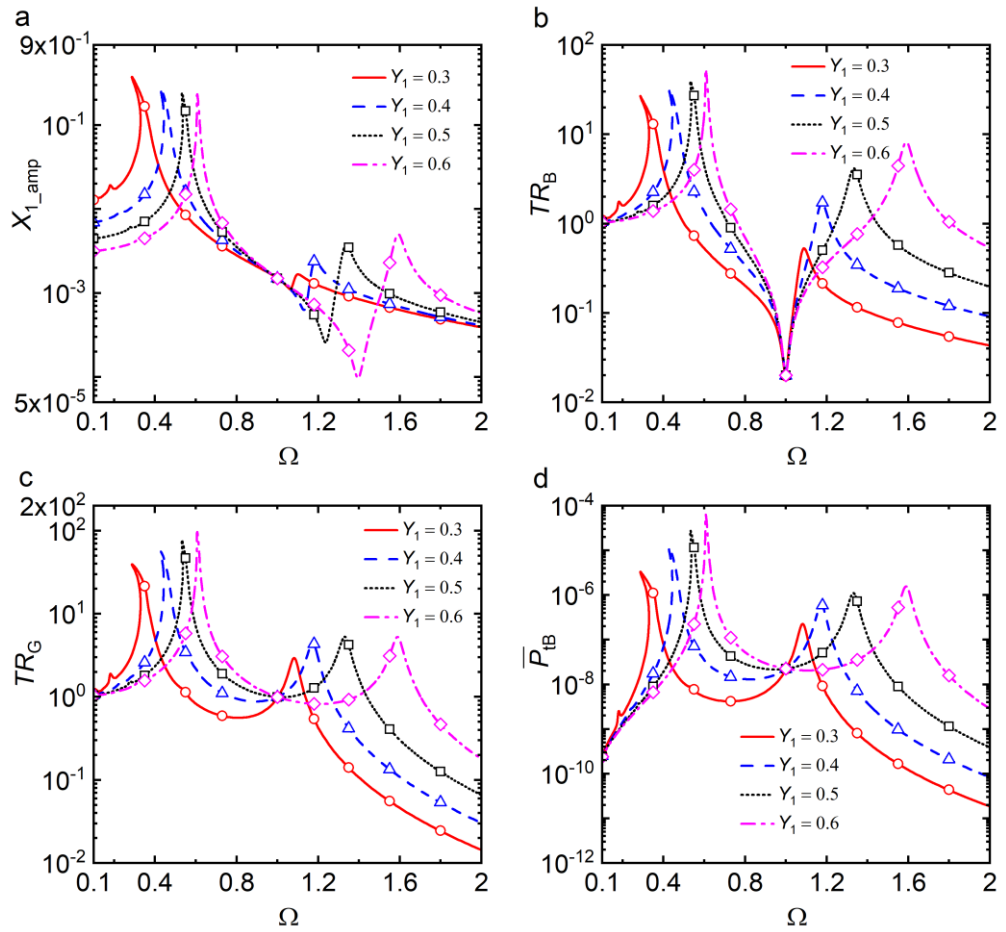


Figure 6.19. Effects of the terminals distance Y_1 of the D-spring on (a) the response amplitude X_{1_amp} , (b) the force transmissibility to the base structure TR_B , (c) the force transmissibility to the ground TR_G and (d) the time-averaged transmitted power to the base structure \bar{P}_{tB} . The solid, dashed, dotted and dash-dotted lines are for $Y_1 = 0.3, 0.4, 0.5$ and 0.6 , respectively. Symbols: RK results.

In Fig. 6.20(a-c) the effects of the stiffness ratio λ , the initial angle θ_0 and the distance Y_1 on the power transmission ratio R_{tB} , i.e. the portion of input power that is transmitted from the machine to the base structure, are examined, respectively. Fig. 6.20(a) shows that when the nonlinear D-spring is used, the power transmission ratio R_{tB}

to the base structure is substantially reduced at the frequencies away from the resonance, which benefits the vibration isolation performance. Moreover, there is a local minimum point of R_{tB} near $\Omega = 0.6$. With the increase of stiffness ratio λ from 3 to 4 and to 5, the R_{tB} is reduced in a broad frequency band and the value of the local minimum is decreased. There is a larger reduction effect on the R_{tB} by increasing λ when the excitation frequency is away from $\Omega \approx 1$. Fig. 6.20(b) and (c) shows that an increase of the initial angle θ_0 or the distance Y_1 can substantially reduce the portion of input power that is transmitted to the base structure when away from $\Omega \approx 1$. In Fig. 6.20(b) and (c), an extra peak can be observed near $\Omega = 0.4$ when the value of θ_0 is high or the value of Y_1 is small, which is related to the presence of the super-harmonic response components.

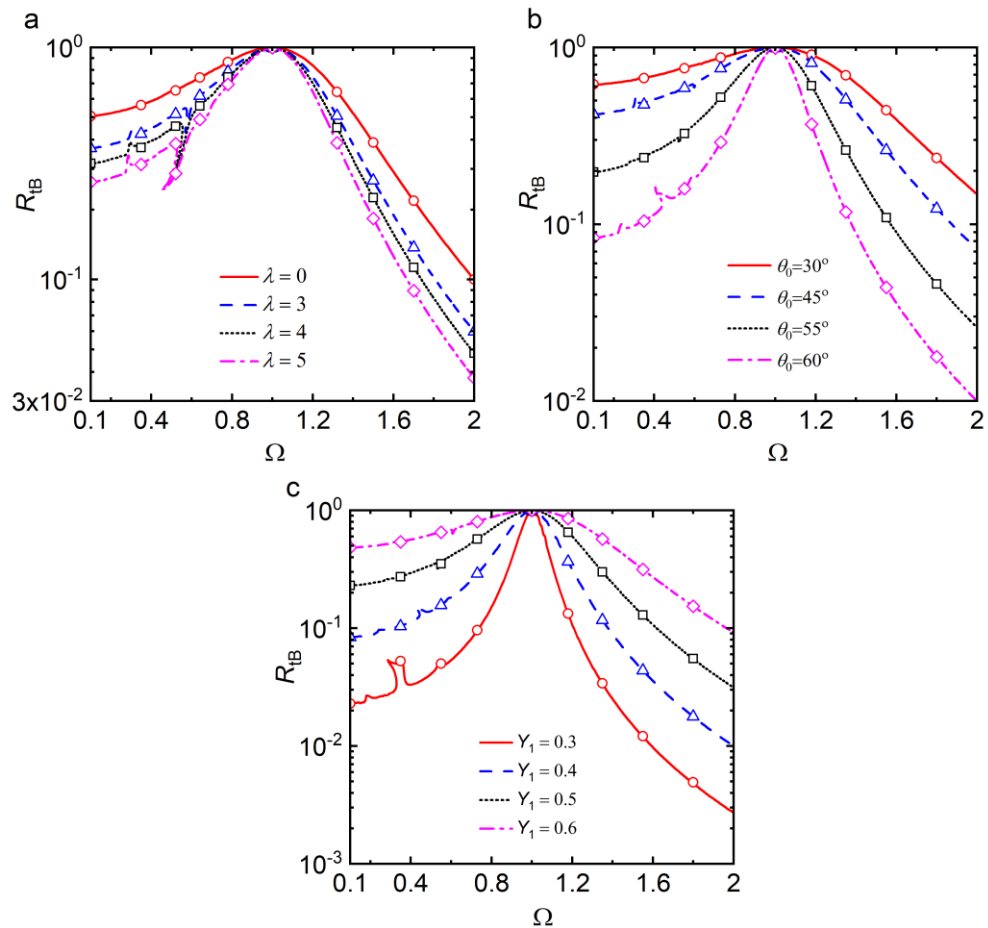


Figure 6.20. Effects of (a) the spring stiffness ratio λ and (b) the initial angle θ_0 and (c) the terminals distance Y_1 of the nonlinear D-spring on the power dissipation ratio R_{tB} . In (a), The solid, dashed, dotted and dash-dotted lines are for $\lambda = 0, 3, 4$ and 5 , respectively; in (b), The solid, dashed, dotted and dash-dotted lines are for $\theta_0 = 30, 45, 55$ and 60 degrees, respectively; in (c), The solid, dashed, dotted and dash-dotted lines are for $Y_1 = 0.3, 0.4, 0.5$ and 0.6 , respectively. Symbols: RK results.

It is also found from Fig. 6.20 that the variations of λ , θ_0 or Y_1 have little influence on the value of R_{tB} near $\Omega = 1$. The reason for this phenomenon is that the responses

of the machine mass m_1 and base mass m_2 are in-phase at this frequency, leading to a small relative displacement between the two masses and hence small changes in the distance Y between the terminals of the D-spring. Therefore there is negligible effect of D-spring on the power transmission from machine to the base at the in-phase mode frequency of the corresponding linear system.

6.5. Summary

This chapter investigated the force transmissibility and power flow behaviour of a nonlinear vibration isolator with a nonlinear D-spring. The D-spring with geometric stiffness nonlinearity consists of a linear spring and a DSLM. The effectiveness of using the proposed nonlinear isolator in SDOF and 2DOF systems subjected to force or base-motion excitations has been examined by using vibration force transmissibility and power flow indices.

The introduction of the D-spring into the linear isolation system can benefit the vibration isolation, which is demonstrated by following findings:

- (1) For the SDOF isolation system under force excitations or base excitations, the addition of the D-spring can shift the peaks in curves of force/displacement transmissibility, kinetic energy and time-averaged input power to low frequencies as well as bend the peaks of those curves to the low-frequency range.
- (2) For the isolation of base-motion excitations, the peak values in the curves of frequency response, displacement transmissibility, kinetic energy and time-averaged input power are reduced.
- (3) For the 2DOF isolation system under force excitations, the use of nonlinear D-spring can shift both peaks in the curves of force transmissibility and time-averaged power transmission towards low frequencies with potential reductions in the peaks values.
- (4) The power transmission in the 2DOF isolation system is reduced at high frequencies and the power transmission ratio is also substantially decreased when the excitation frequency is away from the in-phase mode of the corresponding linear system.

Chapter 7

Vibration transmission and energy flow analysis of oscillators with Coulomb friction element

Dry friction is a typical type of non-smooth nonlinearity which can be found in many dynamic systems having contact surfaces with relative motion, such as turbine blade joints (Claeys et al., 2016), robot joints (Qian et al., 2018), electric motors (Hong et al., 2019) and brake system (Awrejcewicz and Olejnik, 2005). The friction oscillator has been widely used as a representative model for investigating the dynamic behaviour of the engineering systems with dry friction non-smoothness (Popp, 1998). The Coulomb friction law is commonly selected to predict the nonlinear dry friction effect (Mostaghel, 2005). In the Coulomb friction model, the dry friction force is a discontinuous function of velocity and the friction coefficient varies with velocity. This discontinuity in the friction oscillators can lead to rich nonlinear phenomena such as bifurcations with unstable branches (Oestreich et al., 1996) and chaos (Feeny and Moon, 1994). In most cases, the dry friction force is unwanted due to the introduction of nonlinear complexity to the dynamics of the system, the dissipative effect on the kinetic energy and the generation of wear on the contacting surfaces (Marques et al., 2016). However, there are also many useful applications of dry friction, e.g. the contact between the tyres of a vehicle and the road. Given the energy dissipation effect, the friction within mechanical systems can be treated as frictional damper, which may enhance the system performance such as passive vibration control (Marino et al., 2019; Gaul and Nitsche, 2001). Krack et al. (2016) investigated the nonlinear modal interactions in a jointed system induced by friction. It showed the possibility of taking advantage of friction to tune the system so as to obtain a minimum response level. While much research has been carried out on the dynamic response of nonlinear dynamic systems with friction, there are still limited studies on the effects of non-smooth dry friction force on the vibration transmission, especially on the energy transfer and dissipation within the coupled system. PFA is needed to better understand the vibration transmission and energy distribution characteristics in such systems. Guidance on the dynamic design of engineering systems comprising dry friction nonlinearity can be generated based on the findings from PFA. In this chapter, a nonlinear dry friction

element modelled by two established approaches based on Coulomb friction model is used in a SDOF oscillator and the coupling interface of a 2DOF oscillator system. The HB-AFT method with numerical continuations as well as numerical integration method is employed to investigate the vibration transmission in the oscillator systems with dry friction element. The influence of the non-smooth dry friction force on the energy input, transmission and dissipation within the SDOF and 2DOF systems is studied.

7.1. Mathematical modelling

7.1.1. Dry friction force models

Classical Coulomb friction model

Figure 7.1(a) shows a schematic of two contacting solid objects m_A and m_B . The object m_A on the top is subjected to an external force f_{ex} in the horizontal direction. A normal force exits at the contact interface. The interactive dry friction force f_c generated at the interface of the two objects can be represented by a dry friction element shown in Fig. 7.1(b) with two terminals of A and B attached to m_A and m_B , respectively. The relationship between the friction force f_c and the relative velocity v_r of the two objects can be modelled by the classical Coulomb friction model shown in Fig. 7.1(c). When there is relative motion between contact surfaces (i.e., the slip state), there exits dynamic friction force, with its direction opposite to that of the relative motion and its magnitude being the product of the coefficient of dynamic friction and the normal force at the interface. When there is no relative motion between the contacting surfaces (i.e. the stick state), there may be static friction force counteracting the external force. Mathematically, the classical Coulomb friction force is expressed as

$$f_c = \begin{cases} f_d \operatorname{sgn}(v_r), & \text{if } v_r \neq 0 \\ f_s \operatorname{sgn}(f_{ex}), & \text{if } v_r = 0 \text{ and } |f_{ex}| \geq f_s \\ f_{ex}, & \text{if } v_r = 0 \text{ and } |f_{ex}| < f_s \end{cases} \quad (7.1)$$

where f_d is the magnitude of the dynamic friction force, being the product of the coefficient of dynamic friction and the normal force, f_s is the maximum static friction force, v_r is the relative velocity of the contacting objects, f_{ex} is the resultant external force applied to object m_A in tangential direction except the friction, and $\operatorname{sgn}(v_r)$ is the signum function expressed by

$$\operatorname{sgn}(v_r) = \begin{cases} -1, & v_r < 0, \\ 0, & v_r = 0, \\ 1, & v_r > 0. \end{cases} \quad (7.2)$$

The classical Coulomb friction model introduces strong discontinuities at $v_r = 0$, which may create computational challenges for dynamic analysis. For instance, when applying a time marching method to solve dynamic governing equations, the detection of $v_r = 0$ for switching friction state may be inaccurate due to the use of discrete and variable time steps. A modified Coulomb friction model, or the so-called Karnopp model (Karnopp, 1985), is combined with the numerical integration method in this chapter. As shown in Fig. 7.1(d), compared to the classical Coulomb model, the Karnopp model assumes a region of small velocity dead zone $[-v_d, v_d]$, where the contact interface is assumed to be in stuck and the relative velocity v_r is regarded null. In this way, some of the numerical issues encountered when using the classical Coulomb model may be avoided and the main characteristics of the friction model can still be captured. The Karnopp friction model is expressed as

$$f_c = \begin{cases} f_d \operatorname{sgn}(v_r), & \text{if } |v_r| > v_d \\ f_s \operatorname{sgn}(f_{ex}), & \text{if } |v_r| \leq v_d \text{ and } |f_{ex}| \geq f_s \\ f_{ex}, & \text{if } |v_r| \leq v_d \text{ and } |f_{ex}| < f_s \end{cases} \quad (7.3)$$

As in many applications $f_d \approx f_s$, it is assumed that $f_d = f_s$ throughout the chapter.

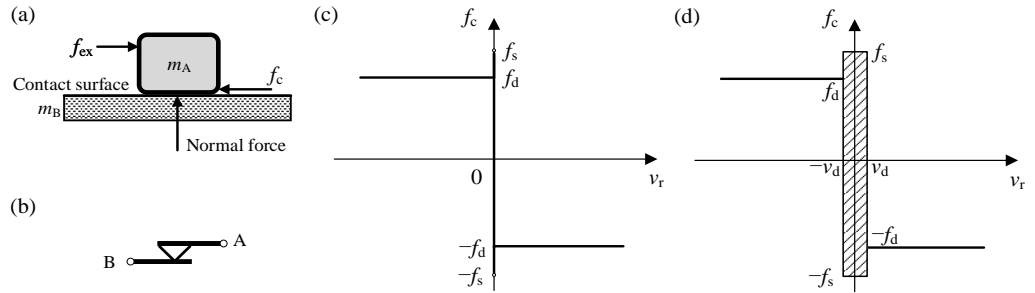


Figure 7.1. Schematic of (a) dry friction between two solid contacting bodies, (b) dry friction element, (c) the classical Coulomb model and (d) the Karnopp model.

Smooth Coulomb model

The classical Coulomb friction force model contains discontinuities at $v_r = 0$, a smooth Coulomb friction model can be used to facilitate the implementation of analytical approximation methods for dynamic analysis of systems with frictions (Pennestrì et al., 2016). The discontinuous classical Coulomb model is replaced with a regularized hyperbolic tangent curve with the friction force expressed by

$$f_c = f_d \tanh\left(\frac{v_r}{\epsilon}\right) = f_d \frac{\exp(\frac{v_r}{\epsilon}) - \exp(-\frac{v_r}{\epsilon})}{\exp(\frac{v_r}{\epsilon}) + \exp(-\frac{v_r}{\epsilon})}, \quad (7.4)$$

where ϵ is the tolerance parameter of the tanh-regularization. The smooth Coulomb model can eliminate the detection of stick-slip state transitions (Mostaghel and Davis, 1997) and therefore the computational cost associated with dynamic analysis can be reduced.

Figure 7.2 shows the variations of the friction force against the relative velocity following both the classical and the smooth Coulomb model. Moreover, the influence of the selection of the tolerance parameter ϵ on the friction force of the smooth Coulomb model with respect to the relative velocity of contact surfaces is examined. Three values of ϵ in the smooth Coulomb model are selected changing from 0.1 to 0.2 and to 0.3, which are represented by different lines. A classical Coulomb friction force model defined in Eq. (7.1) is also added for comparison. The magnitude of the dynamic and static friction force for those four cases are set as $f_d = f_s = 0.06$. It is shown that a smaller value of ϵ can provide a better smooth approximation on the classical Coulomb friction force. In this chapter, the smooth Coulomb model is combined with harmonic balance approximation for simulation.

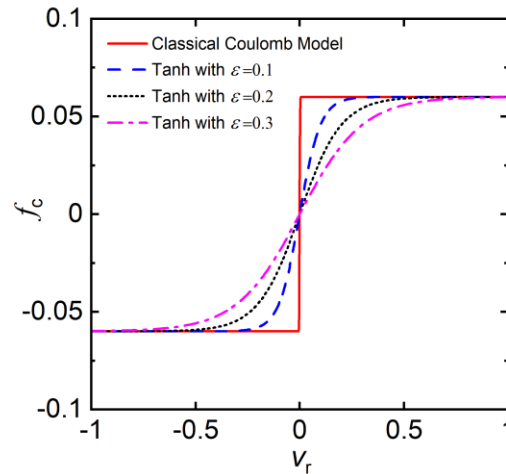


Figure 7.2. Dry friction force f_c by the classical Coulomb friction model and by the smooth Coulomb friction model. The solid line is for the classical Coulomb friction model. The dashed, dotted and dash-dotted lines are for the smooth Coulomb friction model with $\epsilon = 0.1, 0.2$ and 0.3 , respectively.

7.1.2. Dynamic analysis of systems with dry friction

For a general Q -DOF system comprising dry friction element, the non-dimensional general dynamic equation of motion can be expressed in a matrix form as

$$[\mathbf{M}]\{\mathbf{X}''\} + [\mathbf{C}]\{\mathbf{X}'\} + [\mathbf{K}]\{\mathbf{X}\} + \{\mathbf{F}_c(\Delta(\mathbf{X}'))\} = \{\mathbf{F}_{ef}(\tau)\}, \quad (7.5)$$

where $\{\mathbf{X}\}$, $\{\mathbf{X}'\}$ and $\{\mathbf{X}''\}$ denote the displacement, velocity and acceleration response vectors, respectively, $[\mathbf{M}]$, $[\mathbf{C}]$ and $[\mathbf{K}]$ are the mass, damping and stiffness matrices,

respectively, $\{\mathbf{F}_c(\Delta(X'))\}$ is the dimensionless nonlinear friction force induced by dry friction element and $\Delta(X')$ is the relative velocity between the two terminals of the element, $\{\mathbf{F}_{ef}(\tau)\}$ is the harmonic force excitation applied to the q -th DOF ($1 \leq q \leq Q$) of the system with $\{\mathbf{F}_{ef}(\tau)\} = \{\dots, F_0 e^{i\Omega\tau}, \dots\}^T$, of which F_0 and Ω are the non-dimensional force amplitude and excitation frequency, respectively, and τ is the dimensionless time.

For the numerical determination of the steady-state response of the system, the nonlinear friction force $\{\mathbf{F}_c(\Delta(X'))\}$ in Eq. (7.5) can be firstly modelled by the Karnopp model and the Eq. (7.5) can then be solved by the 4th order Runge-Kutta (RK) method. The energy dissipation and the force transmission between sub-systems can then be determined. It should be mentioned that the Karnopp model may be more efficient and accurate than the classical Coulomb model from numerical aspects. However, the resultant external force, which is needed in the Karnopp model, may be difficult to define in a multi-DOF system (i.e. $Q > 2$) (Pennestrì et al., 2016).

As for comparison, the harmonic balance (HB) approximation method is also used for obtaining the steady-state periodic response of the system with dry friction element. Here the dry friction force $\{\mathbf{F}_c(\Delta(X'))\}$ in Eq. (7.5) can be modelled by the smooth Coulomb friction model considering the continuous relationship between the friction force and the relative velocity. The steady-state displacement response $\{\mathbf{X}\}$ and the nonlinear friction force $\{\mathbf{F}_c\}$ can be approximated by a truncated N -order Fourier series with a fundamental frequency of Ω :

$$\{\mathbf{X}\} = \left\{ \sum_{n=0}^N \tilde{R}_{(1,n)} e^{in\Omega\tau}, \dots, \sum_{n=0}^N \tilde{R}_{(q,n)} e^{in\Omega\tau}, \dots, \sum_{n=0}^N \tilde{R}_{(Q,n)} e^{in\Omega\tau} \right\}^T, \quad (7.6a)$$

$$\{\mathbf{F}_c(\Delta(X'))\} = \left\{ \sum_{n=0}^N \tilde{H}_{(1,n)} e^{in\Omega\tau}, \dots, \sum_{n=0}^N \tilde{H}_{(q,n)} e^{in\Omega\tau}, \dots, \sum_{n=0}^N \tilde{H}_{(Q,n)} e^{in\Omega\tau} \right\}^T, \quad (7.6b)$$

where $\tilde{R}_{(q,n)}$ and $\tilde{H}_{(q,n)}$ are the complex Fourier coefficient of the n -th order Fourier approximation corresponding to the q -th DOF, $\{\mathbf{X}'\}$ and $\{\mathbf{X}''\}$ can then be obtained by taking differentiation of $\{\mathbf{X}\}$ with respect to time τ . To determine the Fourier coefficients \tilde{H} of the nonlinear friction force $\{\mathbf{F}_c(\Delta(X'))\}$ in Eq. (7.6b), the Alternating-Frequency-Time (AFT) technique can be used, which has been illustrated in Chapter 3.

After the determination of the Fourier coefficients \tilde{H} , the Eq. (7.6) can be substituted into the governing equation of Eq. (7.5) and by balancing the corresponding coefficients of the n -th ($0 \leq n \leq N$) order harmonic terms of the resultant equation, we have

$$(-(n\Omega)^2[\mathbf{M}] + i(n\Omega)[\mathbf{C}] + [\mathbf{K}])\{\tilde{\mathbf{R}}_n\} = \{\tilde{\mathbf{S}}_n\} - \{\tilde{\mathbf{H}}_n\}, \quad (7.7)$$

where $\{\tilde{\mathbf{R}}_n\} = \{\tilde{R}_{(1,n)}, \dots, \tilde{R}_{(q,n)}, \dots, \tilde{R}_{(Q,n)}\}^T$, $\{\tilde{\mathbf{H}}_n\} = \{\tilde{H}_{(1,n)}, \dots, \tilde{H}_{(q,n)}, \dots, \tilde{H}_{(Q,n)}\}^T$ and $\{\tilde{\mathbf{S}}_n\} = \{0, \dots, F_0, \dots, 0\}^T$. By sorting a number of N harmonics equations of Eq. (7.7), a set of real nonlinear algebraic equations with a total number of $Q(2N + 1)$ can be obtained. The Newton-Raphson iterative method can be employed to solve those equations and the arc-length continuation method presented in Chapter 3 is also used to trace the solution path in the frequency domain. Subsequently, the steady-state response of the system can be obtained. The level of force transmission and power flow behaviour within the oscillator system can then be evaluated.

For the power flow analysis of the chain oscillator system with dry friction element, the total instantaneous input vibration power into the system is product of the harmonic excitation force $F_0 e^{i\Omega\tau}$ and the corresponding velocity X'_q of the q -th DOF. Note that the velocity X'_q can be obtained by taking differentiation of Eq. (7.6a) as $X'_q = \sum_{n=0}^N in\Omega\tilde{R}_{(q,n)} e^{in\Omega\tau}$, hence we have

$$P_{\text{in}} = \Re\{X'_q\}\Re\{F_0 e^{i\Omega\tau}\} = \Re\{\sum_{n=0}^N in\Omega\tilde{R}_{(q,n)} e^{in\Omega\tau}\}\Re\{F_0 e^{i\Omega\tau}\}, \quad (7.8)$$

where symbols \Re represents the operation of taking the real part of a complex number. The steady-state time-averaged input vibration power into the system over an averaging time span τ_p is

$$\bar{P}_{\text{in}} = \frac{1}{\tau_p} \int_{\tau_0}^{\tau_0 + \tau_p} P_{\text{in}} d\tau = \frac{1}{2} F_0 \Re\{(i\Omega\tilde{R}_{(q,1)})^*\}, \quad (7.9)$$

where τ_0 and τ_p are the starting time for averaging and the averaging time span, respectively, and in the current study, τ_p is set as one period of excitation with $\tau_p = 2\pi/\Omega$, symbols $*$ denotes taking the complex conjugate of a complex number.

For the current system, the non-dimensional maximum kinetic energy K_q for the q -th DOF is defined as

$$K_q = \frac{1}{2} (|X'_q|_{\max})^2. \quad (7.10)$$

where $|X'_q|_{\max}$ is the maximum magnitude of velocity for the q -th DOF in the steady-state response.

7.2. SDOF system with friction

7.2.1. Dynamic response

In this section, the dynamics and vibration transmission as well as energy dissipation characteristics of a single-DOF (SDOF) system (i.e., $Q = 1$) with dry friction is studied. Fig. 7.3(a) shows an SDOF oscillator comprising a mass m_1 , a viscous damper with damping coefficient c_1 , a linear spring with stiffness coefficient k_1 and a dry friction element with friction force f_c and magnitude of f_d . The whole system is placed on a horizontal plane. The mass is subjected to a harmonic force excitation with the forcing amplitude f_0 and frequency ω . The equilibrium position of the mass, where the spring k_1 is un-stretched, is set as a reference with $x_1 = 0$. The dry friction element is shown in Fig. 7.3(b) and is placed between the mass and the left-hand wall shown in Fig. 7.3(a). The dry friction element in Fig. 7.3(a) can be replaced by a viscous damper element with damping coefficient c_d so as to facilitate comparisons of their effects on the system dynamics and vibration transmission.

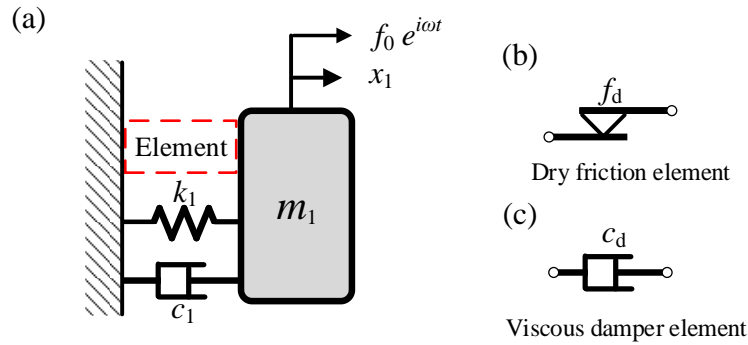


Figure 7.3. (a) A SDOF oscillator with (a) a dry friction element and (b) a viscous damper element.

The governing equation of the system can be written as

$$m\ddot{x}_1 + k_1 x_1 + c_1 \dot{x}_1 + f_c = f_0 e^{i\omega t}, \quad (7.11)$$

where f_c is the nonlinear dry friction force. When the Karnopp model is used, we have $v_r = \dot{x}_1$ and $f_{ex} = f_0 \cos \omega t - k_1 x_1 - c_1 \dot{x}_1$ in Eq. (7.3).

The following parameters are introduced for the later parametric study:

$$\omega_1 = \sqrt{\frac{k_1}{m_1}}, \quad \zeta_1 = \frac{c_1}{2m_1\omega_1}, \quad X_1 = \frac{x_1}{l_0}, \quad \rho = \frac{c_d}{c_1}, \quad F_0 = \frac{f_0}{k_1 l_0},$$

$$\Omega = \frac{\omega}{\omega_1}, \quad \tau = \omega_1 t, \quad F_d = \frac{f_d}{k_1 l_0}, \quad \eta = \frac{\epsilon}{\omega_1 l_0}, \quad V_d = \frac{v_d}{\omega_1 l_0}$$

where ω_1 and ζ_1 are the undamped natural frequency and the damping ratio of the system without considering the friction, respectively, l_0 is the un-stretched length of the spring on the left, X_1 is the non-dimensional displacement of the mass, ρ is used to represent the damping level of the viscous damper element which is used to replace the dry friction element for comparison purpose, F_0 and Ω are the dimensionless external force-excitation amplitude and frequency, respectively, τ is the dimensionless time, F_d is the non-dimensional magnitude of the dynamic dry friction force and is named dynamic friction force hereafter, η is the ratio of tolerance parameter of tanh-regularization in the smooth Coulomb model and V_d is the dimensionless boundary velocity of the dead zone in the Karnopp model. By using those defined parameters, the Eq. (7.11) can be transformed into a non-dimensional form, described as

$$X_1'' + X_1 + 2\zeta_1 X_1' + F_c = F_0 e^{i\Omega\tau}, \quad (7.12)$$

where the prime denotes differentiation with respect to τ , F_c is the non-dimensional friction force expressed by

$$F_c = \begin{cases} F_d \operatorname{sgn}(X_1'), & \text{if } |X_1'| > V_d \\ F_d \operatorname{sgn}(F_{\text{ex}}), & \text{if } |X_1'| \leq V_d \text{ and } |F_{\text{ex}}| \geq F_d \\ F_{\text{ex}}, & \text{if } |X_1'| \leq V_d \text{ and } |F_{\text{ex}}| < F_d \end{cases}$$

based on the Karnopp model,

$$\text{or } F_c = F_d \frac{\exp(\frac{X_1'}{\eta}) - \exp(-\frac{X_1'}{\eta})}{\exp(\frac{X_1'}{\eta}) + \exp(-\frac{X_1'}{\eta})} \quad \text{based on the smooth Coulomb model,}$$

and $F_{\text{ex}} = F_0 \cos \Omega\tau - X_1$ is the non-dimensional resultant external force. It is noted that for the corresponding case of using the viscous damper element to replace the friction element, the friction force F_c in Eq. (7.12) can be replaced with the damping force $F_{\text{cd}} = 2\rho\zeta_1 X_1'$ by the viscous damper element.

To solve Eq. (7.12), the HB-AFT method with numerical continuations described in Subsection 7.1.2 can be employed with the friction element force F_c estimated by the smooth Coulomb model. The steady-state response results can be compared to those obtained from 4th order RK method with F_c determined by the Karnopp model.

In Fig. 7.4, the effects of the dry friction on the steady-state response amplitude X_{1_amp} of the mass are investigated. Fig. 7.4(a) presents the curves of X_{1_amp} in the frequency range of $0 < \Omega < 2$ and Fig. 7.4(b) shows an enlarged view of Fig. 7.4(a) in the range of $1.5 < \Omega < 2$. Cases one and two consider the presence of dry friction element with the dynamic friction force F_d being 0.02 and 0.04, respectively, while setting $\rho = 0$. Cases three and four correspond to linear systems without friction (i.e., $F_d = 0$) with the damping ratio ρ of the viscous damper element set as $\rho = 0$ and $\rho = 2$, respectively. Other parameters are set as $\zeta_1 = 0.01$, $V_d = 1 \times 10^{-4}$, $\eta = 1 \times 10^{-4}$ and $F_0 = 0.1$. The results obtained by HB method using smooth Coulomb friction model are represented by different types of lines, while those obtained by the RK method using Karnopp friction model are denoted by symbols for comparison. With a balanced consideration of the accuracy and the computational efficiency, the order N used in HB-AFT approximations is set as 7 throughout the chapter. The figure shows that the HB-AFT results agree well with the RK results.

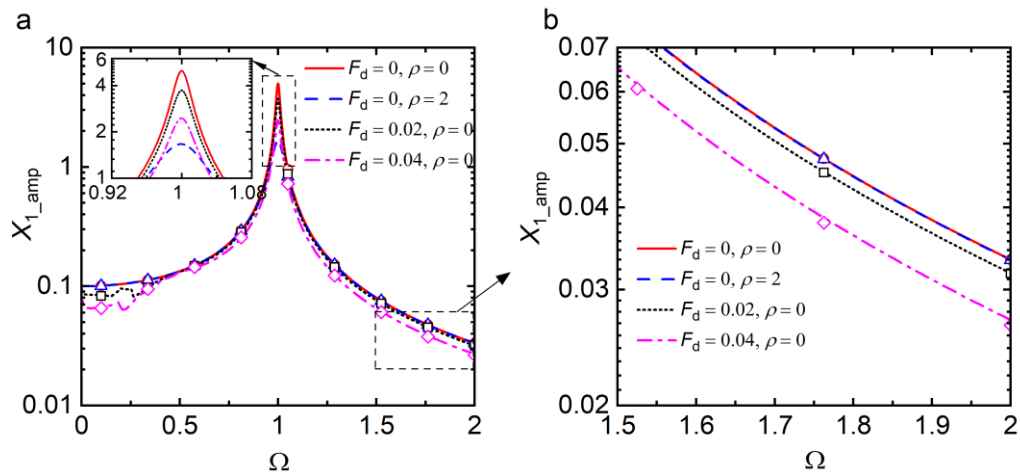


Figure 7.4. Effects of the dynamic friction force F_d on the steady-state response amplitude X_{1_amp} . The solid and dashed lines are for the linear system with $\rho = 0$ and 2, respectively. The dotted and dash-dotted lines are for the nonlinear system having dry friction element with $F_d = 0.02$ and 0.04, respectively.

Figure 7.4 shows that by comparing to the linear system with $F_d = \rho = 0$, the addition of the dry friction element can suppress the steady-state response amplitude X_{1_amp} of the mass in a broad frequency band. In contrast, the use of the viscous damper element with $\rho = 2$ can only reduce the vibration response near the resonant peak frequency. The viscous damper element can have a better vibration suppression effect on the peak value of X_{1_amp} than the friction element. However, when the excitation frequency is away from the resonant peak, the friction element can reduce the values of X_{1_amp} while the viscous damper element has little influence on the X_{1_amp} . The reason for this behaviour is further explored in later content. Fig. 7.4 also shows that as the

dynamic friction force F_d increases from 0.02 to 0.04, there is a stronger suppression effect on the X_{1_amp} in the whole frequency range.

Figure 7.5 presents the steady-state time history of the responses, friction force F_c and damper force F_{cd} at particular frequencies in Fig. 7.4. In Fig. 7.5(a) and (b), the system with a dry friction element is investigated with $F_d = 0.04$ and $\rho = 0$, while in Fig. 7.5(c) and (d), the system with a viscous damper element is examined by setting $F_d = 0$ and $\rho = 2$. The system parameters are set as $\zeta_1 = 0.01$, $V_d = 1 \times 10^{-4}$, $\eta = 1 \times 10^{-4}$ and $F_0 = 0.1$, which are the same as those used in Fig. 7.4. The results are obtained by the RK method based on Karnopp model.

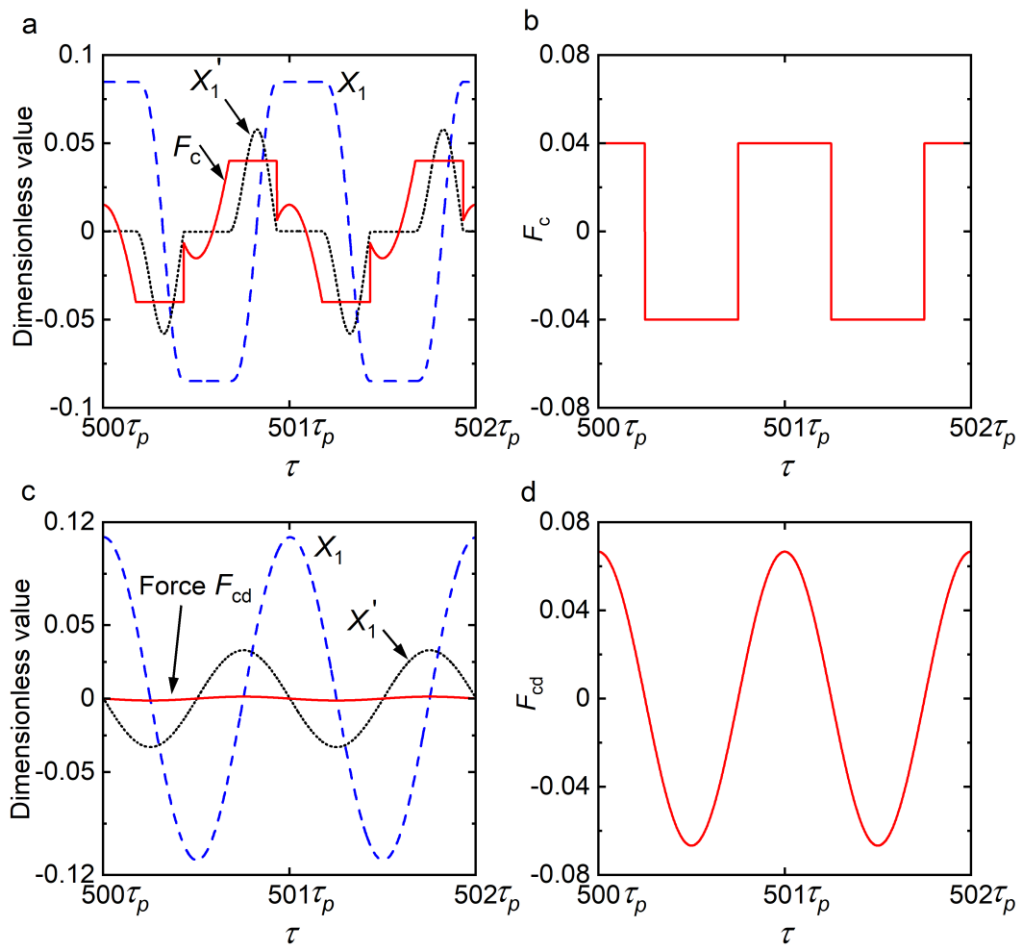


Figure 7.5. Time history of element force and response for friction element case in (a) and (b) with $F_d = 0.04$ and $\rho = 0$, and for viscous damper case in (c) and (d) with $F_d = 0$ and $\rho = 2$. The excitation frequency in (a) and (c) is $\Omega = 0.3$, while in (b) and (d) is $\Omega = 1$.

Fig. 7.5(a) and (c) shows the responses and element force with respect to the dimensionless time at a low excitation frequency, i.e. $\Omega = 0.3$. Fig. 7.5(a) shows that at low frequencies, the system with the dry friction element can exhibit stick-slip behaviour in steady-state motion. By a comparison to the damping force F_{cd} of the viscous damper element in Fig. 7.5(c), it is found that the friction element generates a

much larger amplitude of the friction force than the damping force of the damper element. This is due to that the damping force F_{cd} is a function of velocity. Since the velocity is small in low frequencies, a relatively small damping force is induced by the viscous damper element. As a result, at low frequencies away from the resonance, the friction element can provide a better vibration suppression performance than the viscous damper element. Fig. 7.5(b) and (d) presents the element force against dimensionless time when the system is excited at $\Omega = 1$. Fig. 7.5(b) shows that the amplitude of the friction force F_c remains as $F_c = F_d = 0.04$ which is independent of the excitation frequency, while Fig. 7.5(d) shows that there is a significant growth in the amplitude of damping force F_{cd} of the viscous damper element at $\Omega = 1$ compared to the amplitude of F_{cd} at $\Omega = 0.3$ shown in Fig. 7.5(c). This is due to the relatively large velocity amplitude at the resonant frequency, leading to a larger amplitude of damping force. Therefore, the viscous damper element can provide large resistance force to for the suppression of the peak value of X_{1_amp} than the dry friction element.

7.2.2. Force transmission and power flow

For the current system, the force transmissibility TR_L can be defined as the ratio between the maximum magnitude of the transmitted force from mass m_1 to the left-hand-side (LHS) wall and the amplitude of the input force, given by

$$TR_L = \frac{\max(|\Re\{F_{tL}\}|)}{F_0}, \quad (7.13)$$

where $F_{tL} = F_c + X_1 + 2\zeta_1 X_1'$ represents the non-dimensional transmitted force from mass m_1 to the LHS wall, F_c is the dry friction force of the friction element and it can be replaced with the damping force F_{cd} by the viscous damper element. For enhanced vibration suppression, a low value of force transmissibility is desirable.

The instantaneous input power P_{in} and time-averaged input power \bar{P}_{in} as well as the maximum kinetic energy K_1 of the mass m_1 can be obtained from Eqs. (7.9), (7.10) and (7.11) with $q = 1$, respectively. The instantaneous dissipated power P_{d1} by the system damper c_1 , and the instantaneous dissipated power P_{de} by the additional viscous damper element or the dry friction element are expressed as

$$P_{d1} = 2\zeta_1(\Re\{X_1'\})^2, \quad P_{de} = \begin{cases} 2\zeta_1\rho(\Re\{X_1'\})^2, & \text{For the damper element} \\ \Re\{X_1'\}\Re\{F_c\}, & \text{For the friction element} \end{cases} \quad (7.14a, 7.14b)$$

respectively, and X'_1 is obtained by the differentiation of X_1 from Eq. (7.6a) as $X'_1 = \sum_{n=0}^N in\Omega\tilde{R}_{(1,n)}e^{in\Omega\tau}$. The corresponding time-averaged dissipated power are

$$\bar{P}_{d1} = \frac{1}{\tau_p} \int_{\tau_0}^{\tau_0+\tau_p} P_{d1} d\tau, \quad \bar{P}_{de} = \frac{1}{\tau_p} \int_{\tau_0}^{\tau_0+\tau_p} P_{de} d\tau, \quad (7.15a, 7.15b)$$

respectively. The power dissipation ratio provides the proportion of vibration energy dissipated within the total input energy into the system. The corresponding power dissipation ratios are

$$R_{d1} = \frac{\bar{P}_{d1}}{\bar{P}_{in}}, \quad R_{de} = \frac{\bar{P}_{de}}{\bar{P}_{in}}, \quad (7.16a, 7.16b)$$

respectively, it is noted that according to the conservation of energy, over a cycle of periodic response, we have $R_{d1} + R_{de} = 1$.

In Figs 7.6, 7.7 and 7.8, the influence of the dynamic friction force of the dry friction element on the force transmissibility, power flow behaviour and the maximum kinetic energy of the mass is investigated, respectively. Case one and two examine the system having dry friction element with the dynamic friction force chosen as $F_d = 0.02$ and 0.04 , respectively, while the damping ratio is set as $\rho = 0$. For comparison purpose, case three and four are the corresponding linear systems neglecting friction force (i.e., $F_d = 0$) with the damping ratio of the viscous damper element set as $\rho = 0$ and $\rho = 2$, respectively. The HB-AFT results using smooth Coulomb friction model are represented by different types of lines while the RK results using Karnopp friction model are denoted by different symbols.

Figure 7.6 shows that when the dry friction element is added into the system, compared with the linear system with $F_d = \rho = 0$, the values of the force transmissibility TR_L is reduced near the peak frequency $\Omega = 1$ while increased in the low/high-frequency range away from the peak frequency. This is due to the nonlinearity of the discontinuous friction force introduced into the system. At the peak frequency, the amplitudes of the displacement and velocity responses are suppressed due to the friction force, resulting in a smaller transmitted force F_{tL} to the LHS wall and a smaller value TR_L . In the high/low-frequency range, the response amplitude is smaller while the amplitude of the friction force is not changed shown in Fig. 7.5(a), which can lead to a larger amplitude of the F_{tL} as well as a larger value of TR_L compared to that of linear systems. By comparing to the linear system comprising a replacement viscous damper element with $\rho = 2$, the systems with friction element show a higher peak of TR_L and larger values of TR_L when the excitation frequency is away from peak

frequency. It is suggested that the friction element can be more effective than the damper element in adjusting force transmission when the frequency is high. With the dynamic friction force F_d increasing from 0.02 to 0.04, the peak value of TR_L is decreased while there is a significant increase in the values of TR_L at high frequencies. It is also found that in the frequency band from $\Omega \approx 0.15$ to $\Omega \approx 0.35$, there are fluctuations in the TR_L curves of two friction element cases. The values of TR_L for the friction element case with $F_d = 0.02$ can become higher than the those in the case with $F_d = 0.04$. This is due to that, a smaller dynamic friction force, i.e. $F_d = 0.02$, provides a smaller suppression effect on the response displacement at this frequency. Therefore, it can lead to a larger amplitude of the response displacement and hence a larger maximum restoring force of the linear spring. Consequently the magnitude of the total transmitted force can be increased, resulting in a larger value of TR_L .

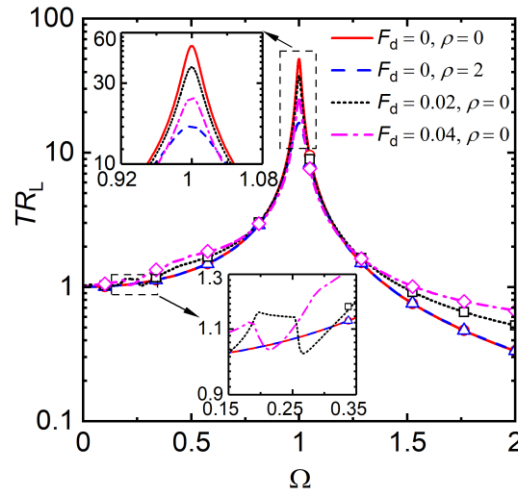


Figure 7.6. Effects of the dynamic friction force F_d on the force transmissibility TR_L . The solid and dashed lines are for the linear system with $\rho = 0$ and 2, respectively. The dotted and dash-dotted lines are for the nonlinear system having dry friction element with $F_d = 0.02$ and 0.04, respectively.

In Fig. 7.7(a) and (b), the effects of the dry friction on the time-averaged input power \bar{P}_{in} into the oscillating system and maximum kinetic energy K_1 of the mass are studied, respectively. Fig. 7.7(a) shows that when friction exists in the system, the peak value of \bar{P}_{in} shows a slight decrease compared with the linear system with $F_d = \rho = 0$. However, when the excitation frequency is away from the peak frequency, there is a substantial increase in the amount of input power into the oscillating system. The reason for this phenomenon will be further explored in later content. Compared to the corresponding case of using a replacement viscous damper element, it is found that the peak value of \bar{P}_{in} in dry friction element cases is close to that of viscous damper element case. However, the dry friction element leads to much larger values of \bar{P}_{in} than the viscous damper element at low or high excitation frequencies. With the increase of the

dynamic friction force F_d from 0.02 to 0.04, the peak value of \bar{P}_{in} is reduced because of the lower velocity amplitude at the resonance frequency due to the stronger frictional resistance, while the values of \bar{P}_{in} is increased when away from the peak. Fig. 7.7(b) shows that the dry friction element can lead to a slight reduction in the peak value of the maximum kinetic energy K_1 . In the frequency range between $\Omega \approx 0.15$ and $\Omega \approx 0.5$, the values of K_1 in friction element cases become larger than those of linear system cases. By a comparison of the time history of the response velocity of the mass between the systems comprising friction element or the viscous damper element at $\Omega = 0.3$ shown in Fig. 7.5(a) and (c), respectively, it is found that the use of friction element can yield a larger maximum velocity of the mass, leading to larger kinetic energy in this frequency band. Fig. 7.7(b) also shows that in the high-frequency range, the addition of the dry friction element can reduce the values of K_1 due to a larger friction damping force. Moreover, an increase of the dynamic friction force F_d from 0.02 to 0.04 can slightly lower the peak height of K_1 and reduce the values of K_1 at high frequencies. However, the values of K_1 become slightly larger with the increasing F_d when Ω locates approximately between 0.25 and 5.

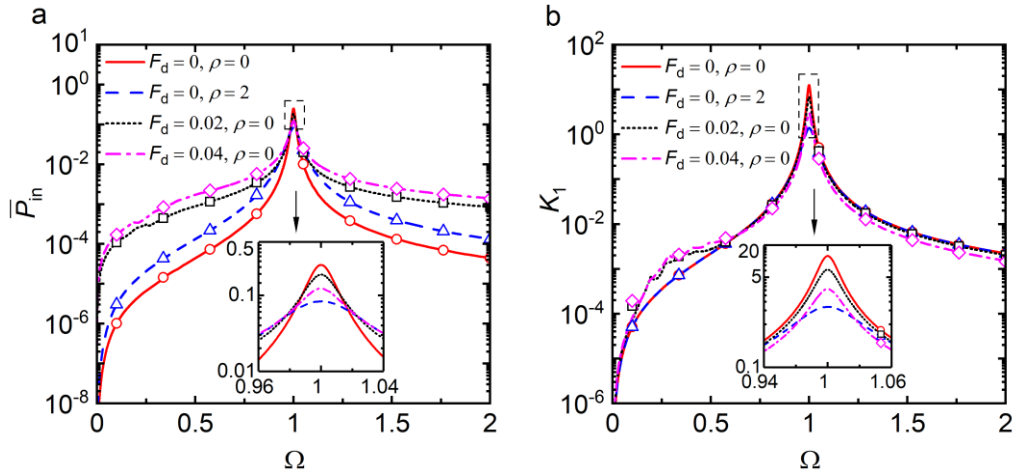


Figure 7.7. Effects of the dynamic friction force F_d on (a) the time-averaged input power \bar{P}_{in} and (b) the maximum kinetic energy K_1 . The solid and dashed lines are for the linear system with $\rho = 0$ and 2, respectively. The dotted and dash-dotted lines are for the nonlinear system having dry friction element with $F_d = 0.02$ and 0.04, respectively.

In Fig. 7.8(a) and (b), the influence of dry friction on the time-averaged dissipated power \bar{P}_{de} by the additional element and the corresponding power dissipation ratio R_{de} is investigated, respectively. Fig. 7.8(a) shows that although the peak values of dissipated power \bar{P}_{de} in the cases of using dry friction element and the case of using the viscous damper element with $\rho = 2$ are close, the dry friction element can dissipate more power than the viscous damper element when the excitation frequency is away from the resonant peak. This is because of the higher magnitude of dry friction force

than the damping force of the viscous damper element at low or high frequencies, as shown in Fig. 7.5(a) and (c). This phenomenon will be further discussed by examining the instantaneous power dissipation in Fig. 7.9. Fig. 7.8(a) also shows that with the increasing excitation frequency Ω from 1 to higher frequencies, the difference of the values of \bar{P}_{de} between dry friction element case and viscous damper element case are increased. When the dynamic friction force F_d increasing from 0.02 to 0.04, there is more power dissipation by the dry friction element in the whole frequency range. Fig. 7.8(b) shows that for the viscous damper case with $\rho = 2$, the proportion of input power that is dissipated by the viscous damper element R_{de} remains unchanged regardless of the variations of the excitation frequency. In comparison, for the dry friction element cases, there is a minimum value of the power dissipation ratio R_{de} by the dry friction element at the corresponding resonant frequency of the response, i.e., $\Omega = 1$. As the excitation frequency increases from 0.1 to 2, the values of R_{de} for the dry friction element cases decrease first from a value close to 1, to the value that is smaller than that of the viscous damper element case, and then increase to the value close to 1. It suggests that the dry friction element is effective for energy dissipation when the system is not in resonance. By increasing the dynamic friction force from 0.02 to 0.04, the absolute value of the minimum point of R_{de} near $\Omega = 1$ is largely increased while the value of R_{de} only shows a small growth when the excitation frequency is away from $\Omega = 1$.

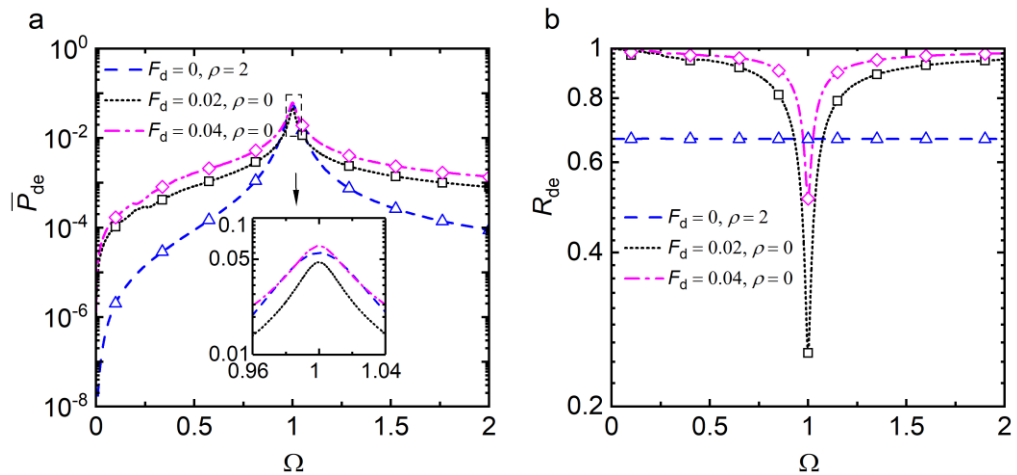


Figure 7.8. Effects of the dynamic friction force F_d on (a) the time-averaged dissipated power by the element \bar{P}_{de} and (b) the power dissipation ratio R_{de} . The solid and dashed lines are for the linear system with $\rho = 0$ and 2, respectively. The dotted and dash-dotted lines are for the nonlinear system having dry friction element with $F_d = 0.02$ and 0.04, respectively.

In Fig. 7.9, the reasons for the characteristics of \bar{P}_{in} and \bar{P}_{de} at low frequencies shown in Fig. 7.7(a) and 7.8(a) are further explored, respectively. Fig. 7.9(a) and (c) presents the instantaneous input power P_{in} into the system against the dimensionless time for the case of considering the dry friction element with $F_d = 0.04$ and for the case

of using the viscous damper element with $\rho = 2$, respectively. The excitation frequency is set as $\Omega = 0.3$ and the system parameters are the same to those used in Figs. 7.6, 7.7 and 7.8. Fig. 7.9(a) shows that due to the stick-slip characteristic at low frequencies, the positive part of the instantaneous input power becomes significantly larger than the negative part. Compared to the instantaneous input power P_{in} in the viscous damper element case shown in Fig. 7.9(c), it is found that the dry friction element can result in a much larger amount of input energy into the system. Fig. 7.9(b) shows the time history of the instantaneous dissipated power P_{de} by the dry friction element and the instantaneous dissipated power P_{d1} by the system damper c_1 at $\Omega = 0.3$. It shows that the dry friction element dissipates most amount of the input power into the system while there is only a little power dissipated by the system damper at this frequency. By a comparison to the time history of P_{de} in the viscous damper element case shown in Fig. 7.9(d), it is found that the dry friction element can dissipate more power than the replacement viscous damper element when the excitation frequency is low.

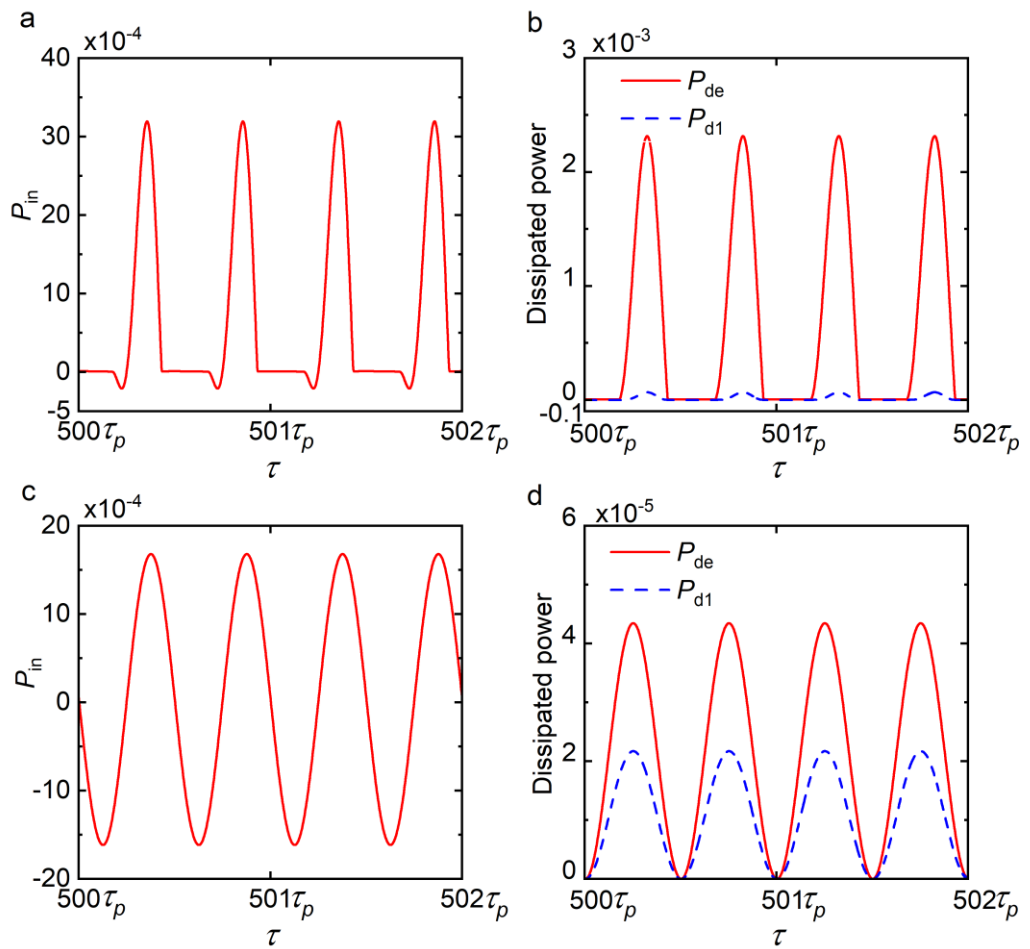


Figure 7.9. Instantaneous power flow indices against time for friction element case with $F_d = 0.04$ and $\rho = 0$ in (a) and (b) while for viscous damper case with $F_d = 0$ and $\rho = 2$ in (c) and (d) at $\Omega = 0.3$. In (a) and (c): the instantaneous input power P_{in} ; in (b) and (d): the instantaneous power dissipation by element P_{de} and by the system damper P_{d1} .

7.3. 2DOF system with friction at the interface

7.3.1. Mathematical modelling

In this section, the dynamics, vibration transmission and energy dissipation behaviour of a coupled 2DOF oscillator system (i.e., $Q = 2$) with interactive dry friction force at the interface are investigated. Fig. 7.10(a) shows the system consisting of two SDOF systems coupled via a spring of stiffness coefficient k_3 and a dry friction element with dry friction force f_c shown in Fig. 7.10(b). Here the dry friction element represents the interactive friction force between the two masses and the magnitude of the dynamic friction force is f_d . The 2DOF system is placed horizontally on the smooth surface. The SDOF primary system on the left comprises the primary mass m_1 subjected to a harmonic force excitation with amplitude of f_0 and frequency of ω , a linear spring with stiffness coefficient k_1 and a viscous damper with damping c_1 . The SDOF secondary system on the right has the secondary mass m_2 , a viscous damper of damping c_2 , and a linear spring with stiffness k_2 . The static equilibrium positions of the two masses, where $x_1 = x_2 = 0$ and the springs k_1, k_2, k_3 are un-stretched, are set as a reference. The dry friction element can be replaced by a viscous damper element with a damping coefficient of c_d as shown in Fig. 7.10(c) for comparison.

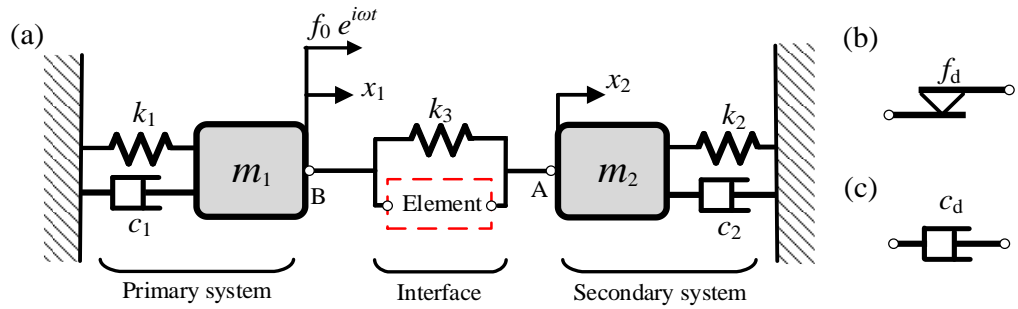


Figure 7.10. (a) A 2DOF oscillator with (b) a dry friction element and (c) a viscous damper at coupling interface.

The equations of motion of the system can be written as

$$\begin{bmatrix} m_1 & 0 \\ 0 & m_2 \end{bmatrix} \begin{Bmatrix} \ddot{x}_1 \\ \ddot{x}_2 \end{Bmatrix} + \begin{bmatrix} c_1 & 0 \\ 0 & c_2 \end{bmatrix} \begin{Bmatrix} \dot{x}_1 \\ \dot{x}_2 \end{Bmatrix} + \begin{bmatrix} k_1 + k_3 & -k_3 \\ -k_3 & k_2 + k_3 \end{bmatrix} \begin{Bmatrix} x_1 \\ x_2 \end{Bmatrix} + \begin{Bmatrix} f_c(\dot{x}_1 - \dot{x}_2) \\ -f_c(\dot{x}_1 - \dot{x}_2) \end{Bmatrix} = \begin{Bmatrix} f_0 e^{i\omega t} \\ 0 \end{Bmatrix}. \quad (7.17)$$

where f_c is the dry friction force at the interface, which can be obtained by the Karnopp model expressed in Eq. (7.3) or by the smooth Coulomb model expressed in Eq. (7.4) with $v_f = \dot{x}_1 - \dot{x}_2$.

In the use of the Karnopp model, when there is no relative motion between masses (i.e. stick state), the resultant external force f_{ex} is balanced by the dry friction force with $f_{\text{ex}} = f_c(\dot{x}_1 - \dot{x}_2)$. Moreover, the relative velocity v_r of two masses is zero with $\dot{x}_1 = \dot{x}_2$ and $\ddot{x}_1 = \ddot{x}_2$. By substituting those expressions into Eq. (7.17) we have

$$f_{\text{ex}} = \frac{m_1}{m_1+m_2} [k_2 x_2 + c_2 \dot{x}_2 - k_3(x_1 - x_2)] + \frac{m_2}{m_1+m_2} [f_0 e^{i\omega t} - k_1 x_1 - c_1 \dot{x}_1 - k_3(x_1 - x_2)]. \quad (7.18)$$

Here the new parameters are defined as

$$\omega_2 = \sqrt{\frac{k_2}{m_2}}, \quad \zeta_2 = \frac{c_2}{2m_2\omega_2}, \quad X_2 = \frac{x_2}{l_0}, \quad \gamma = \frac{\omega_2}{\omega_1}, \quad \mu = \frac{m_2}{m_1}, \quad \kappa = \frac{k_3}{k_1},$$

where ω_2 and ζ_2 are the undamped natural frequency and damping ratio for the secondary system without friction, respectively, X_2 represents the dimensionless displacement of the secondary mass, γ is the ratio of undamped natural frequency between the primary and the secondary oscillator. μ is the mass ratio and κ is the non-dimensional stiffness ratio for the spring at the interface. By using them and the previously defined parameters, the non-dimensional governing equations can be transformed from Eq. (7.17), described as

$$\begin{bmatrix} 1 & 0 \\ 0 & \mu \end{bmatrix} \begin{bmatrix} X_1'' \\ X_2'' \end{bmatrix} + \begin{bmatrix} 2\zeta_1 & 0 \\ 0 & 2\mu\zeta_2\gamma \end{bmatrix} \begin{bmatrix} X_1' \\ X_2' \end{bmatrix} + \begin{bmatrix} 1+\kappa & -\kappa \\ -\kappa & \mu\gamma^2 + \kappa \end{bmatrix} \begin{bmatrix} X_1 \\ X_2 \end{bmatrix} + \begin{Bmatrix} F_c(X_1' - X_2') \\ -F_c(X_1' - X_2') \end{Bmatrix} = \begin{Bmatrix} F_0 e^{i\Omega\tau} \\ 0 \end{Bmatrix}, \quad (7.19)$$

where $F_c(X_1' - X_2')$ is the dimensionless friction force with

$$F_c(X_1' - X_2') = \begin{cases} F_d \operatorname{sgn}(X_1' - X_2'), & \text{if } |X_1' - X_2'| > V_d \\ F_d \operatorname{sgn}(F_{\text{ex}}), & \text{if } |X_1' - X_2'| \leq V_d \text{ and } |F_{\text{ex}}| \geq F_d \\ F_{\text{ex}}, & \text{if } |X_1' - X_2'| \leq V_d \text{ and } |F_{\text{ex}}| < F_d \end{cases}$$

based on the Karnopp model,

or

$$F_c(X_1' - X_2') = F_d \frac{\exp\left(\frac{X_1' - X_2'}{\eta}\right) - \exp\left(-\frac{X_1' - X_2'}{\eta}\right)}{\exp\left(\frac{X_1' - X_2'}{\eta}\right) + \exp\left(-\frac{X_1' - X_2'}{\eta}\right)}$$

based on the smooth Coulomb model,

and F_{ex} is the dimensionless resultant external force which can be transformed from Eq. (7.18), expressed by

$$F_{\text{ex}} = \frac{1}{1+\mu} [\mu\gamma^2 X_2 + 2\mu\zeta_2\gamma X_2' - \kappa(X_1 - X_2)] + \frac{\mu}{1+\mu} [F_0 e^{i\Omega\tau} - X_1 - 2\zeta_1 X_1' - \kappa(X_1 - X_2)]. \quad (7.20)$$

For the corresponding case of using viscous damper element to replace the dry friction element, the friction force $F_c(X_1' - X_2')$ in Eq. (7.19) is replaced with the damping force $F_{\text{cd}}(X_1' - X_2') = 2\zeta_1\rho(X_1' - X_2')$ by the viscous damper element.

The governing equation of Eq. (7.19) can be solved by the HB-AFT method illustrated in Subsection 7.1.2, where the smooth Coulomb model is used for the approximation of friction force. The results are compared with the 4th order RK method with the friction force determined by the Karnopp model.

7.3.2. Force transmission and power flow formulations

The influence of the dry friction on the vibration transmission between the two subsystems and the vibration energy dissipation at the interface is of interest. The force transmissibility from the primary mass m_1 to the secondary mass m_2 is expressed by:

$$TR_S = \frac{\max(\Re\{|F_{\text{ts}}|\})}{F_0}, \quad (7.21)$$

where $F_{\text{ts}} = \kappa(X_1 - X_2) + F_c(X_1' - X_2')$ is the dimensionless transmitted force to mass m_2 for the systems comprising dry friction element. It is noted that in the case of using viscous damper element, the transmitted force can be replaced with $F_{\text{ts}} = \kappa(X_1 - X_2) + F_{\text{cd}}(X_1' - X_2')$ and $F_{\text{cd}}(X_1' - X_2') = 2\zeta_1\rho(X_1' - X_2')$.

For the current system in the steady-state motion, the non-dimensional time-averaged input power \bar{P}_{in} over one cycle of the periodic response is obtained from Eq. (7.9) by setting $q = 1$. The time-averaged dissipated power \bar{P}_{d1} by system damper c_1 is still defined by Eq. (7.15a). Over one cycle of periodic motion, the time-averaged transmitted power to the secondary system is entirely dissipated by the damper c_2 , therefore, the time-averaged transmitted power P_{ts} to the secondary system and the time-averaged dissipated power \bar{P}_{di} by the interfacial element (dry friction element or viscous damper element) are expressed as

$$\bar{P}_{\text{ts}} = \frac{1}{\tau_p} \int_{\tau_0}^{\tau_0+\tau_p} P_{\text{ts}} d\tau, \quad \bar{P}_{\text{di}} = \frac{1}{\tau_p} \int_{\tau_0}^{\tau_0+\tau_p} P_{\text{di}} d\tau, \quad (7.22a, 7.22b)$$

respectively, The corresponding instantaneous transmitted power P_{ts} and the instantaneous dissipated power P_{di} are

$$P_{\text{ts}} = 2\mu\zeta_2\gamma(\Re\{X_2'\})^2, \quad (7.23a)$$

$$P_{\text{di}} = \begin{cases} \Re\{X'_2 - X'_1\}\Re\{F_c(X'_1 - X'_2)\}, & \text{For the friction element} \\ 2\zeta_1\rho (\Re\{X'_1 - X'_2\})^2, & \text{For the damper element} \end{cases} \quad (7.23b)$$

respectively. X'_1 and X'_2 are obtained by taking the differentiation of X_1 and X_2 as $X'_1 = \sum_{n=0}^N in\Omega\tilde{R}_{(1,n)}e^{in\Omega\tau}$ and $X'_2 = \sum_{n=0}^N in\Omega\tilde{R}_{(2,n)}e^{in\Omega\tau}$. The power dissipation ratio R_{d1} by the damper c_1 is still obtained from Eq. (7.16a). The power dissipation ratio R_{di} at the interface and the power transmission ratio R_{ts} are defined as

$$R_{\text{di}} = \frac{\bar{P}_{\text{di}}}{\bar{P}_{\text{in}}}, \quad R_{\text{ts}} = \frac{\bar{P}_{\text{ts}}}{\bar{P}_{\text{in}}}, \quad (7.24)$$

respectively. It is noted that in accordance of the energy conservation, we have $R_{\text{di}} + R_{\text{ts}} + R_{\text{d1}} = 1$.

7.3.3. Dynamics and power flow results

In Figs. 7.11-7.18, the influence of the dynamic friction force of the dry friction element on the dynamics, force transmissibility and power flow behaviour of the 2DOF oscillator system is investigated. Case one and two consider the systems having dry friction element with the dynamic friction force selected with $F_{\text{d}} = 0.10$ and 0.15 , respectively, for the steady-state response analysis in Figs. 7.11 and 7.13, while for the force transmission and power flow analysis in Figs. 7.14, 7.15 and 7.17, the dynamic friction forces in case one and two are set as $F_{\text{d}} = 0.05$ and 0.15 , respectively. The damping ratio in these two cases is fixed as $\rho = 0$. For comparison purpose, case three and case four correspond to the linear system without friction force (i.e., $F_{\text{d}} = 0$) with the damping ratio of the viscous damper element chosen as $\rho = 0$ and $\rho = 4$, respectively. The system parameters are set as $\zeta_1 = \zeta_2 = 0.01$, $\gamma = 1$, $\mu = 1$, $\kappa = 1$, $V_{\text{d}} = 1 \times 10^{-4}$, $\eta = 1 \times 10^{-4}$ and $F_0 = 0.5$. The different types of lines represent the results obtained by the HB method with the friction force approximated by the smooth Coulomb friction model, while the different symbols denote the results by using RK method with the friction force determined by the Karnopp friction model.

In Figure 7.11(a) and (b), the effects of the dynamic friction force F_{d} of the dry friction element on the steady-state maximum response displacement of the primary mass $X_{1_{\text{max}}}$ and secondary mass $X_{2_{\text{max}}}$ are studied, respectively. Two peaks are observed in each curve of $X_{1_{\text{max}}}$ and $X_{2_{\text{max}}}$. An anti-peak is found in each of $X_{1_{\text{max}}}$ curve shown in Fig. 7.11(a). By conducting modal analysis on the corresponding linear system without friction ($F_{\text{d}} = \rho = 0$), it is found that the first peak is corresponding to the in-phase mode while the second corresponds to the out-of-phase mode. Fig. 7.11(a) shows that with the use of dry friction element, the first peak of $X_{1_{\text{max}}}$ near $\Omega = 1$

shows little changes while the second peak value is substantially reduced compared to the linear system with $F_d = \rho = 0$. This is because at the first peak frequency, the relative displacement between two masses are small, therefore, the dry friction force has little effect on the motion of two masses. However, at the second peak frequency near $\Omega = 1.74$, the moving direction of the two masses are opposite and the friction force at the coupling interface opposes the motion of each mass. As a result, the displacement response of the two masses is suppressed by the friction force. Fig. 7.11(a) also shows that compared with the corresponding linear system comprising a replacement viscous damper element with $\rho = 4$, the systems with the dry friction element have lower values of $X_{1,max}$ at a low or high excitation frequency, but the system with the viscous damper element has a lower second peak near $\Omega = 1.74$ and a lower anti-peak near $\Omega = 1.41$. Moreover, when the dynamic friction force F_d of the dry friction element increases from 0.10 to 0.15, there is an increase in the anti-peak value of $X_{1,max}$ while a further reduction can be found in the second peak value as well as the values in the low/high-frequency range. Fig. 7.11(b) shows that compared to the linear system without friction with $F_d = \rho = 0$, the addition of the dry friction element can reduce the second peak value of the response $X_{2,max}$ while minor changes can be found in the first peak. This is again due to the opposite moving directions for two masses at $\Omega \approx 1.74$ such that the dry friction element provides a resistance force for the motion of both masses. It is also found that when the excitation frequency is away from the resonant peaks, the use of the viscous damper element with $\rho = 4$ may have negligible effects on the values of $X_{2,max}$. In contrast, in the dry friction element cases, the values of $X_{2,max}$ are increased significantly in the low/high-frequency range. It is also noticed that with the increase of excitation frequency Ω , the difference of the values of $X_{2,max}$ between the viscous damper element case and dry friction element cases becomes larger. Fig. 7.11(b) also shows that when the dynamic friction force F_d changes from 0.10 to 0.15, the second peak value of $X_{2,max}$ is further reduced due to the stronger friction damping force. However, the values of $X_{2,max}$ at low or high frequencies are further increased. This behaviour will be explored in Fig. 7.12 as follows.

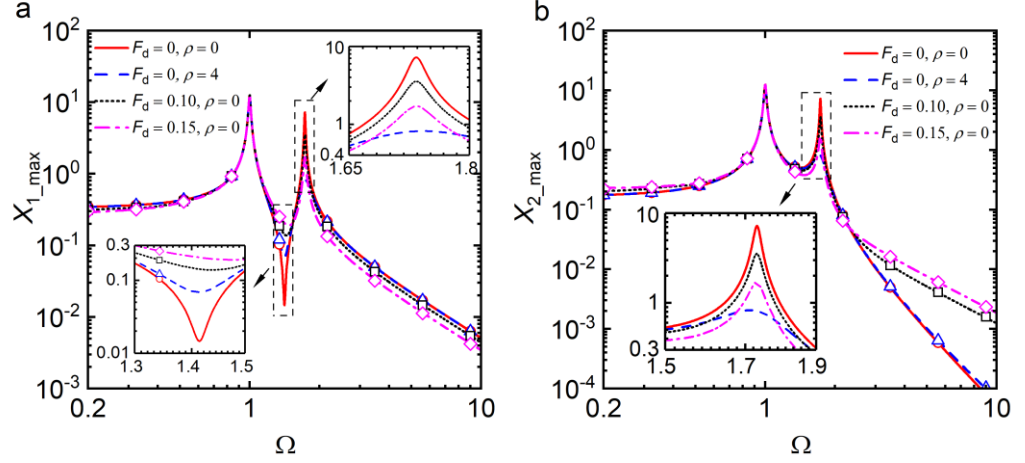


Figure 7.11. Effects of dynamic friction force F_d on the steady-state maximum response displacement (a) $X_{1,max}$ for the primary mass and (b) $X_{2,max}$ for the secondary mass, respectively. The solid and dashed lines are for the linear system with $\rho = 0$ and 4, respectively. The dotted and dash-dotted lines are for the nonlinear system having dry friction element with $F_d = 0.10$ and 0.15, respectively.

Figure 7.12(a), (b), (d) and (e) presents the steady-state time-histories of the friction force and the velocity of the masses for the system comprising dry friction element at the excitation frequency of $\Omega = 0.4$, $\Omega = 1.41$, $\Omega = 1.74$ and $\Omega = 3$, respectively. The dynamic friction force of the dry friction element is considered with $F_d = 0.15$ while setting $\rho = 0$. For comparison purpose, Fig. 7.12(c) and (f) shows the time histories of the velocity of the masses for the system using a replacement viscous damper element with $\rho = 4$ and $F_d = 0$, and the damping force by the viscous damper element at the excitation frequency of $\Omega = 1.41$ and $\Omega = 3$, respectively. The system parameters are the same as those used in Fig. 7.11. The solid lines represent the dry friction force F_c in Fig. 7.12(a), (b), (d) and (e), while representing the damping force F_{cd} by the viscous damper element in Fig. 7.12(c) and (f). The dashed and dotted lines denote the velocity of the primary mass X_1' and secondary mass X_2' , respectively. Fig. 7.12(a) shows that at low frequencies, i.e. $\Omega = 0.4$, there are certain time spans within one oscillation cycle that two masses are moving at the same velocity with $X_1' = X_2'$, suggesting that the interface between the two masses is in stick state. From the variations of the friction force F_c against dimensionless time in Fig. 7.12(a), it is known that the magnitude of the resultant external force F_{ex} has not increased beyond the value of the maximum static friction force (which equals to the dynamic friction force F_d). However, when the absolute value of the velocity X_1' of the primary mass becomes larger than the certain value, the stick-state at the interface is switched to slip-state due to that the value of F_{ex} becomes larger than the value of F_d . In the slip region, the value of the friction force remains as a constant, i.e., $F_c = F_d$. Because of the relative relation between the response velocity of two masses as $|X_1'| > |X_2'|$, the friction force acts in the same

direction to the moving direction of secondary mass m_2 but against to that of the primary mass m_1 . Consequently, the dry friction force can increase the maximum displacement of the secondary mass but suppress the motion of the primary mass.

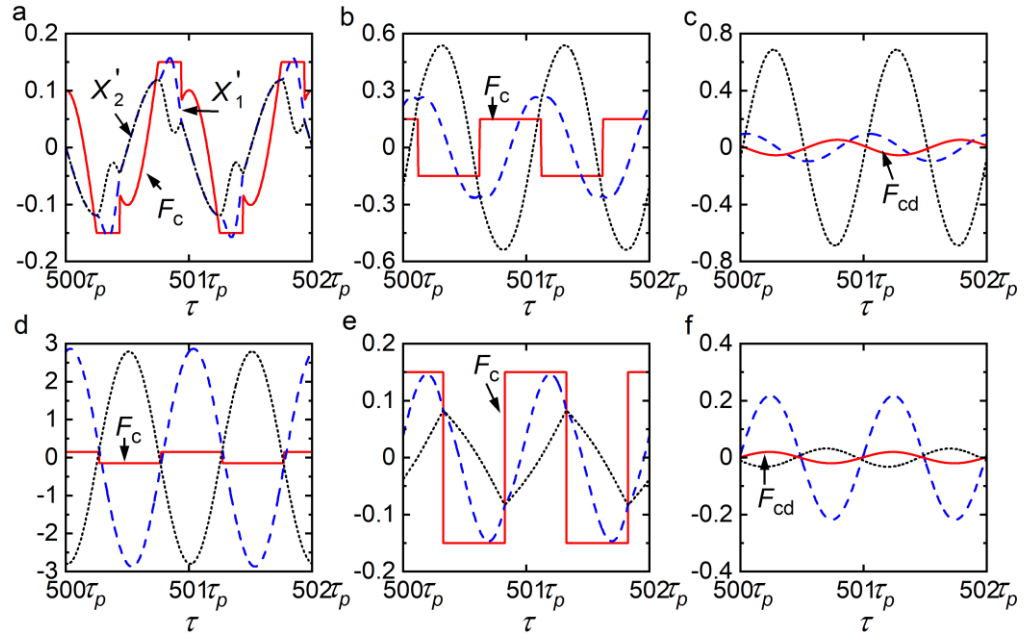


Figure 7.12. Time history of element force and the velocity responses in steady-state for the dry friction element case with $F_d = 0.15$, $\rho = 0$ at (a) $\Omega = 0.4$, (b) $\Omega = 1.41$, (d) $\Omega = 1.74$ and (e) $\Omega = 3$, respectively; For the viscous damper element case with $F_d = 0$, $\rho = 4$ at (c) $\Omega = 1.41$ and (f) $\Omega = 3$, respectively. The solid line is the dry friction force F_c by the friction element at the interface in (a), (b), (d) and (e), while in (c) and (f) is the damping force F_{cd} by the viscous damper element at the interface. The dashed line and dotted lines are the response velocity of the primary mass X_1' and the secondary mass X_2' , respectively.

Fig. 7.12(b) shows that for the case of using dry friction element excited near the frequency of the anti-peak, as shown in Fig. 7.11(a), there exists an approximate $\pi/2$ phase difference between the periodic velocity responses of two masses. By comparing to the velocity responses in the corresponding system comprising a replacement viscous damper element at the same excitation frequency shown in Fig. 7.12(c), it is found that the use of the dry friction element can lead to a much larger amplitude of X_1' but a smaller amplitude of X_2' . Fig. 7.12(d) shows that at the excitation frequency of $\Omega = 1.74$ which corresponds to the second peak frequency shown in Fig. 7.11(a) and (b), the two masses are moving in opposite directions and the motions are hence suppressed by the frictional resistance force at the interface. It explains the reason for the lower peak values of X_{1_max} and X_{2_max} near $\Omega = 1.74$ in the dry friction element cases shown in Fig. 7.11(a). When comparing the time history of the velocity of the masses between dry friction element case and viscous damper element case at high frequencies away from the peaks, i.e., $\Omega = 3$, as shown by Fig. 7.12(e) and (f), respectively, it is found that the friction element provides a much larger amplitude of the friction force than

damping force by the viscous damper element at this frequency. The amplitude of the response velocity X_1' is smaller but the amplitude of X_2' is larger in the dry friction element case.

In Fig. 7.13, the influence of the dynamic friction force of the friction element on the maximum relative displacement $|X_1 - X_2|_{\max}$ between two masses is studied. Only one peak can be found in the relative displacement $|X_1 - X_2|_{\max}$ curves near the out-of-phase mode of the corresponding linear system. It shows that the addition of the dry friction element can reduce the values of $|X_1 - X_2|_{\max}$ in the whole frequency band. This is due to that the friction force generated by the dry friction element at the interface will always restraint the two masses from moving to different directions. As a result, the dry friction element can suppress the relative motion of the two masses in a broad frequency range. Fig. 7.13 also shows that the case of the linear system having viscous damper element with $\rho = 4$ shows a lower peak of $|X_1 - X_2|_{\max}$ compared to that of dry friction element cases. However at low or high excitation frequencies, the systems with dry friction element have much lower values of $|X_1 - X_2|_{\max}$. Fig. 7.13 also shows that as the dry friction force increases from 0.10 to 0.15, there is a further reduction in the values of $|X_1 - X_2|_{\max}$ due to a stronger friction damping force. It can be summarized that the dry friction element has a good suppression performance on the relative motion between the coupled oscillators in the low/high-frequency range.

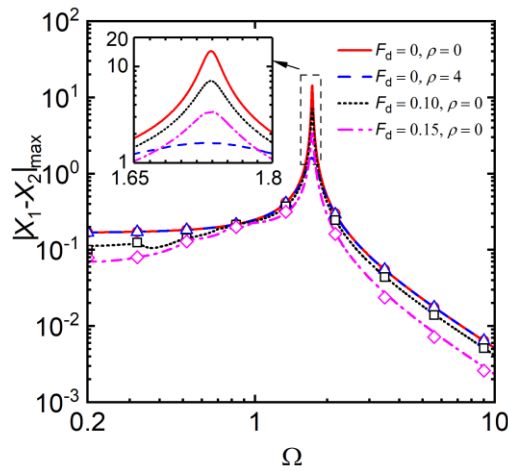


Figure 7.13. Effects of dynamic friction force F_d on the steady-state maximum relative response displacement $|X_1 - X_2|_{\max}$ between two masses. The solid and dashed lines are for the linear system with $\rho = 0$ and 4, respectively. The dotted and dash-dotted lines are for the nonlinear system having dry friction element with $F_d = 0.10$ and 0.15, respectively.

In Fig. 7.14(a) and (b), the effects of the dynamic friction force on the force transmissibility TR_S from the primary system to the secondary mass and the time-averaged input power \bar{P}_{in} into the system are investigated, respectively. Only one peak is observed in the curve of TR_S in Fig. 7.14(a), which is corresponding to the out-of-

phase mode of the linear system. In Fig. 7.14(b), two peaks can be found in the curve of \bar{P}_{in} . Fig. 7.14(a) shows that for the case of using the viscous damper element with $\rho = 4$, the peak value near $\Omega = 1.73$ is substantially reduced and values in the high-frequency range are increased a bit compared to the linear system with $\rho = 0$. In contrast, the use of dry friction element can slightly reduce the peak value of TR_S but significantly increase the values of TR_S when the excitation frequency is away from the peak. This is due to that, the masses are moving in opposite directions near the peak frequency $\Omega = 1.74$, the friction force acting at the coupling interface restrains the relative motion of two masses. Therefore, a smaller spring force at the interface is obtained due to the smaller relative displacement between masses, resulting in a smaller total transmitted force and a smaller value of TR_S . At low or high excitation frequencies, the relative displacement between masses is small, leading to a relatively small spring force at the coupling interface. The damping force by the viscous damper element in the damper element case is also small because of the small relative velocity at low frequencies, while it can be increased slightly in the high-frequency range due to the larger value the frequency component in the damping force expression. In contrast, from the Karnopp model expressed in Eq. (7.3), the magnitude of friction force by the dry friction element is only depending on the magnitude relationship between the resultant external force and the dynamic friction force. In the low/high-frequency range, the amplitude of friction force provided by the dry friction element is a constant which equals to dynamic friction force. Therefore, the addition of the friction element can increase the maximum total transmitted force to the mass m_2 via the interface in those frequency ranges and results in a larger force transmissibility TR_S . As the excitation frequency further increases, the value of TR_S in dry friction element cases becomes close to a constant value. This is due to that with the increasing frequency, the spring force at the interface is smaller and the value of the maximum total transmitted force is becoming close to the value of dynamic friction force. Fig. 7.14(a) also shows that an increase of dynamic friction force F_d from 0.05 to 0.15 can further reduce the peak value of TR_S but increase the values of TR_S when the excitation frequency is away from the resonance. Fig. 7.14(b) shows that the use of viscous damper element or the dry friction element have little effect on the first peak of time-averaged input power at $\Omega = 1$ but can reduce the second peak value of the \bar{P}_{in} near $\Omega = 1.74$. Both two types of elements can also increase the amount of input power into the system in the low/high-frequency range. However, the dry friction element can result in larger values of \bar{P}_{in} when the excitation frequency is away from the peaks. When increasing the dynamic friction force F_d from 0.05 to 0.15, the second peak value of \bar{P}_{in} is further reduced while there

is an increase in the values of \bar{P}_{in} when the excitation frequency is away from the resonant peaks.

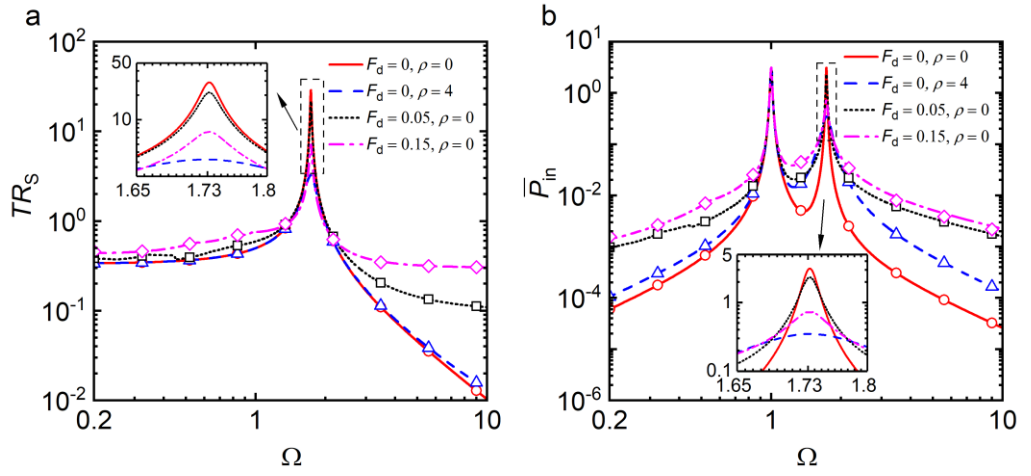


Figure 7.14. Effects of dynamic friction force F_d on (a) the force transmissibility to the secondary system TR_S and (b) the time-averaged input power \bar{P}_{in} into the system, respectively. The solid and dashed lines are for the linear system with $\rho = 0$ and 4 , respectively. The dotted and dash-dotted lines are for the nonlinear system having dry friction element with $F_d = 0.05$ and 0.15 , respectively.

In Fig. 7.15(a) and (b), the influence of the dynamic friction force of the dry-friction element on the time-averaged transmitted power \bar{P}_{ts} to the secondary system and the power transmission ratio R_{ts} is examined, respectively. In Fig. 7.15(a), two peaks can be found in the \bar{P}_{ts} curve. Compared with the linear system with $F_d = \rho = 0$, it is found that the use of the dry friction element can reduce the amount of power transmitted to the secondary system near the second peak when $\Omega \approx 1.738$. When comparing the power transmission between the case of using viscous damper element with $\rho = 4$ and cases of having dry friction element, it is found that the viscous damper element may have little influence on the \bar{P}_{ts} at low or high excitation frequencies while the dry friction element can significantly increase the amount of power transmission \bar{P}_{ts} especially in the high-frequency range. The difference of the values of \bar{P}_{ts} between the dry friction element case and the viscous damper element case becomes larger with the increasing frequency. The reason is that at the high excitation frequency, the addition of the dry friction element can increase the transmitted force to the secondary system and also increase the amount of input power into the integrated system compared to the case of using viscous damper element, as shown by Fig. 7.14(a) and (b), respectively. Therefore, there is an increasing amount of input power that is transmitted to the secondary system. By a comparison of the instantaneous power transmission P_{ts} at $\Omega = 5$ between friction element case with $F_d = 0.15$ and viscous damper element case with $\rho = 4$ as shown in Fig. 7.16(a) and (b), respectively, it is found that much more power

is transmitted to the secondary system in the dry friction element case. Fig. 7.15(a) also shows that an increase of the dynamic friction force F_d in the friction element cases from 0.05 to 0.15 can further reduce the height of the second peak of \bar{P}_{ts} but increase the values of \bar{P}_{ts} in the low/high-frequency range. It is also noted that neither the viscous damper element nor the dry friction element can affect the first peak of \bar{P}_{ts} near the in-phase mode frequency of the corresponding linear system. Fig. 7.15(b) shows that two peaks can be found in the curves of power transmission ratio R_{ts} when the dry friction exists in the system, while only one peak can be found in the linear systems without friction. By comparing to the linear system with $F_d = \rho = 0$, the use of the dry friction element or the viscous damper element can lead to a much smaller portion of input power that is transmitted to the secondary system when $\Omega < 5$ approximately. Moreover, when the system is excited at high frequency, i.e. $\Omega > 6$, the system having the viscous damper element shows a smaller value of power transmission ratio R_{ts} than the linear system with $F_d = \rho = 0$, while the system comprising the dry friction element has a larger value of R_{ts} . Compared with the viscous damper element case, it is found that the dry friction element can lead to smaller values of R_{ts} when $\Omega < 1$, but larger values when $\Omega > 6$ or Ω is near the second peak ($\Omega \approx 1.74$). When the dynamic friction force F_d of the dry friction element increases from 0.05 to 0.15, the values of R_{ts} are increased in the high-frequency range but reduced near the second peak frequency and in the low-frequency range when $\Omega < 1$.

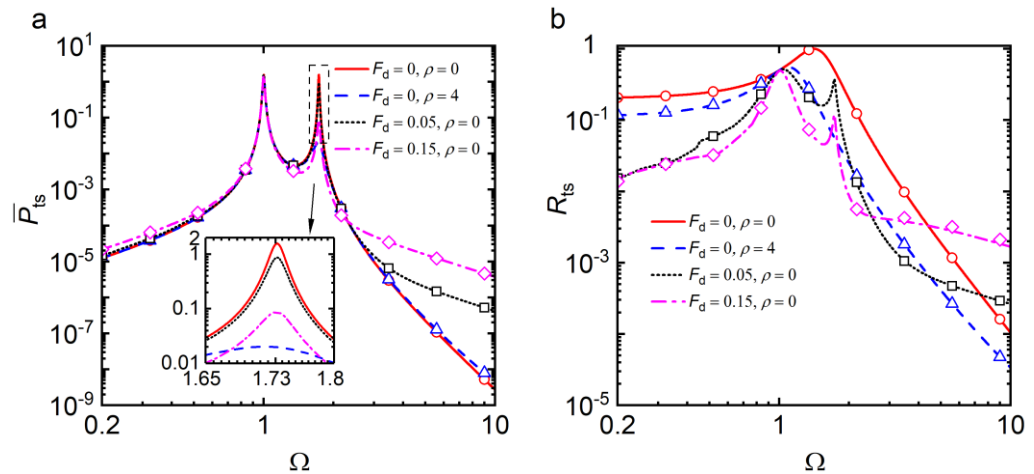


Figure 7.15. Effects of dynamic friction force F_d on (a) the time-averaged transmitted power \bar{P}_{ts} to the secondary system and (b) the power transmission ratio R_{ts} , respectively. The solid and dashed lines are for the linear system with $\rho = 0$ and 4, respectively. The dotted and dash-dotted lines are for the nonlinear system having dry friction element with $F_d = 0.05$ and 0.15, respectively.

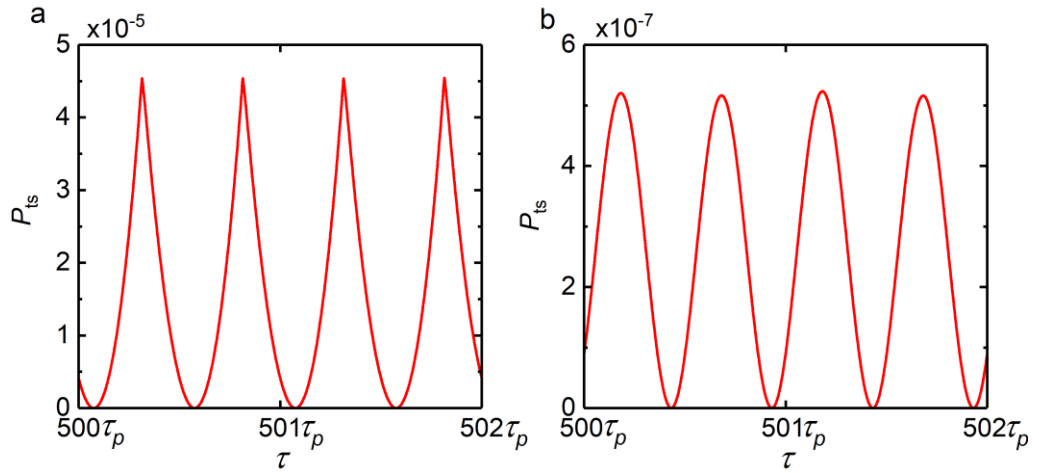


Figure 7.16. Time history of the instantaneous transmitted power P_{ts} to the secondary system when the excited at $\Omega = 5$ for (a) the friction element case with $F_d = 0.15$ and $\rho = 0$ and for (b) the linear damper case with $F_d = 0$ and $\rho = 4$.

In Fig. 7.17(a) and (b), the effects of the dynamic friction force of the friction element on the time-averaged dissipated power \bar{P}_{di} at the interface and the corresponding power dissipation ratio R_{di} are studied, respectively. Fig. 7.17(a) shows that, when the frequency is near the in-phase mode of the corresponding linear system, the system having viscous damper element with $\rho = 4$ shows a similar amount of power dissipation \bar{P}_{di} at the interface compared to the systems comprising dry friction element. However the cases of using dry friction element have larger values of \bar{P}_{di} when the system is excited at low or high frequencies. As the dynamic friction force F_d increases from 0.05 to 0.15, there is a slight reduction in the peak value of the \bar{P}_{di} but a significant increase in the values of \bar{P}_{di} when the excitation frequency is away from the peak. Fig. 7.17(b) shows that in the viscous damper element case, there is a local minimum point near the in-phase mode of the corresponding linear system in the curve of power transmission ratio R_{di} . The replacement of the viscous damper element by the dry friction element can introduce an extra local minimum point of R_{di} near the out-of-phase mode of the linear system. By a comparison between the viscous damper element case and the dry friction element case, it is found that the value of R_{di} at the first local minimum near $\Omega=1$ is smaller in the viscous damper element case. In contrast, a lower value at the second local minimum near $\Omega=1.73$ is observed in the dry friction element cases. In the low/high-frequency range, the values of R_{di} in dry friction element cases are close to 1, indicating that a large portion of the input power is dissipated at the interface. Fig. 7.17(b) also shows that an increase of the dynamic friction force F_d from 0.05 to 0.15 can slightly increase the values of R_{di} near the frequencies of both local minimum point.

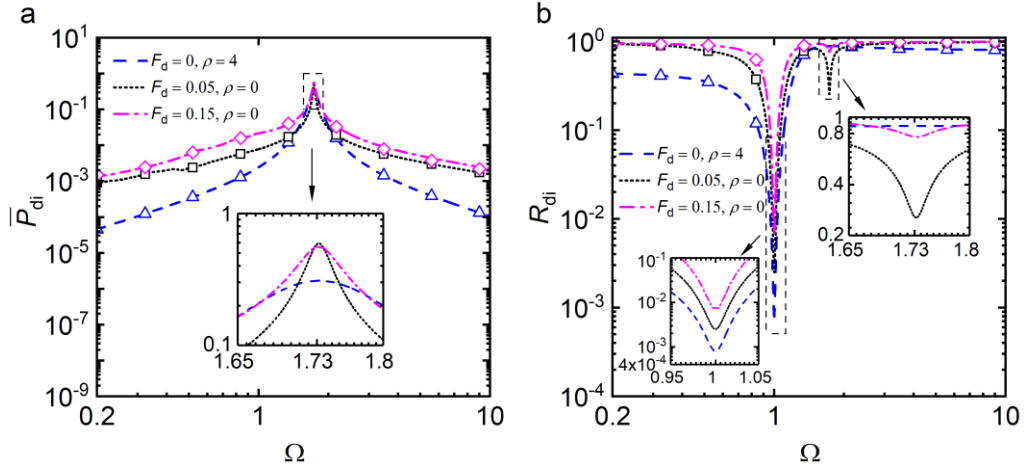


Figure 7.17. Effects of dynamic friction force F_d on (a) the time-averaged dissipated power \bar{P}_{di} at the interface and (b) the power transmission ratio R_{di} , respectively. The solid and dashed lines are for the linear system with $\rho = 0$ and 4, respectively. The dotted and dash-dotted lines are for the nonlinear system having dry friction element with $F_d = 0.05$ and 0.15, respectively.

In Fig. 7.18, the influence of the dry friction force on the steady-state instantaneous power dissipation P_{di} at different frequencies are investigated. Fig. 7.18(a-c) presents instantaneous dissipated power P_{di} for the case of using dry friction element by setting $F_d = 0.15$ and $\rho = 0$, while Fig. 7.18(d-f) presents the P_{di} for the case of using viscous damper element with $F_d = 0$ and $\rho = 4$. The system parameters remain the same to those used in Fig. 7.17. Fig. 7.18(a) shows the instantaneous power dissipation P_{di} by the dry friction element at $\Omega = 0.4$, it is found that the power dissipation by the dry friction element keeps zero for a certain time-length periodically. This is due to the stick behaviour arise by the friction nonlinearity. As the magnitude of resultant external force F_{ex} is lower than the dynamic friction force F_d , the interface keeps in stick-state and there is no relative motion between the masses. As suggested by Eq. (7.23b), the dry friction element cannot dissipate power when there is no relative motion of the masses, i.e., when the interface is in stick state. By comparing to the viscous damper element case excited at the same frequency shown in Fig. 7.18(d), it is found that the dry friction element can lead to a much higher amplitude of P_{di} and hence a larger time-averaged power dissipation \bar{P}_{di} at the interface. Fig. 7.18(b) and (e) compares the steady-state instantaneous power dissipation P_{di} between dry friction element case and viscous damper element case at the excitation frequency of $\Omega = 1.74$ which corresponds to the peak frequency of \bar{P}_{di} curve, as shown in Fig. 7.17(a). It shows that the friction element can dissipate more amount of power than the viscous damper element at the interface. The reason is that the moving directions of two masses are opposite at this frequency, leading to a large amount of energy dissipation by friction. Fig. 7.18(c) and (f) compares the P_{di} at $\Omega = 5$ between friction element case and viscous damper element case. It shows that there is more energy dissipation by the dry friction element. It can be

summarized from Fig. 7.18 that the dry friction element may be more effective than the viscous damper element in dissipating power at the interface when the system is excited at low or high frequencies.

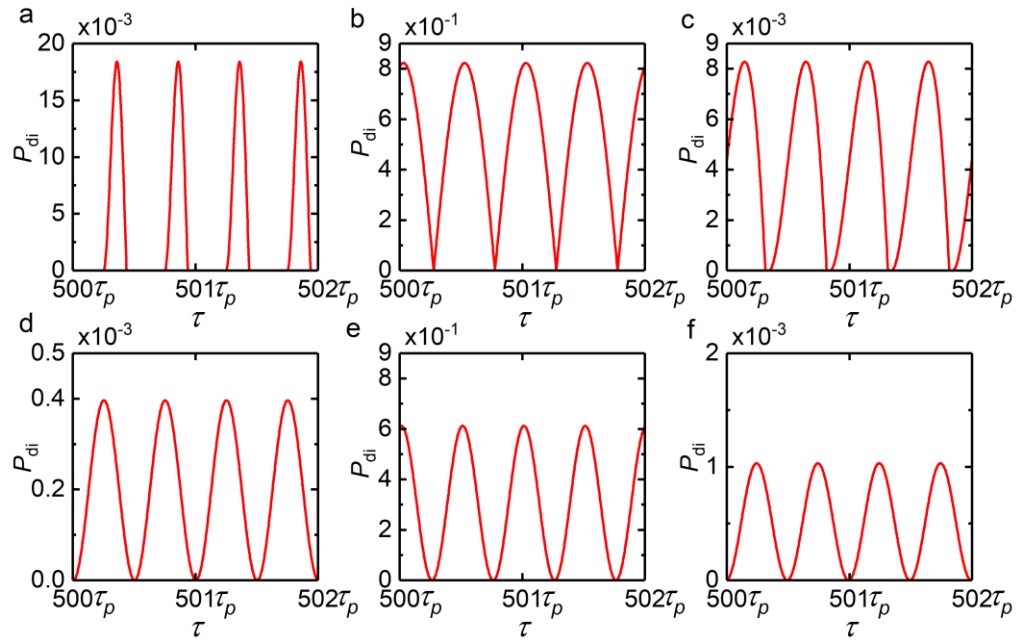


Figure 7.18. Instantaneous dissipated power P_{di} for the dry friction element case with $F_d = 0.15$ and $\rho = 0$ in (a-c) and for the viscous damper element case with $F_d = 0$ and $\rho = 4$ in (d-f). The system is excited at $\Omega = 0.4$ in (a) and (c), at $\Omega = 1.74$ in (b) and (e), and at $\Omega = 5$ in (c) and (f).

7.4. Summary

The dynamics, force transmission and vibration power flow behaviour of a SDOF oscillator system and a coupled 2DOF oscillating system comprising dry friction element were investigated in this chapter. The effects of the dry-friction element on the vibration transmission and energy dissipation within the SDOF and 2DOF systems were evaluated by the force transmissibility and power flow indices. Some main findings can be summarized as below:

- (1) For the SDOF system with a dry friction element, comparing with the viscous damper element, the friction nonlinearity is effective in the suppression of dynamic response in the low/high-frequency range, while it can significantly increase the force transmission and the time-averaged input power into the system in these frequency ranges.
- (2) With the use of the dry friction element, a larger portion of vibration input power is dissipated by the dry friction element when the excitation frequency is away from the peak compared to the case using viscous damper element.

- (3) For the 2DOF system with the dry friction element at the interface, compared to the system having the viscous damper element, the system with friction element shows a larger amount of time-averaged input power and transmitted power at high frequencies. Moreover, there is much more power dissipation at the interface in the dry-friction element case in the low/high-frequency range.

It can be summarized that the nonlinear dry-friction element has a good potential to be used for altering the vibration transmission, energy flow and energy dissipation behaviour within dynamic systems.

Chapter 8

Conclusions and future work

Power flow behaviour has been widely used to quantify vibration transmission within linear systems. However, limited researches have been reported on the power flow characteristics in nonlinear dynamical systems, especially in non-smooth systems. This thesis has considered different types of nonlinearities embedded in the SDOF or 2DOF structures as archetypes of many engineering systems. The vibration transmission and power flow behaviour of impact oscillators and friction oscillators has been investigated. The power flow indices are also applied in the design of the nonlinear passive vibration control system.

A review of different evaluation approaches for vibration transmission and energy flow in linear and nonlinear systems is provided in Chapter 2. In Chapter 3, general vibration transmission formulations are introduced and different methods for determining the response of the nonlinear dynamical systems are discussed. Then the presented approaches are developed to investigate the dynamics and vibration transmission behaviour in the non-smooth impact oscillator systems with a linear or nonlinear QZS constraints in Chapter 4, and with the nonlinear motion constraints formed by a diamond-shaped linkage mechanism in Chapter 5. The impact oscillator systems with a single motion constraint are studied in Chapter 4 while the influence of multiple nonlinear constraints setups is evaluated in Chapter 5. In Chapter 6, a nonlinear passive isolator with the nonlinear spring based on the diamond-shaped linkage mechanism is put forward. The vibration isolation performance of such an isolator under different working environments is evaluated by using force transmission and power flow indices. The energy transmission and dissipation behaviour in the friction oscillator systems considering non-smooth Coulomb dry friction force is investigated in Chapter 7.

8.1. Conclusions

In this thesis, the principal contributions are:

- (1) An in-depth understanding of the vibration transmission and energy flow behaviour in non-smooth impact oscillators with different types of constraints, including linear constraint, nonlinear quasi-zero-stiffness constraint and nonlinear linkage-based

constraint, is provided. The constraint used in the coupled systems is found to largely increase the energy dissipation at the coupling interface.

- (2) The influence of different locations for adding nonlinear constraints to 2DOF impact oscillators on the dynamics and vibration transmission has been studied and compared. A symmetric configuration of two identical nonlinear constraints on the two sides of the primary system is found to be effective in suppressing vibration transmission
- (3) Novel nonlinear vibration isolators based on linkage mechanism are proposed for isolating force or base-motion excitations. The performance of such isolators in real engineering applications such as aircrafts and ships is evaluated by considering a flexible foundation. The proposed isolators have shown a good attenuation effect on vibration transmission.
- (4) The vibration transmission, energy flow and dissipation mechanism in a SDOF non-smooth friction oscillator and a 2DOF coupled oscillator with discontinuous dry friction force acting at the interface are comprehensively investigated.

The research of the vibration transmission and power flow behaviour within the investigated nonlinear dynamical systems in this research yields the following findings, which can provide a deeper understanding of the vibration transmission mechanisms in the nonlinear smooth and non-smooth dynamical systems.

- (1) The effects of motion constraints on the vibration transmission characteristics of impact-oscillator systems are examined in Chapters 4 and 5. It is shown that
 - The nonlinear motion constraint can introduce hardening nonlinearity into the system in certain excitation frequency intervals, and can result in bifurcations as well as super-harmonic and subharmonic responses when the nonlinear constraint stiffness is high, as shown in Chapter 5.
 - For the SDOF impact oscillator, the nonlinear motion constraint can lead to a substantially smaller force transmissibility than the linear motion constraint but result in larger response amplitude.
 - For the 2DOF impact oscillator, the use of a single constraint can significantly increase the peak amount of the dissipated power at the coupling interface, while a local minimum power dissipation can be observed near the peak frequency when two nonlinear constraints are used, as shown in Chapter 5. The peak power transmission between two coupled sub-systems can be largely

reduced when the two identical nonlinear constraints are set symmetrically on the two sides of the primary DOF, as shown in Chapter 5.

- Using the force transmissibility and time-averaged power transmission for the quantification of vibration transmission may give a different prediction result for the 2DOF impact oscillator system. The design parameters of the nonlinear motion constraint can be adjusted to tailor the vibration power flow behaviour within the system.

(2) A nonlinear isolation system formed by adding a geometrically nonlinear element created by a diamond-shaped linkage mechanism to the traditional linear isolator is developed in Chapter 6, with the following results,

- The geometrically nonlinear element can be adjusted to provide a negative stiffness so as to widen the frequency range of the effective vibration mitigation for the vibration isolation system. The curves of the response amplitude, the force / displacement transmissibility and the maximum kinetic energy of the vibration isolation system are all shifting to the low frequencies with the peaks bending to the low-frequency range.
- For the SDOF nonlinear isolation system under base excitation, the peak height of the response amplitude, the force transmissibility and the kinetic energy of the mass become much lower than those of the linear isolation system without the D-spring.
- For the 2DOF nonlinear isolation system, the addition of the nonlinear linkage-based element can largely reduce the power transmission from the mass to the flexible base structure at high frequencies. A substantial decrease can be found in the power transmission ratio when the excitation frequency is away from the in-phase mode of the corresponding linear system.

(3) The influence of the Coulomb dry friction force on the vibration transmission and energy flow characteristics of friction oscillators are investigated in Chapter 7. It is observed that

- The dry friction may be more effective in energy dissipation than the viscous damping in low- and high-frequencies when away from the resonance.
- For the coupled oscillating system considering the interactive dry-friction at the contacting interface, the force transmissibility, energy transfer to the secondary system and the energy dissipation at the interface in the high-

frequency range are all increased compared with those of the corresponding linear system without friction. However, slight reductions can be found in the peaks of those indices for the system with friction near the out-of-phase mode of the corresponding linear system.

- A larger dynamic friction force in the coupled system can increase the power transmission ratio to the secondary system in the high frequencies. The power flow behaviour within the system can be altered by changing the dynamic friction force.

Based on the findings of this research, some guidance on future dynamical design of engineering systems, such as tooling machineries, drilling rigs, transmission systems and vibration isolation platforms, can be provided as below:

1. To improve the operation efficiency of the tooling machinery or drilling platform, the impact frequency of the tools or drill bits can be set at resonance frequencies of the local impact subsystem to transmit the maximum vibration energy to the workpiece or rock. The material and geometry properties of the workpiece or rock should be considered in the design of tools or drill bits since those properties have strong effects on the dynamic stiffness, resonant frequencies and hence the cutting efficiency of the impact subsystem.
2. For the suppression of vibration in the transmission system, nonlinear motion constraints proposed in this thesis can be added onto the vibration transmission path, such as a shafting system on the ship, to substantially reduce the local power transmission in the axial direction. Extensively, the nonlinear constraints can be applied to reduce the longitudinal vibration transmission in any coupled chain structures. The use of multiple nonlinear constraints with a symmetrical configuration can further improve the vibration suppression performance.
3. The proposed nonlinear linkage-based vibration isolators have a relatively simple structure and can be easily employed in various engineering systems for vibration mitigation. The properties of the embedded nonlinear element can be altered to meet different engineering requirements by adjusting its geometric parameters straightforwardly without replacing the embedded linear spring.
4. The dry friction element can be used as an effective power dissipation component in the dynamical systems. A combined use of dry friction element and viscous damper element in the suspension system may effectively absorb and dissipate energy in a broad frequency range, which can improve the ride quality.

8.2. Future work

In light of the complexity of vibration transmission and power flow phenomena in the nonlinear smooth and non-smooth dynamical systems, further work is needed to understand the vibration transmission mechanisms of more integrated and complicated dynamical systems. Several interesting research areas are suggested here for future research.

- Vibration transmission and energy transfer behaviour in MDOF (number of DOF ≥ 3) impact oscillator systems with nonlinear motion constraints remain unexplored. The influence of different configurations of motion constraints on the power flow characteristics of the complex impact oscillator systems should be revealed.
- For a more realistic representation of the engineering applications, vibration transmission analysis on the nonlinear dynamical system comprising multiple types of nonlinearities, such as impact oscillator with motion constraints as well as non-smooth dry-friction nonlinearity, is needed.
- In terms of more efficient passive vibration control, the nonlinear substructures providing discontinuous forces, such as dry friction elements and nonlinear constraints, can be integrated into vibration control systems. PFA is required to evaluate the vibration suppression performance and enhance the dynamical design of such systems.

Appendix List of publications

- Dai, W., Yang, J. and Shi, B. (2020). Vibration transmission and power flow in impact oscillators with linear and nonlinear constraints. *International Journal of Mechanical Sciences*, 168: 105234.
- Dai, W., Yang, J. (2021). Vibration transmission and energy flow of impact oscillators with nonlinear motion constraints created by diamond-shaped linkage mechanism. *International Journal of Mechanical Sciences*, 194:106212.
- Dai, W., Yang, J. (2019). Vibration force transmissibility of a rotor-stator system with potential rub-impact. *The 18th Asian Pacific Vibration Conference (APVC)*, Sydney, Australia.
- Dai, W., Yang, J., Zhang, H., Halim, D., Xu, Z., Li, J. (2019). Rotordynamic analysis of a permanent magnet synchronous motor considering nonlinear unbalanced magnetic pull. *The 22nd International Conference on Electrical Machines and Systems (ICEMS)*, Harbin, China.
- Dai, W., Yang, J. (2019). Vibration analysis of a rotordynamic system with nonlinear bearing supports. *The 26th International Congress on Sound and Vibration (ICSV)*, Montréal, Canada.
- Dai, W., Yang, J. (2021). Vibration analysis of a multi-DOF impact oscillator with multiple linear constraints. *The 2nd International Nonlinear Dynamics Conference (NODYCON)*, Rome, Italy (Accepted).

Bibliography

- Acri, A., Nijman, E., Conrado, E. and Offner, G. (2019). Experimental structure-borne energy flow contribution analysis for vibro-acoustic source ranking. *Mechanical Systems and Signal Processing*, 115: 753-768.
- Ajibose, O. K., Wiercigroch, M., Pavlovskaja, E. and Akisanya, A. R. (2010). Global and local dynamics of drifting oscillator for different contact force models. *International Journal of Non-Linear Mechanics*, 45(9): 850-858.
- Al ba'ba'a, H. and Nouh, M. (2017). An investigation of vibrational power flow in one-dimensional dissipative phononic structures. *Journal of Vibration and Acoustics*, 139(2): 021003.
- Alberdi-Muniain, A., Gil-Negrete, N. and Kari, L. (2012). Direct energy flow measurement in magneto-sensitive vibration isolator systems. *Journal of Sound and Vibration*, 331(9): 1994-2006.
- Alujević, N., Wolf, H., Gardonio, P. and Tomac, I. (2011). Stability and performance limits for active vibration isolation using blended velocity feedback. *Journal of Sound and Vibration*, 330(21): 4981-4997.
- Antonio, J. (1984). *Power flow in structures during steady-state forced vibration*. PhD thesis, University of London.
- Awrejcewicz, J. and Olejnik, P. (2005). Analysis of dynamic systems with various friction laws. *Applied Mechanics Reviews*, 58(6): 389-411.
- Beale, L. S. and Accorsi, M. L. (1995). Power flow in two- and three-dimensional frame structures. *Journal of Sound and Vibration*, 185(4): 685-702.
- Beshara, M. and Keane, A. J. (1998). Vibrational energy flows between plates with compliant and dissipative couplings. *Journal of Sound and Vibration*, 213(3): 511-535.
- Bosetti, P., Biral, F. and Bortoluzzi, D. (2014). Design, manufacturing, and performance verification of a Roberts linkage for inertial isolation. *Precision Engineering*, 38(1): 138-147.
- Bosmans, I. and Nightingale, T. (2001). Modeling vibrational energy transmission at bolted junctions between a plate and a stiffening rib. *The Journal of the Acoustical Society of America*, 109: 999-1010.
- Cameron, T. M. and Griffin, J. H. (1989). An alternating frequency/time domain method for calculating the steady-state response of nonlinear dynamic systems. *Journal of Applied Mechanics*, 56(1): 149-154.
- Cao, Q., Wiercigroch, M., Pavlovskaja, E., Grebogi, C. and Thompson, J. (2006). Archetypal oscillator for smooth and discontinuous dynamics. *Physical review. E, Statistical, nonlinear, and soft matter physics*, 74: 046218.
- Carrella, A., Brennan, M. J. and Waters, T. P. (2007). Static analysis of a passive vibration isolator with quasi-zero-stiffness characteristic. *Journal of Sound and Vibration*, 301(3): 678-689.
- Carrella, A., Brennan, M. J., Kovacic, I. and Waters, T. P. (2009). On the force transmissibility of a vibration isolator with quasi-zero-stiffness. *Journal of Sound and Vibration*, 322(4): 707-717.

- Chang, Y., Kim, N. and Stenfelt, S. (2018). Simulation of the power transmission of bone-conducted sound in a finite-element model of the human head. *Biomechanics and Modeling in Mechanobiology*, 17(6): 1741-1755.
- Chatterjee, S., Mallik, A. K. and Ghosh, A. (1995). On impact dampers for non-linear vibrating systems. *Journal of Sound and Vibration*, 187(3): 403-420.
- Chávez, J. P., Pavlovskaja, E. and Wiercigroch, M. (2014). Bifurcation analysis of a piecewise-linear impact oscillator with drift. *Nonlinear Dynamics*, 77(1): 213-227.
- Chávez, J. P., Brzeski, P. and Perlikowski, P. (2017). Bifurcation analysis of non-linear oscillators interacting via soft impacts. *International Journal of Non-Linear Mechanics*, 92: 76-83.
- Chen, J. and Wang, R. (2014). Wave propagation and power flow analysis of sandwich structures with internal absorbers. *Journal of Vibration and Acoustics*, 136: 041003.
- Chen, L. and Liu, Y. (2019). Analysis of the input power flow characteristics of cylindrical shells with combination boundaries. *Journal of Low Frequency Noise, Vibration and Active Control*, 38(1): 93-109.
- Choi, W. J., Xiong, Y. P. and Shenoi, R. A. (2009). Power flow analysis for a floating sandwich raft isolation system using a higher-order theory. *Journal of Sound and Vibration*, 319(1): 228-246.
- Clarkson, B. L. (1991). Estimation of the coupling loss factor of structural joints. *Proceedings of the Institution of Mechanical Engineers, Part C: Mechanical Engineering Science*, 205(1): 17-22.
- Claeys, M., Sinou, J. J., Lambelin, J. P. and Todeschini, R. (2016). Experiments and numerical simulations of nonlinear vibration responses of an assembly with friction joints – Application on a test structure named “Harmony”. *Mechanical Systems and Signal Processing*, 70-71: 1097-1116.
- Collette, C. and Preumont, A. (2010). High frequency energy transfer in semi-active suspension. *Journal of Sound and Vibration*, 329(22): 4604-4616.
- Cuschieri, J. M. (1990). Structural power-flow analysis using a mobility approach of an L-shaped plate. *The Journal of the Acoustical Society of America*, 87(3): 1159-1165.
- Dai, W., Yang, J. and Shi, B. (2020). Vibration transmission and power flow in impact oscillators with linear and nonlinear constraints. *International Journal of Mechanical Sciences*, 168: 105234.
- Dai, W., Yang, J. (2021). Vibration transmission and energy flow of impact oscillators with nonlinear motion constraints created by diamond-shaped linkage mechanism. *International Journal of Mechanical Sciences*, 194:106212.
- Dong, J. H., Dong, R. G., Rakheja, S., Welcome, D. E., McDowell, T. W. and Wu, J. Z. (2008). A method for analyzing absorbed power distribution in the hand and arm substructures when operating vibrating tools. *Journal of Sound and Vibration*, 311(3): 1286-1304.
- Dormand, J. R. and Prince, P. J. (1980). A family of embedded Runge-Kutta formulae. *Journal of computational and applied mathematics*, 6(1): 19-26.

- Dou, C., Fan, J., Li, C., Cao, J. and Gao, M. (2020). On discontinuous dynamics of a class of friction-influenced oscillators with nonlinear damping under bilateral rigid constraints. *Mechanism and Machine Theory*, 147: 103750.
- Duffing, G. (1918). *Erzwungene Schwingungen bei veränderlicher Eigenfrequenz und ihre technische Bedeutung*. F. Vieweg & sohn.
- Elliott, S. J., Benassi, L., Brennan, M. J., Gardonio, P. and Huang, X. (2004). Mobility analysis of active isolation systems. *Journal of Sound and Vibration*, 271(1): 297-321.
- Fahy, F. J. and Gardonio, P. (2007). *Sound and structural vibration: radiation, transmission and response*: Elsevier.
- Fahy, F. J., Price, W. G. and Keane, A. J. (1994). Statistical energy analysis: a critical overview. *Philosophical Transactions of the Royal Society of London. Series A: Physical and Engineering Sciences*, 346(1681): 431-447.
- Farag, N. H. and Pan, J. (1996). Dynamic response and power flow in two-dimensional coupled beam structures under in-plane loading. *The Journal of the Acoustical Society of America*, 99(5): 2930-2937.
- Feng, G. P., Zhang, Z. Y., Chen, Y. and Hua, H. X. (2009). Research on transmission paths of a coupled beam-cylindrical shell system by power flow analysis. *Journal of Mechanical Science and Technology*, 23(8): 2138-2148.
- Feng, X., Jing, X., Xu, Z. and Guo, Y. (2019). Bio-inspired anti-vibration with nonlinear inertia coupling. *Mechanical Systems and Signal Processing*, 124: 562-595.
- Feeny, B. (1992). A nonsmooth coulomb friction oscillator. *Physica D: Nonlinear Phenomena*, 59(1): 25-38.
- Feeny, B. and Moon, F. C. (1994). Chaos in a forced dry-friction oscillator: experiments and numerical modelling. *Journal of Sound and Vibration*, 170(3): 303-323.
- Gao, R., Zhang, Y. and Kennedy, D. (2018). A hybrid boundary element-statistical energy analysis for the mid-frequency vibration of vibro-acoustic systems. *Computers & Structures*, 203: 34-42.
- Gaul, L. and Nitsche, R. (2001). The role of friction in mechanical joints. *Applied Mechanics Reviews*, 54(2): 93-106.
- Garoi, F., Winterflood, J., Ju, L., Jacob, J. and Blair, D. G. (2003). Passive vibration isolation using a Roberts linkage. *Review of Scientific Instruments*, 74(7): 3487-3491.
- Gerald, C. F. (2004). *Applied numerical analysis*. Pearson Education India.
- Ghandchi Tehrani, M., Wilmshurst, L. and Elliott, S. J. (2013). Receptance method for active vibration control of a nonlinear system. *Journal of Sound and Vibration*, 332(19): 4440-4449.
- Gilardi, G. and Sharf, I. (2002). Literature survey of contact dynamics modelling. *Mechanism and Machine Theory*, 37(10): 1213-1239.
- Goyder, H. G. D. and White, R. G. (1980). Vibrational power flow from machines into built-up structures, part I: Introduction and approximate analyses of beam and plate-like foundations. *Journal of Sound and Vibration*, 68(1): 59-75.

- Goyder, H. G. D. and White, R. G. (1980). Vibrational power flow from machines into built-up structures, part II: Wave propagation and power flow in beam-stiffened plates. *Journal of Sound and Vibration*, 68(1): 77-96.
- Goyder, H. G. D. and White, R. G. (1980). Vibrational power flow from machines into built-up structures, part III: Power flow through isolation systems. *Journal of Sound and Vibration*, 68(1): 97-117.
- Gupta, T. C., Gupta, K. and Sehgal, D. K. (2011). Instability and chaos of a flexible rotor ball bearing system: an investigation on the influence of rotating imbalance and bearing clearance. *Journal of Engineering for Gas Turbines and Power*, 133(8): 082501-082511.
- Guyomar, D., Lallart, M., Petit, L. and Wang, X.-J. (2011). Impact localization and energy quantification based on the power flow: A low-power requirement approach. *Journal of Sound and Vibration*, 330(13): 3270-3283.
- Hambric, S. A. (1990). Power Flow and Mechanical Intensity Calculations in Structural Finite-Element Analysis. *Journal of Vibration and Acoustics-Transactions of the Asme*, 112(4): 542-549.
- Hambric, S. A. and Taylor, P. D. (1994). Comparison of Experimental and Finite Element Structure-Borne Flexural Power Measurements for a Straight Beam. *Journal of Sound and Vibration*, 170(5): 595-605.
- Hao, Z. and Cao, Q. (2015). The isolation characteristics of an archetypal dynamical model with stable-quasi-zero-stiffness. *Journal of Sound and Vibration*, 340: 61-79.
- Hao, Z., Cao, Q. and Wiercigroch, M. (2017). Nonlinear dynamics of the quasi-zero-stiffness SD oscillator based upon the local and global bifurcation analyses. *Nonlinear Dynamics*, 87(2): 987-1014.
- Hawes, D. H., Langley, R. S., Butlin, T. and Ishii, Y. (2019). A hybrid Finite Element-Statistical Energy Analysis method for impulsive and transient loading. *Journal of Sound and Vibration*, 459: 114849.
- Horner, J. L. and White, R. G. (1991). Prediction of vibrational power transmission through bends and joints in beam-like structures. *Journal of Sound and Vibration*, 147(1): 87-103.
- Howard, C., Snyder, S. D. and Hansen, C. (2000). Calculation of Vibratory Power Transmission for use in Active Vibration Control. *Journal of Sound and Vibration*, 233: 569-581.
- Hong, J., Yu, P., Zhang, D. and Ma, Y. (2019). Nonlinear dynamic analysis using the complex nonlinear modes for a rotor system with an additional constraint due to rub-impact. *Mechanical Systems and Signal Processing*, 116: 443-461.
- Hou, L., Chen, H., Chen, Y., Lu, K. and Liu, Z. (2019). Bifurcation and stability analysis of a nonlinear rotor system subjected to constant excitation and rub-impact. *Mechanical Systems and Signal Processing*, 125: 65-78.
- Huang, X., Liu, X. and Hua, H. (2014). On the characteristics of an ultra-low frequency nonlinear isolator using sliding beam as negative stiffness. *Journal of Mechanical Science and Technology*, 28(3): 813-822.

- Huang, T., McFarland, D. M., Vakakis, A. F., Gendelman, O. V., Bergman, L. A. and Lu, H. (2020). Energy transmission by impact in a system of two discrete oscillators. *Nonlinear Dynamics*, 100(1): 135-145.
- Ibrahim, R. A. (2008). Recent advances in nonlinear passive vibration isolators. *Journal of Sound and Vibration*, 314(3): 371-452.
- Ing, J., Pavlovskaja, E. and Wiercigroch, M. (2006). Dynamics of a nearly symmetrical piecewise linear oscillator close to grazing incidence: Modelling and experimental verification. *Nonlinear Dynamics*, 46(3): 225-238.
- Ing, J., Pavlovskaja, E., Wiercigroch, M. and Banerjee, S. (2010). Bifurcation analysis of an impact oscillator with a one-sided elastic constraint near grazing. *Physica D: Nonlinear Phenomena*, 239(6): 312-321.
- Ji, L., Mace, B. R. and Pinnington, R. J. (2003). A power mode approach to estimating vibrational power transmitted by multiple sources. *Journal of Sound and Vibration*, 265(2): 387-399.
- Jiang, H., Chong, A. S. E., Ueda, Y. and Wiercigroch, M. (2017). Grazing-induced bifurcations in impact oscillators with elastic and rigid constraints. *International Journal of Mechanical Sciences*, 127: 204-214.
- Jiang, G., Jing, X. and Guo, Y. (2020). A novel bio-inspired multi-joint anti-vibration structure and its nonlinear HSLDS properties. *Mechanical Systems and Signal Processing*, 138: 106552.
- Jing, X., Zhang, L., Jiang, G., Feng, X., Guo, Y. and Xu, Z. (2019a). Critical factors in designing a class of X-shaped structures for vibration isolation. *Engineering Structures*, 199: 109659.
- Jing, X., Zhang, L., Feng, X., Sun, B. and Li, Q. (2019b). A novel bio-inspired anti-vibration structure for operating hand-held jackhammers. *Mechanical Systems and Signal Processing*, 118: 317-339.
- Karnopp, D. (1985). Computer simulation of stick-slip friction in mechanical dynamic systems. *Journal of Dynamic Systems, Measurement, and Control*, 107(1): 100-103.
- Kandasamy, R., Cui, F., Townsend, N., Foo, C. C., Guo, J., Sheno, A. and Xiong, Y. P. (2016). A review of vibration control methods for marine offshore structures. *Ocean Engineering*, 127: 279-297.
- Kim, Y. B. and Noah, S. T. (1991). Stability and Bifurcation Analysis of Oscillators With Piecewise-Linear Characteristics: A General Approach. *Journal of Applied Mechanics*, 58(2): 545-553.
- Kundu, S., Banerjee, S., Ing, J., Pavlovskaja, E. and Wiercigroch, M. (2012). Singularities in soft-impacting systems. *Physica D: Nonlinear Phenomena*, 241(5): 553-565.
- Krack, M., Bergman, L. A. and Vakakis, A. F. (2016). On the efficacy of friction damping in the presence of nonlinear modal interactions. *Journal of Sound and Vibration*, 370: 209-220.
- Krack, M., Salles, L. and Thouverez, F. (2017). Vibration prediction of bladed disks coupled by friction joints. *Archives of Computational Methods in Engineering*, 24(3): 589-636.

- Krack, M. and Gross, J. (2019). *Harmonic balance for nonlinear vibration problems*. Springer.
- Kwon, H.-W., Hong, S.-Y., Lee, H.-W. and Song, J.-H. (2011). Power flow boundary element analysis for multi-domain problems in vibrational built-up structures. *Journal of Sound and Vibration*, 330(26): 6482-6494.
- Lai, Z. H., Thomson, G., Yurchenko, D., Val, D. V. and Rodgers, E. (2018). On energy harvesting from a vibro-impact oscillator with dielectric membranes. *Mechanical Systems and Signal Processing*, 107: 105-121.
- Lambert, J. D. (1991). *Numerical methods for ordinary differential systems: the initial value problem*. John Wiley & Sons, Inc.
- Langley, R. S. (1989). Application of the dynamic stiffness method to the free and forced vibrations of aircraft panels. *Journal of Sound and Vibration*, 135(2): 319-331.
- Langley, R. S. (1990). Analysis of power flow in beams and frameworks using the direct-dynamic stiffness method. *Journal of Sound and Vibration*, 136(3): 439-452.
- Langley, R. S. (1992). A wave intensity technique for the analysis of high frequency vibrations. *Journal of Sound and Vibration*, 159(3): 483-502.
- Lau, S. L. and Zhang, W. S. (1992). Nonlinear vibrations of piecewise-linear systems by incremental harmonic balance method. *Journal of Applied Mechanics*, 59(1): 153-160.
- Le, T. D. and Ahn, K. K. (2013). Experimental investigation of a vibration isolation system using negative stiffness structure. *International Journal of Mechanical Sciences*, 70: 99-112.
- Lee, C. M., Goverdovskiy, V. N. and Temnikov, A. I. (2007). Design of springs with “negative” stiffness to improve vehicle driver vibration isolation. *Journal of Sound and Vibration*, 302(4): 865-874.
- Lee, S. K. (2000). Application of vibrational power flow to a passenger car for reduction of interior noise. *Shock and Vibration*, 7: 277-285.
- Lee, H. P., Lim, S. P. and Khun, M. S. (2006). Diversion of energy flow near crack tips of a vibrating plate using the structural intensity technique. *Journal of Sound and Vibration*, 296(3): 602-622.
- Li, C., Fan, J., Yang, Z. and Xue, S. (2019). On discontinuous dynamical behaviors of a 2-DOF impact oscillator with friction and a periodically forced excitation. *Mechanism and Machine Theory*, 135: 81-108.
- Li, G. and Ding, W. (2018). Global behavior of a vibro-impact system with asymmetric clearances. *Journal of Sound and Vibration*, 423: 180-194.
- Li, Q. and Wu, D. J. (2013). Analysis of the dominant vibration frequencies of rail bridges for structure-borne noise using a power flow method. *Journal of Sound and Vibration*, 332(18): 4153-4163.
- Li, W. L., Bonilha, M. W. and Xiao, J. (2007). Vibrations and Power Flows in a Coupled Beam System. *Journal of Vibration and Acoustics*, 129(5): 616-622.

- Liao, M., Liu, Y., Páez Chávez, J., Chong, A. S. E. and Wiercigroch, M. (2018). Dynamics of vibro-impact drilling with linear and nonlinear rock models. *International Journal of Mechanical Sciences*, 146-147: 200-210.
- Liu, C. and Yu, K. (2018). A high-static–low-dynamic-stiffness vibration isolator with the auxiliary system. *Nonlinear Dynamics*, 94(3): 1549-1567.
- Liu, C. and Yu, K. (2020). Accurate modeling and analysis of a typical nonlinear vibration isolator with quasi-zero stiffness. *Nonlinear Dynamics*, 100(3): 2141-2165.
- Liu, C.-C., Li, F.-M., Fang, B., Zhao, Y. and Huang, W.-H. (2010). Active control of power flow transmission in finite connected plate. *Journal of Sound and Vibration*, 329(20): 4124-4135.
- Liu, G., Yang, T., Leng, D., Tian, X., Xie, Y. and Mu, W. (2018). Optimization of autonomous underwater vehicle structure shape based on the characteristics of power flow distribution. *Marine Structures*, 62: 77-89.
- Liu, Q., Thompson, D. J., Xu, P., Feng, Q. and Li, X. (2020). Investigation of train-induced vibration and noise from a steel-concrete composite railway bridge using a hybrid finite element-statistical energy analysis method. *Journal of Sound and Vibration*, 471: 115197.
- López, I., Busturia, J. M. and Nijmeijer, H. (2004). Energy dissipation of a friction damper. *Journal of Sound and Vibration*, 278(3): 539-561.
- Liu, Z., Yuan, S., Xiao, S., Du, S., Zhang, Y. and Lu, C. (2017). Full vehicle vibration and noise analysis based on substructure power flow. *Shock and Vibration*, 2017: 8725346.
- López, I., Busturia, J. M. and Nijmeijer, H. (2004). Energy dissipation of a friction damper. *Journal of Sound and Vibration*, 278(3): 539-561.
- López, I. and Nijmeijer, H. (2009). Prediction and validation of the energy dissipation of a friction damper. *Journal of Sound and Vibration*, 328(4): 396-410.
- Lu, Z., Brennan, M. J., Yang, T., Li, X. and Liu, Z. (2013). An investigation of a two-stage nonlinear vibration isolation system. *Journal of Sound and Vibration*, 332(6): 1456-1464.
- Luo, G. W., Lv, X. H., Zhu, X. F., Shi, Y. Q. and Du, S. S. (2018). Diversity and transition characteristics of sticking and non-sticking periodic impact motions of periodically forced impact systems with large dissipation. *Nonlinear Dynamics*, 94(2): 1047-1079.
- Lyon, R. H. (1975). Statistical energy analysis of dynamical systems. *Theory and Applications*: The MIT Press.
- Luo, A. C. J. and Gegg, B. C. (2006). Stick and non-stick periodic motions in periodically forced oscillators with dry friction. *Journal of Sound and Vibration*, 291(1): 132-168.
- Lyon, R. H. and Maidanik, G. (1962). Power flow between linearly coupled oscillators. *The Journal of the Acoustical Society of America*, 34(5): 623-639.
- Ma, Y., Agarwal, M. and Banerjee, S. (2006). Border collision bifurcations in a soft impact system. *Physics Letters A*, 354(4): 281-287.

- Ma, Y., Zhang, Y. and Kennedy, D. (2016). Energy flow analysis of mid-frequency vibration of coupled plate structures with a hybrid analytical wave and finite element model. *Computers & Structures*, 175: 1-14.
- Mace, B. R. (2005). Statistical energy analysis: coupling loss factors, indirect coupling and system modes. *Journal of Sound and Vibration*, 279(1): 141-170.
- Mace, B. R. and Shorter, P. J. (2000). Energy flow models from finite element analysis. *Journal of Sound and Vibration*, 233(3): 369-389.
- Manning, J. E. (1994). Formulation of sea parameters using mobility functions. *Philosophical Transactions: Physical Sciences and Engineering*, 346(1681): 477-488.
- Marino, L., Cicirello, A. and Hills, D. A. (2019). Displacement transmissibility of a Coulomb friction oscillator subject to joined base-wall motion. *Nonlinear Dynamics*, 98(4): 2595-2612.
- Marques, F., Flores, P., Pimenta Claro, J. C. and Lankarani, H. M. (2016). A survey and comparison of several friction force models for dynamic analysis of multibody mechanical systems. *Nonlinear Dynamics*, 86(3): 1407-1443.
- McDaniel, J. G., Li, X., Moore, J. and Chen, S.-E. (2001). Analysis of instabilities and power flow in brake systems with coupled rotor modes. *SAE Technical Paper Series*. SAE International.
- Miller, D. W. and von Flotow, A. (1989). A travelling wave approach to power flow in structural networks. *Journal of Sound and Vibration*, 128(1): 145-162.
- Ming, R. S., Pan, J. and Norton, M. P. (1999). The mobility functions and their application in calculating power flow in coupled cylindrical shells. *The Journal of the Acoustical Society of America*, 105(3): 1702-1713.
- Morse, P. M., Acoustical Society of America and American Institute of Physics (1948). *Vibration and sound*. McGraw-Hill New York.
- Moorhouse, A. (2002). A dimensionless mobility formulation for evaluation of force and moment excitation of structures. *The Journal of the Acoustical Society of America*, 112: 972-980.
- Mostaghel, N. and Davis, T. (1997). Representations of coulomb friction for dynamic analysis. *Earthquake Engineering & Structural Dynamics*, 26(5): 541-548.
- Mostaghel, N. (2005). A non-standard analysis approach to systems involving friction. *Journal of Sound and Vibration*, 284(3): 583-595.
- Nayfeh, A. H. and Balachandran, B. (2008). *Applied nonlinear dynamics: analytical, computational, and experimental methods*. John Wiley & Sons.
- Narimani, A., Golnaraghi, M. E. and Jazar, G. N. (2004). Frequency response of a piecewise linear vibration isolator. *Modal Analysis*, 10(12): 1775-1794.
- Natsiavas, S. (1990). On the dynamics of oscillators with bi-linear damping and stiffness. *International Journal of Non-Linear Mechanics*, 25(5): 535-554.
- Nefske, D. J. and Sung, S. H. (1989). Power flow finite element analysis of dynamic systems: basic theory and application to beams. *Journal of Vibration, Acoustics, Stress, and Reliability in Design*, 111(1): 94-100.

- Nordmark, A. B. (1991). Non-periodic motion caused by grazing incidence in an impact oscillator. *Journal of Sound and Vibration*, 145(2): 279-297.
- Oestreich, M., Hinrichs, N. and Popp, K. (1996). Bifurcation and stability analysis for a non-smooth friction oscillator. *Archive of Applied Mechanics*, 66(5): 301-314.
- Palomares, E., Nieto, A. J., Morales, A. L., Chicharro, J. M. and Pintado, P. (2018). Numerical and experimental analysis of a vibration isolator equipped with a negative stiffness system. *Journal of Sound and Vibration*, 414: 31-42.
- Pascal, M. (2014). Sticking and nonsticking orbits for a two-degree-of-freedom oscillator excited by dry friction and harmonic loading. *Nonlinear Dynamics*, 77(1): 267-276.
- Peletan, L., Baguet, S., Torkhani, M. and Jacquet-Richardet, G. (2014). Quasi-periodic harmonic balance method for rubbing self-induced vibrations in rotor–stator dynamics. *Nonlinear Dynamics*, 78(4): 2501-2515.
- Peksen, M. (2018). *Multiphysics Modelling*. Academic Press.
- Pennestrì, E., Rossi, V., Salvini, P. and Valentini, P. P. (2016). Review and comparison of dry friction force models. *Nonlinear Dynamics*, 83(4): 1785-1801.
- Pinnington, R. and White, R. (1981). Power flow through machine isolators to resonant and non-resonant beams. *Journal of Sound and Vibration*, 75(2): 179-197.
- Plumbridge, W., Matela, R. J. and Westwater, A. (2007). *Structural integrity and reliability in electronics: enhancing performance in a lead-free environment*. Springer Science & Business Media.
- Popp, K. (1998). Non-smooth mechanical systems — an overview. *Forschung im Ingenieurwesen*, 64(9): 223.
- Popp, K. (2000). Non-smooth mechanical systems. *Journal of Applied Mathematics and Mechanics*, 64(5): 765-772.
- Press, W. H., Flannery, B. P., Teukolsky, S. A. and Vetterling, W. T. (1989). *Numerical recipes*. Cambridge University Press Cambridge.
- Qian, Z., Zhang, D. and Jin, C. (2018). A regularized approach for frictional impact dynamics of flexible multi-link manipulator arms considering the dynamic stiffening effect. *Multibody System Dynamics*, 43(3): 229-255.
- Rao, S. S. (2011). *Mechanical Vibrations.[SI]*. Pearson Education, Inc.
- Rivin, E. I. (2004). *Passive Vibration Isolation*: ASME Press.
- Royston, T. J. and Singh, R. (1996). Optimization of passive and active non-linear vibration mounting systems based on vibratory power transmission. *Journal of Sound and Vibration*, 194(3): 295-316.
- Royston, T. J. and Singh, R. (1997). Vibratory power flow through a nonlinear path into a resonant receiver. *The Journal of the Acoustical Society of America*, 101(4): 2059-2069.
- Sciulli, D. and Inman, D. J. (1998). Isolation design for a flexible system. *Journal of Sound and Vibration*, 216(2): 251-267.

- Seo, S.-H., Hong, S.-Y. and Kil, H.-G. (2003). Power flow analysis of reinforced beam–plate coupled structures. *Journal of Sound and Vibration*, 259(5): 1109-1129.
- Seydel, R. (2009). *Practical bifurcation and stability analysis*: Springer Science & Business Media.
- Shaw, S. W. and Holmes, P. J. (1983). A periodically forced piecewise linear oscillator. *Journal of Sound and Vibration*, 90(1): 129-155.
- Shi, B. and Yang, J. (2019a). Quantification of vibration force and power flow transmission between coupled nonlinear oscillators. *International Journal of Dynamics and Control*, 8(2): 418-435.
- Shi, B., Yang, J. and Rudd, C. (2019b). On vibration transmission in oscillating systems incorporating bilinear stiffness and damping elements. *International Journal of Mechanical Sciences*, 150: 458-470.
- Sun, L. L., Hansen, C. H. and Doolan, C. (2015). Evaluation of the performance of a passive–active vibration isolation system. *Mechanical Systems and Signal Processing*, 50-51: 480-497.
- Sun, X. and Jing, X. (2016). A nonlinear vibration isolator achieving high-static-low-dynamic stiffness and tunable anti-resonance frequency band. *Mechanical Systems and Signal Processing*, 80: 166-188.
- Sun, X., Jing, X., Xu, J. and Cheng, L. (2014). Vibration isolation via a scissor-like structured platform. *Journal of Sound and Vibration*, 333(9): 2404-2420.
- Sun, X., Xu, J., Wang, F. and Zhang, S. (2018). A novel isolation structure with flexible joints for impact and ultralow-frequency excitations. *International Journal of Mechanical Sciences*, 146-147: 366-376.
- Sun, Y., Zhou, J., Thompson, D., Yuan, T., Gong, D. and You, T. (2020). Design, analysis and experimental validation of high static and low dynamic stiffness mounts based on target force curves. *International Journal of Non-Linear Mechanics*, 126: 103559.
- Szwerc, R. P., Burroughs, C. B., Hambric, S. A. and McDevitt, T. E. (2000). Power flow in coupled bending and longitudinal waves in beams. *The Journal of the Acoustical Society of America*, 107(6): 3186-3195.
- Tang, B. and Brennan, M. J. (2013). A comparison of two nonlinear damping mechanisms in a vibration isolator. *Journal of Sound and Vibration*, 332(3): 510-520.
- Tang, Y.-Q., Li, T.-J. and Yan, Q.-Y. (2017). Damage Analysis of One-Dimensional Euler–Bernoulli Cracked Beam with Traveling Wave Method. *International Journal of Applied Mechanics*, 09(04): 1750048.
- Theodossiades, S. and Natsiavas, S. (2000). Non-linear dynamics of gear-pair systems with periodic stiffness and backlash. *Journal of Sound and Vibration*, 229: 287-310.
- Ungar, E. E. (1967). Statistical Energy Analysis of Vibrating Systems. *Journal of Engineering for Industry*, 89(4): 626-632.
- Vakakis, A. F., Gendelman, O. V., Bergman, L. A., McFarland, D. M., Kerschen, G. and Lee, Y. S. (2008). *Nonlinear targeted energy transfer in mechanical and structural systems*. Springer Science & Business Media.

- van de Vrande, B. L., van Campen, D. H. and de Kraker, A. (1999). An approximate analysis of dry-friction-induced stick-slip vibrations by a smoothing procedure. *Nonlinear Dynamics*, 19(2): 159-171.
- Virgin, L. N., Santillan, S. T. and Plaut, R. H. (2008). Vibration isolation using extreme geometric nonlinearity. *Journal of Sound and Vibration*, 315(3): 721-731.
- Von Groll, G. and Ewins, D. J. (2001). The harmonic balance method with arc-length continuation in rotor/stator contact problems. *Journal of Sound and Vibration*, 241(2): 223-233.
- Walsh, S. J. and White, R. G. (2000). Vibrational power transmission in curved beams. *Journal of Sound and Vibration*, 233(3): 455-488.
- Wang, Y., Du, J. and Cheng, L. (2019). Power flow and structural intensity analyses of Acoustic Black Hole beams. *Mechanical Systems and Signal Processing*, 131: 538-553.
- Wang, Y., Jing, X., Dai, H. and Li, F. M. (2019). Subharmonics and ultra-subharmonics of a bio-inspired nonlinear isolation system. *International Journal of Mechanical Sciences*, 152: 167-184.
- Wang, Y., Lu, C., Qin, X., Huang, S., Tan, X. and Sun, Y. (2020). Control of structure-borne noise for a vehicle body by using power flow analysis and acoustic path participation method. *Applied Acoustics*, 157: 106981.
- Wang, Z. H., Xing, J. T. and Price, W. G. (2002a). An investigation of power flow characteristics of l-shaped plates adopting a substructure approach. *Journal of Sound and Vibration*, 250(4): 627-648.
- Wang, Z. H., Xing, J. T. and Price, W. G. (2002b). Power flow analysis of indeterminate rod/beam systems using a substructure method. *Journal of Sound and Vibration*, 249(1): 3-22.
- Wang, Z. H., Xing, J. T. and Price, W. G. (2004). A study of power flow in a coupled plate-cylindrical shell system. *Journal of Sound and Vibration*, 271(3): 863-882.
- Wei, H., Jian, X., Da-yong, Z., Ming-yi, H., Jian-wei, L., Kun-lin, L. and Jun-cai, W. (2016). Parameter configuration of composite vibration isolation system using power flow and MOPSO technique. *Mechanics & Industry*, 17: 501.
- Weisser, T., Foltête, E., Bouhaddi, N. and Gonidou, L.-O. (2015). A power flow mode approach dedicated to structural interface dynamic characterization. *Journal of Sound and Vibration*, 334: 202-218.
- Wester, E. C. N. and Mace, B. R. (2005a). Wave component analysis of energy flow in complex structures – Part I: a deterministic model. *Journal of Sound and Vibration*, 285(1): 209-227.
- Wester, E. C. N. and Mace, B. R. (2005b). Wave component analysis of energy flow in complex structures–Part II: ensemble statistics. *Journal of Sound and Vibration*, 285(1): 229-250.
- Wester, E. C. N. and Mace, B. R. (2005c). Wave component analysis of energy flow in complex structures – Part III: two coupled plates. *Journal of Sound and Vibration*, 285(1): 251-265.
- Weaver Jr, W., Timoshenko, S. P. and Young, D. H. (1990). *Vibration problems in engineering*. John Wiley & Sons.

- Wiercigroch, M. and Krivtsov, A. M. (2001). Frictional chatter in orthogonal metal cutting. *Philosophical Transactions of the Royal Society of London. Series A: Mathematical, Physical and Engineering Sciences*, 359(1781): 713-738.
- Wiercigroch, M., Kovacs, S., Zhong, S., Costa, D., Vaziri, V., Kapitaniak, M. and Pavlovskaia, E. (2020). Versatile mass excited impact oscillator. *Nonlinear Dynamics*, 99(1): 323-339.
- Winterflood, J. and Blair, D. G. (1996). A long-period conical pendulum for vibration isolation. *Physics Letters A*, 222(3): 141-147.
- Winterflood, J. and Blair, D. G. (1998). A long-period vertical vibration isolator for gravitational wave detection. *Physics Letters A*, 243(1): 1-6.
- Winterflood, J., Losurdo, G. and Blair, D. G. (1999). Initial results from a long-period conical pendulum vibration isolator with application for gravitational wave detection. *Physics Letters A*, 263(1): 9-14.
- Wohlever, J. C. and Bernhard, R. J. (1992). Mechanical energy flow models of rods and beams. *Journal of Sound and Vibration*, 153(1): 1-19.
- Wong, W. O., Wang, X. Q. and Cheng, L. (2009). Modal power flow analysis of a damaged plate. *Journal of Sound and Vibration*, 320(1): 84-100.
- Wu, W., Yin, X., Li, H. and Zhong, K. (2018). Power flow analysis of built-up plate structures using the dynamic stiffness method. *Journal of Vibration and Control*, 24(13): 2815-2831.
- Wu, W. and Tang, B. (2020). An approximate method for solving force and displacement transmissibility of a geometrically nonlinear isolation system. *International Journal of Non-Linear Mechanics*, 125: 103512.
- Xing, J. T. and Price, W. G. (1999). A power-flow analysis based on continuum dynamics. *Proceedings of the Royal Society of London. Series A: Mathematical, Physical and Engineering Sciences*, 455(1982): 401-436.
- Xing, J. T., Price, W. G. and Du, Q. H. (1996). Mixed finite element substructure—subdomain methods for the dynamical analysis of coupled fluid-solid interaction problems. *Philosophical Transactions of the Royal Society of London. Series A: Mathematical, Physical and Engineering Sciences*, 354(1705): 259-295.
- Xiong, Y. P. and Cao, Q. (2011). Power flow characteristics of coupled linear and nonlinear oscillators with irrational nonlinear stiffness. In *Proceedings of the Seventh European Nonlinear Dynamics Conference*, pages 1-6.
- Xiong, Y. P., Xing, J. T. and Price, W. G. (2001). Power flow analysis of complex coupled systems by progressive approaches. *Journal of Sound and Vibration*, 239(2): 275-295.
- Xiong, Y. P., Xing, J. T. and Price, W. G. (2003). A general linear mathematical model of power flow analysis and control for integrated structure-control systems. *Journal of Sound and Vibration*, 267(2): 301-334.
- Xiong, Y.-P., Xing, J. T. and Price, W. G. (2005a). A power flow mode theory based on a system's damping distribution and power flow design approaches. *Proceedings of The Royal Society A: Mathematical, Physical and Engineering Sciences*, 461: 3381-3411.

- Xiong, Y. P., Xing, J. T. and Price, W. G. (2005b). Interactive power flow characteristics of an integrated equipment—nonlinear isolator—travelling flexible ship excited by sea waves. *Journal of Sound and Vibration*, 287(1): 245-276.
- Xu, X. D., Lee, H. P., Wang, Y. Y. and Lu, C. (2004). The energy flow analysis in stiffened plates of marine structures. *Thin-Walled Structures*, 42(7): 979-994.
- Yan, B., Brennan, M. J., Elliott, S. J. and Ferguson, N. S. (2010). Active vibration isolation of a system with a distributed parameter isolator using absolute velocity feedback control. *Journal of Sound and Vibration*, 329(10): 1601-1614.
- Yan, L., Xuan, S. and Gong, X. (2018). Shock isolation performance of a geometric anti-spring isolator. *Journal of Sound and Vibration*, 413: 120-143.
- Yang, J., Jiang, J. Z. and Neild, S. A. (2019). Dynamic analysis and performance evaluation of nonlinear inerter-based vibration isolators. *Nonlinear Dynamics*, 99(3): 1823-1839.
- Yang, J., Shi, B. and Rudd, C. (2018). On vibration transmission between interactive oscillators with nonlinear coupling interface. *International Journal of Mechanical Sciences*, 137: 238-251.
- Yang, J., Xiong, Y. P. and Xing, J. T. (2013). Dynamics and power flow behaviour of a nonlinear vibration isolation system with a negative stiffness mechanism. *Journal of Sound and Vibration*, 332(1): 167-183.
- Yang, J., Xiong, Y. P. and Xing, J. T. (2014). Nonlinear power flow analysis of the Duffing oscillator. *Mechanical Systems and Signal Processing*, 45(2): 563-578.
- Yang, J., Xiong, Y. P. and Xing, J. T. (2015). Power flow behaviour and dynamic performance of a nonlinear vibration absorber coupled to a nonlinear oscillator. *Nonlinear Dynamics*, 80(3): 1063-1079.
- Yang, J., Xiong, Y. P. and Xing, J. T. (2016). Vibration power flow and force transmission behaviour of a nonlinear isolator mounted on a nonlinear base. *International Journal of Mechanical Sciences*, 115-116: 238-252.
- Yang, K., Harne, R. L., Wang, K. W. and Huang, H. (2014). Investigation of a bistable dual-stage vibration isolator under harmonic excitation. *Smart Materials and Structures*, 23(4): 045033.
- Yin, S., Yu, D., Yin, H., Lü, H. and Xia, B. (2017). Hybrid Evidence Theory-based Finite Element/Statistical Energy Analysis method for mid-frequency analysis of built-up systems with epistemic uncertainties. *Mechanical Systems and Signal Processing*, 93: 204-224.
- Zhang, Z., Zhang, Y.-W. and Ding, H. (2020). Vibration control combining nonlinear isolation and nonlinear absorption. *Nonlinear Dynamics*, 100(3): 2121-2139.
- Zheng, X., Dai, W., Qiu, Y. and Hao, Z. (2019). Prediction and energy contribution analysis of interior noise in a high-speed train based on modified energy finite element analysis. *Mechanical Systems and Signal Processing*, 126: 439-457.
- Zheng, Y., Zhang, X., Luo, Y., Yan, B. and Ma, C. (2016). Design and experiment of a high-static–low-dynamic stiffness isolator using a negative stiffness magnetic spring. *Journal of Sound and Vibration*, 360: 31-52.
- Zheng, Y., Zhang, X., Luo, Y., Zhang, Y. and Xie, S. (2018). Analytical study of a

quasi-zero stiffness coupling using a torsion magnetic spring with negative stiffness. *Mechanical Systems and Signal Processing*, 100: 135-151.

Zhu, C., Yang, J. and Rudd, C. (2021). Vibration transmission and power flow of laminated composite plates with inerter-based suppression configurations. *International Journal of Mechanical Sciences*, 190: 106012.

Zhu, L.-F., Ke, L.-L., Xiang, Y., Zhu, X.-Q. and Wang, Y.-S. (2020). Vibrational power flow analysis of cracked functionally graded beams. *Thin-Walled Structures*, 150: 106626.

Zhu, X., Li, T. Y., Zhao, Y. and Liu, J. X. (2006). Structural power flow analysis of Timoshenko beam with an open crack. *Journal of Sound and Vibration*, 297(1): 215-226.

Zhu, X., Xiao, G. Y., Li, T. Y. and Hu, X. F. (2011) Vibrational power flow analysis of stiffened plate and shell structures. In *Applied Mechanics and Materials*. 66:1897-1901.